

Nanosatellite Store-and-Forward Communication Systems for Remote Data Collection Applications

著者	Salces Adrian Cabuenas
year	2020-09
学位授与年度	令和2年度
学位授与番号	17104甲工第506号
URL	http://hdl.handle.net/10228/00007948

Nanosatellite Store-and-Forward Communication Systems for Remote Data Collection Applications

By: SALCES Adrian Cabueñas

Student Number: 16595906



Kyushu Institute of Technology

Graduate School of Engineering

Department of Applied Science for Integrated Systems Engineering

*A dissertation submitted in partial fulfilment of the requirements for the degree
of Doctor of Philosophy in Engineering*

September 2020

Declaration

I hereby declare that the work presented in this thesis has not been submitted for any other degree or professional qualification, and that it is the result of my own independent work.

SALCES Adrian Cabueñas

Full Name of Candidate

September 18, 2020

Date

Abstract

Due to compact design, cost-effectiveness and shorter development time, a nanosatellite constellation is seen as a viable space-based data-relay asset to collect data from remote places that are rather impractical to be linked by terrestrial means. While nanosatellites have these advantages, they have more inherent technical limitations because of limited space for subsystems and payloads. Nanosatellite S&F communication systems are notably challenging in this respect due to requirements on antennas, transceivers, and signal processing. Although nanosatellites can be scaled up for better resources and capabilities, smaller platforms (i.e., $\leq 6U$ CubeSat) tend to be used for cost-effectiveness and lower risk. This thesis dealt with the problem of designing a nanosatellite S&F communication system for delay-tolerant remote data collection applications considering: (a) technical constraints in hardware, processing capabilities, energy budget and space in both the nanosatellite and ground sensor terminal (GST) sides; (b) physical communication layer characteristics and constraints such as limited available bandwidth, LEO channel Doppler, attenuation and fading/shadowing effects, low transmit power and data rate, and multi-user interference among asynchronously transmitting terminals. We designed, developed, and operated an amateur radio payload with S&F communication and APRS-DP capabilities, and performed a post-launch communication failure investigation. We also investigated suitability of E-SSA protocol for IoT/M2M terminals to nanosatellite communication by analyzing performance and energy efficiency metrics.

The thesis comprises nine chapters. Chapter 1 describes the research background, problem, objectives, state of research, potential contributions of this thesis, and a gist of methodology detailed in later chapters. Chapter 2 and 3 provide an extensive literature review. Chapter 2 reviews the previous research works on using nanosatellites for S&F communication for remote data collection, and the previous nanosatellite S&F missions. Such research works and nanosatellite missions were undertaken primarily in the context of non-commercial/civil applications. Then, Chapter 2 surveys the recent commercial nanosatellite IoT/M2M players and examines their proposed systems in terms of satellite platform, constellation design, communication technology, targeted applications, requirements, and performance. Chapter 3 presents a literature review on communication system architecture, physical layer and random-access schemes, protocols, and technologies relevant to satellite IoT/M2M systems. In the context of IoT/M2M applications, the constraints in energy budget, transmit power and available bandwidth limit the system's capacity in terms of amount of data that can be received and number of GSTs that can be supported. In both nanosatellite and GST sides, there are stringent limitations in hardware complexity, processing capabilities and energy budget. Addressing these challenges requires a simple, spectrally and energy efficient asynchronous random-access communication protocol. This research investigated using the enhanced spread spectrum Aloha (E-SSA) protocol for satellite IoT/M2M uplink (terminal to satellite) communication and analyzed its performance and suitability for the said application.

Chapter 4 discusses the BIRDS-2 CubeSat S&F remote data collection system, payload design, development, tests, and integration with the BIRDS-2 CubeSats. Chapter 5 discusses the investigation

on communication design issues of BIRDS-2 CubeSat S&F payload, tackling both the methodology and findings of investigation. It is noted that there are only a few satellites that have carried an APRS-DP payload but even some of these failed due to communication, power, or software issues. In BIRDS-2 Project, considering tight constraints in a 1U CubeSat equipped with other subsystems and payloads, we developed a S&F/APRS-DP payload and integrated it with each of the three 1U CubeSats of participating countries. After launching the CubeSats from the ISS, several amateur operators confirmed reception downlink beacon messages, but full two-way communication failed due to uplink communication failure. Thus, this research not only studied the design and development of a S&F/APRS-DP payload suitable for a CubeSat platform, but also systematically investigated the causes of communication failure by on-orbit observation results and ground-based tests. We found that uplink failure was caused by two design problems that were overlooked during development, namely, the poor antenna performance and increased payload receiver noise floor due to satellite-radiated EMI coupled to the antenna.

Chapter 6 first describes the enhanced spread spectrum Aloha (E-SSA) based nanosatellite IoT/M2M communication model implemented in Matlab and derives the mathematical definitions of packet loss rate (PLR), throughput (THR) and energy efficiency (EE) metrics. Then, it tackles the formulated baseband signal processing algorithm for E-SSA, including packet detection, channel estimation, demodulation and decoding. Chapter 7 presents the simulation results and discussion for Chapter 6. Chapter 8 tackles the S&F nanosatellite constellation design for global coverage and presents the results and findings. Chapter 9 describes the laboratory setups for validating the E-SSA protocol and then presents the findings. Finally, Chapter 9 also gives the summary, conclusions, and recommendations.

Simulation results showed that for E-SSA protocol with the formulated algorithm, THR, PLR and EE metrics are more sensitive to MAC load G , received power variation σ_{LN} and E_b/N_0 , due to imperfect detection and channel estimation. With loose power control ($\sigma_{LN} = 3$ dB), at $E_b/N_0=14$ dB, the system can be operated up to a maximum load of 1.3 bps/Hz, achieving a maximum THR of 1.25 bps/Hz with $PLR < 0.03$. Without power control ($\sigma_{LN} = 6$ dB, 9dB), at $E_b/N_0=14$ dB, maximum load is also 1.3 bps/Hz, but achievable THR is lower than ~ 1 bps/Hz and PLR values can be as high as ~ 0.23 . Worse PLR results are attributed to misdetection of lower power packets and demodulation/decoding errors. Both are caused by the combined effects of MUI, channel estimation errors, imperfect interference cancellation residue power, and noise. The PLR and THR can be improved by operating with higher E_b/N_0 at the expense of lower energy efficiency. Then, laboratory validation experiments using a SDR-based platform confirmed that with $G=0.1$, $E_b/N_0 = 14$ dB, $\sigma_{LN} = 6$ dB, the formulated algorithm for E-SSA protocol can still work even with inaccurate oscillator (± 2 ppm) at GSTs, obtaining experimental PLR result of 0.0650 compared to simulation result of 0.0352. However, this requires lowering the detection thresholds and takes significantly longer processing time. For the S&F nanosatellite constellation design, it was found that to achieve the target percent coverage time (PCT) of more than 95% across all latitudes, a 9x10 Hybrid constellation or a 10x10 Walker Delta constellation would be required.

Publications associated with this research

This research is associated with the following publications:

参 考 論 文

1. “Proposed Store-and-Forward Lean Satellite-based Remote Data Collection System of the BIRDS-2 Project”
61st Japan Society for Astronautical and Space Sciences (JSASS) Conference, Niigata City, Japan.
(9 pages)
(2017 年 10 月)
著者 A.C. Salces, S. Kim, G. Maeda, H. Masui, M. Cho
2. “Design, Development, Testing and On-Orbit Performance Results of a Low-cost Store-and-Forward Payload Onboard a 1 U CubeSat Constellation for Remote Data Collection Applications”
Proceedings of the 69th International Astronautical Congress (IAC), Bremen, Germany.
(14 pages)
(2018 年 10 月)
著者 A.C. Salces, S.B.M. Zaki, S. Kim, H. Masui, M. Cho
3. “BIRDS-2 1U CubeSat Constellation Missions and Initial Flight Operation Results”
62nd Japan Society for Astronautical and Space Sciences (JSASS) Conference, Kurume City, Japan.
(5 pages)
(2018 年 10 月)
著者 A.C. Salces, P. Faure, S. Kim, G. Maeda, H. Masui, M. Cho
4. “BIRDS-2 Project CubeSat Development Overview, On-orbit Operation Results and Recent Progress of BIRDS-3 Project”
Proceedings of the 32nd ISTS & 9th NSAT, Fukui City, Japan.
(10 pages)
(2019 年 6 月)
著者 A.C. Salces, T. Dayarathna, S.B.M. Zaki, M. Kishimoto, K.K. Pradhan, A. Maskey, A. Jirawattanaphol, S. Kim, G. Maeda, H. Masui, M. Cho

5. “Development and Investigation of Communication Issues on a CubeSat-onboard Amateur Radio Payload with APRS Digipeater and Store-and-Forward Capabilities”

SPACE TAKUMI JOURNAL (Vol.9, No.2, pp. 17-46)

Published online (30 pages)

(2020年6月)

著者 A.C. Salces, M.P. Sejera, S. Kim, H. Masui, M. Cho

In addition, we have submitted a journal manuscript entitled “Performance Analysis and Signal Processing Algorithm for a Spread Spectrum Aloha-based Satellite IoT/M2M Communication System” (30 pages) to the *International Journal of Satellite Communication and Networking*. It is currently under review.

Acknowledgements

To my research supervisor, Prof. Mengu Cho, for providing expertise, guidance, and wisdom throughout my doctoral study in Kyutech. I am grateful for his leadership and mentorship during the BIRDS-2 Project, as well as the numerous opportunities he has given me to develop my skills, character, and networking with colleagues in the BIRDS network.

To all the faculty members who participated as members of the doctoral thesis panel, Prof. Akahoshi, Prof. Ikenaga and Prof. Toyoda, for reviewing my work and providing invaluable comments to improve this thesis.

To all faculty members and staff (Kawano-san, Tsukinari-san, Shirakawa-san) of LASEINE, for their guidance, and support throughout my stay in Kyutech and Japan. To Dr. Sangkyun Kim, Dr. Masui, Dr. Yamauchi, and Maeda-sensei, for their technical expertise, guidance, efforts and contributions in the BIRDS-2 project and satellite development.

To the DOST-PCIEERD and DOST-SEI, for the doctoral study scholarship grant they have given me through the PHL-MICROSAT/STAMINA4Space Program implemented by the University of the Philippines-Diliman (UPD). To the faculty members, researchers, and students of the PHL-MICROSAT/STAMINA4Space Program and STEP-UP Project at UPD, for the discussions on BIRDS-2S satellites (Maya-3 and -4) and S&F/APRS-DP payload development and for testing support. Special mention to Prof. Joel S. Marciano, Jr., for his leadership and mentorship and inspiring me to pursue my doctoral studies.

To all fellow members and colleagues in the BIRDS-2 Project, BIRDS-1 Project, BIRDS-3 Project, BIRDS-4 Project and LASEINE, for the collegiality and friendship. Special mention to my ever-supportive colleague, Mr. Marloun Sejera of the BIRDS-4 Project, for his contributions in improving the design and developing the S&F/APRS-DP payload for implementation on BIRDS-4 satellites. I also appreciate him for the countless times he has generously dedicated for discussions, testing and information support.

To some Japanese locals near my residence in Tobata, Kitakyushu City, who, despite the language, cultural and personal barriers, strived to genuinely converse, interact, and relate with me. Thank you for your hospitality and our cultural exchanges.

To my family and close friends, for always keeping me strong and motivated.

Table of Contents

Declaration	i
Abstract	ii
Publications associated with this research.....	iv
Acknowledgements.....	vi
Table of Contents.....	vii
List of Figures.....	xi
List of Tables.....	xvi
Chapter 1: Introduction.....	18
1.1 Background.....	18
1.2 Research Problem.....	20
1.3 Overview of the State-of-the-Field.....	20
1.4 Research Aim and Objectives	23
1.5 Potential Research Contributions	24
1.6 Overview of Research Methodology.....	25
1.7 Thesis Structure.....	27
Chapter 2: Nanosatellite S&F Research, Missions and Applications	29
2.1 S&F Small Satellites and Microsatellites	29
2.2 The Rise of Nanosatellites and CubeSats for S&F Communications and Wireless Sensor Networks.....	32
2.3 CubeSats with APRS-DP Payloads.....	38
2.4 Survey of Recent Commercial Nanosatellite IoT/M2M Communications Solutions	39
Chapter 3: Satellite S&F Communication Systems and Protocols.....	45
3.1 Communication System Architecture, Configuration and General Considerations	45
3.2 Physical Layer	50
3.2.1 Channel Model.....	50

3.2.2	Modulation and Coding Schemes	50
3.3	Random Access Schemes	59
Chapter 4: BIRDS-2 CubeSat S&F Data Collection System, Payload Design and Development		
.....		67
4.1	System Architecture	67
4.2	Payload Design Considerations and Implementation on the BIRDS-2 CubeSat	68
4.3	Antenna Design and Deployment Mechanism Implemented on the BIRDS-2 CubeSat	74
4.4	BIRDS-2 Project Timeline Overview	76
4.5	APRS-DP/S&F Payload Functionality Tests	76
4.6	EM and FM Satellite Assembly, Integration and Verification	80
4.7	Overview of Ground Sensor Terminal (GST) Segment	84
4.8	On-orbit Operation Results	87
Chapter 5: Investigation on Communication Design Issues of BIRDS-2 CubeSat APRS-DP/S&F Payload, Results and Discussion		
.....		91
5.1	Determining the Actual Payload Receiver Sensitivity by Cabled Communication.....	91
5.2	Locating EMI Sources in the Satellite	94
5.3	Design Improvements Implemented on the BIRDS-2S CubeSat’s APRS-DP/S&F Mission Payload.....	97
5.4	Design Improvements Implemented on the BIRDS-4 CubeSat’s APRS-DP/SF-WARD Mission Payload	100
5.5	Antenna Reflection Coefficient Measurement and Tuning	101
5.6	Antenna Radiation Pattern Test	104
5.7	Wireless Communication Tests Inside the Anechoic Chamber.....	106
5.8	BIRDS-2S Payload Receiver Noise Level Measurements.....	110
5.9	BIRDS-4 Payload Receiver Noise Level Measurements.....	111
5.10	BIRDS-4 Range Communication Test (LRT).....	113
5.11	Communication Link Budget Analysis.....	115

5.12 Lessons Learned and Recommendations from Investigation on Communication Issues 117

Chapter 6: E-SSA-based Nanosatellite IoT/M2M Communication System Model and Signal

Processing Algorithm119

6.1 Communication Scenario Overview 119

6.2 Packet Generation at Terminal Side and Received Signal at the Satellite 120

6.3 LEO Channel Model 123

6.4 Packet Arrival Model 127

6.5 Throughput (THR), Packet Loss Rate (PLR) and Energy Efficiency (EE) Metrics 129

6.6 Overview of Signal Processing Algorithm..... 131

6.7 Packet Detection and Coarse Channel Estimation 132

6.8 Fine Channel Estimation..... 133

6.9 Demodulation and Decoding..... 135

Chapter 7: Simulation Results and Discussion for E-SSA-based Nanosatellite IoT/M2M

Communication System137

7.1 Target Values for Evaluation Metrics 137

7.2 Packet Detection 137

7.3 Channel Estimation..... 141

7.4 THR, PLR and EE Assuming Perfect Detection and Channel Estimation 145

7.5 THR, PLR and EE Considering Actual Processing Algorithm 147

Chapter 8: Nanosatellite Constellation for Global Coverage157

8.1 Constellation Design Considerations..... 157

8.2 Constellation Simulation Setup and Design Procedure 159

8.3 Selecting Transmit Power and Orbital Altitude..... 162

8.4 Coverage for Larger Constellations 163

Chapter 9: Experimental Laboratory Validation for E-SSA Protocol, Research Summary,

Conclusions and Recommendations167

9.1 Four Laboratory Setups for E-SSA Protocol Validation 167

Nanosatellite S&F Communication Systems for Remote Data Collection Applications

9.2	Examination of Received Baseband Signal Recorded at RX Side	180
9.3	Experimental Performance Results For E-SSA Protocol	189
9.4	Summary, Conclusion and Recommendations on APRS-DP/S&F Payload Development 191	
9.5	Summary, Conclusion and Recommendations on E-SSA Protocol-based Nanosatellite S&F Communication System for IoT/M2M Applications	193
9.6	Summary, Conclusion and Recommendations on S&F Nanosatellite Constellation Design.....	195
	References.....	197
	Appendix 0: BIRDS-2 S&F Packet Format	208
	Appendix 1: Derivation of terminal sdf	211
	Appendix 2: Derivation of dA/dt	212
	Appendix 3: Working Equations for Packet Detection and Rough Channel Estimation	213
	Appendix 4: Working Equations for Fine Channel Estimation	215
	Appendix 5: Other E-SSA Simulation Results.....	217
	Appendix 6: Constellation Design Details.....	226

List of Figures

Figure 1. Technical challenges in a nanosatellite S&F communication system	21
Figure 2. Overview of methodology for objectives 1-2.....	25
Figure 3. Overview of methodology for objectives 3-4.....	26
Figure 4. Overview of methodology for objective 6.....	27
Figure 5. Mission concept of WAPOSAT and block diagram of autonomous multi-sensor system. Data from polluted water is sent to a Central Hub in Lima (Peru) through 2U cubesat constellation (source: [25])	33
Figure 6. Wireless sensor network using store-and-forward nanosatellite (source: [26])	34
Figure 7. The HumSat architecture composed of three parts: space segment, ground segment and user segment (source: [34])	35
Figure 8. Irazu project concept of operations. The overall system consists of three segments: remote station, flight and ground segments. The experimental station measured monitoring data that relate to carbon sequestration, including tree growth and environmental parameters (source: [35])	36
Figure 9. Operational concept of APRS satellites [44].....	38
Figure 10. Two types of satellite-WSN configuration (examples): (left) direct sensor to satellite communication, (right) sensor gateway to satellite communication (source: [117]).....	46
Figure 11. Signal space of hybrid 4-FSK/QPSK modulation (source: [137])	54
Figure 12. Technical specifications of various LPWAN technologies (source: [140])	56
Figure 13. Technical specifications for standardization bodies and special interest groups for IoT solutions. ETSI, European Telecommunications Standards Institute (source: [142])	56
Figure 14. Conceptual operation of the APRS-DP mission.....	67
Figure 15. System architecture of the BIRDS-2 S&F CubeSat constellation-based remote data collection system	68
Figure 16. Block diagram of the BIRDS-2 APRS-DP/S&F payload and communication subsystem	70
Figure 17. BIRDS-2 APRS-DP/S&F payload flight model boards: mission board hosting the APRS-DP/TNC module, S&F MCU and flash memory; VHF transceiver board; assembled with other internal boards (lower right)	70
Figure 18. Communication layers and protocols	71
Figure 19. Program flow diagram of the S&F payload's MCU	72
Figure 20. BIRDS-2 1U CubeSat drawings showing the internal and external boards	73
Figure 21. Monopole antennas of the BIRDS-2 satellite in deployed condition (left); external side of antenna board showing the stowed elements (upper right); internal side showing the antenna connectors and burner circuit (lower right).....	75
Figure 22. BIRDS-2 project timeline.....	76
Figure 23. Basic APRS-DP communication tests performed with an APRS-capable Kenwood handheld radio	77

Figure 24. Testing communication between the payload and dummy GST: (a) simple setup inside the BIRDS room, (b) sensor packet received by payload from GST, (c) (b) ACK packet received by GST from payload..... 78

Figure 25. Spectrum measurement on BIRD-BT (BHUTAN-1) VHF transmitter’s RF output after putting a 20 dB attenuator, indicating an total output power of 26.5 dBm..... 79

Figure 26. Spectrum measurement on BIRD-PH (MAYA-1) VHF transmitter’s RF output after putting a 20 dB attenuator, indicating an total output power of 26.6 dBm..... 79

Figure 27. Spectrum measurement on BIRD-MY (UiTMSAT-1) VHF transmitter’s RF output after putting a 20 dB attenuator, indicating an total output power of 27.1 dBm..... 80

Figure 28. BIRDS-2 flight model assembly, integration and verification..... 81

Figure 29. Actual temperatures of the APRS-DP/S&F payload during thermal vacuum test on the engineering model 81

Figure 30. Thermal vacuum test on BIRDS-2 flight models: (left) thermocouples attached assembled satellite; (right) test setup with flight models inside the large vacuum chamber in Kyutech CENT..... 82

Figure 31. Actual vibration test setup for flight models 83

Figure 32. BIRDS-2 CubeSat flight models inside the cleanroom at Kyutech CENT 83

Figure 33. Photos of BIRDS-2 CubeSat flight models delivered to JAXA facility and assembly with the pod (photos courtesy of JAXA)..... 84

Figure 34. Rocket launch to the ISS in June 29, 2018 through the SpaceX Falcon 9 84

Figure 35. Deployment of BIRDS-2 CubeSats from the ISS in August 10, 2018 (photos courtesy of Alexander Gerst)..... 84

Figure 36. Block diagram of ground sensor terminal (GST) segment..... 85

Figure 37. GST prototypes developed by collaborators in UPD (Philippines) and UiTM (Malaysia)..... 86

Figure 38. GST prototype developed at Kyutech 86

Figure 39. Kyutech GST prototype actual data logging activity as displayed by serial monitor 87

Figure 40. APRS-DP regular beacon message packets received at Kyutech GS: (left) using UISS software on PC; (right) using Kenwood handheld radio 88

Figure 41. APRS-DP regular beacon message packets received by some amateurs around the world..... 89

Figure 42. RF power measurements of BIRD-BT’s APRS-DP beacon message signal through Kyutech BIRDS GS 90

Figure 43. RF power measurements of BIRD-MY’s APRS-DP beacon message signal through Kyutech BIRDS GS 90

Figure 44. Cabled communication test setup to determine the optimum uplink and downlink receiver sensitivities: (top) diagram, (bottom) photo of actual setup 92

Figure 45. Measured uplink and downlink receiver sensitivities in cabled test condition (matched TX and RX frequencies, representing no Doppler shift) 93

Figure 46. Measured uplink and downlink receiver sensitivities in cabled test condition (mismatched TX and RX frequencies, representing 5 kHz Doppler shift, L=100 bytes)..... 94

Figure 47. Test setup for locating the EMI-emitting sources in the satellite	95
Figure 48. Some test points for determining EMI sources in the satellite	95
Figure 49. New antenna design for BIRDS-2S CubeSat consisting of VHF and UHF dipole antennas: drawing (left), photos of actually implemented antennas for engineering model (right)	98
Figure 50. PCB layout of the four-layer antenna board for the BIRDS-2S CubeSat	99
Figure 51. Photo of copper plate shielding on the OBC/EPS board of BIRDS-2S satellite: front side (left), back side (right)	99
Figure 52. BIRDS-4 CubeSat’s APRS-DP/SFWARD mission payload (top) and aluminum plate shielding method employed for BIRDS-4 OBC/EPS board (bottom)	100
Figure 53. BIRDS-4 CubeSat’s VHF dipole antenna for the APRS-DP/SFWARD payload.....	101
Figure 54. Actual setup for antenna S11 measurement and tuning	102
Figure 55. Setup diagram for antenna S11 measurement and tuning	102
Figure 56. Circuit representation of the BIRDS-2S VHF dipole antenna parts and measurement setup (left) with a closer view of the actual antenna circuit implemented (right)	102
Figure 57. Measured S11 of the BIRDS-2S VHF dipole antenna after tuning.....	103
Figure 58. Antenna radiation pattern measurement setup at UPD’s full-anechoic chamber (FAC) facility	105
Figure 59. Radiation pattern of BIRDS-2 VHF monopole antenna on E-plane (left) and H-plane (right). Gain is shown in dB.....	105
Figure 60. Radiation pattern of BIRDS-2S VHF dipole antenna on E-plane (left) and H-plane (right). Gain is shown in dB.....	106
Figure 61. Wireless communication test setup at UPD FAC for testing the payload receiver sensitivity using BIRDS-2S dipole antenna (APRS-DP communication test).....	106
Figure 62. Wireless communication test setup at Kyutech FAC for testing the payload receiver sensitivity using a commercial dipole antenna (S&F communication test)	108
Figure 63. Wireless communication test setup at Kyutech FAC for testing the payload receiver sensitivity using a commercial dipole antenna (S&F communication test, with only mission board, VHF TRX and external power supply)	109
Figure 64. Test setup for detecting noise level increase in the payload receiver due to satellite-radiated EMI captured by the antenna. This was done inside UPD FAC.....	110
Figure 65. BIRDS-4 SFWARD payload receiver noise measurement by RSSI voltage	112
Figure 66. BIRDS-4 OBC board wrapped with commercially available EMI shielding/absorber sheet. 113	
Figure 67. BIRDS-4 long-range communication test setup involving the BIRDS-4 EM satellite	114
Figure 68. Uplink and downlink margins for the two GS antenna cases.....	116
Figure 69. Satellite IoT/M2M Communication Scenario	119
Figure 70. Uplink packet format.....	120
Figure 71. Preamble and postamble formats	121
Figure 72. Block diagram of baseband signal generation on terminal side	122

Figure 73. A snapshot of satellite orbit and footprint 124

Figure 74. Terminal spatial and cumulative distribution functions in terms of ε and α (h=600 km) 125

Figure 75. Pdfs and cdfs for Ak, dB, fk and dk due to LEO channel without lognormal fading/shadowing or $\sigma LN = 0dB$ (h=600 km, $f_c=402$ MHz, $\mu LN = 0dB$)..... 127

Figure 76. Pdfs and cdfs for Ak, dB due to LEO channel with and without lognormal fading/shadowing for different σLN (h=600 km, $f_c=402$ MHz, $\mu LN = 0dB$) 127

Figure 77. Illustration of time processing window with total duration $T_w=11T_p$ (top); an example of received baseband signal for $G = 1.0$ (bottom)..... 128

Figure 78. Signal processing algorithm overview 131

Figure 79. Packet detection decision, shown for E-SSA iterations 1-5 (red line: detection threshold, $\sigma LN = 6dB, G = 0.7$)..... 133

Figure 80. Fine channel estimation illustrative example 134

Figure 81. IFAR, IMDR and CMDR for different G values ($\sigma LN = 6dB, Eb/N0 = 14dB$)..... 138

Figure 82. IFAR, IMDR and CMDR for different σLN values ($G = 1.0, Eb/N0 = 14dB$)..... 140

Figure 83. Fine channel estimation mean absolute (mabs) and standard deviation (std) errors for different G values ($\sigma LN = 6dB, Eb/N0 = 14dB$)..... 143

Figure 84. Fine channel estimation mean absolute (mabs) and standard deviation (std) errors for different σLN values ($G = 1.0, Eb/N0 = 14dB$) 145

Figure 85. Simulation PLR, THR and ηEE for different G and σLN values ($Eb/N0 = 14dB$, perfect detection and channel estimation, 5 iterations)..... 146

Figure 86. IPLR and CPLR for different G values ($\sigma LN = 3dB, Eb/N0 = 14dB$, actual algorithm). 148

Figure 87. IPLR and CPLR for different G values ($\sigma LN = 6dB, Eb/N0 = 14dB$, actual algorithm). 149

Figure 88. IPLR and CPLR for different G values ($\sigma LN = 9dB, Eb/N0 = 14dB$, actual algorithm). 150

Figure 89. IPLR and CPLR for different σLN values ($G = 0.4, Eb/N0 = 14dB$, actual algorithm) .. 151

Figure 90. IPLR and CPLR for different σLN values ($G = 1.0, Eb/N0 = 14dB$, actual algorithm) .. 152

Figure 91. Simulation PLR, THR and ηEE for different G and σLN values ($Eb/N0 = 14dB$, actual algorithm, 5 iterations)..... 153

Figure 92. Simulation PLR, THR and ηEE for different G and σLN values ($Eb/N0 = 14dB$, actual algorithm, 5 vs 6 iterations)..... 155

Figure 93. Simulation PLR, THR and ηEE for different $Eb/N0$ values ($\sigma LN = 6dB$, actual algorithm, 5 vs 6 iterations)..... 156

Figure 94. Nanosatellite approximate orbits after launch (source: www.nanosats.edu)..... 159

Figure 95. Nanosatellite launches by launchers (source: www.nanosats.edu) 159

Figure 96. 3D illustration of the system model in STK showing the GST and satellite antenna radiation patterns and visibility area 162

Figure 97. 3x3 Hybrid constellation simulated in STK..... 162

Figure 98. Average percent coverage time (across all latitudes) vs orbital altitude for different P_{TX} 163

Figure 99. Percent coverage time across different latitudes for Walker Delta constellations (h=700 km, $P_{TX}=50$ mW) 164

Figure 100. Percent coverage time across different latitudes for Hybrid constellations (h=700 km, $P_{TX}=50$ mW) 164

Figure 101. Percent coverage time across different latitudes for Walker Delta and Hybrid constellations (h=700 km, $P_{TX}=50$ mW)..... 165

Figure 102. 8x8 Hybrid constellation simulated in STK 166

Figure 103. 9x10 Hybrid constellation simulated in STK 166

Figure 104. 10x10 Walker Delta constellation simulated in STK 166

Figure 105. Laboratory setup 1 for validating E-SSA protocol with additional impairments 169

Figure 106. Laboratory setup 2 for validating E-SSA protocol with additional impairments (diagram) .. 171

Figure 107. Laboratory setup 3 for validating E-SSA protocol with additional impairments 173

Figure 108. Laboratory setup 4 for validating E-SSA protocol with additional impairments (diagram) .. 174

Figure 109. USRP B200mini SDR TX side GNU Radio program for laboratory setups 2-4..... 178

Figure 110. LimeSDR RX side GNU Radio program for laboratory setups 2-4..... 179

Figure 111. RF spectrum measurements of SDR TX output (left) and SDR RX input (right) for laboratory setup 1 (different σ_{LN} , G and gain settings as in Table 27) 179

Figure 112. RF spectrum measurements of SDR TX output (left) and SDR RX input (right) for laboratory setups 2-4 (same σ_{LN} , G and gain settings as in Table 28) 179

Figure 113. RF spectrum measurements of signal generators’s RF outputs: (left) Agilent N9310A, set to 9.999998 MHz, 13 dBm; (right) R&S SMBV100V, set to 10.000000 MHz, 13 dBm..... 180

Figure 114. Plot of I and Q components of $R(t)$ vs time for reference case 184

Figure 115. Normalized magnitude plot of $r\Omega$ for reference case 184

Figure 116. Plot of I and Q components of $R(t)$ vs time for Lab Setup 1..... 185

Figure 117. Normalized magnitude plot of $r\Omega$ for Lab Setup 1 185

Figure 118. Plot of I and Q components of $R(t)$ vs time for Lab Setup 2..... 186

Figure 119. Normalized magnitude plot of $r\Omega$ for Lab Setup 2..... 186

Figure 120. Plot of I and Q components of $R(t)$ and $r(t)$ vs time for Lab Setup 3..... 187

Figure 121. Normalized magnitude plot of $r\Omega$ for Lab Setup 3..... 187

Figure 122. Plot of I and Q components of $R(t)$ and $r(t)$ vs time for Lab Setup 4..... 188

Figure 123. Normalized magnitude plot of $r\Omega$ for Lab Setup 4..... 188

List of Tables

Table 1. Categories and definitions of data rates.....	23
Table 2. Some S&F small satellite and microsatellite missions	31
Table 3. Some nanosatellite S&F missions for academic, research and civilian (non-commercial) purposes	37
Table 4. Commercial nanosatellite solutions for IoT/M2M communications	40
Table 5. Symbol error probabilities and RF amplifier parameters of different modulation schemes (sources: [133][134][146][147]).....	58
Table 6. Modulation spectral efficiency of different modulation schemes (source: [146]).....	59
Table 7. Publications investigating modulation, coding and random access schemes for satellite IoT/M2M communications.....	62
Table 8. S&F onboard memory organization.....	72
Table 9. S&F packet types.....	72
Table 10. Energy budget of the satellite operating in APRS-DP/S&F mission mode.....	74
Table 11. Recorded deployment times at different temperatures	75
Table 12. Payload VHF transmitter output RF signal spectral measurements.....	77
Table 13. EMI sources determination test points and corresponding PSD measurements	96
Table 14. Experimental values for APRS packet success rate at different payload receiver input power using BIRDS-2S dipole antenna (whole satellite assembled).....	107
Table 15. Experimental values for S&F packet success rate at different payload receiver input power using a commercial dipole antenna (whole satellite assembled)	108
Table 16. Experimental values for S&F packet success rate at different payload receiver input power using a commercial dipole antenna (with only mission board, VHF TRX, and external power supply)	109
Table 17. BIRDS-2S payload receiver noise level from RSSI voltage without copper plate shielding	111
Table 18. BIRDS-2S payload receiver noise level from RSSI voltage with copper plate shielding	111
Table 19. BIRDS-4 payload receiver noise level from RSSI voltage measurements under three shielding conditions.....	113
Table 20. Parameters used in link margin calculation	115
Table 21. Parameters for Generating the Gold Sequences for Preamble/Postamble using a Matlab Function	121
Table 22. Simulation Parameters	128
Table 22. Target Values for the Evaluation Metrics	137
Table 24. Typical range of channel estimation mean absolute (mabs) and standard deviation (std) errors across different G and σ_{LN} (5 iterations).....	141
Table 25. GST Transmitter, Receiver and Satellite Constellation Models in STK AGI	161
Table 26. Percent Area Coverage (PAC) of Different Constellations	165

Nanosatellite S&F Communication Systems for Remote Data Collection Applications

Table 27.	Reference Clocks Accuracies in Different Setups	175
Table 28.	Expected Signal Impairments in Different Setups	175
Table 29.	SDR TX and RX Settings for Laboratory Setup 1	176
Table 30.	SDR TX and RX Settings for Laboratory Setups 2-4	177
Table 31.	Observed Additional Signal Impairments in Recorded Received Baseband Signal	183
Table 32.	Experimental Cumulative PLR for $G=0.1$, $E_b/N_0 = 14\text{dB}$, $\sigma_{LN} = 6\text{dB}$ (with mistake in iteration 4)	189
Table 33.	Experimental Cumulative PLR for $G=0.1$, $E_b/N_0 = 14\text{dB}$, $\sigma_{LN} = 6\text{dB}$ (corrected iteration 4)	189
Table 34.	Experimental Cumulative PLR for $G=0.1$, $E_b/N_0 = 26\text{dB}$, $\sigma_{LN} = 6\text{dB}$ (with mistake in iteration 4)	190
Table 35.	Experimental Cumulative PLR for $G=0.1$, $E_b/N_0 = 26\text{dB}$, $\sigma_{LN} = 6\text{dB}$ (corrected iteration 4)	190
Table 36.	Experimental Cumulative PLR for $G=0.1$, $E_b/N_0 = 14\text{dB}$, $\sigma_{LN} = 6\text{dB}$ (thresholds lowered to improve packet detection rate)	191
Table 37.	Constellation Configurations Simulated	226

Chapter 1: Introduction

1.1 Background

Traditional satellite missions and programs prioritized reliability, which normally demands long delivery time, high project cost, very big and complex spacecrafts, as well as conservative development and management approaches. Hence, development of space technologies and engagement in space-related activities had been previously afforded only by a few space agencies and private companies with large budget and resources. This began to change in the past three decades when the infusion or adoption of what many now refer to as “lean satellite development” philosophy in space programs has reduced the entry barrier.

As defined in [0], “a lean satellite is a satellite that utilizes non-traditional, risk-taking development and management approaches to provide value of some kind to the customer at low-cost and without taking much time to realize the satellite mission.” A small satellite size arises as a result of “seeking low-cost and fast-delivery”, which, in addition, are achieved by cost/waste-cutting approaches such as use of non-space-graded commercial-off-the-shelf (COTS) components, acceptance of certain level of risks, keeping team size smaller, etc. [0]. Small satellites of various sizes and shapes – including minisatellites (100-500 kg), microsattellites (10-100 kg), nanosatellites (1-10 kg) and picosatellites (0.1-1 kg) – subsequently emerged and their adoption progressively democratized access to space technologies and activities by government agencies, research institutes, non-profit organizations and universities in both developed and developing countries. Many organizations around the world have built small satellites for various scientific/technological, research and development (R&D), academic/educational, and public purposes. These include, among others, addressing a myriad of needs for remote sensing data, telecommunications, disaster risk mitigation and response, climate change studies, etc.

In more recent years (after 2010), we have seen a surge of new players in the private sector – including many start-up companies – engaging in space enterprises [1]. Miniaturization and advances in electronics, power, computing, signal processing, mechanical, manufacturing, and other relevant technologies have enabled small satellites to carry out more complex missions. Thus, small satellite utilization experienced a significant paradigm shift from primarily research/academically motivated or program/institution-centered (for some) to more focus on practical and commercial applications. Also, standardization of interfaces for intra-satellite subsystems and between satellite and launcher systems, coupled with growing number of small launchers accessible at lower prices, has enabled shorter project timelines, easier collaborations, and remarkable growth of the small satellite industry. The proliferation of small satellites across different sectors of the space industry may be attributed to these factors, among others.

Since around 2012, there has been a rapid growth in the number of launched satellites within the 1-10 kg. mass range, while slow growths in the 11-50 kg. and 51-100 kg. mass ranges [2]. As of April 19, 2020, 66 countries have launched nanosatellites and the total number of nanosatellites launched is 1317, from which 1210 are CubeSats [1] (note: broader definition of nanosatellites in [1]). Although there is no

universally set definition for a “nanosatellite”, many authors refer it to the 1-10 kg. mass range. From here onwards in this document, the term “nanosatellite” is *loosely* used, to also include larger CubeSats that can exceed 10 kg. (e.g., 8U, 10U, 12U, 16U, etc.). These bigger CubeSats are not commonly used but sometimes appear in missions requiring additional resources.

While nanosatellites have been utilized by several start-up companies aiming to revolutionize earth observation [1], there has also been increasing interests in using nanosatellites to address communication requirements, for civil and commercial purposes. Due to compact design, cost-effectiveness and shorter development time, a nanosatellite constellation is seen as a viable space-based data-relay asset to collect data from stations deployed in remote places that are rather impractical to be linked by terrestrial means. In such scenarios, each nanosatellite in the constellation collects sensor data or other data types from ground terminals (GTs) in remote locations and then downloads it to an accessible station later. This data collection approach is generally referred to as a *store-and-forward* (S&F) mechanism.

S&F nanosatellite constellations have increasing commercial potential and actual use cases related to the Internet-of-Things (IoT) and Machine-to-Machine (M2M) paradigms [4]. In fact, many start-up companies have been getting traction by offering nanosatellite-based solutions for IoT/M2M communications, typically using CubeSat platforms, at a fraction of the cost in traditional satellite solutions. The latter are not only prohibitive in terms of subscription cost, GT device cost and power consumption, but are also not designed to support a large number of terminals that generate very low data-rate burst transmissions – which are typical characteristics of many emerging IoT/M2M applications. With a much lower cost of establishing a nanosatellite constellation and the limitations of traditional satellite systems, nanosatellites can help extend the capabilities and potential addressable IoT/M2M market of satellites [4].

Even before the excitement on IoT/M2M paradigms, S&F nanosatellites had been considered for similar scenarios such as in satellite-integrated wireless sensor networks (WSNs). In the context of non-commercial applications, many universities and non-profit organizations have launched nanosatellites, commonly CubeSats, with some communication capabilities for amateur radio community use. This is because of strong support from the international amateur radio community in frequency coordination, use of the service and promotion of activities. Recently, there have been proposals and actual implementations of CubeSats supporting a message/packet repeating application known as Automatic Packet Reporting System Digipeater (APRS-DP). The idea proposed in [5] is for present and future APRS-DP satellites in orbit to share a common channel (145.825 MHz) and a generic digipeater alias (APRSAT and ARISS) to accumulate all user traffic on an Internet server, hence integrating all worldwide users and stations. Although an APRS-DP application normally re-transmits any received packet, the underlying physical and link communication layers can be used for S&F type of communication. Therefore, it would be useful to develop an amateur radio payload for CubeSats that can support both APRS-DP and S&F communication capabilities.

1.2 Research Problem

Due to compact design, cost-effectiveness and shorter development time, a nanosatellite constellation is seen as a viable space-based data-relay asset to collect data from remote places that are rather impractical to be linked by terrestrial means. While nanosatellites have these advantages, they have more inherent technical limitations because of limited space for subsystems and payloads. Nanosatellite S&F communication systems are notably challenging in this respect due to requirements on antennas, transceivers, and signal processing. Although nanosatellites can be scaled up for better resources and capabilities, smaller platforms (i.e., $\leq 6U$ CubeSat) tend to be used for cost-effectiveness and lower risk.

This thesis dealt with the problem of designing a nanosatellite S&F communication system for delay-tolerant remote data collection applications considering: (a) technical constraints in hardware, processing capabilities, energy budget and space in both the nanosatellite and ground terminal sides; (b) physical communication layer characteristics and constraints such as limited available bandwidth, LEO channel Doppler, attenuation and fading/shadowing effects, low transmit power and data rate, and multi-user interference among asynchronously transmitting terminals.

1.3 Overview of the State-of-the-Field

In the past, government/research, academic and civil organizations have launched microsatellites and nanosatellites with S&F communication capabilities. Since 1990s, there have been several publications related to successfully working S&F microsatellites utilizing traditional communication protocols. With the emergence of nanosatellites and CubeSats, since 2005s, there have been publications on S&F nanosatellite application concepts, studies discussing communication constraints and random-access protocols. There have been several works describing initial implementations and successful demonstrations of nanosatellite S&F systems, including the HumSat Project [34], Irazu Project [35], TriCOM-1 [36], and TriCOM-1R [38][39]. These nanosatellite missions were undertaken primarily to achieve research objectives, exploring for instance, environmental monitoring applications (temperature, pressure, soil moisture, water level, etc.).

However, there are not many publications discussing details, challenges, and results of operation. There are still many things that can be contributed to the practical aspects. Also, there is a lack of publications completely tackling from nanosatellite S&F payload design, development to post-launch failure investigation. It is well noted that communication system issues remain one of the most common causes of post-launch CubeSat failures, along with power system issues [6]. Many university CubeSats failed to even establish communication with a ground station. Besides S&F communication, as mentioned, recently there have been proposals and actual implementations of CubeSats supporting a message/packet repeating application known as Automatic Packet Reporting System Digipeater (APRS-DP), which re-transmits received packets in a more real-time fashion. There have been a handful of satellites with APRS-DP payload, including the Amateur Radio on the ISS (ARISS), PCSAT (10 kg, 2001), LAPAN-A2 (68 kg, 2015), Diwata-2 (56 kg, 2018), PSAT-1 (1.5U, 2015), PSAT-2 and BRICSAT-2 (1.5U, 2019). However, even some of these failed or only partially operated due to communication, power, or software issues.

In the context of more recent IoT/M2M applications, considering the disadvantages of traditional satellite-based solutions (mentioned above), nanosatellites have a potential to cater to newly emerging IoT/M2M applications which are latency-tolerant, price-sensitive, demanding very low data rates, and involving remotely deployed, simple, low energy-consuming ground terminals (GTs). Overall, the system must also support a large number of simultaneous connections. The constraints in energy budget, transmit power and available bandwidth naturally limit the system’s capacity in terms of the amount of data that can be received and number of GTs that can be supported.

Also, in both nanosatellite and GT sides, there are stringent limitations in hardware complexity and processing capabilities. Because GTs normally operate only on batteries and/or solar panels, energy constraint can also limit their operational lifetime. Thus, to maximize GTs’ operational lifetime, transmissions should be kept as infrequent and low-energy as possible. On the nanosatellite side, it is very challenging to design a compact and low-power payload that can be accommodated on a nanosatellite platform. The system must also be able to decode overlapping packets from many transmitting GTs, which cause a high level of multiuser interference (MUI). Furthermore, the high propagation loss, dynamic LEO channel characteristics due to Doppler effect, and power imbalance, can degrade the quality of received signals and make decoding packets difficult. Figure 1 summarizes the technical challenges in a nanosatellite S&F communication system.

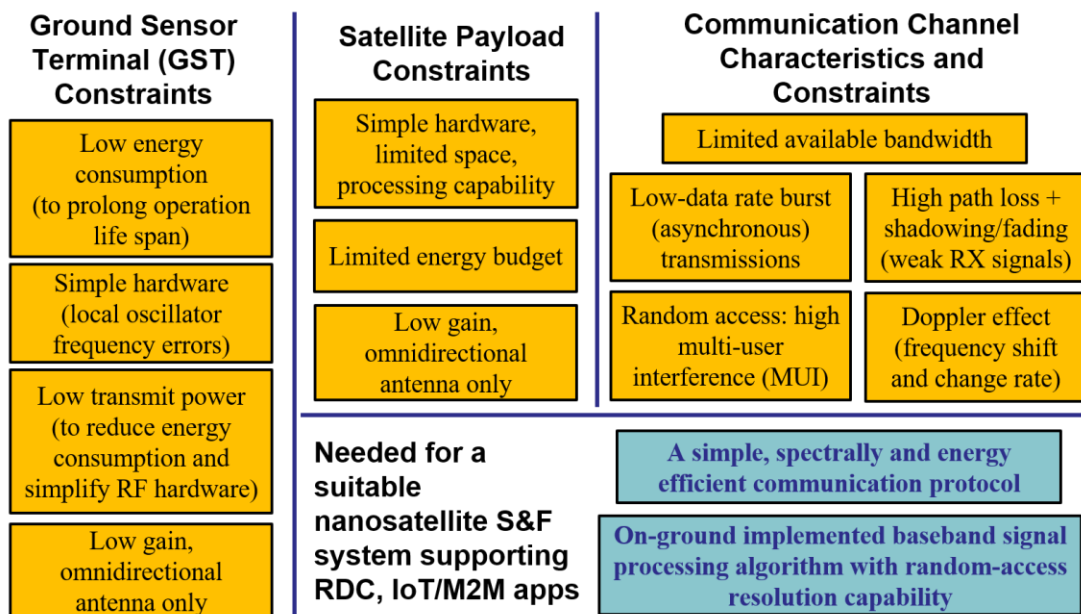


Figure 1. Technical challenges in a nanosatellite S&F communication system

Key to addressing these challenges is that a suitable satellite IoT/M2M system must employ a communication protocol that is optimized for spectral efficiency (i.e., scalable throughput) and energy efficiency while achieving a reasonably low packet loss rate (e.g., PLR<5%). It also requires a simple communication system design on GTs and a signal processing algorithm with random access resolution capability implemented satellite-onboard or on-ground (for nanosatellite platforms). Even with high multi-user interference and power imbalance, the signal processing algorithm must be able to detect the packets,

accurately estimate their individual channel parameters (amplitude, phase, frequency shift and rate) and demodulate/decode the whole packet.

Compared with traditionally employed multiple access control (MAC) schemes according to fixed assignment (e.g., TDMA, FDMA, CDMA) or demand-based adaptive assignment, random access (RA) scheme is more suitable for a satellite IoT/M2M system servicing a very large population of burst-transmitting GTs sharing a common channel. However, ordinary RA schemes such as pure Aloha (PA), time-slotted Aloha (SA), and even modified forms such as diversity slotted Aloha (DSA), exhibit low efficiency and attains low packet collision rates only at very low MAC loads. Moreover, time-asynchronous RA is preferable over time-slotted RA since it avoids the latter's need for maintaining accurate time-slot synchronization among terminals.

Various modulation schemes supporting RA capability, which are applicable to satellite IoT/M2M systems, have been proposed and investigated in literature. These include time- and frequency-asynchronous Aloha (TFAA) [154][155], chirp spread spectrum (CSS) Aloha [150][151][152], and direct-sequence spread spectrum (DSSS) Aloha [7][8][9]. Previous works in all three types of schemes either ignored the impact of imperfect packet detection and channel estimation or did not consider any contention resolution algorithm. It is noted that imperfect packet detection and channel estimation significantly impede packet demodulation/decoding while contention resolution can greatly increase performance in presence of high MUI.

In [7], the authors proposed to apply a Recursive Successive Interference Cancellation (R-SIC) algorithm to DSSS Aloha (or SSA) and showed that this overcomes performance degradation of conventional SSA due to power imbalance in satellite channel. Hence, the protocol has been dubbed as Enhanced Spread Spectrum Aloha (E-SSA). By combining SSA with a rate 1/3 Turbo code for forward error correction and R-SIC, E-SSA can achieve a higher throughput with more received signal power variation, although with higher floor PLR [7][8]. E-SSA has also been successfully validated in laboratory and actual satellite payload [9]. E-SSA is particularly attractive for our application because it requires only a simple GT transmitter design. Although it involves computationally intensive signal processing to decode many packets [8][9], for delay-tolerant applications, it is acceptable to perform on-ground processing on baseband samples. This delay-tolerant MAC approach is a practical turnaround for micro/nanosatellite-based IoT/M2M systems to still take advantage of advanced RA schemes (as also proposed in [132]).

The previous works in [7][8][9] were done in the context of a GEO satellite and involving a shorter packet duration (<250 ms, due to higher data rate (5 kbps)) that makes it less susceptible to channel estimation errors. In the scenario we are concerned with, we consider a LEO nanosatellite constellation. And, to maintain enough average bit-energy to noise spectral density (E_b/N_0) with limited transmit power, an ultra-low* data rate (target: <500 bps) should be used, but this makes packet duration comparable to coherence time due to channel estimation errors. Therefore, considering greater extent of Doppler effect in LEO, it is crucial to employ a very accurate channel estimation algorithm. Also, the previous works did

not sufficiently tackle the impact of power imbalance and MUI on the signal processing algorithm performance (packet detection, channel estimation, and demodulation/decoding). These issues have not been sufficiently studied for E-SSA within the said context and to our knowledge, *an investigation on using E-SSA for nanosatellite IoT/M2M uplink communication* has not been previously reported.

*Note that considering the characteristics of more recent IoT/M2M communications technologies, for the purpose of this thesis, we can extend the definition in [117] as follows:

Table 1. Categories and definitions of data rates

Data Rate Category	Range of Data Rates	Other Terminologies
High	$r > 500$ kbps	“broadband”
Medium	$50 \text{ kbps} < r < 500$ kbps	
Low	$5 \text{ kbps} < r < 50$ kbps	“narrowband”
Very Low	$500 \text{ bps} < r < 5$ kbps	
Ultra-Low	$r < 500$ bps	“ultra-narrowband”

1.4 Research Aim and Objectives

This thesis aims to contribute to the development of nanosatellite S&F communication systems by (a) developing a CubeSat-onboard S&F payload considering technical constraints (hardware, processing capability, space and energy constraints), and (b) investigating a physical communication layer protocol with asynchronous random-access resolution capability that is suitable for nanosatellite IoT/M2M communications. Specifically, this thesis aims to accomplish the following smaller objectives:

1. Design and develop a low-cost and compact amateur radio payload with S&F communication and APRS-DP capabilities that is suitable for a CubeSat platform. Then, integrate it with each of the three 1U CubeSats of the BIRDS-2 Project.
2. Evaluate the on-orbit performance of the S&F/APRS-DP payload and systematically investigate communication design issues by a combination of on-orbit observation results and ground-based tests.
3. Investigate suitability of E-SSA protocol for nanosatellite-based IoT/M2M uplink communication (terminals to nanosatellite) by analyzing its packet loss rate (PLR), throughput and energy efficiency at different MAC load, E_b/N_0 and received power imbalance conditions expected in LEO.
4. Formulate the details and assess the performance of a baseband signal processing algorithm for E-SSA, including packet detection, channel estimation, and demodulation/decoding.
5. Experimentally validate in a laboratory setup the performance of E-SSA protocol with the formulated algorithm.
6. Elucidate the relationship between LEO nanosatellite constellation design parameters and communication coverage by applying the findings on E-SSA protocol simulation.

It is noted that store-and-forward mechanism consists of the “store” phase (uplink communication, i.e., data collection from terminals nanosatellite and storage) followed by “forward” phase (download of stored data from nanosatellite to a mission ground station). This thesis focuses only on the store phase because it already faces formidable challenges and constraints (the download phase, which can be done with a very high data rate downlink communication system such as an X-band transmitter, has its own challenges). However, the signal processing algorithm is performed on the digitized baseband samples of received signal after they have already been completely downloaded to a ground facility.

1.5 Potential Research Contributions

This doctoral thesis has the following potential research contributions:

- Unlike the previous nanosatellites carrying an amateur radio payload with only either APRS-DP or S&F communication capability, we developed a CubeSat-onboard payload with both APRS-DP and S&F communication capabilities. Since we dealt with the tight constraints of a 1U CubeSat hosting other subsystems and payloads, this research will be relevant especially to other university-based nanosatellite projects undertaking similar missions.
- Note that many previously launched nanosatellites also failed due to communication design-related problems, but a systematic investigation of failure after launch is rarely documented in literature. Therefore, by describing our work from payload design, development, to post-launch failure investigation, this research could help enlighten similar issues commonly faced especially in university-based nanosatellite projects.
- This serves as an extension to the previous works [15][16][17] by evaluating not only throughput and PLR but also energy efficiency at various MAC load, E_b/N_0 and received power imbalance conditions expected in a low-earth orbit (LEO), instead of geostationary earth orbit (GEO).
- While there have been a few research works discussing the idea of using nanosatellites for store-and-forward remote data collection applications, as well as papers describing technology demonstration and Aloha-based random-access protocol, there is very limited research on jointly optimizing the physical communication layer and random-access scheme for nanosatellite-based IoT/M2M communication. Such topics have only been recently emerging and gaining attention of some researchers. Also, most companies offering nanosatellite-based solutions use proprietary technologies (as surveyed in Section 2.5) so there still a lack of reports and publications on how effective real systems and technologies are for the said application. This dissertation would be one of those first few research works on this topic. Specifically, since an investigation on using E-SSA protocol for nanosatellite IoT/M2M uplink (terminal to satellite) communication has not been done before, this would provide results and findings relevant to the said application.
- We considered different Doppler frequency shifts, rates, and amplitudes among received packets by accounting for terminals’ spatial distribution.
- We derived an appropriate energy efficiency (EE) metric based on average energy per successfully received information bit.

- We formulated and described details and performance of the baseband signal processing algorithms used (packet detection, channel estimation, decoding), thus providing insights for implementation to researchers.
- We considered a data rate (333.33 bps) that is lower than in previous works (5 kbps or higher) to maintain enough E_b/N_0 with low transmit power, but long packet duration inadvertently exposes it symbol phase rotations (or reversals) caused by channel frequency shift and rate estimation errors. The conditions described here are different from those in [15][16][17], where packet duration is shorter (<250 ms). Since we deal with a long packet duration comparable to coherence time due to estimation errors, so it crucial to employ a very accurate channel estimation algorithm.
- We experimentally validated the formulated E-SSA protocol in a laboratory setup involving software-defined radio (SDR) transmitter and receiver.

1.6 Overview of Research Methodology

Objectives (1) and (2) were accomplished by practical research and experimental activities performed in parallel with the BIRDS-2 Project, including satellite design, development, integration, verification, and operation. The APRS-DP/S&F payload was designed considering the constraints and interfaces of the BIRDS-2 1U CubeSat, which hosts other subsystems and mission payloads that may have conflicting requirements and compete for space and resources. It was developed and integrated to the satellites within a 15-month time frame from December 2016 to February 2018 – about 11 months for engineering model and four months for final assembly, integration, and test of flight models. Details are described in Chapter 4. On-orbit performance evaluation was based on operation results and communication tests between ground radio and the satellite payload. Investigation of communication issues was done by a comparing on-orbit operation results and ground-based tests including wired (cable) test, wireless tests inside anechoic chamber and long-range test. Overview is given in Figure 2 and details are described in Chapter 5.

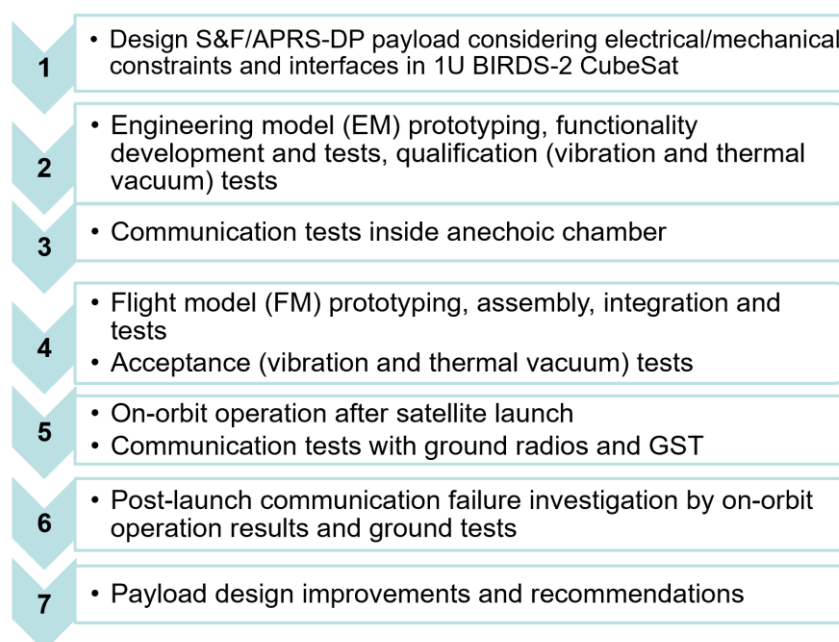


Figure 2. Overview of methodology for objectives 1-2

Objectives (3) and (4) were concerned on evaluating the performance and energy efficiency of E-SSA (which is a direct-sequence spread spectrum modulation scheme with asynchronous random-access capability) for the said application as well as formulating detailed signal processing algorithm to obtain as high performance as possible. To do this, a communication system model was implemented in Matlab, emulating the packet generation behavior of many terminals, LEO channel Doppler and attenuation effects, and baseband signal processing algorithm. At the receiver, arriving packets are modeled as Poisson traffic with random phase offsets, amplitudes, Doppler frequency shifts and rates expected in a LEO channel, combined with complex additive white gaussian noise (AWGN). Details of communication system modeling and baseband signal processing are discussed in Chapter 6. We focused on assessing the E-SSA protocol with the formulated signal processing algorithm in terms of three defined metrics (THR, PLR and EE) through simulations of the model that closely emulate the actual physical communication layer design envisaged. Overview of simulation model is given in Figure 3.

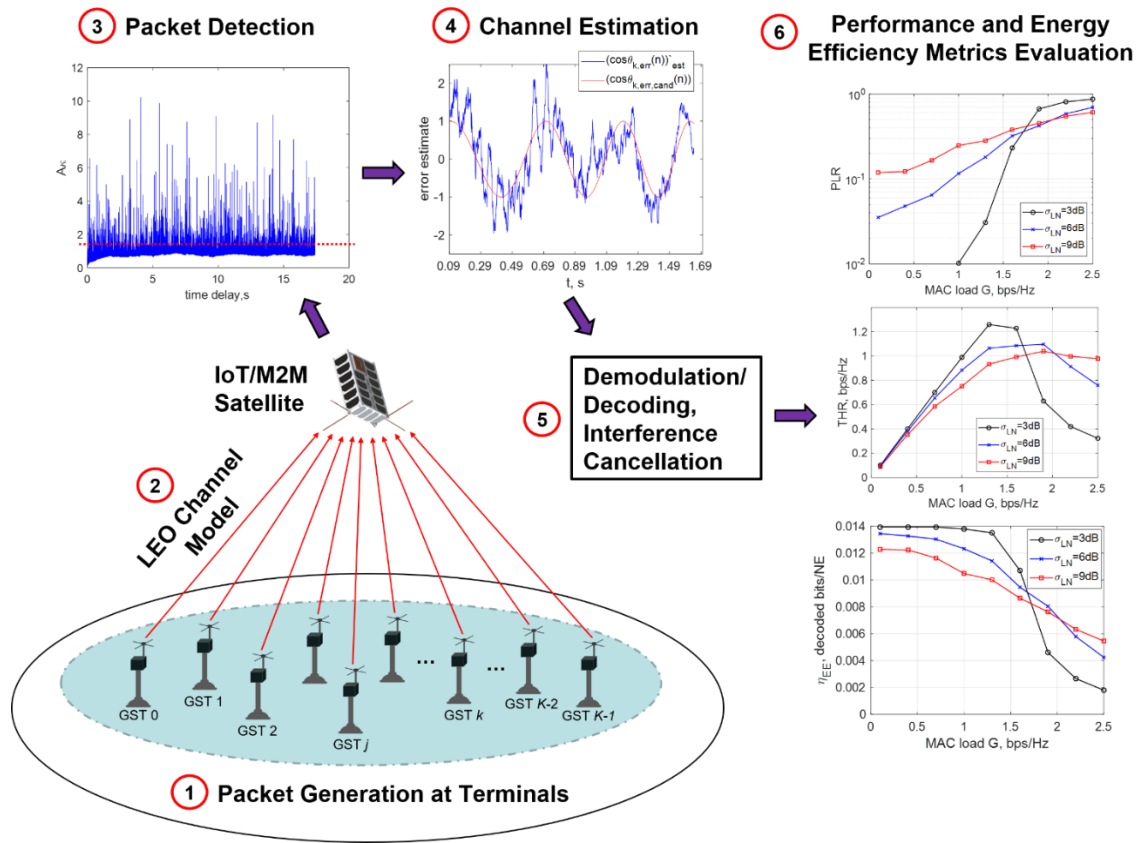


Figure 3. Overview of methodology for objectives 3-4

For objective (5), we used a laboratory setup involving one SDR acting as transmitter and another SDR acting as receiver. Received baseband signal generated by the MATLAB simulation program was allowed to go through the whole chain: from digital filter, digital-to-analog converter (DAC), analog baseband filter, RF transmitter mixer, cables, attenuator, RF receiver mixer, analog baseband filter, to analog-to-digital converter (ADC) and digital filter at the receiver. The MATLAB simulation program was then used to post-process the recorded received baseband signal. Details are described in Chapter 9.

For objective (6), we utilized AGI’s System Tool Kit (STK) to model and simulate communication system parts, constellation and also to compute the coverage. Overview is given in Figure 4 and details are described in Chapter 8.

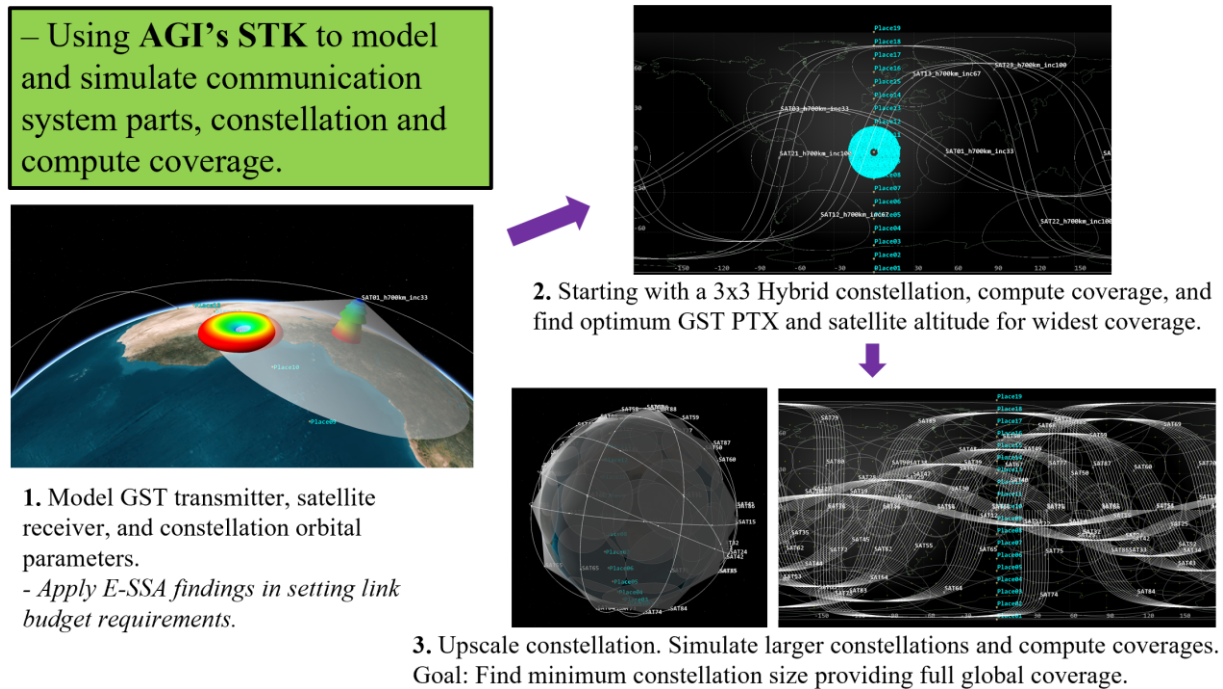


Figure 4. Overview of methodology for objective 6

1.7 Thesis Structure

This thesis comprises of nine chapters. Chapter 1 (this chapter) discussed the research background, research problem, state of research, and potential contributions of this thesis, and provided a gist of research methodology detailed in later chapters. Chapter 2 and 3 provides an extensive literature review to elaborate on the state of research. Chapter 2 reviews the previous research works on using nanosatellites for S&F communication for remote data collection, and the previous nanosatellite S&F missions. Such research works and nanosatellite missions were undertaken primarily in the context of non-commercial applications. It also surveys the recent commercial nanosatellite IoT/M2M players and examines their proposed systems in terms of satellite platform, constellation design, communication technology, targeted applications, requirements, and performance.

Chapter 3 presents a literature review on communication system architecture, physical layer and random-access schemes, protocols, and technologies relevant to satellite-based IoT/M2M system. Chapter 4 discusses the BIRDS-2 CubeSat S&F remote data collection system, payload design, development, tests, and integration with the BIRDS-2 CubeSats. Chapter 5 discusses the investigation on communication design issues of BIRDS-2 CubeSat S&F payload, tackling both the methodology and findings of investigation. Chapter 6 first describes the enhanced spread spectrum Aloha (E-SSA) based nanosatellite IoT/M2M communication model and derives the mathematical definitions of packet loss rate (PLR), throughput (THR) and energy efficiency (EE) metrics. Then, it tackles the formulated baseband signal

Nanosatellite S&F Communication Systems for Remote Data Collection Applications

processing algorithm for E-SSA, including packet detection, channel estimation, demodulation and decoding. Chapter 7 presents the simulation results and discussion for Chapter 6.

Chapter 8 tackles the S&F nanosatellite constellation design for global coverage and presents the results and findings. Chapter 9 describes the laboratory setups for validating the E-SSA protocols and then discusses the results and findings. Finally, Chapter 9 also gives the summary, conclusions, and recommendations.

Chapter 2: Nanosatellite S&F Research, Missions and Applications

There are varying definitions of the Internet of Things (IoT) [10] but it may be described as a paradigm envisioning a giant network of uniquely identified “things” (such as objects, devices, physical or virtual machines, or even sensors attached to animals or people) that can sense (by sensors) their environment or interact (by actuators) with their environment (or entities to which they are attached) and can communicate with one another (by wire or wireless means). Data obtained from these things can be used to extract pertinent information about how they are used and the environment around them (or attached entities) and to induce an appropriate response, thus supporting the automation or optimization of processes or operations.

On the other hand, Machine-to-Machine (M2M) [11] simply refers to the communication or exchange of data between devices without human intervention. M2M can be a relatively closed network that may be considered part of the IoT. In this thesis, for brevity, we use “IoT/M2M” when referring to a broad range of scenarios, systems or technologies involving interconnected or communicating things within the context of IoT and M2M.

Store-and-forward (S&F) is a communication technique in which data from a source node arrives at a final destination node through one or more intermediate nodes that keep and send data at a later time, following a route that leads to a final destination. A “node” refers to a point in a communication path and is in practice associated with a computing device or station located somewhere. S&F communication is applied in networks with intermittent connectivity, such as in delay-tolerant and disruptive-tolerant networks. For instance, data from sensing stations deployed in remote locations can be collected through a satellite acting as a relay node. Remote data collection is one application of a satellite-based S&F system that may be part of a bigger IoT/M2M system and this is a niche use for nanosatellites explored in this work.

This chapter reviews the previous research works on using nanosatellites for S&F communication for remote data collection, and the previous nanosatellite S&F missions. Such research works and nanosatellite missions were undertaken primarily in the context of non-commercial applications. Then, it surveys the recent commercial nanosatellite IoT/M2M players and examines their proposed systems in terms of satellite platform, constellation design, communication technology, targeted applications, requirements, and performance.

2.1 S&F Small Satellites and Microsatellites

The LEO microsatellites developed in the 1980s and 1990s by research and amateur radio organizations, which were capable of S&F communication, have demonstrated their use as simple, small-size, efficient and low-cost space-based asset for remote data collection and messaging [12]. The first digital S&F microsatellite, UoSAT-2, was launched in March 1984, and then followed by a series of other experimental and operational S&F microsatellites [13]. These S&F microsatellites served complementary

roles to those of 'big' LEO systems (whose focus had been to provide global mobile communications) including [12][13]:

- Enable non-real-time communication, low data transfer rate and volume (~up to a few tens of kbps),
- Provide personal communication services to amateur community such as email and file forwarding, messaging, and broadcasts,
- Form the basis of both experimental and operational microsatellite missions for remote site data collection and messaging

The succeeding commercial S&F satellite systems had higher data capacity to support various markets, including tele-learning, file-transfer on-demand, data transfer to/from remote sites (e.g., remote environment monitoring and automatic sensor reading), tele-control of remote instrumentation and tele-medicine [14]. After year 2000, there were other S&F satellites for remote data collection or messaging which were built by government, research, or academic institutions. A good example is Sina-1, a 160 kg. satellite and the first satellite of Iran [15] which was launched in 2005. In addition to its main imaging payload, it carried a S&F payload that provides the handling of exchanging packet type messages via satellite between two ground terminals, which may not be on the same footprint at the same time. A message received from one ground terminal is stored in the onboard memory and then delivered as the satellite passes over the destination ground terminal. Communication is done using phase-shift keying modulation, VHF and UHF radio links, and split channel reservation multiple access (SRMA) protocol (one random access channel for transmitting a slot reservation request and a reserved mode channel for data transmission).

Paper [15] analyzed the effect on channel efficiency performance of different parameters such as number of users, packet length and visibility time. Another example is the 38 kg. microsatellite, ANUSAT, which was used for amateur radio service to transfer electronic mail among ground terminals in the footprint in non-real-time (or immediately if the source and destination terminals are simultaneously in the footprint) [16]. Then, S&F microsatellites Hodoyoshi-3 and 4 [17] were developed in Japan to demonstrate the use of small-size satellites for remote data collection. For a simplified onboard payload, the satellites demonstrated the use of ground signal processing instead of onboard demodulation, and this was shown to improve the signal demodulation rate.

Table 2. Some S&F small satellite and microsatellite missions

Satellite	Launch Year	Orbit	Mass	S&F User Uplink	S&F User Downlink	Mission Data Downlink
SSTL/UoSAT series [13] (e.g., UoSAT-2, -3, -5, S-80/T, KITSAT-1, PoSAT, HEALTHSAT-2, etc.)	1980s – 1990s	~700-800 km, SSO, $i \sim 98^\circ - 99^\circ$	~50 kg class	VHF (amateur/experimental, licensed); 1200, 4800, 9600, 38400 bps; AFSK, FSK; up to 10W TX	VHF/UHF (amateur/experimental, licensed); 1200, 4800, 9600, 38400 bps; AFSK, FSK, up to 5W TX	(not for S&F data downlink to GS)
Maroc-Tubsat (Zarkae Al Yamama) [18][19]	2001	986/1014 km, SSO, $i=99.7^\circ$	47 kg	144 MHz VHF band, 1200 bps, AFSK, 5W TX	144 MHz VHF band, 1200 bps, AFSK, 3.5W TX, (for ACK DL)	436 MHz AFSK, 1200/2400 bps, 5W TX; 2208 MHz, BPSK, FEC, max 250 kbps, 2W TX
Sina-1 [15]	2005	700 km, SSO, near polar	160 kg	146 MHz, 4.8 kbps, BPSK, 5W TX, $\frac{1}{2}$ rate conv. coding, Viterbi decoding	435 MHz, 4.8 kbps, BPSK, 5W TX	(not for S&F data downlink to GS)
ANUSAT [16]	2009	402/552 km, $i=41.2^\circ$, polar	38 kg	VHF (amateur), 9.6 kbps, FSK, turbo coding	UHF (amateur), 9.6 kbps, FSK, turbo coding	(not for S&F data downlink to GS)
Hodoyoshi-3 & 4 [17]	2014	612/665 km; 612/650 km; SSO, $i=97.97^\circ$	56kg; 64 kg	400 MHz licensed band, 1W TX, no onboard demodulation, BPSK used for testing, 10/40 kHz A/D sampling frequency	-	X-band, 10 Mbps, 2W (download recorded S&F signal to GS)

Table 2. Some S&F small satellite and microsatellite missions (part 2)

Satellite	Multiple Access Scheme (for S&F user uplink)	Link Layer	Upper or Application Layer
SSTL/UoSAT series [13] (e.g., UoSAT-2, -3, -5, S-80/T, KITSAT-1, PoSAT, HEALTHSAT-2, etc.)	ALOHA-type (pure, slotted, SRMA); some satellites in this series have multiple receivers	AX.25 protocol, ARQ with FEC	PACSAT protocol suite – transaction-oriented (file server, file transfer/messaging, broadcast, email networking, etc.)
Maroc-Tubsat (Zarkae Al Yamama) [18][19]	Purely random (ALOHA)	Stop-and-Wait ARQ, likely AX.25 protocol	MCU program
Sina-1 [15]	SRMA (1 RA UL for slot request, 1 reserved mode TDM UL for data transmission, 1 DL for data transmission)	Only simple ACK of received packet	None described
ANUSAT [16]	Polling and reservation scheme	Sliding window, go-back-N ARQ, HDLC	3 phases: Directory broadcast, allocation, data transfer; file & memory handling; RTOS for multi-tasking
Hodoyoshi-3 & 4 [17]	None	None	None

2.2 The Rise of Nanosatellites and CubeSats for S&F Communications and Wireless Sensor Networks

In recent years, with the rise of even smaller classes of satellites, including nanosatellites and picosatellites, especially the popular CubeSat standard [24] platforms, there have also been ideas to utilize them as space-based data relay for remote data collection. The value proposition is that a S&F nanosatellite or nanosatellite constellation can be launched at relatively low cost to serve a niche practical use as relay for collecting data from stations deployed in remote or isolated sites – those usually not served by regular communication infrastructure or where access by humans is challenging.

An example of a mission concept utilizing a nanosatellite for remote data collection is the WAPOSAT [25], which aimed to retrieve water pollution parameters from sensors (pH, oxygen concentration, temperature, fluidity, etc.) distributed over Peruvian lakes and rivers. The mission concept is shown in Figure 5.

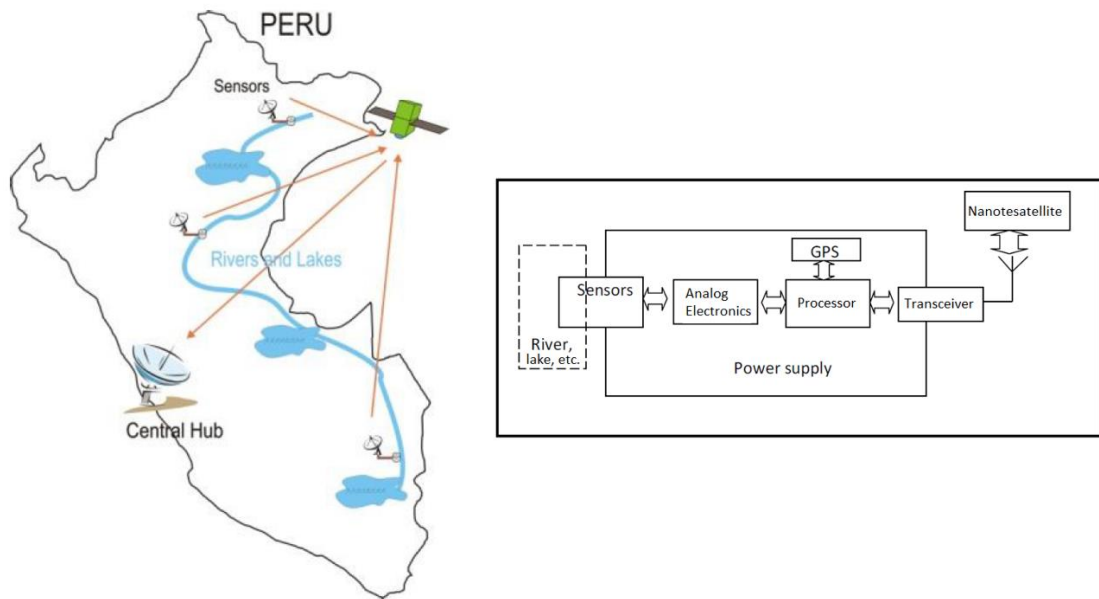


Figure 5. Mission concept of WAPOSAT and block diagram of autonomous multi-sensor system. Data from polluted water is sent to a Central Hub in Lima (Peru) through 2U cubesat constellation (source: [25])

Since many remote data collection scenarios also involve low-volume data, low-data rate and latency is tolerable, a S&F nanosatellite or nanosatellite constellation can be considered as a practically suitable solution (the size of constellation depends on application requirements). Previous work on this topic range from academic research, actual satellite missions by academic/research/civil organizations (typically non-constellation), and those by companies aiming to provide commercial services and are in the process of realizing their envisioned constellations. Commercial nanosatellite IoT/M2M solutions are surveyed in Section 2.5. This section focuses on the academic, research and non-commercial work.

Several published work in literature have tackled S&F nanosatellites/picosatellites as an important component of satellite-connected wireless sensor networks (WSN) [26], intermittent and disruptive/delay-tolerant networks (DTN) [27], Internet of Remote Things (IoRT) [28] and sparse network of tiny satellites supporting store-and-forward routing [29]. Paper [30] presents a futuristic idea in which terrestrial and space based WSNs may be seamlessly integrated, consisting of distributed systems of smaller space and ground nodes.

In [26], the authors considered a WSN scenario depicted in Figure 6 in which ground relay nodes (RNs) transmit data to a nanosatellite during a duration-limited pass using a slotted ALOHA (SALOHA) random access protocol with a re-transmission scheme for collided packets. The nanosatellite sends an acknowledgment for every successfully received packet, and if no acknowledgment is received, collision is assumed, and each colliding RN re-transmits after a random back-off time. By assuming employment of a very simple payload, whereas all the complexity is brought back to the relay nodes (RNs), the RNs are expectedly equipped with synchronization clocks for SALOHA to properly work.

The paper [26] calculated the energy consumption and lifetime of each RN (which takes into account all parameters involved for determining the lifetime of a RN, such as current consumption and duty cycle of each operation mode and average re-transmission rate) and a discrete-event simulation showed the maximum number of RNs that can be served at the same service area of the nanosatellite without reaching traffic saturation. Since the energy consumption depends heavily on the average re-transmission rate, which is influenced by the number of deployed RNs within a service area (due to collision rate), this work showed that a lower number of RNs should be decided to optimize the RN's battery lifetime (in addition to traffic saturation limit). An earlier work also investigated slotted ALOHA in a small S&F satellite-based remote data collection system [31].

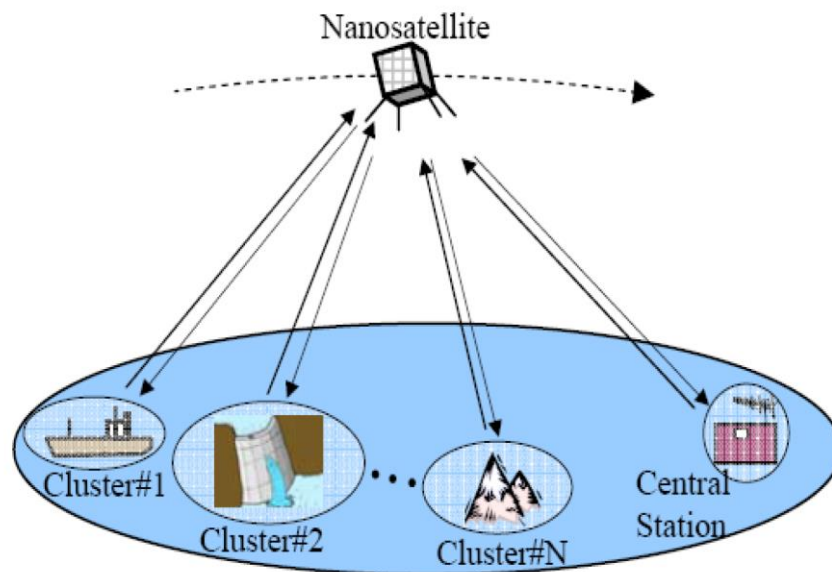


Figure 6. Wireless sensor network using store-and-forward nanosatellite (source: [26])

A succeeding work by the same authors [32] presents a modified random-access protocol, called slotted ALOHA with collision avoidance (SALOHA-CA), to improve the throughput and energy efficiency compared to the traditional SALOHA. In SALOHA-CA, RNs listen to the activity of the channel through the acknowledgment packet meant for another RN. If an acknowledgment for another RN is received, the RN waits for a random number of time slots and checks the channel again. In this way, occurrence of collisions is reduced. If the channel is vacant, an RN transmits a packet and the reception of first acknowledgment serves as a reservation allowing the RN to transmit a set number of packets in the succeeding slots. In case two or more RNs transmit after observing a vacant channel, those colliding RNs back-off from transmission and check the channel at the later time.

With SALOHA-CA, numerical results showed that the improvement can be substantial and the maximum throughput approaches 100% (compared to 36% in traditional SALOHA) when the relay nodes have several packets of data to send during the visibility period but at the expense of the number of RNs on the ground. On the other hand, un-slotted ALOHA is more desirable for a simpler ground terminal at the expense of half the throughput of slotted ALOHA (or 18%). A previous work [33] studied unslotted

ALOHA performance for a single microsatellite data collection system with ground terminals, considering channel throughput, network capacity, packet transmission delay (which impact terminal queue size).

A few works have implemented nanosatellite-based S&F systems, including the HumSat system [34], Irazu project [35] and TriCOM project [36]. HumSat (Humanity Satellite) project [34] was an ESA-supported educational initiative allowing university students to participate in an international collaboration for implementing a swarm of CubeSats providing worldwide communication capabilities to those areas without infrastructure, especially in developing countries. The HumSat S&F system was designed to provide free, non-guaranteed non-commercial data-relay services to one-way and bidirectional sensors built by users according to their desired applications.

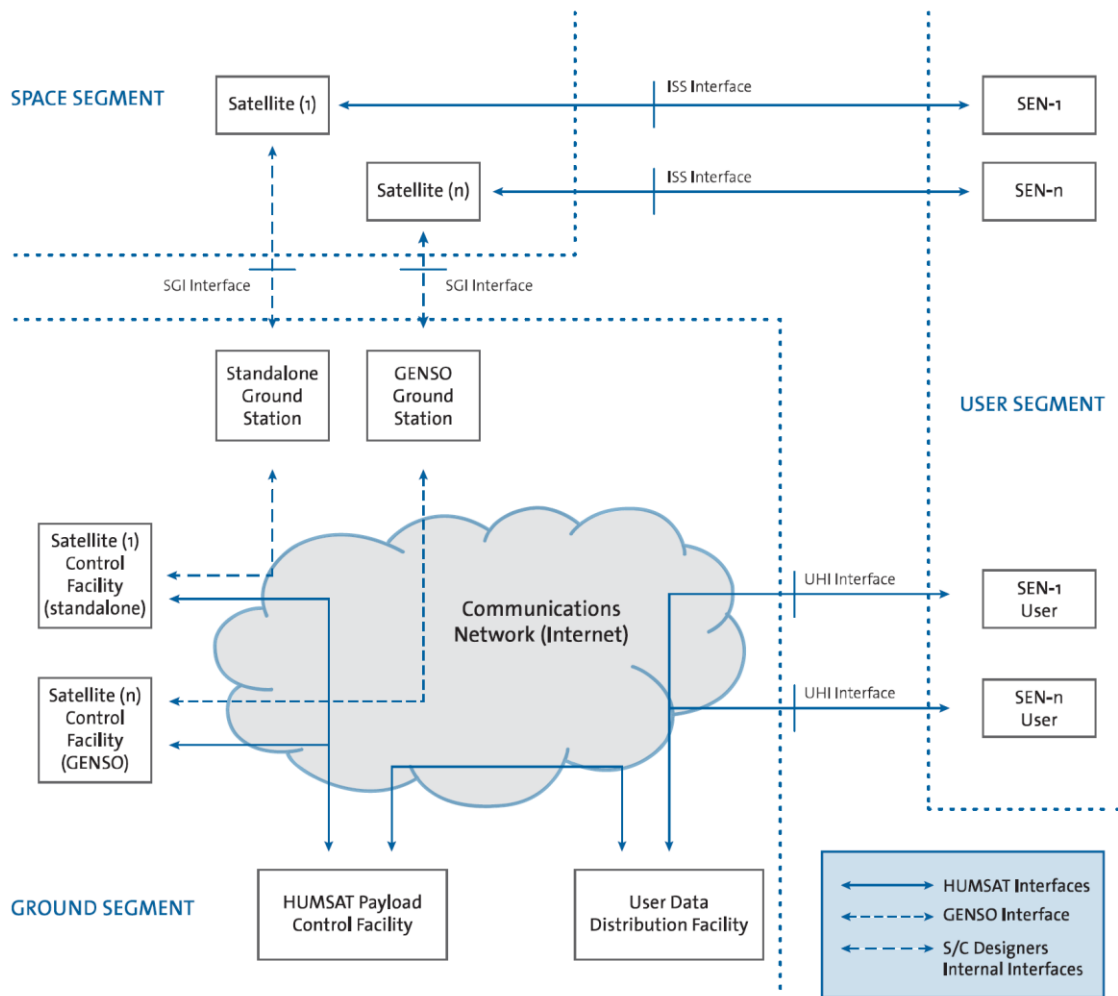


Figure 7. The HumSat architecture composed of three parts: space segment, ground segment and user segment (source: [34])

The HumSat architecture, shown here on Figure 7, consists of the space segment, ground segment and user segment, which to be built by collaborators following a defined set of communication protocols and interfaces. Sensor stations in the user segment send data to the onboard payload of any member satellite (space segment), and the collected data are subsequently downloaded through the GENSO ground station network. All radios of the HumSat communication system operate in various amateur radio bands (VHF,

UHF, S-band) [34]. The HumSat-D satellite payload developed by the University of Vigo consists of four receivers, which makes it capable to receive four simultaneous packets from different sensor stations [37].

The Irazu project [35] of Costa Rica Institute of Technology (TEC) operated an environmental data collection system using a 1U CubeSat (deployed last April 2018), with a concept of operations shown here on Figure 8. The Irazu CubeSat served as a data relay to obtain data from an experimental environmental station consisting of distributed sensors for measuring tree growth (dendrometers and ultrasonic sensors) and environmental parameters (temperature, humidity, pressure). The project reported a successful demonstration of the CubeSat-based S&F data collection system by being able to obtain relayed data from the station. The payload communication utilized a frequency in the 430 MHz band as secondary service.

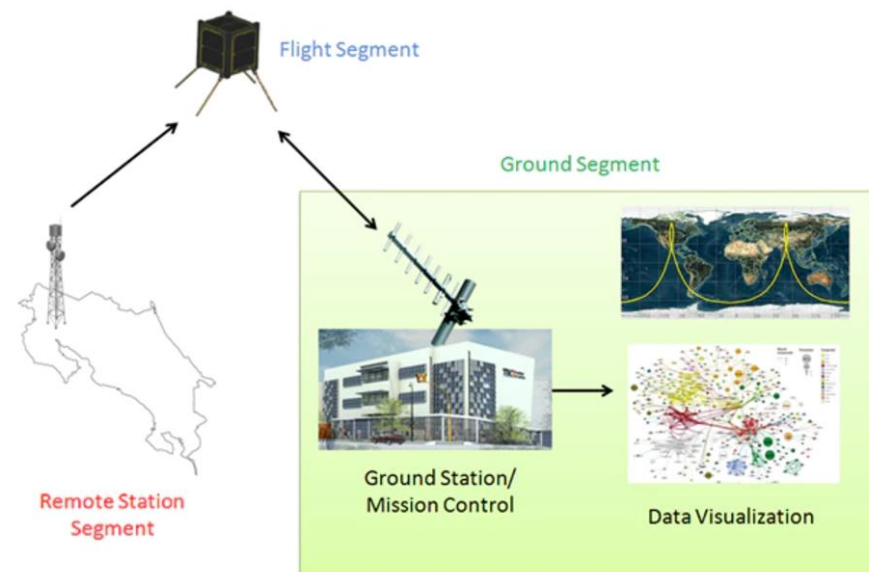


Figure 8. Irazu project concept of operations. The overall system consists of three segments: remote station, flight and ground segments. The experimental station measured monitoring data that relate to carbon sequestration, including tree growth and environmental parameters (source: [35])

The TriCOM project of the University of Tokyo aims to build and operate 3U CubeSats carrying a S&F payload that relays data from beacon-transmitting remote stations (temperature, soil moisture, water level, etc.) and download the data to a main ground station in Japan [36]. The S&F payload onboard the TriCOM-1 CubeSat consists multiple LoRa modules that support a total of 16 channels, thus it is capable of receiving up to 16 simultaneous transmissions from different stations (with specified receiver sensitivity within -132 to -145 dBm depending on data rate). The remote stations transmit a maximum of 20 mW at the 920 MHz ISM band at very low data rates (45/146/293/488/976 bps).

Data download is done at a licensed frequency within the 460 MHz band. After the launch failure of TriCOM-1 in January 2017, an identical CubeSat, TriCOM-1R was built and launched in February 2018 [38][39]. The payload operated well and the team reported that through tests from various locations around the world (e.g. Chile, Costa Rica, Japan, Rwanda), successful uploading of data from the sensors to the payload was demonstrated with a signal power as low as 8mW, well below the original target of 20mW. Then, another 3U CubeSat named RWASAT-1 carried the same S&F payload to perform the S&F mission.

It is first satellite of the Republic of Rwanda, co-developed with the University of Tokyo based on the modified TriCOM bus design (TriCOM-2), and was deployed from the ISS in November 2019.

Table 3. Some nanosatellite S&F missions for academic, research and civilian (non-commercial) purposes

Satellite	Launch Year	Orbit	Mass	S&F User Uplink	S&F User Downlink	Mission Data Downlink
Humsat-D	2013	596 × 639 km, $i=97.80^\circ$	1U	437 MHz, amateur, 4 receivers	Not yet implemented on this mission	145 MHz amateur, SP-L, 9600 bps
Irazu	2018	400 km, $i=51.64^\circ$ (ISS release)	1U	437 MHz, amateur, 9600 bps, GRUH FSK, up to 50W TX	-	437 MHz, amateur, 9600 bps, GRUH FSK
TriCOM-1R; RWASAT-1	2018; 2019	183/2010 km; 400 km, $i=51.64^\circ$ (ISS release)	3U	920 MHz ISM band, LoRa modulation, 20 mW TX, 16 receivers, 45-976 bps	-	460 MHz,
(3) BIRDS-2 CubeSats	2018	400 km, $i=51.64^\circ$ (ISS release)	1U	145.825 MHz, amateur, 1200 bps, AFSK, up to 5W TX	145.825 MHz, amateur, 1200 bps, AFSK, up to 0.5W TX (for ACK)	437.375 MHz, amateur, 9600 bps, GMSK, 0.8 W

Table 3. Some nanosatellite S&F missions for academic, research and civilian (non-commercial) purposes (part 2)

Satellite	Multiple Access Scheme (for S&F user uplink)	Link Layer	Upper or Application Layer
Humsat-D	custom MAC (not described in detail)	CCSDS protocol	-
Irazu	None (single remote ground terminal)	AX.25 protocol	CSP
TriCOM-1R; RWASAT-1	LoRa – chirp spread spectrum (can receive up to 16 simultaneous packets at different data rates)	-	-
(3) BIRDS-2 CubeSats	Purely random (ALOHA)	AX.25 protocol	Simple S&F MCU program

2.3 CubeSats with APRS-DP Payloads

As since 2000s, a few satellites (mostly non-CubeSats ranging from 10kg to 70kg) have carried an Automatic Packet Reporting System (APRS) digipeater payload for global amateur community use, including the Amateur Radio on the ISS (ARISS), PCSAT [40], LAPAN-A2 [41], Diwata-2 [42]. More recently, with the rise of even smaller classes of satellite, especially the standardized CubeSat platforms, there have also been proposals and actual implementations of CubeSats carrying an APRS-DP. These include, among others, PSAT-1 (1.5U, 2015) [43], PSAT-2 [44] and BRICSAT-2 (1.5U, 2019) [45].

APRS originated as a terrestrial amateur radio-based real-time packet communication protocol that enabled operators to exchange various situational information in their local area (e.g., weather reporting, object/vehicle position tracking, messaging, and emergency response). Later on, with stations having been interconnected by the Internet (called IGates) through the APRS Global Internet System (APRS-IS), global monitoring of local activities and two-way end-to-end messaging between any two APRS users have been supported [46]. Due to a satellite's capability to provide a geographically broad coverage directly below its moving footprint, an APRS digipeater (APRS-DP) onboard a satellite would subsequently play a significant role of covering remote areas not reached by terrestrial means.

With a satellite-onboard APRS-DP, using an APRS-capable radio, a “ham” (a common term for amateur radio operator) sends an APRS packet (message, position, beacon, telemetry, etc.) to the satellite and then the payload retransmits it immediately (and can be set to re-transmit automatically at a later time), allowing other hams or amateur stations on the footprint to receive it (Figure 9). This also works for fixed and mobile amateur stations, such as weather/telemetry/environmental stations, buoys, and GPS-equipped vehicles of remote travelers [50]. The idea proposed in [50] is for existing and future APRS-DP satellites in orbit to share a common channel (145.825 MHz) and a generic digipeater alias (APRSAT and ARISS) to accumulate all user traffic on an Internet server, hence integrating all worldwide users and ground stations.

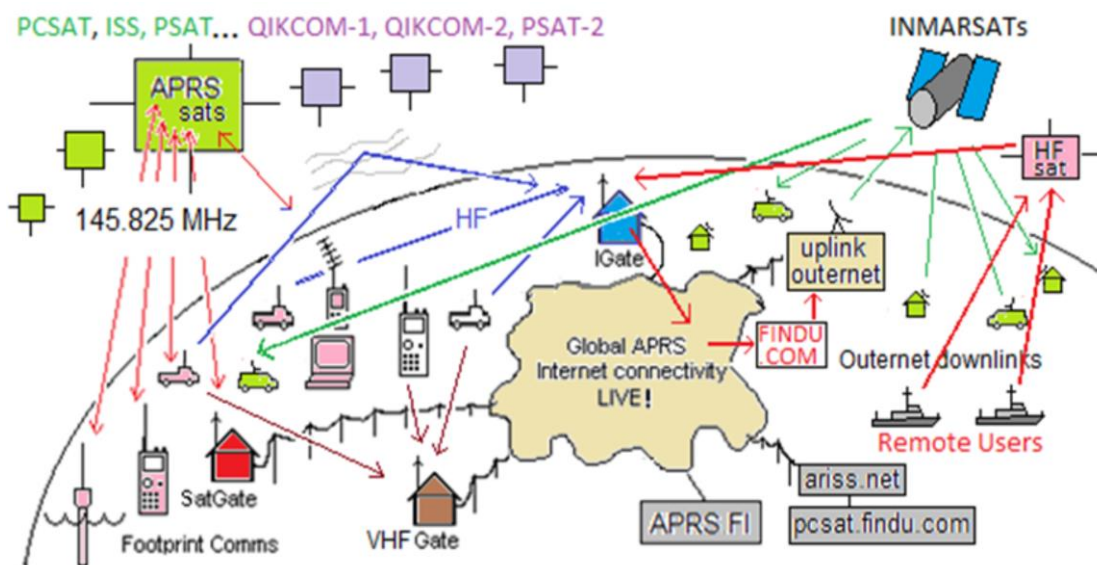


Figure 9. Operational concept of APRS satellites [44]

In the BIRDS-2 Project, we developed an amateur payload consisting of mostly commercial-of-the-shelf components and supports both APRS-DP and S&F communication, which are considered complementary applications. The payload was carried as a technology demonstration mission of a 1U CubeSat constellation (BHUTAN-1 of Bhutan, MAYA-1 of Philippines and UiTMSAT-1 of Malaysia) developed at the Kyushu Institute of Technology under the BIRDS-2 Project. The payload design, development, testing, and integration with the CubeSats are detailed in Chapter 4.

Other inexpensive implementations of nanosatellite-onboard APRS-DP/S&F payload have been described in literature [164]-[166]. In [164], the communication program, modem, packet handling and onboard data handling are handled by one MCU on a single board, and a half-duplex COTS VHF amateur transceiver is used for transmitting and receiving RF signal. This integrated approach results in a more compact onboard system, although it requires more programming work on the part of the developer to implement the APRS application, AX.25 protocol, and AFSK modulator/demodulator (modem) on the MCU.

On the other hand, in BIRDS-2, we used a compact COTS module (supporting APRS-DP functions, AX.25 protocol and AFSK modem) was used in combination with 0.5 W VHF transceiver from another company and an MCU implementing the S&F communication program. This allowed the developer to focus more on the S&F program development and payload integration. The payload developed for PSAT-1, PSAT-2 and BRICSAT-2, albeit developed only for supporting APRS-DP, evolved from a complete APRS packet transponder (including the radio) product commercially available but modified to fit in a standard CubeSat form factor [47][48].

2.4 Survey of Recent Commercial Nanosatellite IoT/M2M Communications Solutions

The surveyed commercial nanosatellite solutions for IoT/M2M communications are given in Table 4. As almost all companies utilize patented communications technology, it is not possible to obtain details on physical and MAC layers. From the surveyed information, the following trends may be stated:

- Since most of these companies are recent start-ups founded in the past five years or so, only a few of them have reached preliminary or pilot commercial services to customers. These more advanced companies have already rolled out development kits including modems to communicate with satellites. Others (most) have only recently launched a few experimental/demonstration satellites or payloads to their communications technologies or expected to launch demonstration missions in 2020.
- Most target to utilize the CubeSat-based platforms of various sizes, depending on the complexity of the mission or service, and perhaps on the developed payload. Predominant are 3U and 6U CubeSats.
- In terms of satellite orbit, most target polar LEO orbits between 500 km. and 800 km.

- In terms of communication topology, most support only direct-to-satellite mode. One supports both direct-to-satellite solution and gateway solution (end device to ground gateway to satellite), and another supports only gateway solution.
- Among those direction-to-satellite solutions, a significant portion adopt the originally terrestrial LPWAN technologies such as the proprietary protocols LoRa/LoRaWAN and SigFox, as well as the open standard cellular technology NB-IoT. The idea is to provide connectivity to existing regular end devices (originally equipped with capabilities for terrestrial networks) and integrate them to existing terrestrial infrastructure, or even allowing capability to seamlessly connect to either terrestrial or satellite network, whichever is available. The design of satellite-onboard base station receiver or transceiver remains proprietary and hence serves as the company’s leverage. Meanwhile, those providing gateway solutions focus on supporting LoRaWAN protocol, but also open to supporting other protocols such as WiFi and Bluetooth. Still, a significant number of others have developed their novel proprietary communications protocols and technologies.
- Some support only one-way (uplink) communication while others support two-way (uplink and downlink) communication. Operators supporting both types are significantly numbered.
- In terms of frequencies, both licensed and ISM bands are utilized or planned to be utilized: For ISM bands: the ~433 MHz and ~860/920 MHz bands; for licensed bands: VHF (137/148 MHz bands), UHF (~400 MHz), L-band (~1500 to ~1600 MHz), S-band, Ku-band.

Table 4. Commercial nanosatellite solutions for IoT/M2M communications

Satellite Operator	Satellite Platform	Constellation	Channels	Communication Architecture and Schemes	Targeted Markets or Highlighted Application Cases	Status/Targets
Astrocast SA, formerly ELSE SA (Switzerland) [51]-[54], in partnership with Thuraya	3U CubeSat	-Originally 64 satellites (8 planes, 8 satellites each) -Changed to 80 satellites -500 km to 600 km orbit -Polar and equatorial orbits	-L-band -Bidirectional, “highly secure connection”	-Direct-to-satellite solution -Uplink message sizes up to 160 Bytes -Downlink message sizes are either 8 or 40 Bytes -Multiple messages (few kB)/day -Average end-to-end latency of 5-7 minutes -No info on modulation and MAC -Peak power consumption of modem = 0.45W	-Maritime applications and tracking; environmental monitoring; mining, oil and gas (equipment/infrastructure monitoring)	-Currently doing pilot programs with our pre-commercial service -Have 2 operational satellites in orbit -Set to launch 30 by late 2021 -Full constellation by 2023/2024 -Developed terminal comm. module (Astronode™ S), full commercial development kit will be released in 2020
Hiber, formerly Magnitude Space (Netherlands) [55]-[58], in partnership with Iridium	3U & 6U CubeSats	-600 km, polar SSO -Consists initially of 18 to 24 satellites, later to expanded to 48 or 50	<i>Direct-to-satellite (D2S)</i> -One-way (uplink) S&F communication -399.90-400.05 MHz (sensor uplink)	-Supports direct-to-satellite and gateway (LoRa/LoRaWAN) solutions -144 bytes/message -Up to 4 messages/day for direct-to-satellite solution and 100 messages/day for gateway solution	-Maritime tracking; environmental monitoring; smart agriculture (e.g. soil moisture, crop monitoring); animal tracking	-Launched first 2 satellites in 2018 -Launched commercial IoT satellite trials worldwide in November 2019 -Expects to launch 2 more satellites in early 2020

Nanosatellite S&F Communication Systems for Remote Data Collection Applications

			<p>-400.15-401.00 MHz (downlink, perhaps for ACK?) communication only</p> <p>Gateway (GW) -433/868/915 MHz</p>	<p>-Current consumption of modem in transmission mode = 4.13W (D2S) -GW: 8-channel LoRa concentrator, can support up to 500 devices -5.3 dBi RHCP antenna -No info on modulation and MAC</p>		<p>-Developed Hiber LPGAN modem, a low-power communication front-end</p>
<p>Kepler Communications (Canada) [59]-[63]</p>	<p>3U & 6U CubeSats</p>	<p>-575 km polar orbit -140 satellites to provide "total global coverage"</p>	<p>-Bidirectional communications for data acknowledgments and firmware updates -Ku-band (14.0-14.5 GHz uplink, 10.7-12.7 GHz downlink)</p>	<p>-Direct-to-satellite solution -Uplink capability: 2 kB/day or 60 kB/month -Flexible SDR communications payload -Antenna array onboard satellite for creating highly directional RF beam -Its everywhereIoT™ service provides a "cellular-quality" and standardized connection for IoT devices; aiming to support hundreds of millions of low-cost devices globally -No info on modulation and MAC -In addition, its Global Data Service™ provides a secure non-time sensitive backhaul service for transferring large data files between remote sites and the Internet -Tracking antenna needed to communicate with satellites</p>	<p>-Logistics and transportation; fleet tracking; asset monitoring; energy and natural resources monitoring; smart agriculture; environmental monitoring</p>	<p>-Operates two satellites currently in orbit (Kepler 1 & 2 launched in 2018) -Demonstrated the capabilities of its technology by delivering a high-speed internet data connection to the North Pole in late 2019 [60] -Kepler 3 to be launched 2020 -Rolled out development test kit (Kepler IoT DevKit™)</p>
<p>Fleet Space Technologies (Australia) [64]-[67]</p>	<p>First four are 1.5U and 3U CubeSats, will launch 6U/12U CubeSats in future</p>	<p>-580 km SSO orbit ~100 satellites</p>	<p>-LoRa™ Supported: 902-928 MHz, 863-870 MHz, 433 – 434 MHz -S-band and L-band</p>	<p>-Gateway (LoRaWAN) solution -GW supports up to 500 devices (for 8-channel) or 1000 devices (for 16-channel) within 15 km range -In addition, GW supports a range of IoT protocols developed for terrestrial infrastructures, including Bluetooth 4.0 and 802.11ac Wi-Fi -Supported message types: Confirmed Uplink, Confirmed Downlink, Un-Confirmed Uplink, Un-Confirmed Downlink</p>	<p>-Demands from customers in energy, natural resources, and mining applications (asset tracking and asset management) -Also agriculture (e.g. herd management), environmental monitoring, logistics</p>	<p>-4 CubeSats launched in 2018 -Developed and made available Fleet Portal, an Edge Server, a LoRaWAN™ gateway and a satellite modem and antenna all wrapped into one fully integrated module. It is optimized for remote scalable IoT applications -Currently uses Iridium and Inmarsat services while establishing their own constellation -Likely to launch another 4</p>

Nanosatellite S&F Communication Systems for Remote Data Collection Applications

				-GW RF output: 24 dBm -GW power consumption: 10-15 W -No info on satellite communication		CubeSats by late 2020
Kineis, a spin-off from CLS, CNES subsidiary which was responsible for Argos (France) [68]-[69], in partnership with Thales Alenia	16U CubeSats/ Microsats	-25 CubeSats, in addition to existing Argos satellites -650 km orbit	-Two-way communication -Likely to use the same frequency band as Argos satellites (UHF)	-Direct-to-satellite solution -Draws on the Argos system legacy (6 Argos satellites in orbit) -Likely, pure ALOHA MAC -Objects connected through Kineis will be geo-located -Secondary AIS payload for ship tracking	-Outdoor sports, agriculture, artisanal fishing, logistics, boating, security, science	-Angels prototype nanosatellite launched in 2019 -Planned full constellation by 2022 -Keneis supplies radio chipset to provide satellite network connectivity to any mobile device
Myriota (Australia) [70]-[74]	CubeSats (5kg)	-600 km SSO orbit -50 satellites planned	-Two-way communication -Uplink: UHF (399-403 MHz) or VHF (156-165 MHz) -Downlink: UHF (400-401 MHz) -ISM (433-435 MHz)	-Direct-to-satellite solution -TX RF power: 27 dBm (UHF/VHF), 14 dBm (ISM) -Uplink message of 20 bytes	-Agriculture, transport and logistics, maritime, defense, environment, mining, utilities	-Developed Myriota Module, a sophisticated edge computing and modem device -First tested transmission of IoT data directly to nanosatellite in 2013 -System deployed by some customers and delivered data and service -Offers Developer Toolkit -Four satellites currently in orbit (1 own, 3 from others)
Swarm Technologies (US) [75]-[79]	~0.25 U (SpaceBEE)	-150 satellites planned -300-550 km, equatorial and polar orbits	-Two-way communications -VHF bands: 148-149.95 MHz (uplink), 137-138 MHz (downlink)	-Direct-to-satellite and gateway (LoRa, WiFi) solutions	-Maritime shipping, agriculture, energy, ground transportation, global development (e.g., air and water quality monitoring, emergency comms, weather/climate changes)	-Launched 9 satellites in 2018 -Developed a communications modem
Lacuna Space (UK) [80]-[82]	3U, 6U CubeSats	-500 km orbit -32 planned satellites	-One-way (uplink) communication -Sub-GHz ISM bands	-Direct-to-satellite (satellite-onboard LoRaWAN™ gateway) -Receives signals from ordinary LoRa-based devices through the LoRa™ RF communication protocol -Pure ALOHA -Works seamlessly with terrestrial networks	-Applications that involve sending short messages -E.g., maritime tracking, wildlife and marine monitoring, asset tracking, environmental monitoring	-Hosted payload on one launched nanosatellite M6P (LacunaSat-1, BTD-1) and on several to be launched nanosatellites -Expected launch of own satellite, LacunaSat-1, in 2020 -Announced successful global test campaigns with on-orbit satellite payload
Helios Wire, acquired by EchoStar in October 2019 (Canada) [83]-[85]	6U, 16U CubeSats	-30 planned satellites (during Helios Wire time)	-S-band (30 MHz)	-“To receive tiny data packages from huge number of sensors”		-Launched 2 satellites -To launch three satellites in 2020 -Conducting tests across the network probably

Nanosatellite S&F Communication Systems for Remote Data Collection Applications

						by late 2020, and certainly by the first quarter of 2021
Eutelsat LEO for Objects (ELO) [86]-[94] in partnership with SigFox	3U CubeSats, 8-kilogram payload on 80-kg multi-customer condensats	-25 planned nanosatellites -600-700 km SSO orbit	-One-way (uplink) communication -Sub-GHz ISM bands	-Direct-to-satellite solution (satellite-onboard SigFox base station receiver) -Receive signals from ordinary SigFox-based end devices -15-20 mW power -Eutelsat acts as a full Sigfox Network Operator, while Sigfox seamlessly integrates the satellite network to its existing terrestrial infrastructure and connectivity services (i.e., end-devices' transmissions can be captured by both the satellites and any terrestrial networks).	-Asset tracking in oceans and other remote locations -Applications that involve sending short messages/ Beacons -Transportation, agriculture, and oil and gas industries	-Demo satellite will be launched in 2020, to confirm the technical performance of various waveforms between a satellite in low Earth orbit and objects on the ground -4 ELO satellites will be launched between 2020 and 2021 for commercial service -Full constellation by 2022
Sky & Space Global (Australia, UK, Israel, Poland) [95]-[100]	-8U, 6U and 3U CubeSats	-200 planned satellites -500-800 km orbit -Five orbital planes: one equatorial and four inclined near equatorial orbits	-S-band and L-band	-Voice, data and M2M communications service with ISL -Constellation creates a mesh topology where each satellite serves as both a base station and a router -Utilizing unique IP-nanosat network software protocol -Considered narrowband communication	-Communication service (voice, data, personal messaging and IoT/M2M)	-Launched 3 satellites (the 3 diamonds) -Delayed financing, planning to launch only 8 satellites by end of 2020
Sateliot (Spain) [101]-[104]	-3U CubeSats, also Microsats?	-500 km orbit -70 satellites planned	-Two-way communication	-Direct-to-satellite solution: acts like a satellite-onboard 5G NB-IoT base station -Support NB-IoT standard with the formalization of the non-terrestrial component expected in Release 17 of the 3GPP standard in the 2021-2022 timeframe -Will use the SDR technology (TOTEM) designed by Alén Space for R&D of new protocols and modulations on small platforms, that enable connection of objects in any remote place	-Aims to offer global continuous connectivity to all elements regarding the IoT under a 5G architecture -IoT/M2M, direct-to-phones -E.g., asset tracking, logistics, agriculture, remote infrastructure monitoring and control	-To launch first test CubeSat by middle of 2020 -Aims to launch 16 satellites by end of 2021
OQ Technology (Luxembourg) [105]-[108]	-Strategy is to use existing small satellites such as CubeSats to upload software or hosted payload, or if necessary, to build and launch their own satellites -No info on how many payloads or satellites to be launched		-Two-way communication	-Direct-to-satellite solution: acts like a satellite-onboard 5G NB-IoT base station -Support NB-IoT standard with the formalization of the non-terrestrial component expected in Release 17 of the 3GPP standard in the 2021-2022 timeframe	-Global 5G NB-IoT connectivity	-During TIGER mission, performed testing of communications protocol using GOMX-4A and-4B (6U CubeSats) -Expecting to launch their own 1U CubeSat, Finch-1, in 2020 for IoT demonstration

Nanosatellite S&F Communication Systems for Remote Data Collection Applications

<p>Lynk, formerly Ubiquitilink (US) [109]-[111]</p>	<p>Hosted payload, CubeSats</p>	<p>-Envisioned 1000 satellites</p>	<p>-Two-way communication</p>	<p>-Connect regular mobile phones from everywhere on the planet, especially those without terrestrial cellular coverage</p>	<p>-Global IoT/M2M, direct-to-phone connectivity (data and text messaging) -“Cell tower in space”</p>	<p>-Launched hosted payload in 2019 -Successfully transmitted a text message from space to an unmodified mobile phone on Earth in February 2020 -To commence service in 2020 with 24-36 satellites -Verifying GSM (2G) operations and plans expansion to include LTE (4G)</p>
<p>Blink Astro, a subsidiary of SpaceWorks (US) [112]-[115]</p>	<p>-Likely 3U CubeSats</p>	<p>?</p>	<p>-One-way (uplink) communication</p>	<p>-Direct-to-satellite solution</p>	<p>-Precision agricultural applications (e.g., soil moisture, ambient temperature and humidity, GPS location)</p>	<p>-Rolled out the BlinkR™ Series 1000 ground terminal device in November 2017 -Technology demonstration payload flown on M6P in 2019</p>

Chapter 3: Satellite S&F Communication Systems and Protocols

This chapter presents a literature review on communication system architecture, physical layer and random-access schemes, protocols, and technologies relevant to satellite-based IoT/M2M system.

3.1 Communication System Architecture, Configuration and General Considerations

Wireless sensor network (WSN) is simply defined as a network of tiny devices (“sensor nodes”) spatially distributed and cooperatively communicate information gathered from the monitored field by wireless links [116], without necessarily infusing the ideas of device-to-device communications (machine-type, without human intervention) and “all things being interconnected through the Internet” in the IoT and M2M and IoT paradigms. Nonetheless, several concepts and practical considerations of WSN have been applied to M2M/IoT. Sensor nodes in a WSN are typically constrained in terms of hardware and energy resources, complexity, computational power, and sensing rate, and due to bandwidth and power constraints, a WSN is usually characterized by low data rate.

Even before the rise of IoT/M2M, several works in literature had already described integration of a terrestrial wireless-sensor network (WSN) to a satellite network. When communication aspects are concerned, works on satellite-integrated WSN find relevance in satellite-integrated IoT/M2M, although the unique requirements of the emerging IoT/M2M applications should be differentiated (as will be discussed below).

Reference [117] surveyed the architectural and system design aspects of satellite-connected WSNs and matched the requirements of common WSN applications to the characteristics of various satellite systems. The satellite systems described therein, however, were mainly for global mobile personal communication services, including narrowband and broadband, real-time, and S&F types, LEO, MEO, HEO and GEO satellites. Five kinds of WSN applications were studied: surveillance and monitoring of remote areas; emergency communications; support for SCADA (supervisory control and data acquisition) systems; critical infrastructures (CIs); and environmental monitoring. Traffic volume was classified into low (<50 kbps), medium (50 to 500 kbps) and high (>500 kbps) while disruption tolerance is classified into low (interactive/responsive services), medium (timely services) and high (non-critical services). Among these, environmental monitoring applications were considered to have low traffic rate and high disruption tolerance (non-critical) while surveillance of remote areas were considered low traffic and medium disruption tolerance.

It identified two configurations of satellite-connected WSN for environmental monitoring, as illustrated in Figure 10: direct (sensors -> satellite communication), and indirect (sensors -> sink node + sensor gateway -> satellite communication). Three broad classes of sensor network applications were identified in terms of traffic generation: time-driven (sensor nodes periodically send their data to the sink node), event-driven, demand-driven (network queries the nodes for data). Two main types of network

architecture/topology were identified depending on application requirement: star (communication between devices and a satellite only) and mesh (communication among devices also supported). Standards for terrestrial WSN (ZigBee, 6LoWPAN and IEEE 802.15.4) and satellite technologies (DVB-RCS, GMR and GSPS) were reviewed and it was pointed out that the ETSI BSM SI-SAP can be used as the convergent technology for the integration of WSNs with heterogeneous satellite technologies. The paper [117] concluded that the traffic volume, disruption tolerance and architectural requirements of future WSNs can be met by the diverse existing satellite systems.

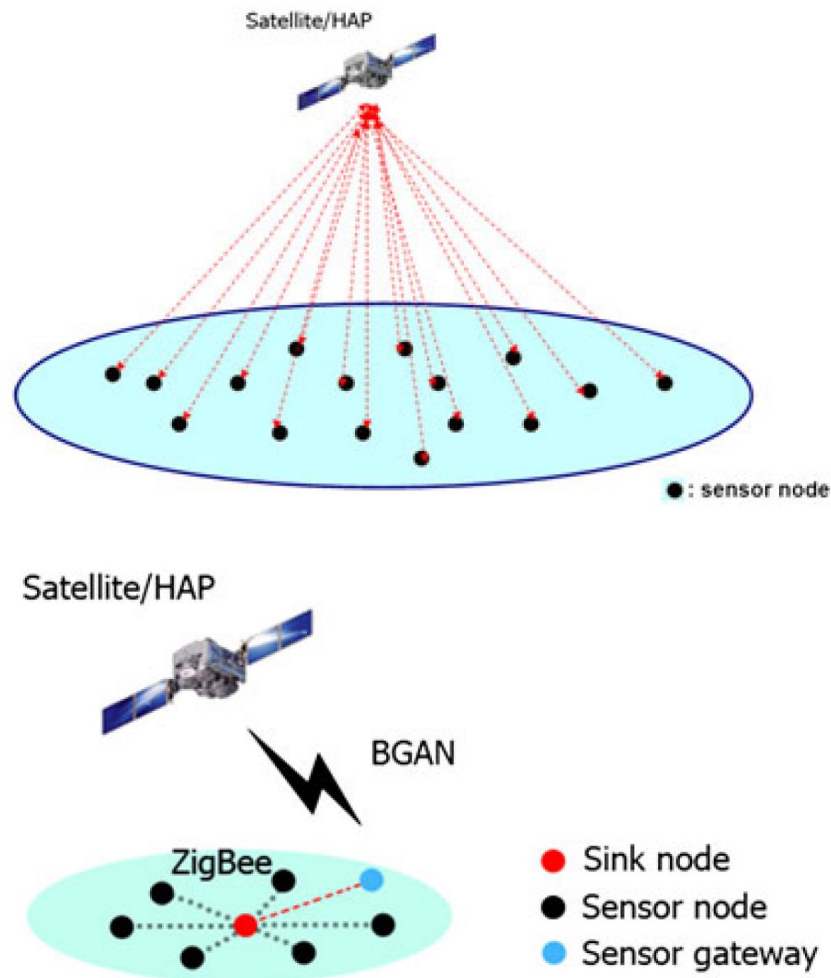


Figure 10. Two types of satellite-WSN configuration (examples): (left) direct sensor to satellite communication, (right) sensor gateway to satellite communication (source: [117])

However, newly burgeoning and traditional but evolving applications have led to different requirements that are not met by the current implementations of M2M via satellite, which provide low data rate and access to a few nodes via proprietary standards [118]. Reference [118] focused on the use of satellite communication systems for “Internet of Remote Things” (IoRT), which relates to IoT scenarios where smart objects are remote or dispersed over a wide geographical area. Unlike [117], which had focused on WSN scenarios, [118] provided an integrated view of satellite-based IoT, dealing with various topics such as MAC protocols for satellite-routed sensor networks, efficient IPv6 support, heterogeneous

networks interoperability (terrestrial and satellite), quality of service (QoS) management, and group-based communications.

Three IoRT scenarios where the use of satellites is of paramount importance were considered: (1) smart grids, (2) environmental monitoring, and (3) emergency management. Reference [118] considered that existing satellite-based M2M services cannot meet latency and bandwidth requirements for smart grids and the latency requirements for emergency management applications. Meanwhile, it considered environmental monitoring applications can be supported, although critical issues should be addressed including the need for more energy efficient multiple access, the varying topology and high number of nodes in several applications. Reference [118] also cited other previous works on MAC schemes and noted the importance of delay-tolerant networking (DTN) for low-cost small satellites (<50 kg) which are prone to intermittent and disruptive communication links due to limitations of such platforms (hardware constraints and non-optimized orbital plan and coverage).

For enabling interconnection between satellite and sensors/actuators, two modes of interoperability were also compared: direct access and indirect access. The indirect access mode, wherein a wireless sensor/actuator communicates with a satellite through a sink node, has the advantage of lower number of complex satellite terminals required for the same number of sensors/actuators. When several sensors are needed in a deployment location, indirect approach decreases system costs and installation complexity. In indirect access mode, a gateway attached/connected to the sink node forwards the aggregated traffic to satellite. There are many possible scenarios for implementation, but a good example would be an interconnection between a satellite system and a terrestrial LPWAN performing the sensor sink + gateway functions for a set of sensors nodes in a remote local vicinity. This deployment approach may also be considered a “hybrid terrestrial-satellite network”, where the satellite and ground communication components are interconnected, but operate independently (in contrast to “integrated satellite-terrestrial network”, where ground components are complementary to the satellite components) [119].

Of course, proper implementation of the gateway requires interfaces to be coordinated and managed between the LPWAN and satellite operators. A good practical example is the partnership between Inmarsat (a GEO satellite operator) and Actility (LPWAN operator) to deliver an end-to-end global LoRaWAN IoT network empowering business applications by combining Inmarsat’s global L-band satellite connectivity platform with Actility’s ThingPark IoT management platform [120]. By exploiting the respective advantages of an LPWAN system (suitable for connecting large number of very low-end, low-power, low data rate nodes) and an existing satellite platform (suitable for connecting more expensive/complex terminals sending higher data rates, as in a gateway node), the hybrid network deployment circumvents the previously mentioned limitations of existing satellite systems in catering emerging IoT/M2M applications. Reference [121] presents an architecture for a hybrid IoT-satellite network, which includes a terrestrial LoRaWAN (LPWAN) network for data collection and an Iridium satellite system for backhaul connectivity.

However, in a lot of other scenarios, it might not even be practical (i.e., either too costly to establish, or infrastructure-less deployment required or inapplicable such as in mobile wildlife tracking) or beneficial/profitable (e.g., only one or very few nodes in a vicinity so no need to aggregate traffic) to install an LPWAN gateway. Thus, in such cases, a direct access mode might be the better, if not the only possible, approach. Moreover, while the indirect access approaches (e.g., use of ground LPWAN gateway) can leverage existing satellite and LPWAN protocols, direct access approach better exemplifies the idea of connecting remote and ubiquitous IoT devices.

A research funded by EU Horizon 2020, called IoTEE project (“Internet of Things Everywhere on Earth”), envisages a solely space-based IoT system for bringing connectivity to sensors/devices in very remote and inaccessible places of the world which occupy most portion of the globe [122]. Thus, complementary to terrestrial LPWAN and to hybrid terrestrial LPWAN-satellite network deployments, this space-based LPWAN is the realization of a truly ubiquitous global coverage. For this approach, a new communication protocol and corresponding satellite receiver and ground transmitting devices that address the above-mentioned unique requirements of satellite-based M2M (i.e., can simultaneously receive low-power low-data rate burst packets from a large number of devices) should be developed.

In relation to this, SAT4M2M (the coordinator of IoTEE project) has been developing a receiver/emitter chip implementing a unique communication protocol for satellite-based LPWAN that operates on the same frequency bands as Sigfox and Lora, and utilizing the ISS as a testbed and “sentinel” for initial services [122]. SAT4M2M announced successful initial test results, partnership with Fujitsu Electronics on delivering preliminary services, and development of TELDASAT (“a novel technology platform, network and architecture based on Space IoT”), but because they use patented technology, no technical information on the system is available [122][123]. Recently, synonymous terminologies were created to refer to such systems as LP(U)WAN (Low Power Ultra-Wide Area Network) and LPGAN (Low Power Global Area Network).

Other papers in literature have also recognized the advantages and challenges of direct-access mode. Reference [124], for one, provides a state-of-the-art survey on “Direct-to-Satellite-IoT” (DtS-IoT), mentioning some challenges and future research efforts on revising/adapting existing protocols to support this idea. Topics tackled in [124] and the references therein include physical layer aspects (frequency spectrum, multi-beam antennas, spread spectrum modulation vs narrowband modulation), link layer multiple access scheme and upper layers (IPV6 addressing support, transport and application protocols such as MQTT and CoAP). It stated that a survey among relevant technologies showed LoRa is an appealing approach towards DtS-IoT but imposes severe challenges such as extremely low data rate and lack of knowledge on satellite channel effects on the behavior of the proprietary technology.

Meanwhile, Lacuna Space, a start-up nanosatellite IoT company, has developed a satellite-onboard LoRaWAN gateway in collaboration with Semtech Corporation (inventors and owners of LoRa) [125]. Like that of IoTEE project, Lacuna Space’s system also exemplifies direct-access to satellite, allowing

normal LoRa-equipped devices to transmit signal directly to a passing satellite. In addition, the devices on the Lacuna Network will seamlessly integrate with any LoRaWAN infrastructure on the ground within reach. Thus, this may also be considered as an example of an integrated satellite-terrestrial network (in contrast to hybrid satellite-terrestrial network).

It must be noted that the direct-access and indirect-access modes have their own advantages and disadvantages and the correct choice would depend on the application scenario, resources, and requirements. There are application scenarios where only direct-access mode would be possible and other scenarios where indirect-access mode would offer a more effective solution such as simpler sensor node design. Naturally, direct access would put most burden of complexity on the satellite segment (if ground sensor/device design is simple), while indirect access would bring some of the burden to the ground terminal (gateway) segment. Reference [126] compares the direct and indirect access modes as means of connecting LPWAN-based IoT ground devices, and focuses on the open technical challenges and research directions in integrating/interoperating satellite and LoRaWAN networks by indirect access method. It tackles issues in the context of LoRaWAN standard such as gateway and end-devices synchronization (given satellite condition), gateway selection and replicas cancellation, cross-layer (physical, MAC and application layers) optimization.

While there are works that adopt proprietary LPWAN technologies operating in ISM band such as LoRa (either in direct access or indirect access mode), there are also those that adopt the Narrowband-IoT (NB-IoT), which is an open standard cellular LPWAN technology (i.e., operating in the licensed band) developed by the 3GPP. It targets IoT applications that require very wide coverage of low-cost, low-power (20/23 dBm) and low-throughput devices. NB-IoT, first specified in the 3GPP Release 13 (LTE Advanced Pro) in June 2016 [127], supports smaller bandwidth (down to one single subcarrier transmission of 3.75 or 15 kHz) and provides 20 dB high link budget than legacy LTE for low throughput terminals. Reference [128] discusses coverage extension of a LPWAN using a LEO satellite constellation, considering device uplink transmissions (unidirectional) that comply with the NB-IoT standard. In terms of implementation, OQ Technology, a Luxembourg-based satellite IoT/M2M service company, announced it has successfully tested NB-IoT waveforms and synchronization schemes using GomSpace's GOMX-4A and GOMX-4B satellites during its Tiger mission [129].

Satellite constellation design aspects fundamentally affect satellite IoT coverage and communication performance so these also must be carefully considered. Reference [130] provides an overview of the architecture of the LEO satellite constellation-based IoT including the following topics: LEO satellite constellation structure, efficient spectrum allocation, interference analysis and mitigation approaches, heterogeneous networks compatibility (between LEO constellation-based and terrestrial IoT systems), and access and routing protocols. It also tackles two types of network architecture in terms of presence of inter-satellite link (ISL): (1) Earth ground station-centralized network architecture (without ISL, for delay-tolerant applications) and (2) dynamic satellite topology network architecture (with ISL, for delay-sensitive applications).

3.2 Physical Layer

3.2.1 Channel Model

The propagation channel between a ground device and a satellite physically affects the characteristics of the signal arriving on both sides of communication – in terms of amplitude/power level attenuation, phase, frequency, multi-path and other distortion effects, as well as noise and interference from other transmitters. As the received signal quality fundamentally determines the communication reliability performance in terms of bit-error rate (BER) or other similar metrics – in addition to signal processing (e.g. modulation and channel encoding), link layer and multiple access schemes – it is of outmost importance to accurately model the propagation channel characteristics. The propagation channel characteristics, which depend on certain physical and statistical assumptions of the channel, are necessary to properly perform link budget analysis.

Reference [131] provides an overview of the existing satellite communications channel models in literature, which mostly consider land mobile satellite (LMS) communication systems (see Table III of reference [131]). Among these models, Loo's model is the most well-known statistical models used for LMS systems and has shown agreement with measurement results in rural environment. While this model does not consider the Doppler effect usually present in LEO satellites, it suffices to represent the received signal amplitude distribution. Doppler effect can be separately accounted during demodulation by incorporating the Doppler shift and rate in the received signal's mathematical model. Loo's model is planned to be used in our work. In Loo's model, the amplitude of the line of sight (LoS) signal is modeled by using a log-normal probability density function (PDF), while the multi-path signals are modeled using a Rayleigh PDF. The distribution of the signal envelope in Loo's model is given by

$$f(r) = \frac{r}{\sigma_m^2} \int_0^\infty \exp\left(-\frac{r^2+a^2}{2\sigma_m^2}\right) I_0\left(\frac{ra}{\sigma_m^2}\right) f(a) da \quad (1)$$

where σ_m^2 is the variance of the multi-path,

$$f(a) = \frac{1}{a\sqrt{2\pi\sigma_s^2}} \exp\left(-\frac{(\log(a)-\mu_s)^2}{2\sigma_s^2}\right), a > 0 \quad (2)$$

μ_s and σ_s^2 are the mean and variance of the shadowing component, respectively, and $I_0(\cdot)$ is the zero-order Bessel function.

3.2.2 Modulation and Coding Schemes

For the satellite-based IoT communication scenario being considered, there are constraints on energy (due to requirements to maximize the operation lifetime of small-size low-cost devices, as well as regulatory constraints on transmission power) and available bandwidth. With both energy and bandwidth constraints, the system should be able to receive as many packets as possible from devices wanting to transmit data at any time. To prolong operation lifetime, not only should transmit power be lowered but more importantly, *energy efficiency* should be maximized. On the other hand, for greater communication system performance, the achievable *throughput* must be maximized. With a limited available bandwidth,

the throughput normalized to the available bandwidth, in terms of *effective information rate per bandwidth* (in bps/Hz), is a quantification of *spectral efficiency*. Furthermore, energy efficiency and throughput must be traded-off in the context of supporting as many transmitting devices as possible.

Reference [132] reflected on energy efficiency and spectral efficiency issues related to nanosatellite IoT networks and found that maximizing one efficiency is conflicting to maximizing the other efficiency. In [132], energy efficiency was simply defined as $\eta_{EE} = R_b/P_r \approx E_b$ (= average transmission energy per bit), but this does not account for the circuitry energy consumption (i.e., mainly from RF power amplifier) in the expended energy for communication and any reception errors. Paper [133] accounted for circuit power consumption, DC-DC converter efficiency, active mode duration and channel bandwidth in calculating the energy consumption of various modulation schemes (M-MFSK, M-QAM, OQPSK, OOK) without coding. For energy efficiency analysis, one can adopt the insights and approaches in WSN research literature for evaluating the energy efficiency of a modulation + coding scheme.

A more appropriate energy efficiency metric can be defined based on the *average energy per successfully received bit (ESB)* [134], which considers circuit energy consumption, demodulation errors and coding. In many WSN research works, it has been important to minimize ESB. Since the metric in [134] was applied in the context of finding an optimal relay distance (i.e., in short-range mesh-topology WSN) and did not consider any multiple access, our work will have to define a modified metric accordingly.

Overall, attaining spectral and energy efficiency requires careful joint design of the physical and data link layers of communication. For the physical layer, we are referring to the hardware aspects and techniques of effective signal transmission in a propagation channel marred with various degradation effects (noise, attenuation, interference, distortion, and Doppler effects). The physical layer covers the modulation (as well as symbol-waveform representation and waveform shaping such as filters), channel coding, transmit power, transmission rate, hardware design, among others. For the data link layer, we are referring to the logical link control sublayer (i.e., the protocol followed by two ends of communication in handing packet errors or losses, handshaking, re-transmission request, etc.) and multiple access control (MAC) sublayer (i.e., the protocol for sharing channel spectrum and time resources among multiple users based on rules of priority, fairness, delay, possibility of coordination, channel access efficiency optimization, etc.).

The choice of modulation and coding scheme is a trade-off among several factors including energy efficiency, spectral efficiency, transceiver, and processing complexity, as well as programmatic, interoperability and compatibility constraints. Channel coding scheme has been traditionally employed in communication systems to improve data transmission reliability (in terms of bit-error-rate, BER or packet-error rate, PER) in power-limited scenarios in the presence of channel impairments. To do this, redundancy bits are included in the transmitted packet, which can be used at the receiver to recover the packet even when some bits are received in error (i.e., forward error correction (FEC)) or simply to detect packet error for further action (such as repeat request). So, if transmit power is constrained but the BER is unacceptable, channel coding can lower the BER to the target value. Or, for a target BER, the minimum required transmit power can be lowered compared to the case without coding. However, transmission of extra (coding) bits

consumes more bandwidth, hence resulting in a spectral efficiency loss. Nonetheless, this is worth doing in exchange for getting better energy efficiency because increased reliability of packet transmission can avoid or reduce the required number of re-transmissions before successfully receiving the packet. Therefore, to properly trade-off energy efficiency and performance in an energy-constrained and bandwidth-constrained communication system, it is necessary to derive the relationship among energy efficiency, spectral efficiency, reliability (PER or BER), and input physical layer parameters: modulation scheme and order, channel coding scheme and order, transmit power, packet length, etc.

In addition, as mentioned, this must be done in the context of satellite-based IoT scenario where a large number of devices must share access to the channel with limited available bandwidth and communication time. Because nanosatellites have very limited hardware, energy, and computational resources, it is unimaginable for it to support a bidirectional logical link control scheme that requires downlink packet transmission to each device in a large population. Fortunately, for many IoT applications we are interested in, a guaranteed end-to-end connection is unnecessary and a reasonable level of packet loss rate (in uplink) is tolerated. Thus, even without a downlink channel to support both data downlink and logical link control, many applications can be supported by CubeSats as long as a reasonable level of packet loss rate can be achieved (depends on application, a good example would be $PLR < 5\%$). Furthermore, for multiple access, a purely random-access scheme (time-unslotted, frequency-unslotted) is the most suitable knowing the impracticality of maintaining time and frequency synchronization among large number of low-end devices operating in a satellite propagation channel.

Previous works on modulation and coding schemes for CubeSat communication normally aimed to improve reliability (in terms of BER or PER) and throughput (in terms of achievable data transfer rate in bps) given limited link budget (i.e., limited transmit power, very long propagation distance, limited antenna gains and pointing capability, etc.) or available bandwidth. However, there are not significant research works that aim to optimize or trade-off both spectral and energy efficiencies.

Reference [131] cited some related works on modulation and coding schemes for CubeSat communications. It is said in [131] that if there is wide available bandwidth (i.e., higher frequency bands like X-band), binary (low-order) modulation methods along with low rate channel codes with high error-correction capabilities are preferable over higher-order modulation schemes with high rate forward error correction (FEC) codes. The low-order modulation scheme reduces the required transmit power while more redundant data in the latter increases error correction effectiveness, thus overall leading to higher power efficiency. On the contrary, if available bandwidth is narrow, higher-order modulations with high rate channel codes are preferable, although this assumes link budget is not constrained and throughput is to be optimized [131].

The BER performance of different modulation and coding schemes in the context of CubeSat communication were compared in [135], where the channel model used is a mixture of log-normal fading and Rician fading channel (Corazza-Vatalaro Model). Among M-FSK, M-QAM, QPSK, MSK and GMSK modulation schemes that were initially evaluated based on BER vs E_b/N_0 performance curves, only the QPSK, MSK and GMSK are considered suitable for CubeSat due to balance of (less) complexity and

performance. While $\pi/4$ -QPSK is better than classical QPSK because its signal envelope has no zero crossings and thus reduces the performance degradation impact of amplifier non-linearities, the possibility of 180° phase jumps will have negative impact on spectral characteristics. Offset QPSK (OQPSK) provides a solution to avoid this problem while having the same BER performance as QPSK. GMSK is also considered a good alternative for having a significantly improved spectral characteristics (occupies less bandwidth) compared to QPSK/OQPSK, but with slightly worse (~ 1 - 2 dB) BER performance curve. According to [135], combining Viterbi decoding algorithm with GMSK results in a better BER performance than QPSK especially at higher SNR (>6 dB), albeit with added complexity. Since OQPSK and GMSK have constant envelope, both can be operated with a nonlinear amplifier, hence this increases power efficiency compared to QPSK. Then, [135] evaluates the BER performance of QPSK/OQPSK in conjunction with Reed-Solomon (RS) and convolutional codes with respect to uncoded case. It recommends a rate $2/3$ convolutional code or a RS (255,243) code for the uplink in light shadowing, and a rate $1/2$ convolutional code for strong shadowing, and stronger coding schemes for downlink (since the study assumed less constrained uplink budget).

The CCSDS standard [136] recommends using a filtered OQPSK implemented using a linear phase modulator (OQPSK/PM) to improve the spectral shape of OQPSK. CCSDS standard also recommends using residual carrier for phase modulation for Earth-to-Space communication; PCM/PM/bi-phase-L, BPSK modulation for telecommand; and 8PSK TCM/GMSK/OQPSK modulations for high data rate transmissions, and GMSK (BTS=0.5)/GMSK/OQPSK modulations for high-coded transmissions for telemetry. However, it is important to note that the CCSDS standard was not created for satellite IoT/M2M communication scenarios, so the said standard is not fine-tuned for such application scenarios.

Hybrid modulation schemes, wherein carrier phase and frequency are simultaneously modulated, were studied in [137], offering a possibility of increasing spectral and energy efficiencies while also suitable for implementation and adaptation in CubeSat communications. The authors focused on the hybrid M-FSK/QPSK modulation scheme, in which the basic idea is to perform QPSK modulation on M subcarriers at the transmitter side. This is illustrated on Figure 11 for a 4-FSK/QPSK modulation, in which every transmitted symbol is selected from a total of 16 possible symbols, comprising of 4 frequencies, 4 phases each. Thus (for the same occupied bandwidth as 4-FSK?), each transmitted symbol contains 4 bits, compared to only 2 bits in either 4-FSK or QPSK. According to [137], this scheme combines the benefits of increasing energy efficiency of M -FSK as M increases and the spectral efficiency of QPSK. The authors also proposed memory-stored samples-based modulator, an FFT analysis-based demodulator (frequency component for M-FSK and phase component for QPSK), as well as advance modifications such as M-FSK/DQPSK (D=differential), DM-FSK/DQPSK.

Differential-phase encoding avoids the need for coherent phase demodulation while differential-frequency encoding makes it robust to Doppler shift compensation error (if the difference of Doppler frequency shift between two symbols is much smaller than the MFSK frequency spacing). Various hybrid (D)M-FSK/(D)QPSK schemes were modeled in Matlab Simulink and the performance in terms of spectral efficiency (calculated for the null to null frequency bandwidth) and energy efficiency (in terms of required

E_b/N_0 for a target BER) were evaluated. The results from [137] showed their proposed hybrid modulations have better energy and spectral efficiencies, and with more significant enhancement for lower order FSK modulations. Among the limitations of [137] are performance evaluation only in AWGN channel and neglecting Doppler effect. It is interesting to extend their works considering satellite propagation channel.

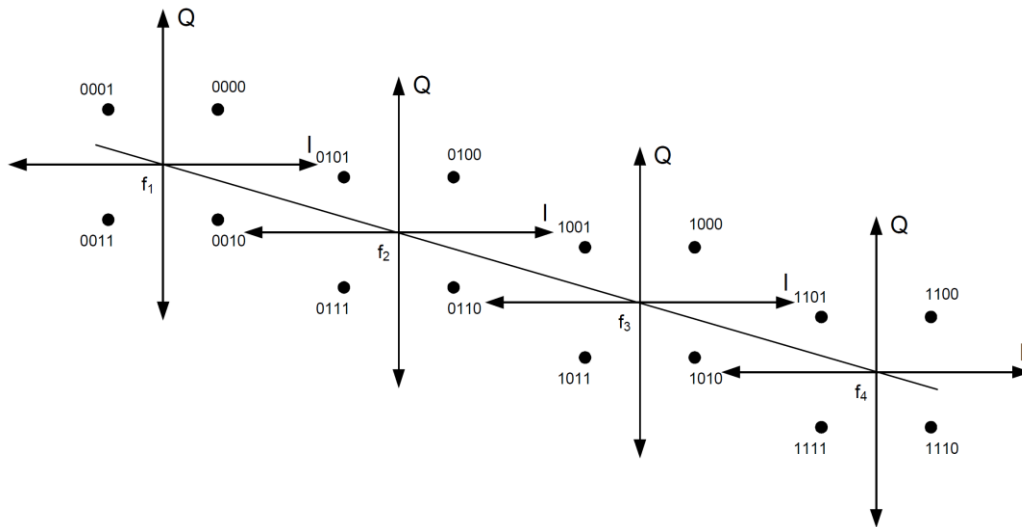


Figure 11. Signal space of hybrid 4-FSK/QPSK modulation (source: [137])

In [138], highly spectrally efficient but power-inefficient modulation schemes – such as high-order M-QAM and M-PSK – were jointly designed with orthogonal frequency division multiplexing (OFDM) and one of three error-correcting coding schemes (convolutional code, trellis-coded modulation, and Turbo code) to achieve coding gain, hence improving the power efficiency. The authors in [138] concluded that Turbo Coded OFDM outperforms the other two coding schemes (CC and TCM) for all modulation schemes considered, although at the expense of more decoding complexity. However, due to high-order modulation to start with, this scheme will naturally require much more complex transmitter and receiver implementations to achieve the promised performance gains.

Nonetheless, in relation to bandwidth-efficient schemes for space missions, CCSDS recommends several low-order and high-order modulation schemes combined with coding [139]. Again, it must be noted that while CCSDS standards were created for space missions, these are not specifically optimized for satellite-based IoT/M2M communications.

- For Category A – GMSK (BTs=0.25) with precoding, filtered OQPSK with various baseband filter options;
- For Category B – GMSK (BTs=0.5) with precoding.

For EECS – 4D 8PSK TCM, SRRC-QPSK, SRRC-OQPSK, SRRC-8PSK, SRRC-16APSK, SRRC-32APSK, and SRRC-64APSK, filtered OQPSK with various baseband filter options.

Recently, concurrent with the expanding deployments of LPWAN technologies, there have been commercial and research interests to utilize some of the long-range low-data rate RF communication technologies – originally developed for terrestrial LPWAN but have interesting modulation features – for satellite IoT communications specifically in the context of satellite-onboard LPWAN gateway (as in direct-

access mode). The specifications of some of the most well-known LPWAN technologies [140] are given here in Figure 12. Broadly speaking, the modulation schemes may be categorized into: (1) ultra-narrowband modulation or (2) spread spectrum modulation. Ultra-narrowband (UNB) means that the modulated carrier signal occupies about the same or the minimum necessary bandwidth to transmit data at a certain low data rate, but some articles describe UNB as a modulation scheme in which the occupied bandwidth is in the same degree as the uncertainty in the carrier oscillator frequency. The latter may be a result, though, of using low-cost oscillators in practical implementations. A perfect example is that of SigFox, whose 100 bps DBPSK modulation in the uplink is known to occupy only roughly 100 Hz bandwidth.

On the other hand, spread spectrum (SS) modulation intentionally occupies much wider bandwidth than essentially required to transmit at a given data rate, and this is purposefully done to attain enhancements such as interference immunity, lower spectral density of each RF transmission, and in some cases achieve more receiver sensitivity or support multiple access among users. There are various SS techniques, but some representative techniques are direct-sequence spread spectrum (DSSS), frequency-hopping spread spectrum (FHSS), and chirp spread spectrum (CSS). In DSSS, the digital data is modulated (or multiplied) by a much higher rate pseudo-noise (PN) sequence (each element in the sequence is called a “chip”), and the resulting occupied bandwidth is about the bandwidth of the original data multiplied by the ratio of the chip rate to the symbol rate. Ingenu’s uplink employs a proprietary random-phase multiple-access (RPMA) DSSS; the random phase allows numerous users to transmit on the same channel.

In Chirp Spread Spectrum (CSS), a set of symbols is mapped to a set of unique chirp waveforms which inherently occupy wider bandwidth, e.g. linearly increasing/decreasing frequency with time with different slope or starting point [141]. LoRa employs a proprietary CSS modulation, which also permits a few number of devices to simultaneously transmit on the same channel, as long as they utilize different spreading factors (or effectively, different data rates, up to 7 spreading factors can be supported on each channel). Other standardized IoT communication protocols and their technical specifications are given in Figure 13.

TABLE I
TECHNICAL SPECIFICATIONS OF VARIOUS LPWA TECHNOLOGIES (?=NOT KNOWN)

	SIGFOX	LoRAWAN	INGENU	TELENSA
Modulation	UNB DBPSK(UL), GFSK(DL)	CSS	RPMA-DSSS(UL), CDMA(DL)	UNB 2-FSK
Band	SUB-GHZ ISM:EU (868MHz), US(902MHz)	SUB-GHZ ISM:EU (433MHz 868MHz), US (915MHz), Asia (430MHz)	ISM 2.4GHz	SUB-GHZ bands including ISM:EU (868MHz), US (915MHz), Asia (430MHz)
Data rate	100 bps(UL), 600 bps(DL)	0.3-37.5 kbps (LoRa), 50 kbps (FSK)	78kbps (UL), 19.5 kbps(DL) [39]	62.5 bps(UL), 500 bps(DL)
Range	10 km (URBAN), 50 km (RURAL)	5 km(URBAN), 15 km (RURAL)	15 km (URBAN)	1 km (URBAN)
Num. of channels / orthogonal signals	360 channels	10 in EU, 64+8(UL) and 8(DL) in US plus multiple SFs	40 1MHz channels, up to 1200 signals per channel	multiple channels
Link symmetry	×	✓	×	×
Forward error correction	×	✓	✓	✓
MAC	unslotted ALOHA	unslotted ALOHA	CDMA-like	?
Topology	star	star of stars	star, tree	star
Adaptive Data Rate	×	✓	✓	×
Payload length	12B(UL), 8B(DL)	up to 250B (depends on SF & region)	10KB	?
Handover	end devices do not join a single base station	end devices do not join a single base station	✓	?
Authentication & encryption	encryption not supported	AES 128b	16B hash, AES 256b	?
Over the air updates	×	✓	✓	✓
SLA support	×	×	×	×
Localization	×	✓	×	×

Figure 12. Technical specifications of various LPWAN technologies (source: [140])

Standardization Bodies and Special Interest Groups	Name	Modulation	Band	MAC	Data Rate	Coverage	Number of Channels
IEEE	802.15.4 k	DSSS, FSK	ISM SUB-GHz and 2.4 GHz	CSMA/CA, ALOHA with PCA	1.5–128 kbps	5 km (urban)	multiple (depends on channel and modulation)
	802.15.4 g	FSK, OFDMA, OQPSK	ISM SUB-GHz and 2.4 GHz	CSMA/CA	4.8–800 kbps	up to several km	multiple (depends on channel and modulation)
Weightless-SIG	-W	16QAM, DBPSK	TV white spaces (470–790 MHz)	TDMA/FDMA	1 kbps–10 Mbps	5 km (urban)	16 or 24
	-N	DBPSK	ISM SUB-GHz	ALOHA	30–100 kbps	up to 3 km (urban)	multiple, 200 Hz each
	-P	GPSK, QPSK	ISM SUB-GHz or licensed	TDMA/FDMA	200 bps–100 kbps	up to 2 km (urban)	multiple, 12.5 kHz each
DASHAlliance	DASH7	GFSK	SUB-GHz	CSMA/CA	9.6,55.6 or 166.7 kbps	up to 5 km (urban)	multiple, 25 or 200 kHz each
3GPP	EC-GSM	8PSK, GMSK	Licensed GSM	TDMA/FDMA	74–240 kbps	up to 15 km	124 channels, 200 kHz each
	NB-IoT	QPSK, 16QAM, 64QAM	Licensed LTE	SC-FDMA (UL) OFDMA (DL)	20 kbps (UL) 200 kbps (DL)	35 km	multiple, 180 kHz each
	eMTC	QPSK, 16QAM, 64QAM	Licensed LTE	OFDMA/SC-FDMA	1 Mbps (UL,DL)	up to 15 km	multiple, 200 kHz each
ETSI	LTN	BPSK (UL) GFSK (DL) or OSSS	ISM SUB-GHz (433, 868 and 915 MHz)	BPSK (UL) GFSK (DL)	10–100 bps	up to 60 km	multiple, 200 Hz each

Figure 13. Technical specifications for standardization bodies and special interest groups for IoT solutions. ETSI, European Telecommunications Standards Institute (source: [142])

The aforementioned modulation schemes and technologies were originally intended for terrestrial IoT communications. These have not been extensively studied and tested for the satellite channel, which, in addition to much longer communication distance, introduces further impairments such as Doppler effect. Nonetheless, as mentioned, there have been interests to utilize some of them for satellite IoT communications, as well as ground-based and space-based communication experiments. In particular, Lacuna Space has developed a satellite-onboard LoRaWAN gateway that would allow normal LoRa-equipped devices to transmit signal directly to a passing satellite [125]. For this, Lacuna Space, in collaboration with Semtech, announced that they had modified the LoRaWAN gateway to become capable of receiving a larger number of simultaneously transmitting devices, though these are proprietary engineering designs.

Research articles [143][144], which described an experimental laboratory study on the suitability of LoRa modulation for CubeSat communications, concluded that LoRa modulation can be used in the radio communication between a ground station and a satellite in a circular orbit more than 550 km. altitude without any restrictions. Moreover, it was concluded that at lower orbits, the immunity of LoRa modulation from Doppler rate degrades more when higher spreading factor (SF) is used, although there is significant immunity to both Doppler shift and rate for all orbits up to as low as 200 km as long as SF of 11 or lower is used. However, only higher bandwidths (125 kHz and 250 kHz, corresponding to data rates higher than 440 bps) were considered in the study. Paper [145] reported results on communication tests between on-ground LoRa transmitters and LoRa receivers onboard TRICOM-1R CubeSat, which demonstrated successful uploading of data with a signal power as low as 8mW, although no information on which bit rates worked was mentioned.

Meanwhile, Eutelsat, in partnership with Sigfox, is set to launch 25 nanosatellites for IoT by 2022, called ELO constellation [87]-[91]. The ELO constellation, flying on around 600-700 km. orbit, is intended to provide global IoT coverage enabling end-devices to transmit data from anywhere (within 15-20 mW power), including asset tracking in oceans and other remote locations. In this partnership, Eutelsat acts as a full Sigfox Network Operator (i.e., each satellite carries a Sigfox base station *receiver*), while Sigfox seamlessly integrates the satellite network to its existing terrestrial infrastructure and connectivity services (i.e., end-devices' transmissions can be captured by both the satellites and any terrestrial networks). A test satellite is targeted for early 2020 launch to investigate the performance of various waveforms [87]-[91].

In [128], the authors investigated the impact of Doppler effect on demodulating the NB-IoT waveform (QPSK on SC-FDMA) in terms of PER performance, as well as proposed a ground-based processing algorithm for signal synchronization/detection, channel estimation and demodulation. OQ Technology experimented NB-IoT waveforms and synchronization schemes [129]. Compared to Sigfox's UNB RF technology that supports 100 bps DBPSK within ~100 Hz bandwidth, NB-IoT supports the lowest data rate of 3.5 kbps QPSK within 3.75 kHz, so it would not be adversely affected by Doppler drift as much as the SigFox system.

The characteristics of common modulation schemes are summarized here in Tables 5 and 6. In Table 5, α is the parameter for RF amplifier overhead power such that the RF amplifier power consumption is α times the actual RF output power P_{TX} . Then, total power consumption expended by the transmitter for transmission is given by (4) and (5). The value of α is determined based on the type of RF power amplifier required for the type and order of modulation used. In Table 6, SE_{mod} is the modulation spectral efficiency as normally defined in textbooks, indicating the transmission bit rate R_b that can be achieved over an occupied bandwidth B_T , as expressed in (6). Note that since B_T itself is determined by R_b (proportionally) and modulation type and order, SE_{mod} represents the characteristic spectral efficiency corresponding to a modulation type and order.

Another spectral efficiency metric can be defined, the *spectral efficiency of reception*, SE_{rec} , which is expressed simply as the product of modulation spectral efficiency SE_{mod} , coding rate R_c , and bit-success-rate (BSR) after FEC processing $(1 - P_{be,ac})$, as expressed in (7). The coding rate R_c equates to coding efficiency, accounting for the reduction in spectral resource utilization efficiency due to transmission of redundant bits for the FEC coding scheme, while the BSR reflects the effectiveness of FEC. Since both ESB and SE are both related to $P_{be,ac}$, then we can draw a relationship between the SE and ESB (this will be dealt with later). Also, a more objective technical definition of occupied bandwidth (e.g. 90% power, 99% power, etc.) must be used so more accurate SE_{mod} values will be used. MAC scheme is not yet considered in these metrics. ESB and SE will be reconsidered in a multiple access scenario.

$$P_{RFA} = \alpha P_{TX} \quad (3)$$

$$P_{consumed} = P_{TX} + P_{RFA} + P_c \quad (4)$$

$$P_{consumed} = (1 + \alpha)P_{TX} + P_c \quad (5)$$

$$SE_{mod} = \frac{R_b}{B_T} \text{ [bps/Hz]} \quad (6)$$

$$SE_{rec} = SE_{mod} \times r_c \times (1 - P_{be,ac}) \text{ [bps/Hz]} \quad (7)$$

Table 5. Symbol error probabilities and RF amplifier parameters of different modulation schemes (sources: [133][134][146][147])

Modulation Scheme	P_{se} in AWGN Channel	Corresponding RF Amplifier Parameter $\alpha = \frac{\xi}{\eta} - 1$
BPSK	$P_{se} = Q\left(\sqrt{\frac{2E_{s,RX}}{N_0}}\right) = Q\left(\sqrt{\frac{2E_{b,RX}}{N_0}}\right)$	$\xi = 1, \eta = 0.35$ $\alpha = 1.8571$
QPSK	$P_{se} = 2Q\left(\sqrt{\frac{E_{s,RX}}{N_0}}\right) - \left[Q\left(\sqrt{\frac{E_{s,RX}}{N_0}}\right)\right]^2$	$\xi = 1, \eta = 0.35$ $\alpha = 1.8571$
MPSK	$P_{se} = 2Q\left(\sqrt{\frac{4E_{s,RX}}{N_0}} \sin\left(\frac{\pi}{M}\right)\right)$ [133] $P_{se} = 2Q\left(\sqrt{\frac{2E_{s,RX}}{N_0}} \sin^2\left(\frac{\pi}{M}\right)\right)$ [146] $P_{se} \approx 2Q\left(\sqrt{\frac{4E_{s,RX}}{N_0}} \sin\left(\frac{\pi}{2M}\right)\right)$ [147]	$\xi = ?, \eta = 0.35$ $\alpha = ?$
Coherent BFSK (Sunde's FSK)	$P_{se} = Q\left(\sqrt{\frac{E_{s,RX}}{N_0}}\right) = Q\left(\sqrt{\frac{E_{b,RX}}{N_0}}\right)$	$\xi = 1, \eta = 0.75$ $\alpha = 0.3333$

Non-coherent BFSK (NC-BFSK)	$P_{se} = 0.5e^{-\left(\frac{E_{s,RX}}{2N_0}\right)} = 0.5e^{-\left(\frac{E_{b,RX}}{2N_0}\right)}$	$\xi = 1, \eta = 0.75$ $\alpha = 0.3333$
Coherent MFSK	$P_{se} \leq (M - 1)Q(\sqrt{\gamma_b \log_2 M})$ [146] $\gamma_b = E_b/N_0$ $E_s = bE_b$ $P_{se} \leq (M - 1)Q\left(\sqrt{\frac{E_{s,RX}}{N_0}}\right)$	
Non-coherent MFSK	$P_{se} \leq \frac{M-1}{2} e^{-\frac{1}{2}\gamma_b \log_2 M}$ [146] $P_{se} \leq \frac{M-1}{2} e^{-\frac{1}{2}\frac{E_{s,RX}}{N_0}}$	
GMSK (e.g., $\beta=0.65$)	$P_{se} = Q\left(\sqrt{\frac{2\beta E_{s,RX}}{N_0}}\right) = Q\left(\sqrt{\frac{2\beta E_{b,RX}}{N_0}}\right)$	$\xi = 1, \eta = 0.75$ $\alpha = 0.3333$
MQAM	$P_{se} = 1 - \left(1 - 2\left(1 - \frac{1}{\sqrt{M}}\right)Q(arg)\right)^2$ $arg = \sqrt{\frac{3}{M-1} \frac{E_{s,RX}}{N_0}}$ [133] $P_{se} \approx 4\left(1 - \frac{1}{M}\right)Q\left(\sqrt{\frac{2E_{ave}}{N_0}}\right)$ [147] $E_{ave} = \text{average signal energy}$	$\xi = ?, \eta = 0.35$ $\alpha = ?$

Table 6. Modulation spectral efficiency of different modulation schemes (source: [146])

Modulation Scheme	Rough Estimate of SE_{mod} $\left[\frac{\text{bps}}{\text{Hz}}\right]$
BPSK	≈ 1
QPSK	≈ 2
MPSK	$\approx \log_2 M = b$
MFSK	$\approx \frac{2\log_2 M}{M} = \frac{2b}{2^b}$
GMSK	≈ 2
MQAM	$\approx 2\log_2 M = 2b$

3.3 Random Access Schemes

Earlier satellite systems, such as those in the mobile satellite service, traditionally employed multiple access control (MAC) schemes according to fixed assignment (e.g., TDMA, FDMA, CDMA) and in some cases in conjunction with a random access (RA) protocol to perform demand-based adaptive assignment. However, due to a massive number of terminals with burst transmission, it is more efficient to use RA schemes in satellite-based IoT. Reference [148] presents a survey and review of RA schemes for satellite networks while reference [149] evaluates the suitability of different MAC protocols for application to nanosatellites considering both performance and complexity. It presents a taxonomy of the RA schemes

which are categorized into slotted and unslotted RA. Unslotted RA schemes are better suited for the application considered due to impracticality to time-synchronize a massive number of low-end ground terminals. The Table 2 in [149] evaluates several RA protocols in terms of performance: maximum throughput (S_{max}) and packet loss rate (PLR, C_{PLR}) at corresponding MAC load (C_{smax}), as well as complexity, energy efficiency and topology impact on performance. The Figure 14 in [149] shows a relative comparison among the various schemes. Overall, higher performance can be achieved at the expense of more complexity while less complex schemes can achieve lower performance. The suitable choice depends on the application scenario and what implementation complexity can be afforded at the transmitter (terminal) and receiver (satellite) sides.

As previously mentioned, low-end terminals in a satellite-based IoT/M2M have limited capabilities in terms of digital processing, modulation, coding, RF blocks implementation, oscillator accuracy/stability and must operate for long duration (up to years) even with limited power generation/storage capacity. Thus, wasteful RF transmissions (i.e., those that do not result in successful reception) must be avoided. In other words, an *energy-efficient asynchronous RA scheme with reasonably good performance but can be implemented on a low-cost terminal hardware must be employed in the uplink*. However, the RA protocols that can meet this requirement are those that entail very high computation complexity at the receiver that is too challenging, if not impossible, to implement on normal nanosatellite platform. One approach to circumvent this limitation is to perform on-ground digital signal processing (filtering, detection, channel estimation, demodulation, decoding, etc.) later after downloading the signal samples. This approach, in which the nanosatellite only receives the signal and stores the samples on its onboard memory for later on-ground processing, is in line with what is recently called “delay-tolerant MAC protocol”, like those referred to in [132][17]. The research then would be directed to addressing the challenges of storage capacity and stored data downlink capacity.

Our research is leaning toward a delay-tolerant MAC protocol. In a delay-tolerant MAC protocol, since there is no immediate response to the terminals, such as in the form of acknowledgement packet, it is crucial to achieve a reasonably low PLR within the context of applications wherein intermittent connection and packet losses below some defined PLR threshold are acceptable (i.e., non-critical missions). Moreover, even when sending a delayed acknowledgment, or negative acknowledgement or re-transmission request packet can be envisaged for some delay-tolerant applications, it is hardly possible for a nanosatellite to support downlink transmissions to thousands of terminals. Therefore, we should concede to this fundamental limitation and resort to exploring novel schemes for achieving reasonably good PLR and throughput even without downlink. These include, for example, employing a very robust low-rate FEC scheme, diversity and contention resolution schemes (i.e., transmitting a packet multiple times within a frame and canceling the interference after resolving one of the copies), and so-called physical layer network coding (i.e., schemes that divide a packet into sub-packets and enable recovery of the whole packet even with some lost sub-packets).

Unslotted or pure ALOHA (PA) is the simplest conventional RA scheme wherein users asynchronously transmit on a single common frequency channel without any coordination among them.

The maximum throughput (the ratio of channel resource (in this case, time) that is successfully utilized to the available resource) is very low (18%) and this is achieved at 50% MAC load (percentage of channel resource that is actively utilized). Also, the PLR is high for PA due to collisions, which not only result in low throughput but also wasted transmission power.

With Spread Spectrum ALOHA (SSA), each transmitter's signal is spread throughout a much wider frequency band than originally necessary through a spectrum spreading technique, such as direct-sequence spread spectrum (i.e., multiplying each bit in the original data with a known pseudo-noise (PN) sequence). With a fixed signal power, the resulting power spectral density (PSD) becomes much lower (high spreading factor results in wider bandwidth and lower PSD). The spread signal has noise-like appearance and may have a PSD lower than the background or thermal noise. At the receiver side, the received signal is de-spread by multiplying it with the same PN sequence, so the original signal can be recovered. To compensate for the much wider band used, multiple users can asynchronously transmit their spread signal at the same band, and by employing a low-rate forward error correction (FEC) scheme, the multiple signals can be decoded successfully up to some MAC load limit. In other words, SSA combines spectrum spreading and FEC to support multiple access. Unlike code division multiple access (CDMA), wherein a unique PN sequence must be used by each user, a common PN sequence can be used by all users in SSA (the PN sequence used must exhibit low time-offset autocorrelation), thus simplifying implementation.

SSA achieves a maximum throughput of 0.62 bps/Hz at MAC load = 0.70 bps/Hz with PLR of 10^{-1} . A PLR of 10^{-3} and throughput of 0.50 bps/Hz can be achieved at MAC load = 0.50 bps/Hz. In fact, the throughput vs MAC load plot of SSA is linear up to 0.60 bps/Hz MAC load. While SSA can provide a significantly improved performance compared to PA, its Achilles heel lies in its abrupt performance degradation when there is power imbalance among received signals. Unfortunately, power imbalance is naturally expected in a LEO satellite channel even when employing a power control mechanism.

Paper [156] proposed an enhanced SSA (E-SSA) scheme which benefits from power imbalance. E-SSA applies a recursive successive interference cancellation (R-SIC) algorithm: it removes each decoded packet from the signal memory in every successive decoding steps, starting with the higher power signals. When higher power signals have been removed, the lower power signals may be possibly decoded. Paper [156] provides performance analysis and simulation of E-SSA and reports a maximum throughput of 1.9 bps/Hz at MAC load = 1.9 bps/Hz with PLR = 10^{-3} can be achieved in a lognormal channel model with signal power variance $\sigma=3$ dB. While E-SSA has a promising performance as shown in previous studies, its performance in LEO satellite channel has not been investigated. Also, the performance of E-SSA considering the difficulties of channel (amplitude, frequency shift and rate, phase) estimation, demodulation and decoding in high MAC load scenario, the design of effective signal processing algorithms (channel estimation, demodulation, decoding), and optimization of physical layer parameters (e.g. packet length, FEC scheme, coding rate) should be extensively studied to fully take advantage of the promised performance within the LEO satellite IoT/M2M scenario. In this dissertation research, we focus on investigating and addressing these challenges.

Some other more recent publications proposing or tackling novel modulation + coding + MAC schemes for satellite IoT/M2M are given in Table 7. Most of these publications have not been included in the surveys in [148][149].

Table 7. Publications investigating modulation, coding and random access schemes for satellite IoT/M2M communications

Authors (Publication Year)	Modulation	FEC Scheme	MAC Scheme	Contributions & Limitations
Y. Quian, et. al. [150]-[152] (2018, 2019)	Chirp Spread Spectrum (CSS) [20]: LoRa Chirp Signal (LCS), Symmetry Chirp Signal (SCS), Asymmetry Chirp Signal (ACS)	-	CSS-PA: Multiple CSS transmitters transmit on one common frequency channel using PA	-Modified waveform from LCS to improve correlation characteristics for better MAC support (SCS and ACS) -Analyzed the BER performance impact of Doppler shift, but not Doppler rate -Investigated Extended Matched Filter Method (EMFM) for fast acquisition -No analysis on maximum number of terminals, spectral efficiency, energy efficiency
C. Hoffman, A. Knopp [153] (2019)	M-DPSK with Unipolar Coded (CDMA-like) Chirp-Spread Spectrum (UCSS)	rate 1/2 BCH (not a focus of the study)	UCSS-PA: Multiple UCSS transmitters transmit on one common frequency channel using PA	-Presents UCSS as a novel modulation and signaling scheme in close combination with the synchronization concept to allow direct RA of large number of users -Detection of signals from a single user in AWGN has been investigated theoretically and the required SNR a given probability of detection -Analysis of the detection probability in a MA scenario is performed by Monte Carlo simulations -Throughput and frame loss rate analysis over lognormal fading -Did not deal with Doppler effect, energy and spectral efficiencies
Zamora, et. al. [154][132] (2017)	Ultra-narrowband modulation (UNB-BPSK)	Low-rate convolutional coding (with hard-decision)	TFAA: Multiple UNB transmitters transmit at random frequencies	-Analysis of TFAA performance (throughput and PLR) under collision channel, capture channel, detailed channel model

		Viterbi decoding)	within a wide frequency band using TFAA	considering PHY layer design (BPSK modulation, pulse-shaping filter bandwidth or roll-off parameters, modulation order, FEC) -To improve performance, proposed and analyzed Contention-Resolution TFAA (CR-TFAA) -Trading delay for MAC performance and energy efficiency using transmission control and packet-layer erasure coding -Analyses do not consider Doppler effect -Assumed perfect signal detection & demodulation and no details on signal processing
M. Anteur, et. al. [155] (2018)	Ultra-narrowband modulation (BPSK)	3GPP Turbo Code (rate 1/3)	TFAA: Multiple UNB transmitters transmit at random frequencies within a wide frequency band using TFAA	-Proposed a semi-analytical model to derive the PLR and throughput of random-access protocols (PA, SA, STFA, TFAA) considering Doppler drift (shift and rate) -Showed that the Doppler effect experienced with LEO satellite communications increases the performance of TFAA with UNB signals -Did not consider impact of Doppler effect on signal detection and demodulation -Did not consider Contention Resolution
O. del Rio Herrero, R. De Gaudenzi [156] (2012)	BPSK + Direct Sequence Spread Spectrum (DSSS)	3GPP Turbo Code (rate 1/3)	E-SSA: Multiple DSSS transmitters transmit on one common frequency channel using PA (Spread Spectrum ALOHA with Recursive Successive Interference Cancellation or SSA-RSIC or E-SSA)	-Proposed to combine Iterative Successive Interference Cancellation with SSA to overcome the performance degradation of conventional SSA in power imbalance condition in satellite RA communication -Derived the PLR and throughput equation of SSA and E-SSA in lognormal shadowing process -Performed simulations with and without power

				<p>imbalance which showed robustness of E-SSA to power imbalance</p> <ul style="list-style-type: none"> -Study in the context of GEO orbit so did not consider higher LEO channel Doppler effect -Did not consider packet detection and channel estimation (assumed perfect channel estimation)
<p>O. del Rio Herrero, R. De Gaudenzi, G. Gallinaro [157] (2014)</p>	<p>BPSK + Direct Sequence Spread Spectrum (DSSS)</p>	<p>3GPP Turbo Code (rate 1/3)</p>	<p>E-SSA (same as above)</p>	<ul style="list-style-type: none"> -Proposed physical layer design for E-SSA based on 3GPP WCDMA RA channel physical layer with some adaptation -Considered preamble design for packet detection and data-aided channel estimation -Considered enhanced channel estimation prior cancellation by exploiting the detected payload bits in a decision directed mode. -Study in the context of GEO orbit so did not consider higher LEO channel Doppler effect -Limited treatment on the performance of channel estimation in various Doppler conditions -Did not consider performance of channel estimation when there is Doppler rate
<p>M. Andrenacci, G. Mendola, F. Collard, et. al. [158][159] (2014)</p>	<p>BPSK + Direct Sequence Spread Spectrum (DSSS)</p>	<p>3GPP Turbo Code (rate 1/3)</p>	<p>E-SSA (same as above)</p>	<ul style="list-style-type: none"> -E-SSA demodulator implementation based on combined SDR with processing via commercial graphics processing units (GPUs) -Software architecture of the ESSA demodulator is composed of the following DSP modules: preamble detection, channel estimation (timing, phase and frequency), descrambling/de-spreading, turbo decoding, SIC -Validation tests performed both in laboratory conditions and directly on the GEO

				<p>satellite EUTELSAT 10A are presented</p> <ul style="list-style-type: none"> -Traffic and channel emulator generates thousands of messages, each with its independent channel realization (amplitude, phase and frequency), thus testing the estimation algorithms -[159] showed that PLR starts increasing at increasing frequency error after 1.5 kHz
M. Zhao, et al. [160] (2018)	16-QAM + non-orthogonal 32-multicarrier modulation	Not considered	Not considered	<ul style="list-style-type: none"> -Presents a new non-orthogonal multi-carrier modulation scheme for satellite-based M2M communication system -Did not clearly deal with the impact of Doppler effect -Does not consider spectral and energy efficiencies
T. Xu, I. Darwazeh [161] (2018)	BPSK + bandwidth-compressed non-orthogonal frequency division multiplexing (Fast OFDM)	Not considered	Not considered	<ul style="list-style-type: none"> -Study's context is terrestrial NB-IoT but included here because other researches have proposed to use NB-IoT for satellite-based IoT/M2M communications -Proposes a novel signal waveform solution, Fast-OFDM, that compresses the occupied bandwidth of each device to 50% without compromising data rate and bit error rate performance -SDR-based test bed developed -Results indicate the same BER performance of Fast-OFDM with that of single-carrier FDMA, but with 50% bandwidth saving -Does not consider Doppler effect
Our research work	BPSK and other potential modulation schemes	Turbo and other potential FEC schemes	E-SSA	<ul style="list-style-type: none"> -Study performance of E-SSA considering LEO channel with Doppler effects (shift and rate) and imbalance of amplitudes among received packets by accounting for terminals' spatial distribution

				<p>-Evaluating the energy efficiency (ESB), throughput indicating spectral efficiency (i.e., achievable throughput over available bandwidth), and packet loss rate</p> <p>-Formulated the details and performance of the complete baseband signal processing algorithms used, including packet detection, channel estimation and demodulation/decoding</p> <p>-Considered an ultra-low data rate (333.33 bps, compared to 5 kbps or higher in previous works) to maintain enough E_b/N_0 with low transmit power, but longer packet duration (about 1 order of magnitude) inadvertently exposes it to channel estimation errors</p> <p>-Target satellite platform is nanosatellite so the necessity of delay-tolerant MAC and on-ground processing algorithm (to circumvent technical limitations) is highlighted;</p> <p>-Aside from considering applications with lower data rate requirement (~100-1000 bps), with nanosatellite, we cannot really support higher data rates due to link budget and hardware constraints (e.g., only low gain antennas, no beamforming technology, etc.)</p> <p>-Limitation: no experimental validation yet</p>
--	--	--	--	---

PA = pure ALOHA (time-asynchronous, single common frequency channel)

SA = slotted ALOHA (time-synchronous, single common frequency channel)

STFA = slotted time and frequency ALOHA (time-synchronous, frequency-synchronous, wide common frequency band)

TFAA = time and frequency-asynchronous ALOHA (time-asynchronous, frequency-asynchronous, wide common frequency band)

Chapter 4: BIRDS-2 CubeSat S&F Data Collection System, Payload Design and Development

This chapter discusses the BIRDS-2 CubeSat S&F remote data collection system, S&F/APRS-DP payload design, development, tests, and integration with the BIRDS-2 CubeSats.

4.1 System Architecture

The S&F/APRS-DP mission payload onboard the BIRDS-2 CubeSat constellation provides both APRS-DP and S&F communication capabilities using a common hardware and amateur radio frequency of 145.825 MHz. The APRS-DP mission supports real-time packet (message, position, beacon, telemetry, etc.) repeating between amateur radios and stations located on the same footprint, as illustrated in Figure 14. The satellite-based APRS-DPs of the BIRDS-2 constellation were aimed to complement the existing terrestrial APRS network, as well as an addition to other APRS satellites previously launched into orbit. Using an APRS-capable radio, a “ham” sends an APRS message or packet to the satellite and then the payload retransmits it immediately, allowing other hams or amateur stations to receive it.

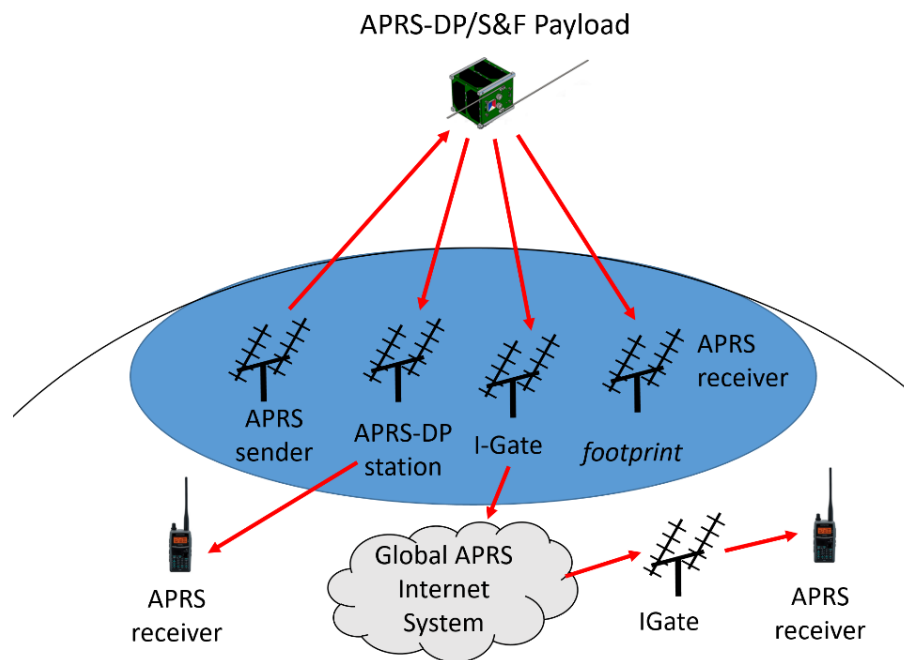


Figure 14. Conceptual operation of the APRS-DP mission

On the other hand, the system architecture of the BIRDS-2 S&F CubeSat constellation-based remote data collection system (RDCS) is given in Figure 15. It consists of three main segments: (1) Ground Sensor Terminal (GST) Segment, (2) CubeSat-onboard S&F Payload (“Payload”) Segment, and (3) Mission Control and Data Management (MCDM) Segment. Each GST consists of one or more sensors, a microcontroller unit (MCU), a VHF half-duplex transceiver, an antenna with rotator (for satellite tracking) mounted on a mast, and solar-battery power system for autonomous operation. In “store” phase, the payload receives sensor packet from any GST that transmits during satellite pass and saves them in an onboard flash memory. In “forward” phase, after receiving an uplink command, gathered data are downloaded to a

BIRDS ground station. Downloaded data are transferred to an online storage, processed at the mission control center, and distributed to data users. Mission operation control, data download, storage, processing, and distribution to users are handled by the MCDM. By employing a CubeSat constellation, the upload data throughput will be roughly a multiple of that of single CubeSat case. Also, by using a network of ground stations, more data download flexibility and frequency can be achieved. The onboard payload, GSTs and handheld radios operate in the VHF amateur radio band at 145.825 MHz to achieve a low-cost system that is easily available for use by the amateur community (like in [31][165]).

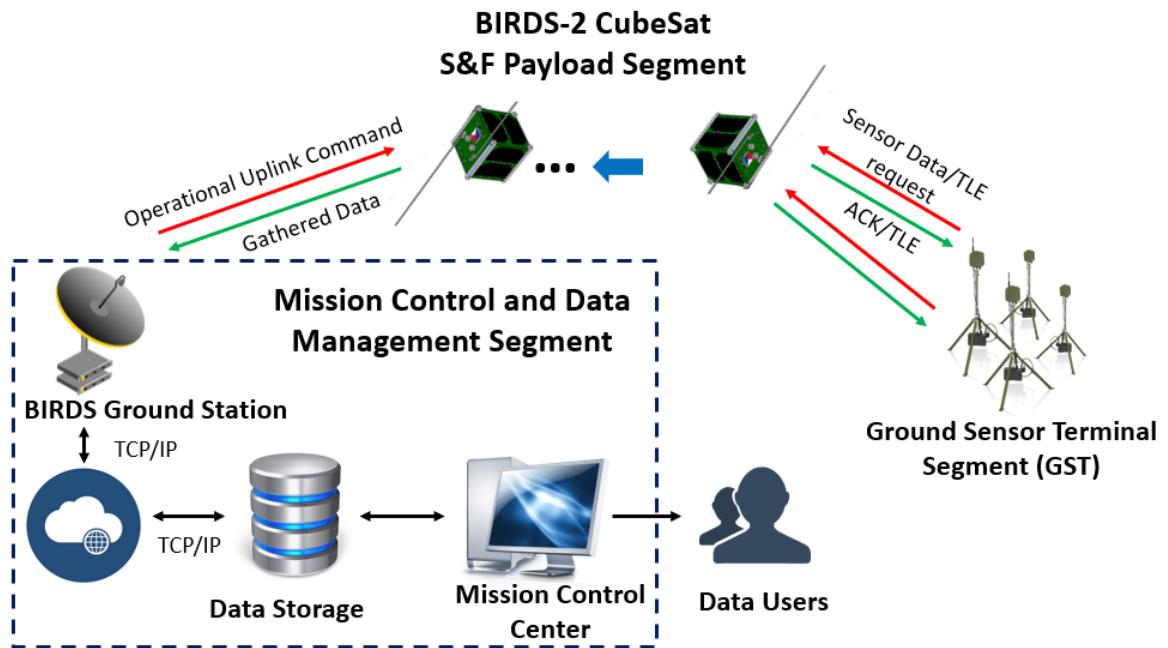


Figure 15. System architecture of the BIRDS-2 S&F CubeSat constellation-based remote data collection system

4.2 Payload Design Considerations and Implementation on the BIRDS-2 CubeSat

Since APRS radios typically use a traditional modulation scheme (AFSK/FM) and communication link layer protocol (AX.25), it follows that for payload implementation, the main consideration was not novelty but the wise selection of commercial-off-the-shelf (COTS) components suitable for the electrical and mechanical constraints/interfaces in the BIRDS-2 1U CubeSat. When designing the payload, the following factors were considered: (a) utilizing low cost COTS components, (b) simple design requiring short development time for hardware and software, (c) having low energy consumption and small form factor so it can be accommodated on a CubeSat. These factors were crucial because the payload had to be accommodated on the BIRDS-2 1U CubeSat that was expected to carry other subsystems and mission payloads sharing in the satellite resources. The payload had to be built, tested, and integrated with the satellite within the project's original development timeline of about one year and three months, from mission planning to completion of flight models. The use of COTS components was possible due to availability of transceivers and modules supporting the modulation and communication protocol commonly used for amateur radio.

Inexpensive implementations utilizing COTS components have been described in previous works, for the satellite-onboard payload [165][166] and ground terminals [20][33]. In [165] and similarly in [166], the modulator/demodulator (modem), AX.25 link layer protocol, APRS or S&F application program, packet handling and onboard data handling are all handled by one MCU on a single board. A half-duplex COTS VHF amateur transceiver is used for transmitting and receiving RF signal. This integrated approach results in a more compact onboard system, although it requires more programming work on the part of the developer to implement the APRS or S&F application, AX.25 protocol [167], and AFSK modulator/demodulator (modem) on the MCU.

The block diagram of our own APRS-DP/S&F payload implementation is shown in Figure 16 and the flight model boards are shown in Figure 17. Figure 18 shows an overview of the communication system layers and protocols. The payload is made by integrating individual COTS components – including a VHF FM transceiver (Radiometrix’s BIM1H), a stand-alone APRS-DP module (Byonics’ TT4), a MCU running the S&F program (Microchip’s PIC16F1788), a multiplexer (ADI’s ADG774) and a 64-Mbyte flash memory (Cypress’ S25FL512S). Aside from being very low cost, these components were selected based on size, power consumption, ease of interfacing and little programming work required for the development. The VHF transceiver has an output RF power of 0.5 W, dimensions of 33 mm (L) x 23 mm (W) x 12 mm (T) and operates at 145.825 MHz for both uplink and downlink, in half-duplex mode. A VHF monopole antenna with nichrome wire heating deployment mechanism is connected to the VHF transceiver. The TT4 is a stand-alone module providing all necessary functionalities – APRS digipeater, AX.25 protocol terminal node controller (TNC) with KISS protocol support for UART communication between it and the S&F MCU, and a 1200 bps AFSK modem. Taking advantage of TT4’s features, the developer could focus on rendering the S&F program on the S&F MCU within a short time. Note that TT4 already implements the APRS-DP application so the developer only needs to test the functionality (no need to develop it). The original TT4 package was altered and soldered to the mission board using a customized adaptor board.

The US Naval Academy (NA) had adopted a similar approach in developing their APRS CubeSats (including the BRICSAT-2). Their APRS-DP payload evolved from the Byonics’ MTT4B, a complete module consisting of both the TT4 and a built-in VHF transceiver, which they modified to fit a standard CubeSat platform [45]. Using MTT4B was found inappropriate for the BIRDS-2 CubeSat due to higher power consumption (e.g., higher output RF power) and difficulty of interfacing with other subsystems. Instead, as mentioned above, a lower power-consuming transceiver (Radiometrix’s BIM1H) was used. Also, it is not clear whether the payload of US NA supports S&F communication capability (received packets are stored and downloaded later to a ground station) in addition to APRS-DP functionality (which immediately re-transmits received APRS packets). In the BIRDS-2 implementation, both APRS and S&F packets are stored in onboard memory, but S&F packets are distinguished by a different packet format because the S&F MCU implements a specific S&F communication application program as described below.

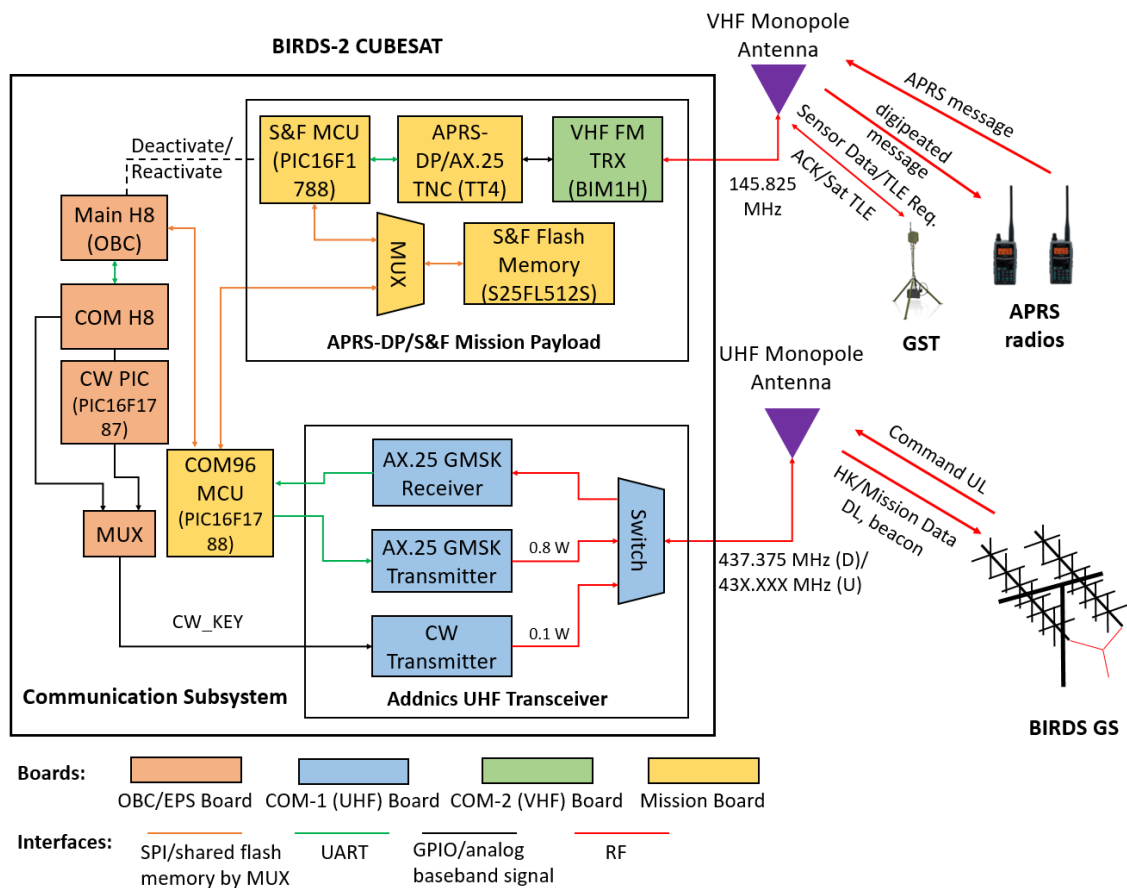


Figure 16. Block diagram of the BIRDS-2 APRS-DP/S&F payload and communication subsystem

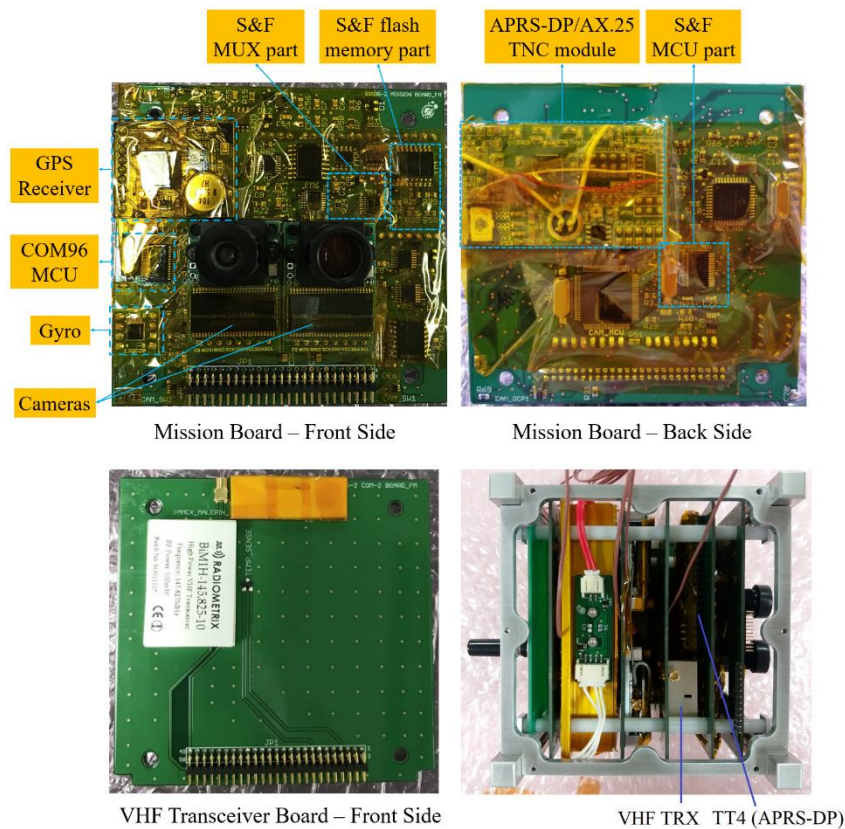
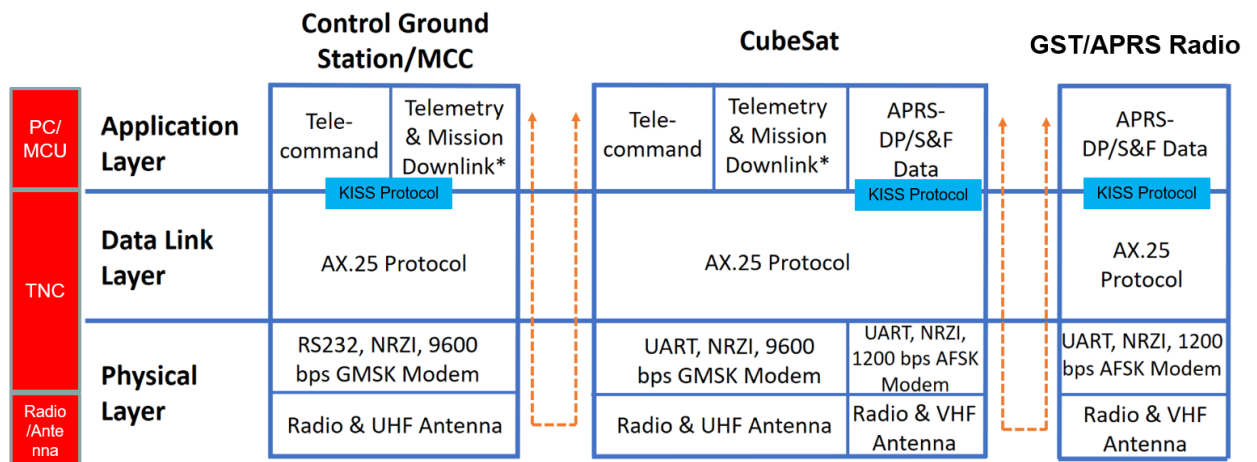


Figure 17. BIRDS-2 APRS-DP/S&F payload flight model boards: mission board hosting the APRS-DP/TNC module, S&F MCU and flash memory; VHF transceiver board; assembled with other internal boards (lower right)



*E.g., collected S&F sensor data, image data, etc.

Figure 18. Communication layers and protocols

The payload directly interacts with the GSTs (or with APRS-DP users’ handheld radios) during the “store” phase. Whenever it receives a valid packet from any GST, it saves the packet in the flash memory and automatically sends an ACK packet. As an added feature, upon receiving a special request packet from any GST to download the two-line elements (TLE), it transmits a packet bearing the satellite’s latest TLE information (which is sent from the command ground station). The S&F onboard memory has a total size of 512 Mbit (64 Mbyte) and is organized according to Table 8. It has 256 sectors, each containing 256 kbytes. The S&F program keeps a pointer to where the next data will be saved. The pointer is a 32-bit (4-byte) address of the next vacant location and it is saved from 0x00000000 to 0x00000003. Whenever a new packet is received from the TNC, this pointer is read and after saving the data, the pointer is incremented accordingly. The latest satellite TLE is saved starting from 0x00040000 and it is overwritten whenever an updated TLE is received. Every received packet from the TNC is fully saved as it is received (in KISS format) to allow further processing at the ground station. This means that all received packets, whether APRS-type or S&F-type, are saved in memory. The KISS header and footer (0xC0) serve as delimiters between packets. A total of 254 sectors are available for storage. The S&F packet types are given in Table 9 and packet formats are provided in the Appendix.

The S&F MCU runs the S&F program sequence including packet generation (in transmit side) and parsing (in receive side). In reception, it decomposes the packet into separate fields and recognizes the GST’s identification callsign, packet header and footer, packet type and sensor data. In transmission, it does the reverse to compose the appropriate downlink packet to send to the GST. The program flow diagram of the S&F MCU is very simple, as illustrated in Figure 19. The stored data are downloaded to the Mission Control Center (or any BIRDS ground station) through the UHF communication transceiver at the rate of 9600 bps (GMSK modulation, AX.25 protocol). The same UHF transceiver receives uplink command from the ground station, including the commands to download the stored data and to upload the latest satellite TLE.

Table 8. S&F onboard memory organization

Sector Number	Address	Content
0	0x00000000	Start address where the next data will be saved
1	0x00040000	Latest satellite TLE
2 to 255	0x00080000 to 0x03FFFFFF	Collected Data

Table 9. S&F packet types

Packet type	Description	Sent by	Total length (bytes)
0	Sensor data packet	Any GST	Up to 175
1	TLE request packet	Any GST	21
4	Acknowledgment (ACK) packet	Payload (satellite)	23
6	TLE packet (compressed TLE information of satellite)	Payload (satellite)	109

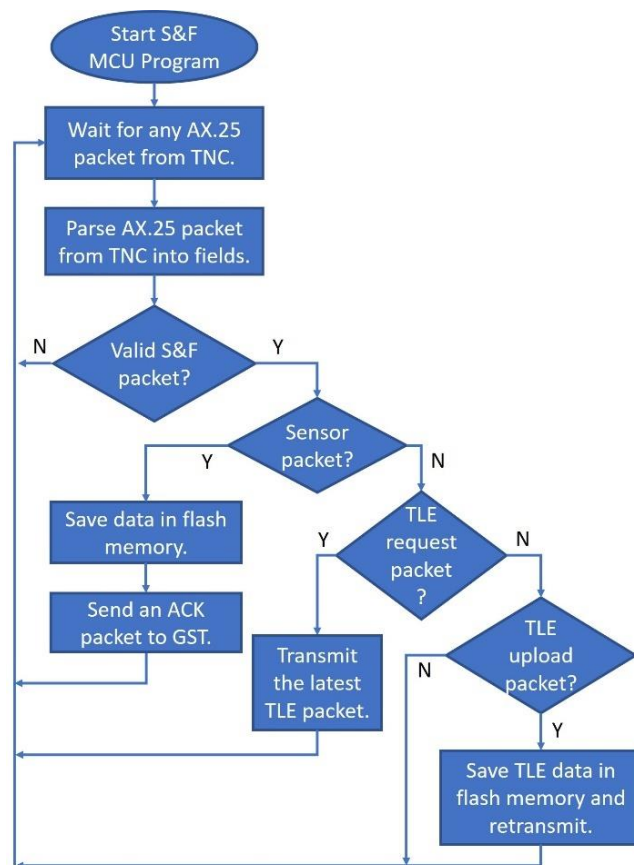


Figure 19. Program flow diagram of the S&F payload's MCU

For better context on how the payload is integrated with the whole satellite, satellite drawings are given in Figure 20. Overall, the components of the payload occupy about ¼ of the space on the mission board (which also hosts ADCS, the COM96 MCU portion of the communication subsystem, and other mission payloads such as camera, GPS receiver, and magnetic field sensor), except for the VHF transceiver that is placed on a separate board. The payload alone, when powered by a 5V supply, consumes only about 0.29 W while in receive or standby mode and 1.4 W during active RF signal transmission.

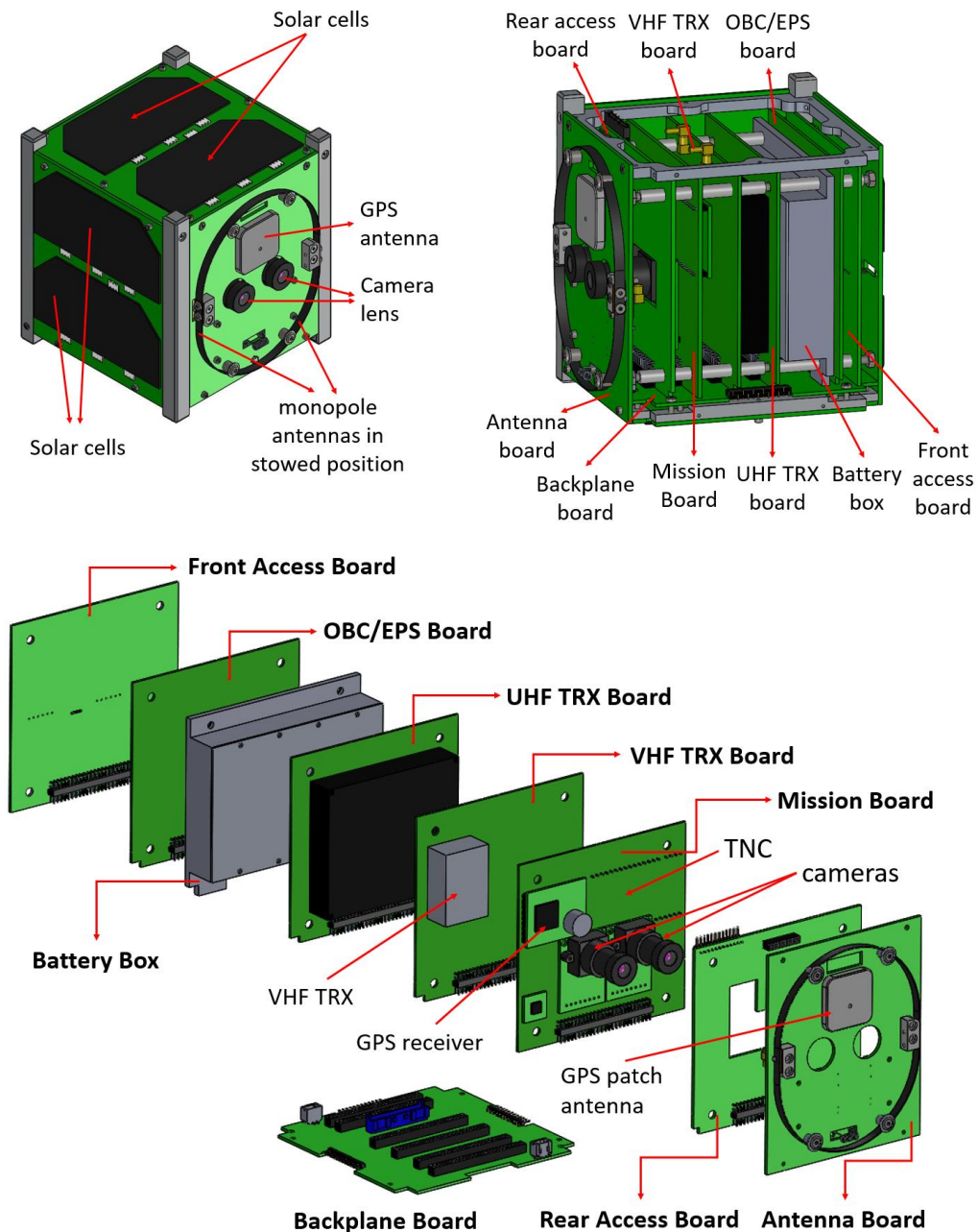


Figure 20. BIRDS-2 1U CubeSat drawings showing the internal and external boards

Table 10 shows the energy budget for operating the satellite in APRS-DP/S&F mission mode, assuming the payload is operating for 45 minutes in one orbit (~50% of one orbit duration) and RF transmission is active 25% of this time. Indeed, the energy budget is tight due to limited energy generation capacity from the solar cells for a 1U CubeSat and so a practical way to deal with this limitation is to

activate the payload within a specified duration and timing (delay of turning on from receipt of command) through a ground station in one country before passing over the desired operation location in another region. The energy budget will be greatly improved by utilizing a 2U or 3U CubeSat platform for a full-time operational mission.

Table 10. Energy budget of the satellite operating in APRS-DP/S&F mission mode

Parts	Current (A)	Power (W)	Duration/Orbit (h)	Energy/Orbit (Wh)
Non-mission operation (OBC/EPS board, mission board, CW beacon TX, command RX)	0.0160	0.632	1.5	0.948
S&F payload (RX/standby)	0.080	0.316	0.5625 (75%)	0.178
S&F payload (TX)	0.390	1.541	0.1875 (25%)	0.289
Total for running APRS- DP/S&F payload on	-	-	-	1.415
Average energy generation/orbit (estimate)	-	-	-	~1.2 (conservative estimate)

4.3 Antenna Design and Deployment Mechanism Implemented on the BIRDS-2 CubeSat

The BIRDS-2 satellite consists of two deployable monopole antennas, as illustrated in Figure 21. One is a UHF antenna covering the UHF amateur band (430-440 MHz) and is used for uplink command reception, CW covering the UHF amateur band (430-440 MHz) and is used for uplink command reception, CW beacon transmission, and telemetry and mission data downlink. The other is a VHF antenna operating at 145.825 MHz and is used for both user uplink and downlink of the APRS-DP/S&F mission. These antennas are expected to have omnidirectional radiation patterns because the satellite only has a passive stabilization mechanism. The antenna elements are made up of carbon tool steel (SK85(SK5) [168]) with thickness of 0.3 mm, width of 4 mm and quarter-wave lengths of 17.5 cm (UHF) and 50.1 cm (VHF). These elements are separately attached to a 3D printed plastic on the external side of +Y panel, secured to the plastic by tiny screws and carefully soldered to the inner conductors of MMCX connectors mounted on the panel’s internal side. Then, short RF cables connect the antennas to respective transceivers. The whole structure is electrically connected to the satellite system ground. There are no matching networks in the BIRDS-2 design.

On the way to and during deployment from the ISS, antenna elements are stowed around mounting screws. Their ends are tied to a single fishing string (GOHSEN PE Hunter Lock No. 8 [169]) made of polyethylene (PE) material, which is securely tied to two lower mounting screws. The string passes through a coiled nichrome wire that will be heated up by a burner circuit 30 minutes after satellite deployment to

burn the string and release the elements. The burner circuit draws high current from the battery through the EPS's unregulated voltage output. The nichrome wire resistance (i.e., number of turns) and burner circuit electrical settings were optimized for shorter burning time and higher deployment reliability.

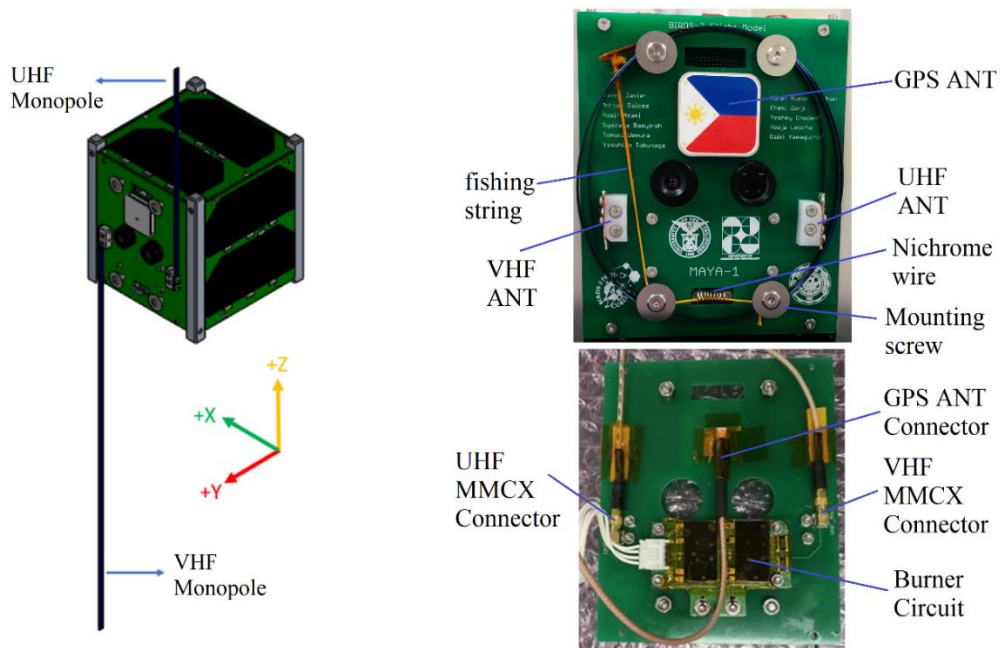


Figure 21. Monopole antennas of the BIRDS-2 satellite in deployed condition (left); external side of antenna board showing the stowed elements (upper right); internal side showing the antenna connectors and burner circuit (lower right)

After successful antenna deployment in cold vacuum condition had been demonstrated previously, to demonstrate the reliability of the antenna deployment mechanism, four units of burner circuit each attached to antenna assembly were tested inside a non-vacuum thermostatic chamber in different cold temperatures from -40°C to -20°C. Doing the test in a non-vacuum condition enabled more test runs to be done quickly and effectively without the risk of undertest considering more severe environment for the burning mechanism (due to presence of convection). The recorded deployment times at 80% charged battery are summarized in Table 11, suggesting that antenna can be expected to deploy within 13-18 seconds in these temperature conditions. Further tests showed that deployment is possible even as low as 30% charged battery.

Table 11. Recorded deployment times at different temperatures

Burner Circuit	Temperature (°C)	Current (A)	Deployment Time (s)	Battery Voltage (V _i /V _f)
1	-30	2.068	15.8	4.02 / 3.83
2	-25	2.154	15.9	3.99 / 3.90
3	-40	2.045	17.8	4.00 / 3.79
4	-20	2.007	13.2	4.02 / 3.83

4.4 BIRDS-2 Project Timeline Overview

The APRS-DP/S&F payload was designed, developed, and integrated to the satellites within a 15-month time frame from December 2016 to February 2018 – about 11 months for engineering model and four months for final assembly, integration, and test of flight models. Figure 22 shows an overview of the BIRDS-2 project timeline. During BIRDS-2 satellite development, the functionality of payload was developed and tested by communicating with a handheld radio and a dummy GST setup at Kyutech. Tuning and radiation pattern testing of antennas were done separately from other payload parts during PDR and CDR stages, but there were unnoticed mistakes in the procedure and undetermined design problems during development.

Integration of APRS-DP/S&F payload with antennas and other satellite parts was done late (after CDR), so were the verification tests with the whole satellite assembled. Wireless communication tests were performed with a flight model spare in the anechoic chamber to confirm the link budget, but the results were not as good as we expected. Also, at a time when we were debugging several other problems occurring on the flight models, we could not manage to obtain conclusive and replicable results in the anechoic chamber. Due to time constraints (as this was already during flight model AIV phase and we had to prioritize other activities), we were not able to fully determine the condition and test the performance of the payload when completely integrated with the antenna and whole satellite.

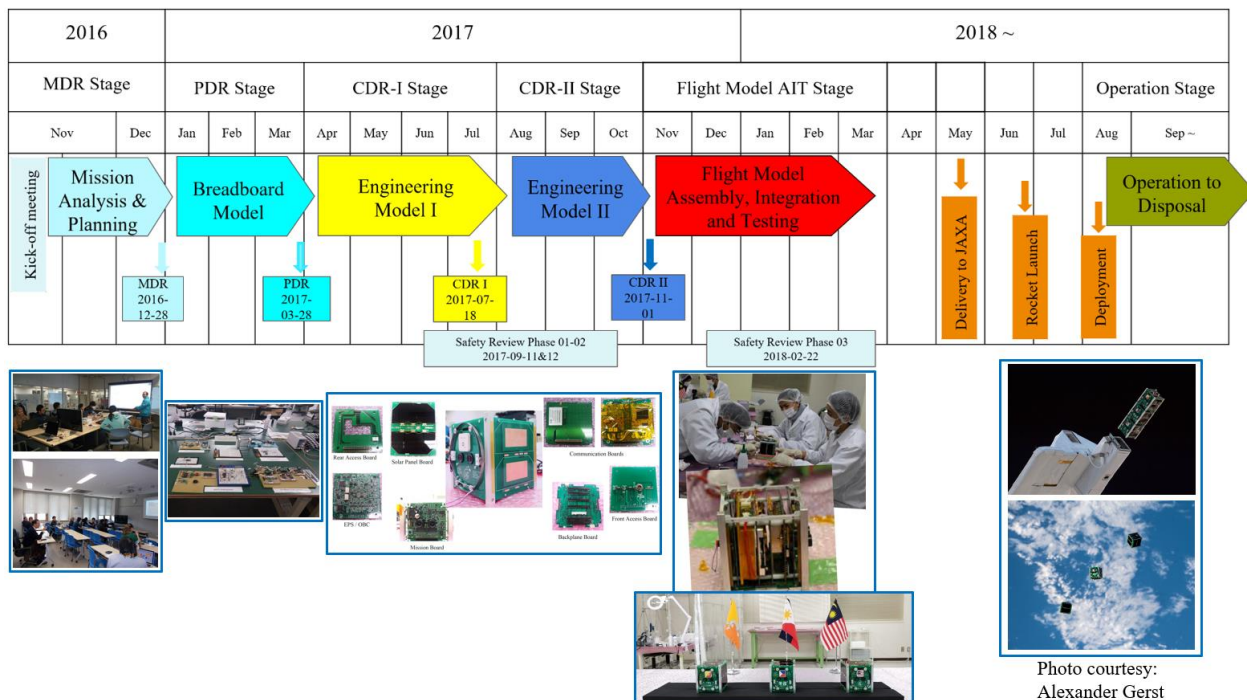


Figure 22. BIRDS-2 project timeline

4.5 APRS-DP/S&F Payload Functionality Tests

Before wireless communication tests in anechoic chamber, payload functionalities were developed and confirmed in the workplace in BIRDS room. APRS-DP communication functionalities, such as exchanging messages and beacon with the payload acting as relay, were confirmed inside the BIRDS room

Nanosatellite S&F Communication Systems for Remote Data Collection Applications

and outdoor, using two handheld radios as shown in Figure 23. In outdoor tests, the satellite was placed between two users distanced far enough so that direct communication between their handheld radios (with attenuators attached) could not be established. Digipeating was confirmed because the message/beacon could only be received by the other side when the payload was on. The S&F functionalities were confirmed with a dummy GST sending a sensor packet to the payload and checking if the GST could receive acknowledgment packet from the payload, as shown in Figure 24.

The integrity and functionality of the APRS-DP/S&F payload was confirmed before integrating it with the whole satellite. Both APRS-DP and S&F communication functionalities were verified with a handheld radio. As for the payload's VHF transceiver, the output RF power, bandwidth, and spectrum were measured using a spectrum analyzer. The spectrum measurements are given in Figures 25, 26 and 27 and tabulated in Table 12. The output RF power are within the product specification value of 27 dBm \pm 1dB. The -30 dB and -50 dB bandwidths do not exceed the 15 kHz coordinated license. The measured payload power consumption was 0.29 W during receiving or idle and 1.40 W during active RF transmission.

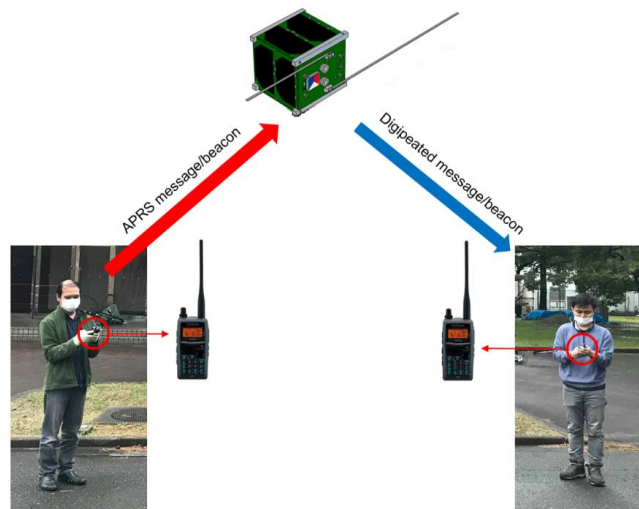


Figure 23. Basic APRS-DP communication tests performed with an APRS-capable Kenwood handheld radio

Table 12. Payload VHF transmitter output RF signal spectral measurements

Satellite	-30 dB bandwidth (kHz)	-50 dB bandwidth (kHz)	Channel Power within 30 kHz (dBm)
BIRD-BT (BHUTAN-1)	5.1	9.4	26.5
BIRD-PH (MAYA-1)	5.1	9.2	26.6
BIRD-MY (UitMSAT-1)	5.0	9.2	27.1

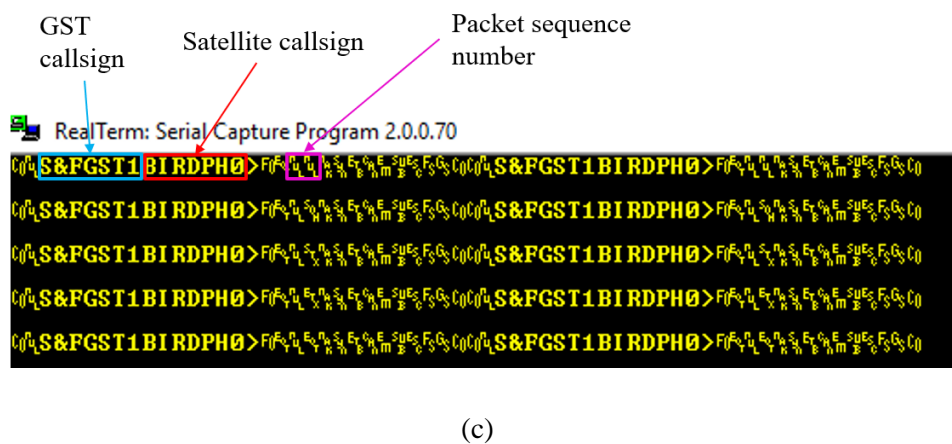
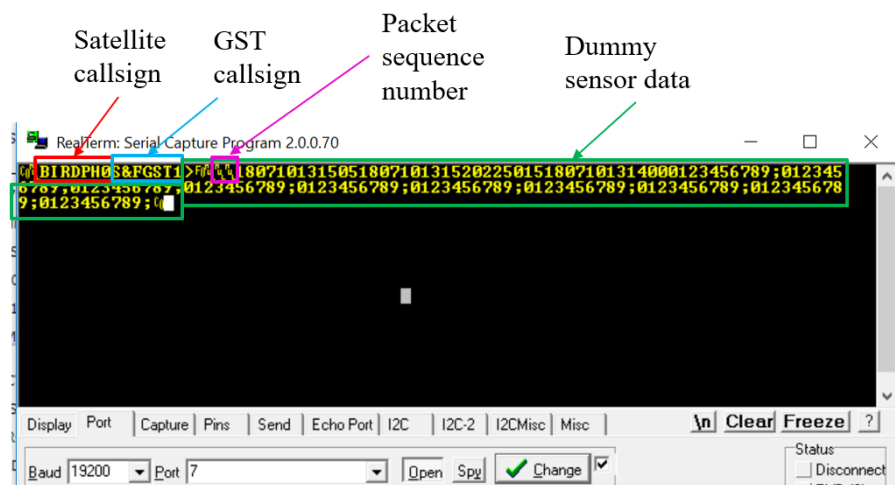
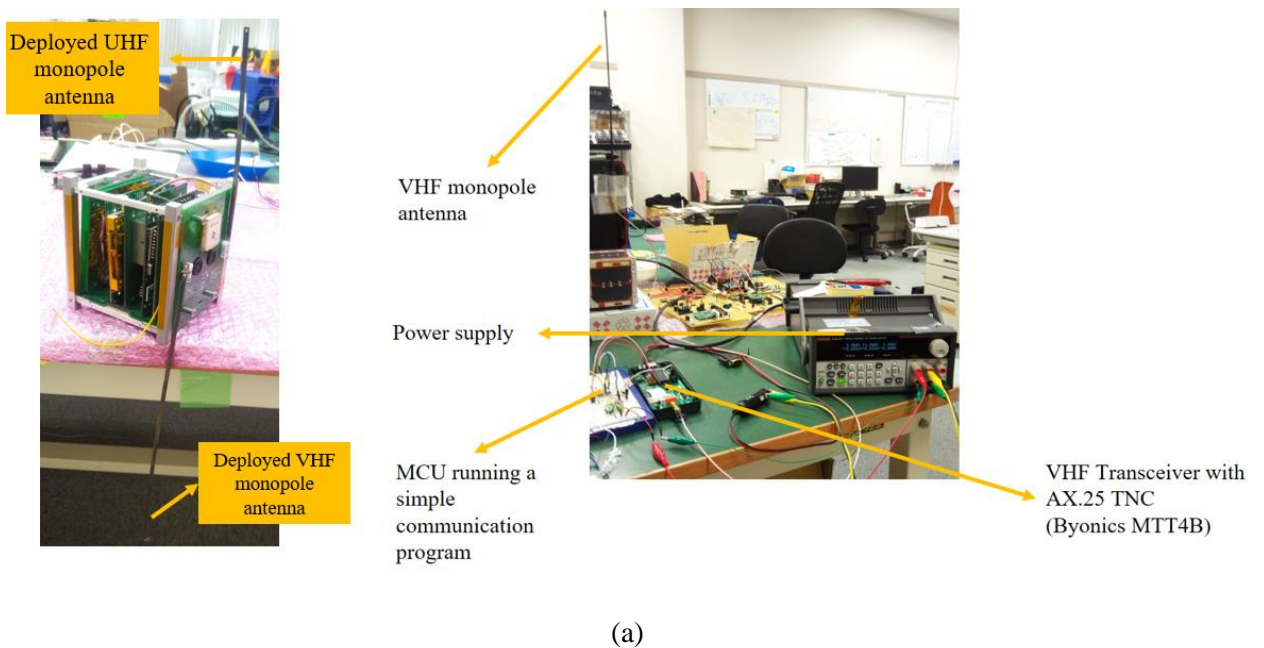


Figure 24. Testing communication between the payload and dummy GST: (a) simple setup inside the BIRDS room, (b) sensor packet received by payload from GST, (c) (b) ACK packet received by GST from payload

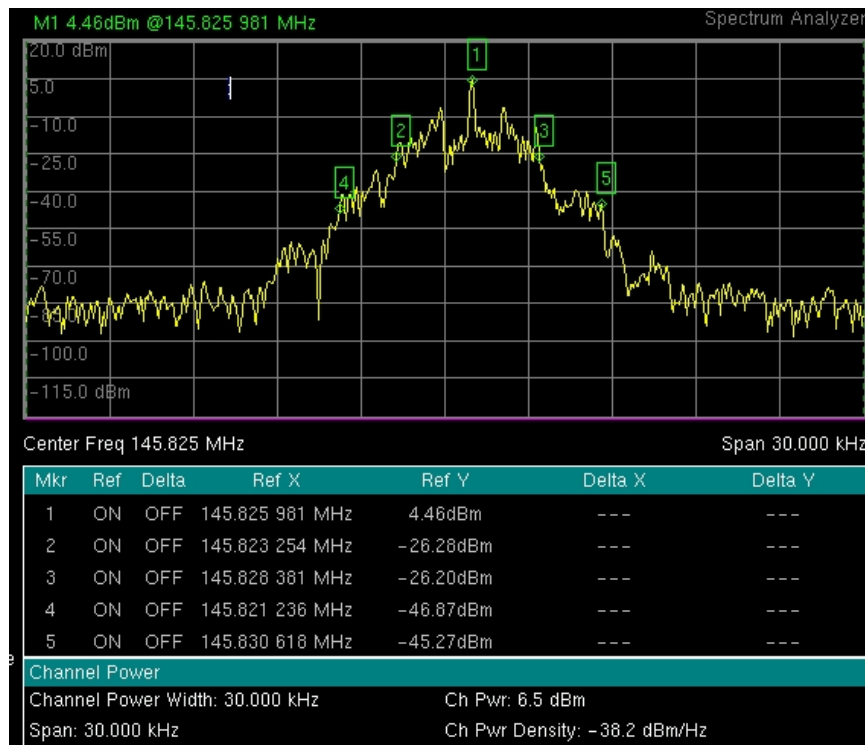


Figure 25. Spectrum measurement on BIRD-BT (BHUTAN-1) VHF transmitter’s RF output after putting a 20 dB attenuator, indicating an total output power of 26.5 dBm

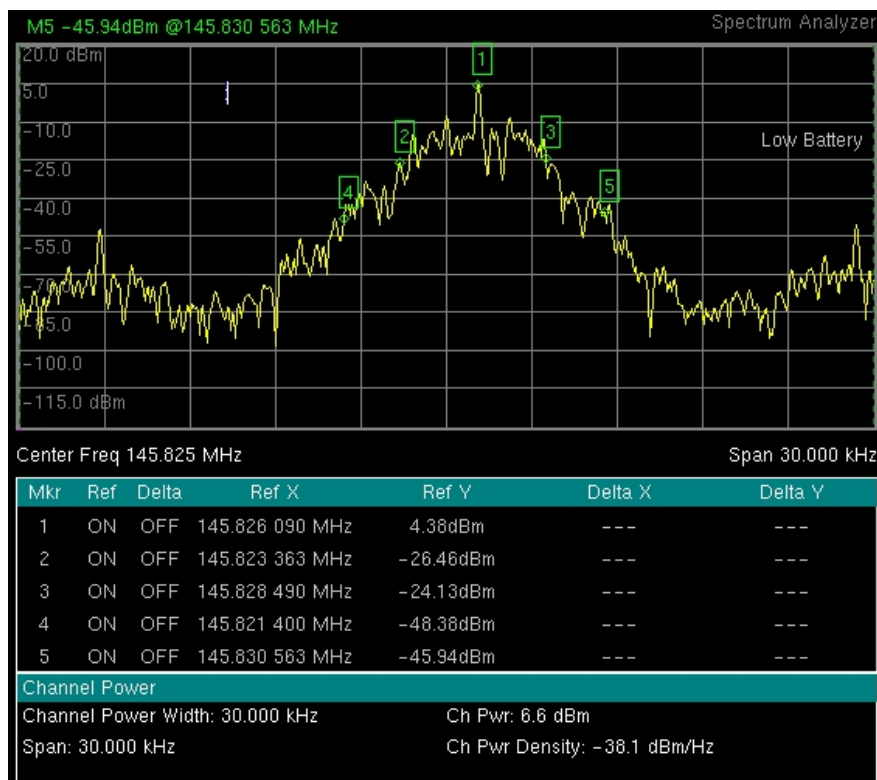


Figure 26. Spectrum measurement on BIRD-PH (MAYA-1) VHF transmitter’s RF output after putting a 20 dB attenuator, indicating an total output power of 26.6 dBm

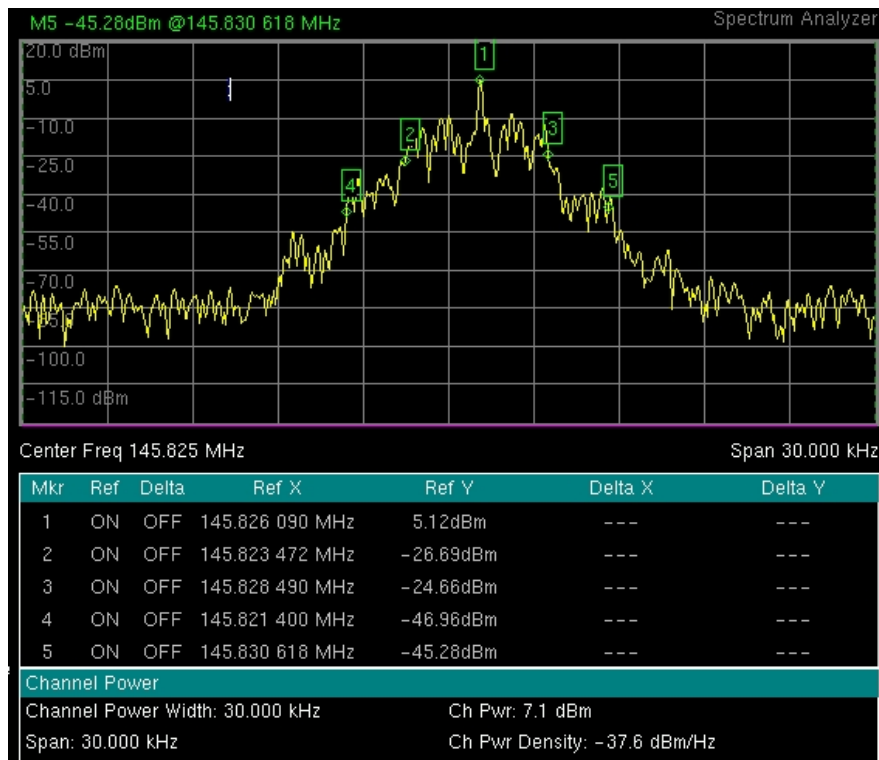


Figure 27. Spectrum measurement on BIRD-MY (UiTMSAT-1) VHF transmitter’s RF output after putting a 20 dB attenuator, indicating an total output power of 27.1 dBm

4.6 EM and FM Satellite Assembly, Integration and Verification

During the flight models’ assembly, integration, and verification (AIV) stage, the BIRDS-2 project members were grouped into respective country teams, each assigned a workstation (some photos of AIV activities are shown in Figure 28). Thermal vacuum and vibration tests were conducted on the fully integrated satellite to demonstrate the satellite would operate properly in space environment and would satisfy the launcher’s safety requirements. Thermal vacuum tests were done on both the engineering model and flight models to verify the functionality of the whole satellite and subsystems, including the APRS-DP/S&F payload, under vacuum condition and extreme cold and hot temperatures of space. This test would also confirm if the satellite and its parts can withstand the thermal stress under vacuum condition. This test was performed directly on the integrated satellite and unit level and subsystem level tests were skipped to save time and effort.

In engineering model test, the satellite was subjected to -25°C worst cold and +55°C worst hot temperatures (control temperature is defined as the average of the six external panels’ temperatures) for four thermal cycles. The actual control temperature and VHF transceiver temperature are shown in Figure 29. The payload was confirmed to be functional and survived the thermal cycling. In flight model test, the satellites were subjected to -25°C worst cold and +65°C worst hot temperatures for two thermal cycles. Flight model thermal vacuum test setup is shown in Figure 30.



Figure 28. BIRDS-2 flight model assembly, integration and verification

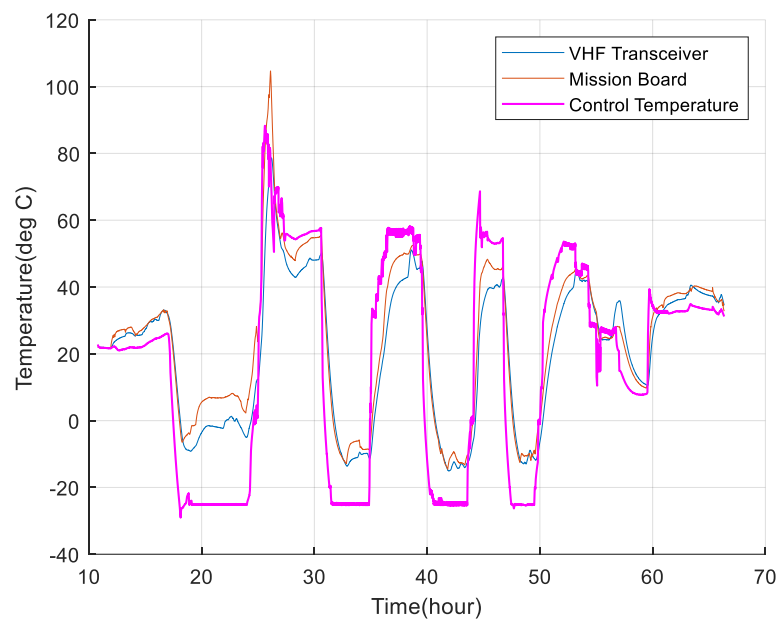


Figure 29. Actual temperatures of the APRS-DP/S&F payload during thermal vacuum test on the engineering model

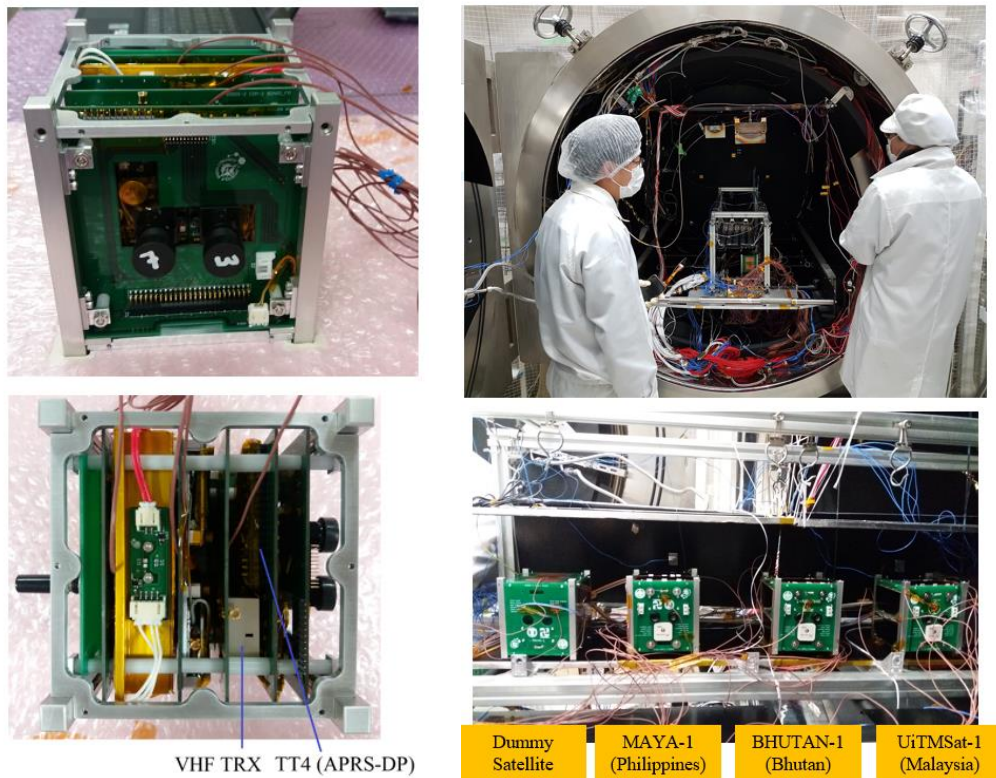


Figure 30. Thermal vacuum test on BIRDS-2 flight models: (left) thermocouples attached assembled satellite; (right) test setup with flight models inside the large vacuum chamber in Kyutech CENT

Random vibration (20-2000 Hz, 6.53 Grms for QT, and 4.83 Grms for AT) and sine-burst vibration (18.1 G for QT) tests were performed on the engineering and flight models to demonstrate structural integrity of the satellites in rocket launch environment and to satisfy the launcher requirements. These were done as part of JAXA's acceptance process. The vibration test setup for the flight models are shown in Figure 31. The random vibration test profile used followed the combined envelopes for HTV and SpaceX launch vehicle profiles. The natural frequencies in all three axes were shown to be way higher than the minimum requirement of 100 Hz. During vibration test, the stowed antennas did not inadvertently deploy and there were neither dislocated nor removed parts. Thus, the satellites passed both qualification and acceptance vibration tests. The three BIRDS-2 flight models ready for delivery are shown in Figure 32. Photos of satellite hand-over to JAXA, rocket launch and satellites' deployment from the ISS are given in Figures 33, 34 and 35.

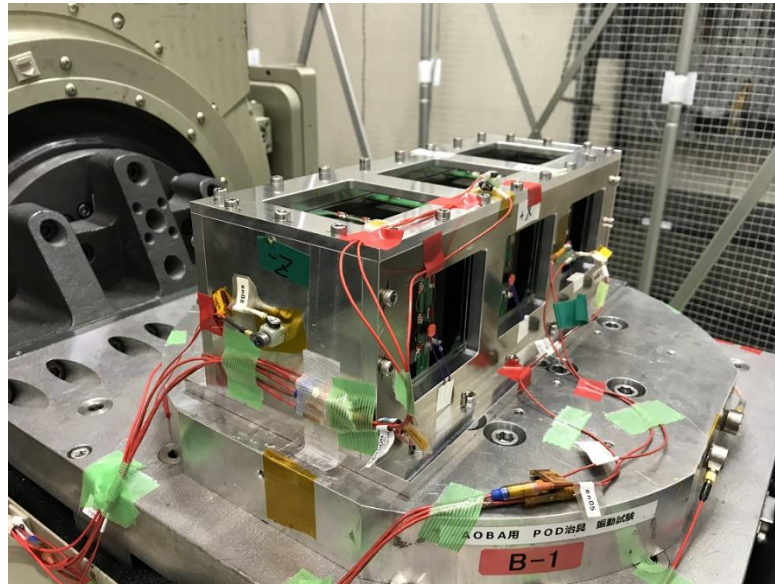


Figure 31. Actual vibration test setup for flight models

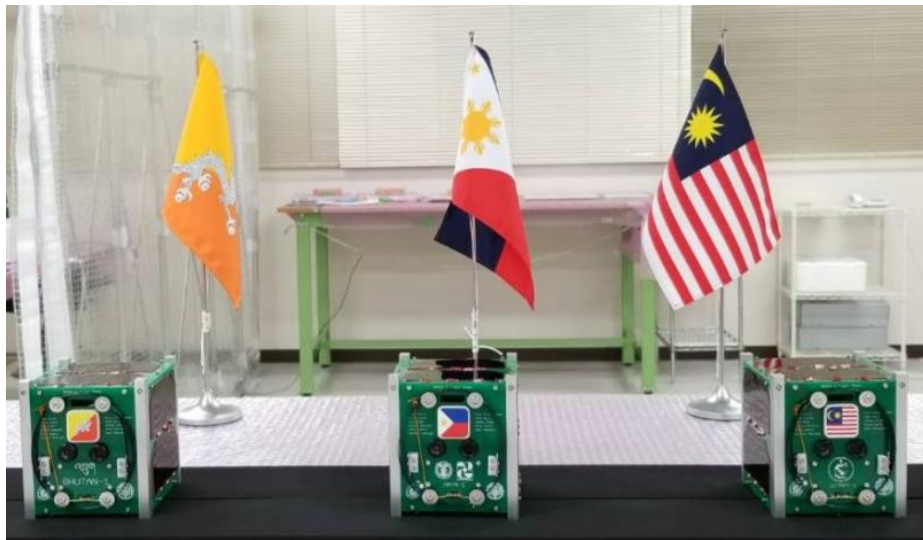


Figure 32. BIRDS-2 CubeSat flight models inside the cleanroom at Kyutech CENT



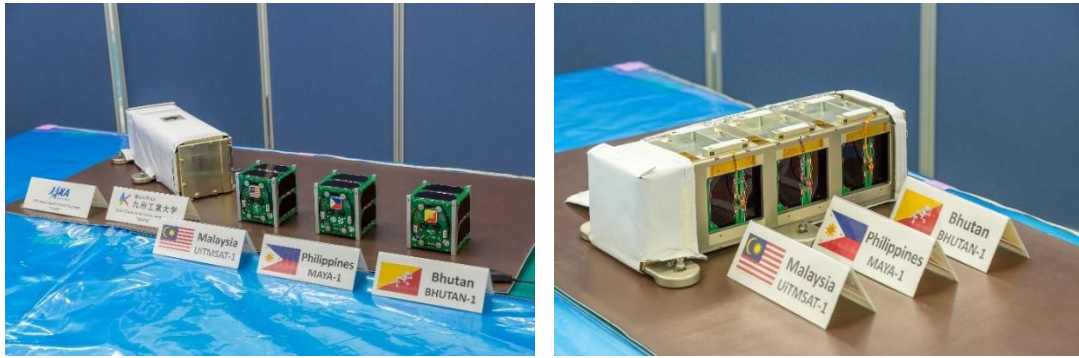


Figure 33. Photos of BIRDS-2 CubeSat flight models delivered to JAXA facility and assembly with the pod (photos courtesy of JAXA)



Figure 34. Rocket launch to the ISS in June 29, 2018 through the SpaceX Falcon 9

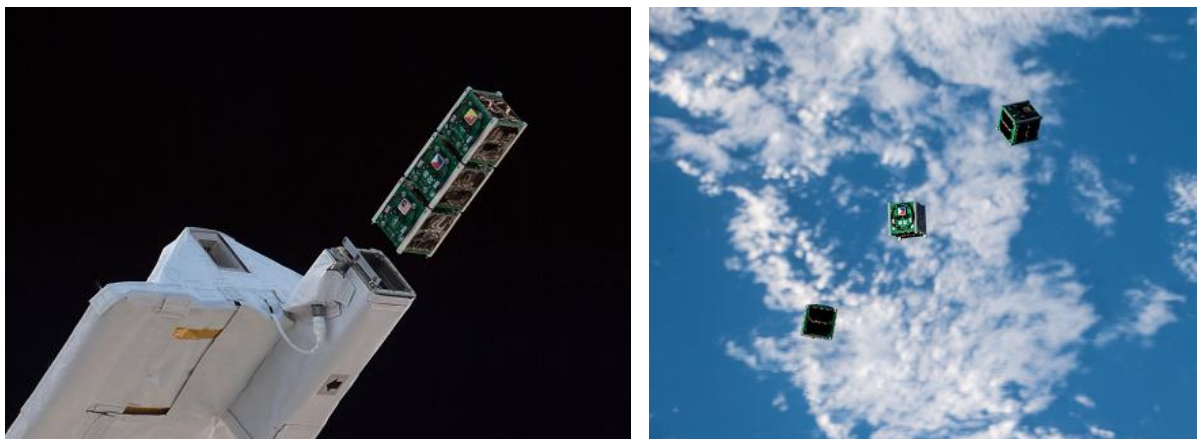


Figure 35. Deployment of BIRDS-2 CubeSats from the ISS in August 10, 2018 (photos courtesy of Alexander Gerst)

4.7 Overview of Ground Sensor Terminal (GST) Segment

The block diagram of the GST segment is given in Figure 36. It consists of a control and communication unit (CCU), real time clock (RTC) for time information in UTC, a half-duplex VHF transceiver, an SD card for sensor data storage, an antenna with rotator mounted on a mast (needed in the case of a directive GST antenna), and a solar-battery power system for autonomous operation even in an isolated location. The CCU performs data logging at regular time interval, implements the communication sequence and protocol with the payload, and hosts an orbital calculation software. The use of an orbital software to predict satellite passes is adopted to calculate the time of satellite passes. This enables an

intelligent automation of the GST, avoiding unnecessary RF emissions, and saving energy. Before any satellite pass, the orbital calculator computes the time of arrival (TOA or acquisition of signal (AOS)) and time of departure (TOA or loss of signal (LOS)) of each CubeSat using the GST's position (latitude, longitude and altitude which are programmed prior to deployment), accurate time information from RTC and the satellite's updated TLE. Initial TLE information of all CubeSats will be saved in the SD card, but these will be updated regularly because the GST is programmed to send a TLE download request packet to the payload when the last saved TLE is older than five days.

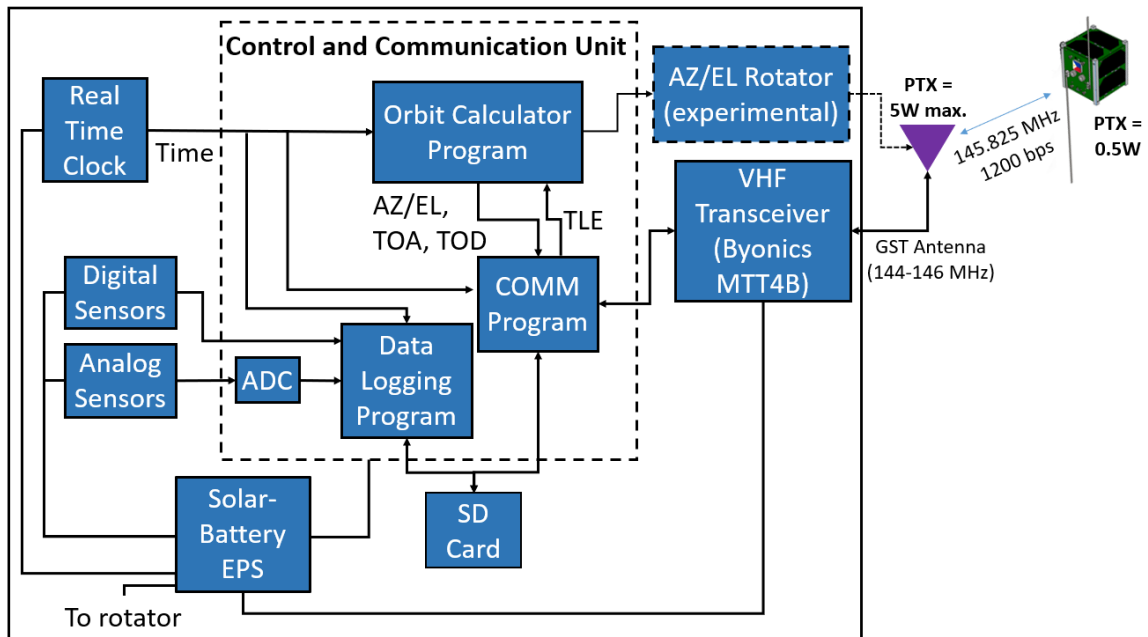


Figure 36. Block diagram of ground sensor terminal (GST) segment

The VHF transceiver is a low-cost COTS product, MTT4B, from Byonics. It has an FM transceiver with adjustable transmit power (up to 8W), programmable transmit and receive frequencies that were set to 145.825 MHz, internal 1200 bps AFSK modem and AX.25 protocol TNC support. Because the GSTs operate within the VHF amateur radio band, they must be registered as amateur stations to an amateur operator at the respective national telecommunication ministry. GST prototypes developed at Kyutech and by collaborators at the University of the Philippines – Diliman (UPD, Philippines) and the Universiti Teknologi Mara (UiTM, Malaysia) are shown in Figures 37 and 38. For Bhutan, the target application is weather monitoring with stations sensing temperature, pressure, humidity, wind speed and direction, rain gauge. For Malaysia, the target application is ground-based magnetic field measurements with anisotropic magnetoresistance sensor. For the Philippines, the target application is soil monitoring for agriculture with temperature and humidity sensors. Figure 39 shows data logging activity of the Kyutech GST prototype as displayed by serial monitor.

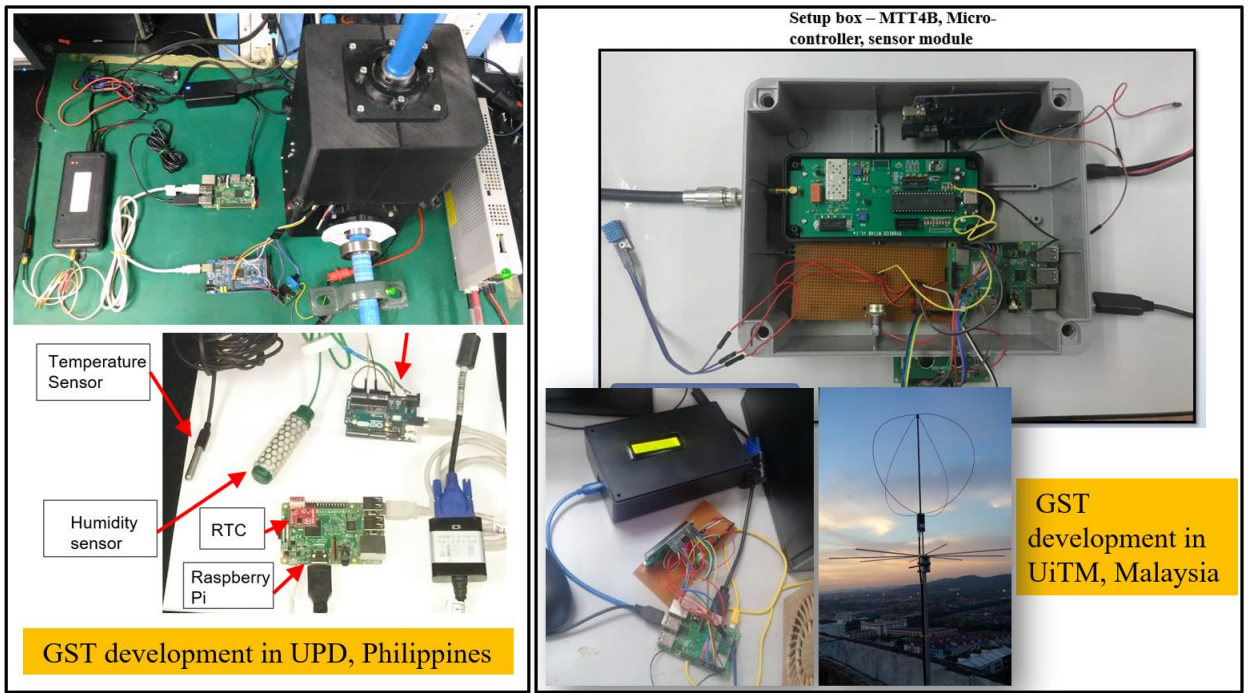


Figure 37. GST prototypes developed by collaborators in UPD (Philippines) and UiTM (Malaysia)

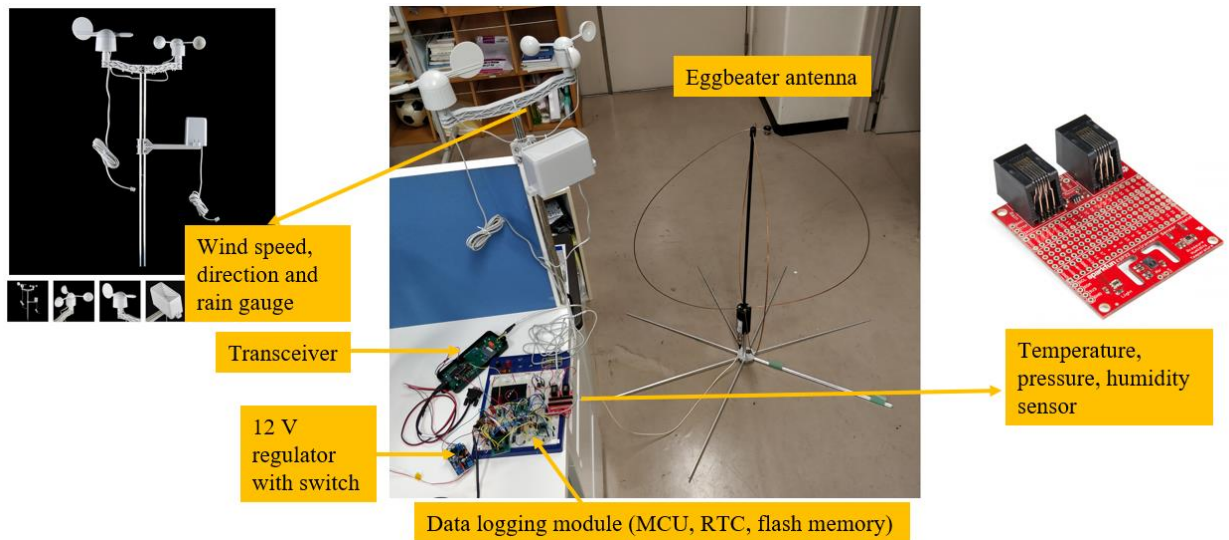


Figure 38. GST prototype developed at Kyutech

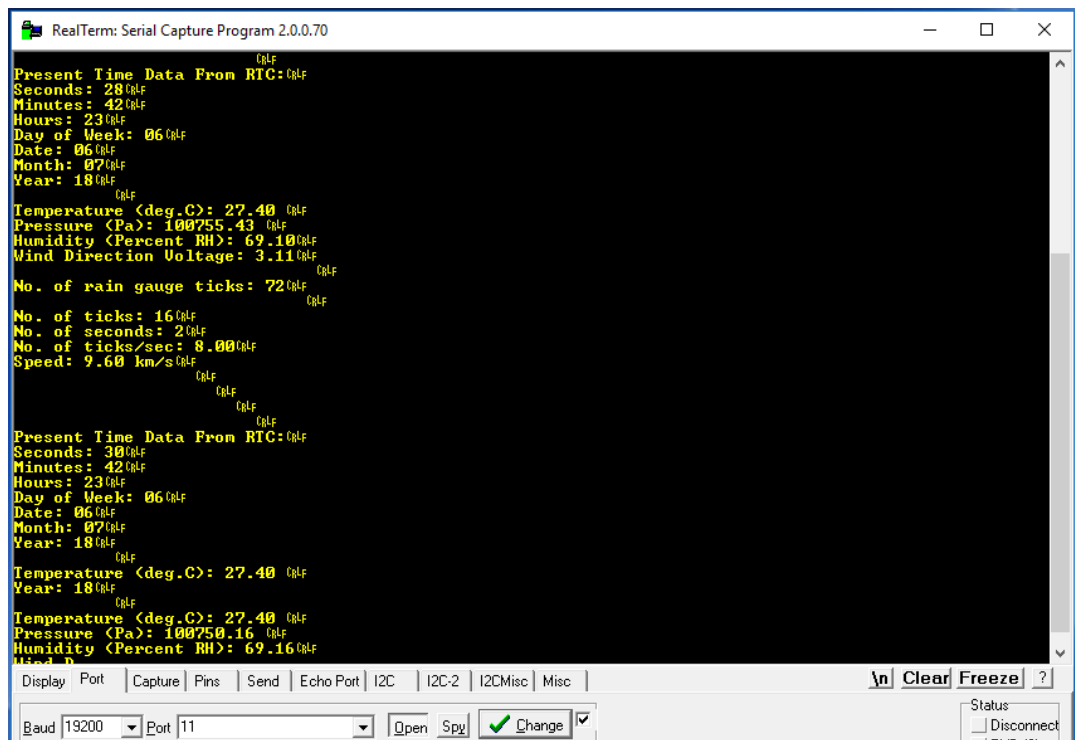


Figure 39. Kyutech GST prototype actual data logging activity as displayed by serial monitor

4.8 On-orbit Operation Results

Two weeks after the satellites' deployment from the ISS, command uplink from ground station to all BIRDS-2 satellites could still not be established. As programmed, the APRS-DP/S&F payload was automatically activated by the OBC in all three satellites (automatic mission mode). At Kyutech GS, we received the beacon signals regularly transmitted by the payloads, but we could only decode those from BIRD-BT and BIRD-MY as shown in Figure 40. Radio amateurs around the world also reported their reception of the beacon signals but only one amateur reported to have decoded from BIRD-PH. Downlink signal from BIRD-PH was weaker according to some amateurs. Beacon transmissions from BIRD-PH apparently stopped early so it was likely its VHF transmitter failed. Recorded RF power measurements on beacon signals (shown in Figures 42 and 43) indicate that the threshold downlink reception power for decoding is about -105 dBm. Unfortunately, full two-way communication with the payload, i.e., digipeating functionality, did not work because of uplink communication problem. The payload could not receive and decode uplink packets from users on the ground even with a highly directive antenna.

Nanosatellite S&F Communication Systems for Remote Data Collection Applications

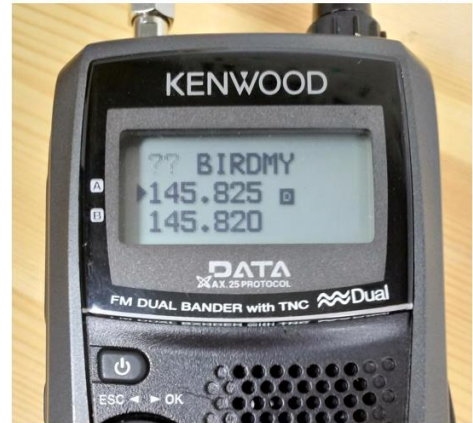
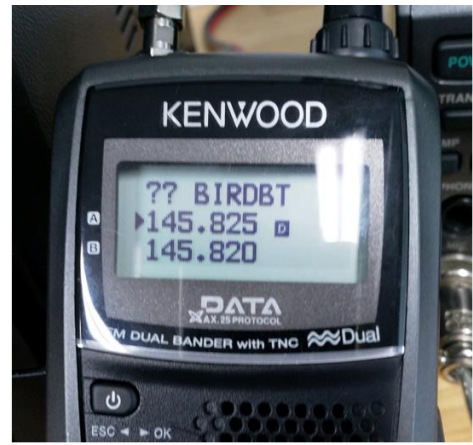
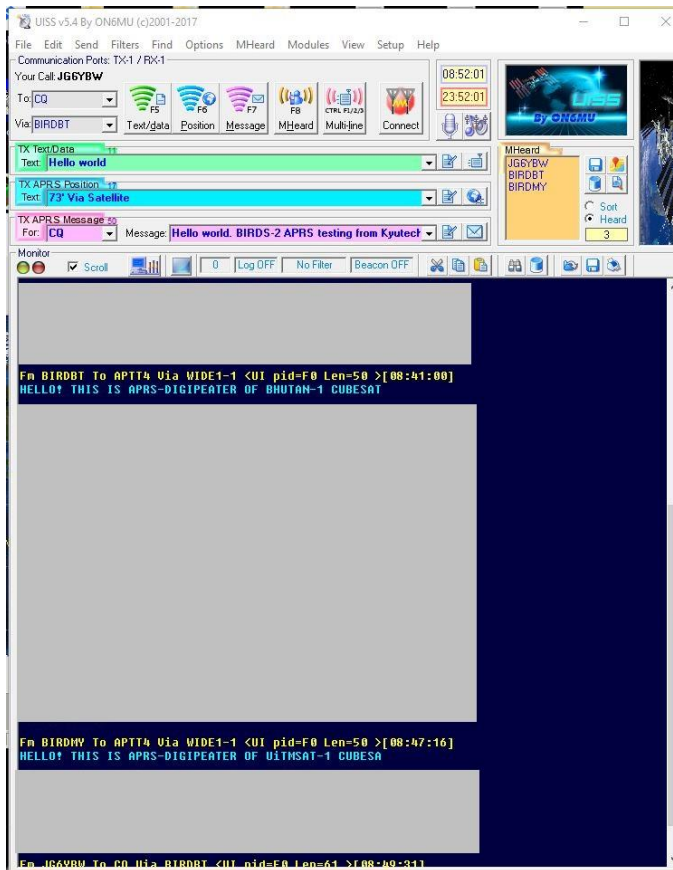
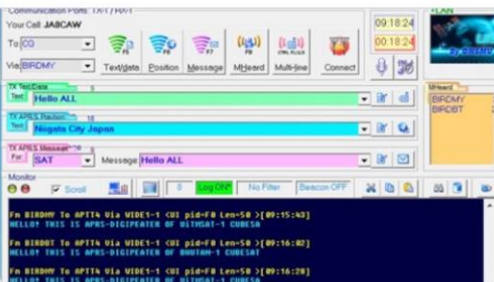


Figure 40. APRS-DP regular beacon message packets received at Kyutech GS: (left) using UISS software on PC; (right) using Kenwood handheld radio


JA0CAW @JA0CAW Japan

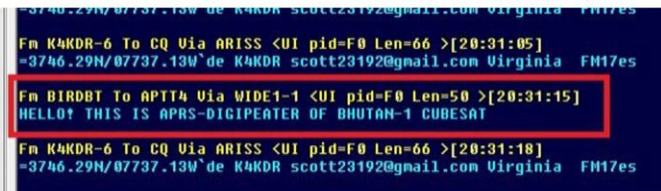
Birds-2 23:56 UTC digipeater beacon BHUTAN-1/UiTMSat-1 good signal but MAYA-1 weak signal (no decoded) over Japan (replay-WAV)@BIRDS2CubeSat @uitmsat #amsat #issham #cubesats



The screenshot shows a radio software interface with a map of Japan. The map highlights the location of the digipeater. Below the map, there is a list of APRS messages, including one from BIRDBT to APTT4 via WIDE1-1.

USA

 **Scott Chapman @scott23192 · 1d** ✓
 BIRD-BT 145.825 APRS over NE USA; first packets I've heard from the BIRDS-2 cluster! No digipeats yet



The screenshot shows APRS messages received by Scott Chapman. The messages are from K4KDR and BIRDBT. The message from BIRDBT is highlighted with a red box: "HELLO! THIS IS APRS-DIGIPEATER OF BHUTAN-1 CUBESAT".

Italy



The screenshot shows APRS messages received in Italy. The messages are from BIRDBT to APTT4 via WIDE1-1. The messages are: "HELLO! THIS IS APRS-DIGIPEATER OF BHUTAN-1 CUBESAT".

Germany

BIRD-2 APRS digipeaters

MONDAY, AUGUST 20, 2018 DK3WN LEAVE A COMMENT

beacons active

20180820105512: fm BIRDPH To APTT4 Via WIDE1-1 ctl UI pid F0 HELLO! THIS IS APRS-DIGIPEATER OF MAYA-1 CUBESAT

20180820122929: fm BIRDBT to APTT4 via WIDE1-1 ctl UI pid F0 HELLO! THIS IS APRS-DIGIPEATER OF BHUTAN-1 CUBESAT

20180820123014: fm BIRDBT to APTT4 via WIDE1-1 ctl UI pid F0 HELLO! THIS IS APRS-DIGIPEATER OF BHUTAN-1 CUBESAT

20180820105355: fm BIRDMY To APTT4 Via WIDE1-1 ctl UI pid F0 HELLO! THIS IS APRS-DIGIPEATER OF UITMSAT-1 CUBESA

20180820105440: fm BIRDMY To APTT4 Via WIDE1-1 ctl UI pid F0 HELLO! THIS IS APRS-DIGIPEATER OF UITMSAT-1 CUBESA

Figure 41. APRS-DP regular beacon message packets received by some amateurs around the world

Nanosatellite S&F Communication Systems for Remote Data Collection Applications

Date	Time (JST)	Elevation	Peak Received Power (dBm)	Decoded (D) / Not Decoded (ND)	Date	Time (JST)	Elevation	Peak Received Power (dBm)	Decoded (D) / Not Decoded (ND)
2018/11/20	2:43	12	-114	ND	2018/11/21	18:24	20	-120	N/A
2018/11/20	2:43	22	-105	D	2018/11/21	18:24	22	-108	N/A
2018/11/20	2:43	30	-110	ND	2018/11/22	19:05	11	-108	ND
2018/11/20	4:19	4	-110	ND	2018/11/22	19:05	27	-106	D
2018/11/20	4:19	7	-111	ND	2018/11/22	19:05	42	-105	ND
2018/11/20	4:19	11	-105	ND	2018/11/22	19:05	55	-110	ND
2018/11/20	4:19	21	-105	D	2018/11/22	19:05	17	-109	ND
2018/11/20	4:19	25	-104	D	2018/11/26	17:05	53	-112	D
2018/11/20	19:18	21	-117	ND	2018/11/26	23:36	9	-110	ND
2018/11/20	19:18	22	-114	ND	2018/11/26	23:36	12	-115	ND
2018/11/20	19:18	48	-116	ND	2018/11/27	1:11	7	-115	ND
2018/11/20	19:18	50	-102	D	2018/11/27	1:11	12	-108	ND
2018/11/21	1:48	13	-	D	2018/11/27	1:11	19	-106	D
2018/11/21	3:24	9	-115	ND	2018/11/27	1:11	29	-102	D
2018/11/21	3:24	14	-110	ND	2018/11/27	1:11	45	-98	D
2018/11/21	3:24	22	-105	ND	2018/11/27	1:11	51	-104	D
2018/11/21	3:24	35	-100	D	2018/11/27	1:11	36	-110	ND
2018/11/21	3:24	56	-97	D	2018/11/29	0:56	7	-110	ND
2018/11/21	3:24	35	-115	ND	2018/11/29	0:56	10	-104	ND
2018/11/21	3:24	14	-110	ND	2018/11/29	0:56	20	-102	D
2018/11/21	18:24	16	-112	N/A	2018/11/29	0:56	18	-108	D

Figure 42. RF power measurements of BIRD-BT's APRS-DP beacon message signal through Kyutech BIRDS GS

Date	Time (JST)	Elevation	Peak Received Power (dBm)	Decoded (D) / Not Decoded (ND)	Date	Time (JST)	Elevation	Peak Received Power (dBm)	Decoded (D) / Not Decoded (ND)
2018/11/20	2:43	24	-115	ND	2018/11/26	18:43	8	-115	ND
2018/11/20	2:43	14	-115	ND	2018/11/26	23:36	5	-120	ND
2018/11/20	4:19	21	-110	ND	2018/11/26	23:36	11	-117	ND
2018/11/20	4:19	18	-115	ND	2018/11/26	23:36	16	-115	ND
2018/11/20	19:18	65	-105	D	2018/11/26	23:36	14	-114	ND
2018/11/20	19:18	43	-110	ND	2018/11/26	23:36	11	-115	ND
2018/11/20	19:18	26	-115	ND	2018/11/26	23:36	8	-114	ND
2018/11/20	19:18	17	-112	ND	2018/11/27	1:11	42	-105	D
2018/11/20	19:18	11	-116	ND	2018/11/27	1:11	38	-108	D
2018/11/20	20:55	11	-118	ND	2018/11/27	1:11	26	-118	ND
2018/11/21	1:48	9	-115	ND	2018/11/29	0:56	14	-105	D
2018/11/21	18:24	22	-112	N/A	2018/11/29	0:56	16	-111	ND
2018/11/21	18:24	26	-115	N/A	2018/11/29	0:56	16	-115	ND
2018/11/21	18:24	24	-120	N/A	2018/11/29	0:56	14	-114	ND
2018/11/21	18:24	14	-118	N/A	2018/11/29	0:56	11	-116	ND
2018/11/21	18:24	9	-117	N/A	2018/11/29	0:56	8	-116	ND
2018/11/22	19:05	13	-116	ND	2018/12/02	16:23	5	-112	ND
2018/11/22	19:05	8	-116	ND	2018/12/02	16:23	7	-118	ND
2018/11/22	19:05	4	-119	ND	2018/12/02	12:17	18	-115	ND

Figure 43. RF power measurements of BIRD-MY's APRS-DP beacon message signal through Kyutech BIRDS GS

Chapter 5: Investigation on Communication Design Issues of BIRDS-2 CubeSat APRS-DP/S&F Payload, Results and Discussion

Although we had performed a few communication tests during development, it was only in hindsight we realized that our test approach had limitations and that we committed serious mistakes in executing the test procedures. Some important aspects of communication verification test had been overlooked during development due to other pressing design issues, assembly, integration, and test activities. Moreover, since the antenna design had undergone two iterations before being finalized, the team members working on the payload and antenna design did not have ample time to detect the antenna matching, grounding, and electromagnetic interference (EMI) problems during integration.

The failure to identify the real design issues was complicated by the fact that our existing measurement results at that time on antenna gain and reflection coefficient were incorrect, as well as the fact that we overlooked the satellite-radiated EMI. Also, between UHF and VHF communication subsystem verification tests, the team had to prioritize and dedicate more time for UHF communication subsystem because of its criticality for the whole satellite operation. Later it turned out, however, that both communication subsystems were facing similar problems.

In this chapter, we discuss the process and results on the investigation conducted after the satellite had been delivered to the launch provider (and mostly after confirming failure of uplink communication after deployment from ISS). The presentation below reflects the improved and more systematic communication verification test procedure to address the limitations and mistakes from our previous communication tests during the satellite development.

5.1 Determining the Actual Payload Receiver Sensitivity by Cabled Communication

Applying the SNR method [170], assuming a receiver bandwidth of 12 kHz and effective receiver noise temperature of 606 K, the estimated thermal noise power in the band is about -130 dBm. Then, for a threshold SNR of 21 dB (for AFSK/FM modulation at 10^{-4} BER), the minimum receiver input power required is roughly -109 dBm. On the other hand, according to the product's datasheet, the receiver sensitivity is -120 dBm for 12 dB SINAD (signal-to-noise and distortion ratio, referring to analog signal quality). Thus, we can approximate that the 21 dB SINAD is 9 dB above -120 dBm or equal to -111 dBm, which is not far from the theoretical value (-109 dBm).

To determine the actual optimum sensitivities of uplink and downlink receivers, communication test between a Kenwood TH-D72 handheld radio (representing an APRS user or GST) and payload was performed in a cabled test condition. Figure 44 shows the test setup wherein the received RF power at the input of payload receiver was controlled by varying the attenuator value. The packet success rate was characterized for different values of receiver input power. The satellite (a flight spare) was placed inside

an RF shield box to reduce the effect of possible leakage from the handheld radio transmitter to the payload receiver and vice-versa.

The packet downlink success rate (PDSR) and packet uplink success rate (PUSR) are plotted in Figure 45 for the case of matched frequencies and in Figure 46 for case of mismatched frequencies. In the figures, L is the total length in bytes of the test packet sent. To facilitate the discussion below, a threshold success rate of 80% is considered for sensitivity. For the case of matched frequencies, the optimum (cabled condition) uplink receiver sensitivity is within the range of -110 dBm to -114 dBm while the optimum downlink receiver sensitivity is within the range of -109 dBm to -111 dBm, depending on packet length. For the case of mismatched frequencies, a 5 kHz Doppler shift (only about 3 kHz is expected in practice) would result in a 4-7 dB worse receiver sensitivities – uplink receiver sensitivity of about -105 dBm and downlink receiver sensitivity of about -106 dBm, for a 100-byte packet length.

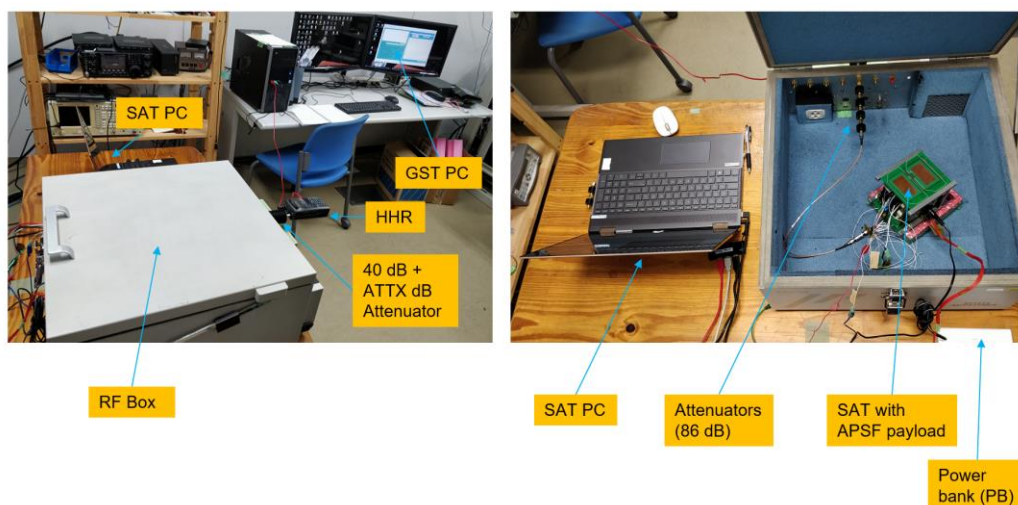
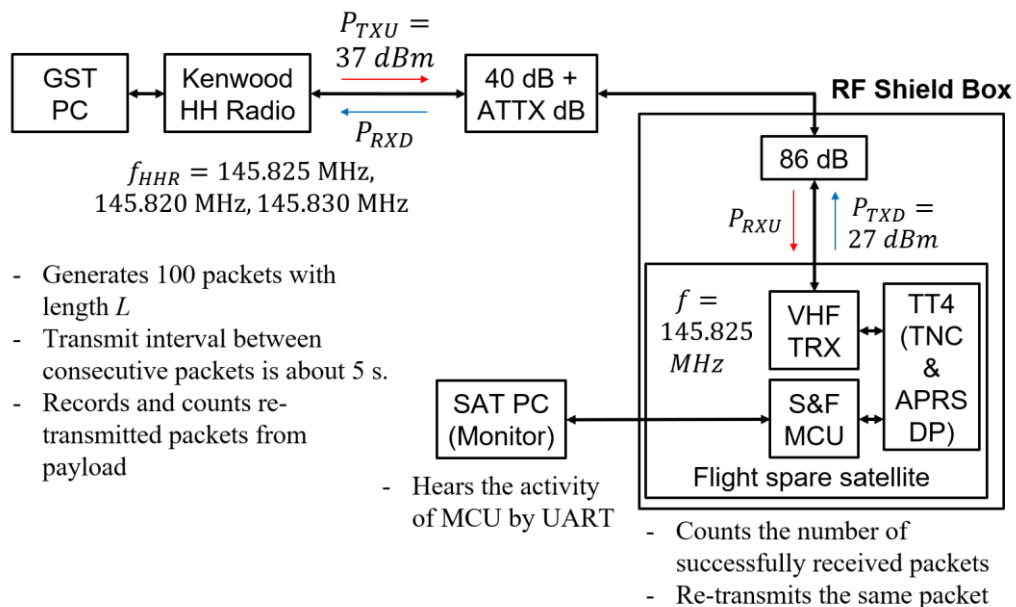


Figure 44. Cabled communication test setup to determine the optimum uplink and downlink receiver sensitivities: (top) diagram, (bottom) photo of actual setup

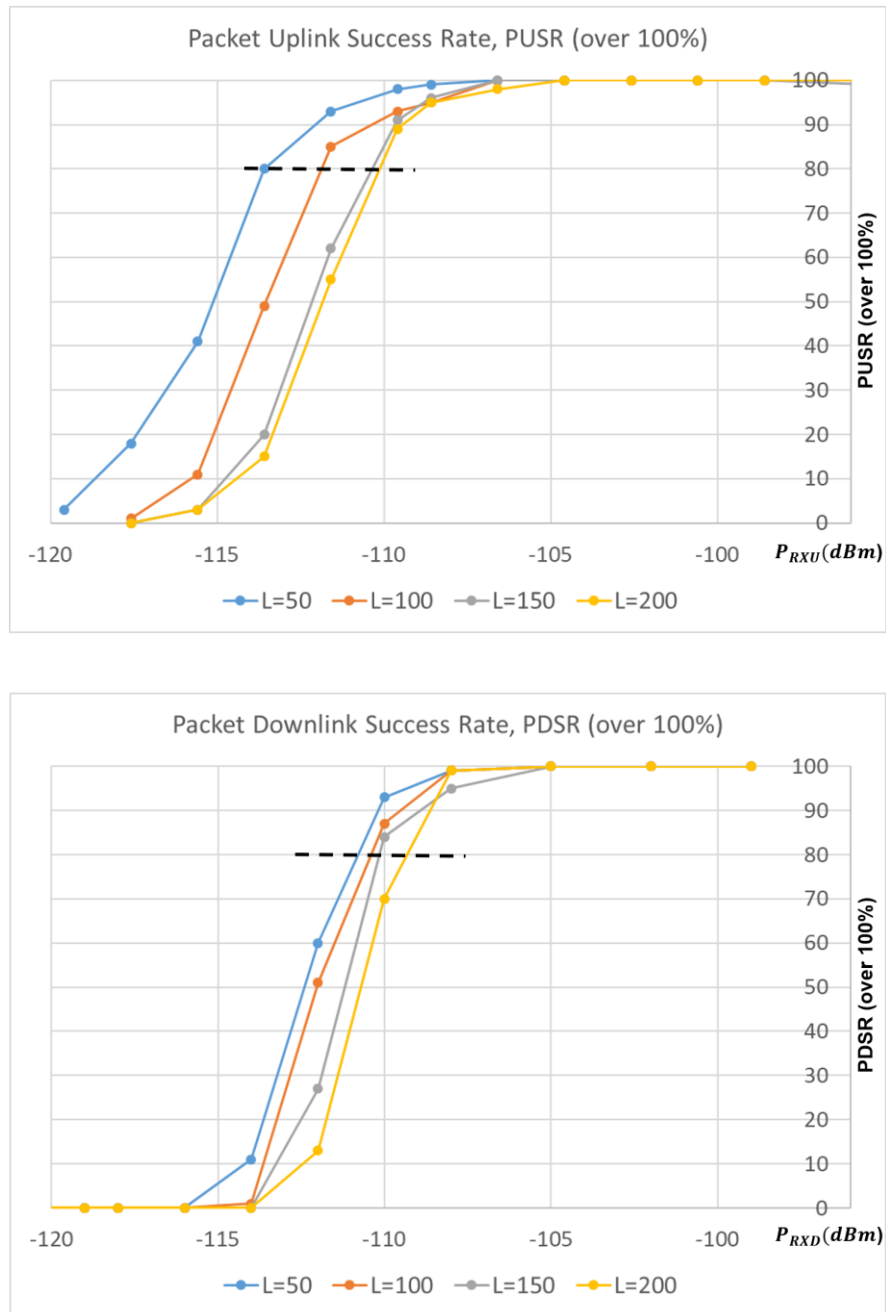


Figure 45. Measured uplink and downlink receiver sensitivities in cabled test condition (matched TX and RX frequencies, representing no Doppler shift)

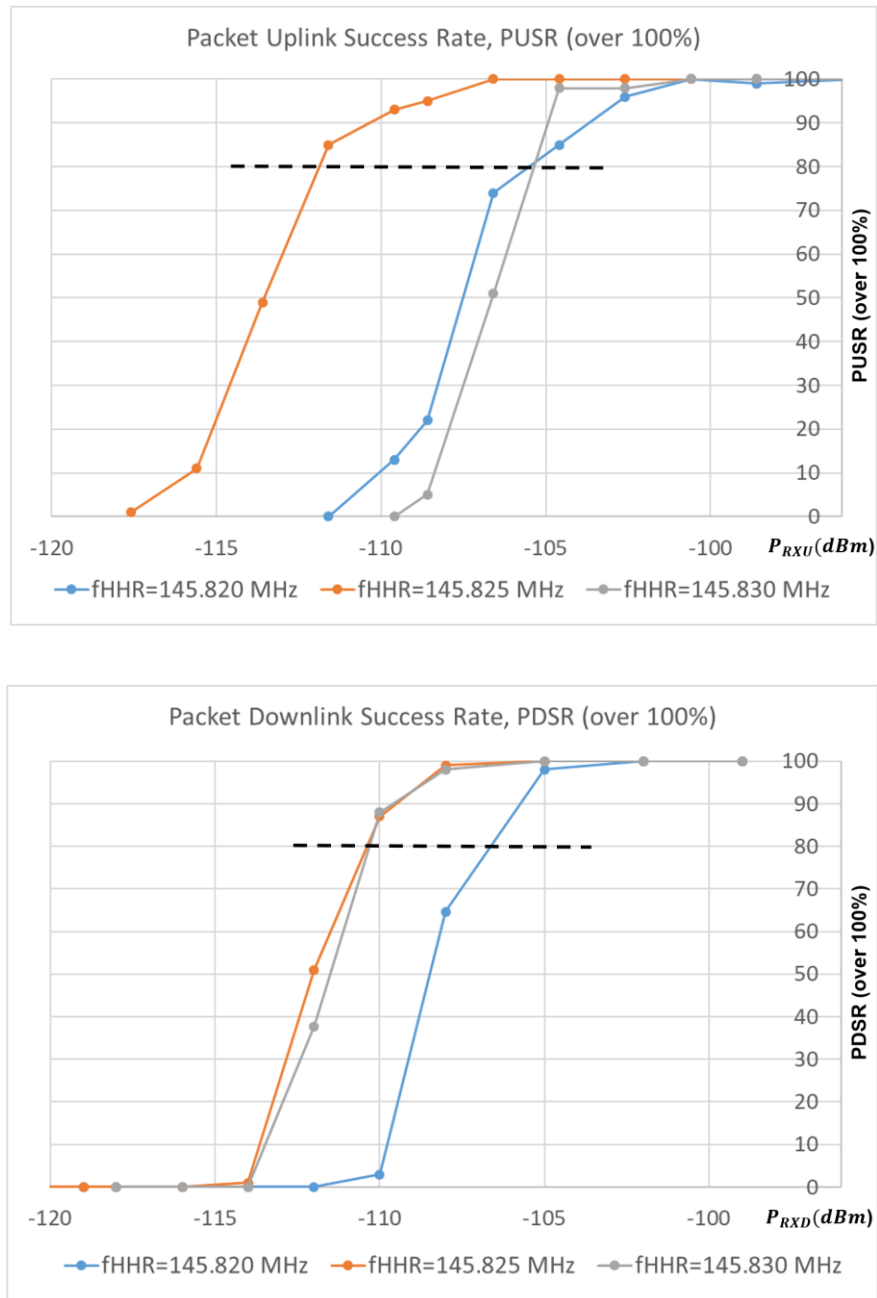


Figure 46. Measured uplink and downlink receiver sensitivities in cabled test condition (mismatched TX and RX frequencies, representing 5 kHz Doppler shift, L=100 bytes)

5.2 Locating EMI Sources in the Satellite

In one of the communication tests in anechoic chamber performed after satellite delivery, it was accidentally found that the noise floor measurement of spectrum analyzer (with satellite’s antenna connected) increased when the satellite was turned on compared when it was turned off. This observation led to a suspicion that the satellite might be emitting electromagnetic interference (EMI). To locate the EMI sources in the satellite, we probed different parts of the satellite and boards using a small loop antenna connected to a spectrum analyzer for EMI signal detection. The test setup is shown in Figure 47. The test points and corresponding power spectral density (PSD) measurements are given in Table 13. This test demonstrated that areas near some inductors of the switching power supplies (on the OBC/EPS board), a

level converter IC chip in mission board and power pins in the 50-pin connector (GND and SUP_5V routes) were emitting significantly higher EMI levels compared to other parts of the board and the satellite.

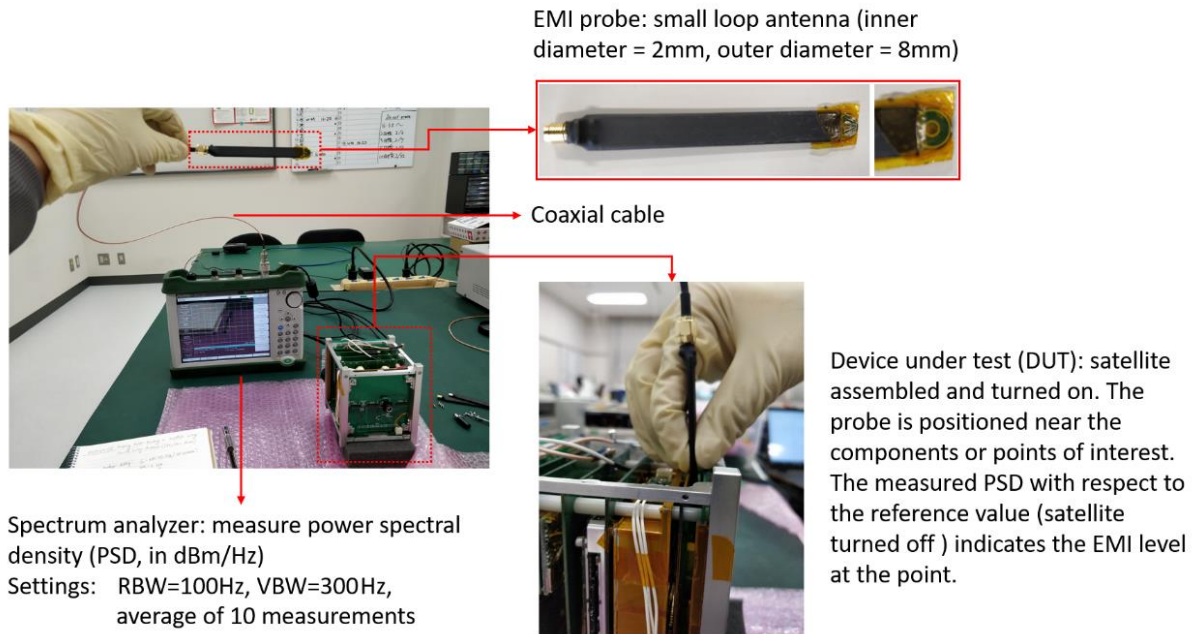


Figure 47. Test setup for locating the EMI-emitting sources in the satellite

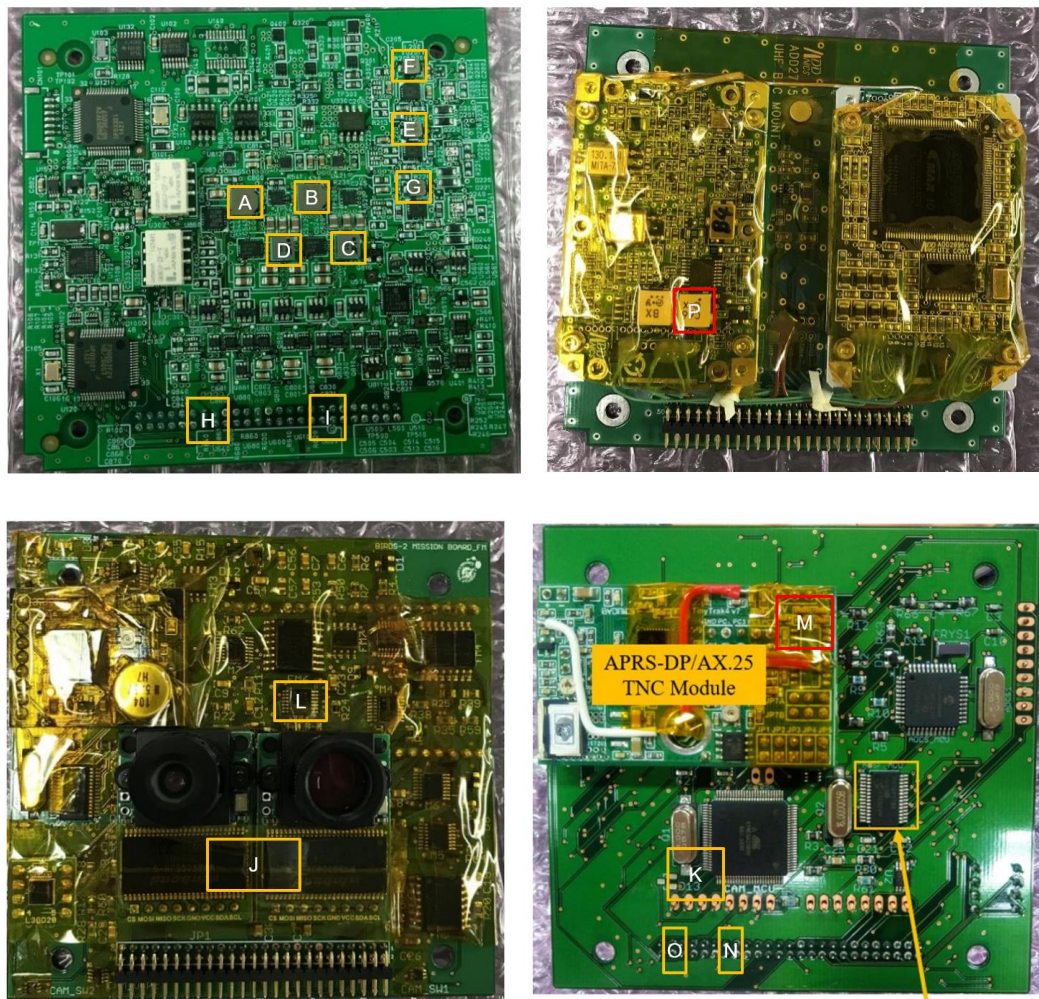


Figure 48. Some test points for determining EMI sources in the satellite

Table 13. EMI sources determination test points and corresponding PSD measurements

Component/Part	Label	PSD in dBm/Hz at 145.825 MHz (increase from D_{VREF} in dB)
L540 – inductor of buck-boost converter for FMR5V	A	-151 (+3)
L520 – inductor of buck-boost converter for SUP_5V0 (supplying Addnics TRX)	B	-139 (+15)
L510 – inductor of buck-boost converter for OBC3.3 (supplying OBC)	C	-135 (+19)
L500 – inductor of buck-boost converter for GPS3.3 and SUP_3.3 (MCUs and GPS)	D	-146 (+8)
L220 – inductor of BCR for PWR_SCY	E	D_{VREF} (0)
L200 – inductor of BCR for PWR_SCZ	F	D_{VREF} (0)
L240 – inductor of BCR for PWR_SCX	G	D_{VREF} (0)
Near 50-pin connector pins #13, 14, 15, 16 (GND and SUP_5V routes)	H	-142 (+12)
Near 50-pin connector pins #35 and 36 (GND_ROOT)	I	-142 (+12)
Near MCUs of CAM modules	J	-145 to -150 (+4 to +9)
Trace near CAM MCU (Atmega)	K	-141 to -146 (+8 to +13)
Near MAX3378 (3.3 V to 5 V converter)	L	-135 to -140 (+14 to +19)
Below power supply pin of TNC board	M	-151 (+3)
Near 50-pin connector pins #13, 14, 15, 16 (GND and SUP_5V routes)	N	-132 (+22)
Near 50-pin connector pins #4, 5 (MCU_3V3)	O	-142 (+12)
Lower part of transceiver left part	P	D_{VREF} (0)
Other parts of transceiver	Q	D_{VREF} (0)
Other pins of MB 50-pin connector	-	Generally about -147 (+7)

D_{VREF} = reference value (noise floor PSD of SA) = -154 ~ -155 dBm/Hz

5.3 Design Improvements Implemented on the BIRDS-2S CubeSat's APRS-DP/S&F Mission Payload

When the APRS-DP/S&F payload of the BIRDS-2 CubeSats were automatically activated about a week after deployment from the ISS, it was found that downlink communication was working. We confirmed this at Kyutech ground station by being able to receive and decode the APRS beacon messages regularly transmitted by the payload (except for MAYA-1, which worked only a few times). Several reports from amateur operators around the globe submitted through an online submission platform of BIRDS-2, as well as received packets forwarded to Internet servers, supported this result. However, full digipeating and two-way communication with users failed due to uplink communication problem. The payload receiver could not properly receive and decode packets from users. The causes of failure uncovered from ground communication tests are:

- 1) satellite's VHF monopole antenna has poor matching and low gain due to improper RF grounding;
- 2) satellite's OBC/EPS board emits electromagnetic interference (EMI) that is captured by the antenna, thereby increasing the noise floor of payload receiver.

To address these problems, we explored two main changes targeted to be implemented on the BIRDS-2S satellite (an educational satellite project at the University of the Philippines-Diliman using a modified BIRDS-2 CubeSat design):

- 1) To minimize the dependence on grounding, a new antenna board was designed, consisting of a UHF dipole antenna for communication with GS and another VHF dipole antenna for the APRS-DP/S&F payload;
- 2) To reduce the EMI captured by the antenna, we tried shielding the satellite's OBC/EPS board with copper plate connected to ground. However, since this was determined to be ineffective, in future work, we plan to use an EMI absorber and shielding sheet commercially available.

The drawing and photos of the new antenna design for BIRDS-2S CubeSat are given in Figure 49, consisting of UHF and VHF dipole antenna elements that are purposefully oriented perpendicular to each other. Due to space constraint on the antenna board, the two respective elements of both dipole antennas could not be positioned directly beside each other. Thus, as shown in the antenna board layout drawing on Figure 40, they are fed by striplines routed on the second layer of the board through pads that are accessible on the top and bottom layers. A jumper wire is attached to each element – one end of jumper wire is tightened by screw to the element while the other end is inserted into and soldered the pad on the back side of the board. (Note: the actual EM board in Figure 49 slightly differs from the PCB layout drawing on Figure 50, in which we adopted some modifications). Each stripline leads to the balanced input of either VHF or UHF balun. The unbalanced output of each balun is connected to a low-pass type L-matching network, which in turn is connected to a connector (SMA for UHF and MMCX for VHF) to which a cable going to respective transceiver will be connected. Due to limitation on available space, only the striplines

of UHF dipole could be made equally long (which is more sensitive to phase offset than those of the VHF dipole).

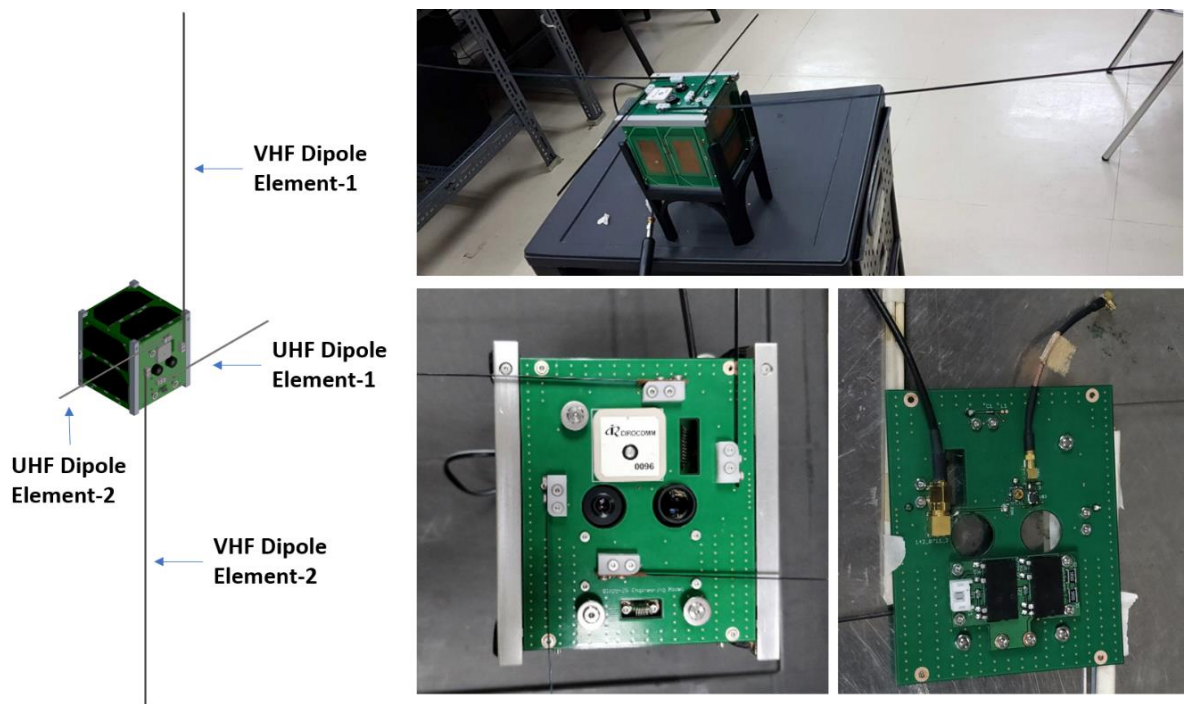


Figure 49. *New antenna design for BIRDS-2S CubeSat consisting of VHF and UHF dipole antennas: drawing (left), photos of actually implemented antennas for engineering model (right)*

To reduce the EMI captured by the antenna, copper plates were attached to the front and back sides of the satellite's OBC/EPS board using Kapton tape, as shown in Figure 51. The copper plates were placed on a portion of the board in a way that would cover the inductors of switching power supplies and were electrically connected to the ground pins of the board by soldering jumper wires. In terms of electrical properties, copper and aluminum are practically the same for this usage. In terms of density, copper is about 3-4 times the density of aluminum, so for the same volume, copper plate will be 3-4 times heavier. However, only small volume is required, the total mass or weight is not a big concern. The main reason for choosing copper plate in BIRDS-2S (over aluminum plate in BIRDS-4) is that it is much easier to solder it to the ground using a normal wire. In BIRDS-4, a mechanical way was needed to ensure aluminum plate was firmly and electrically connected to a wire soldered to the ground. To evaluate the effectiveness of the copper shield, a slightly different procedure was done using the satellite's own VHF antenna to directly measure the captured EMI, and this is described in Section 5.8.

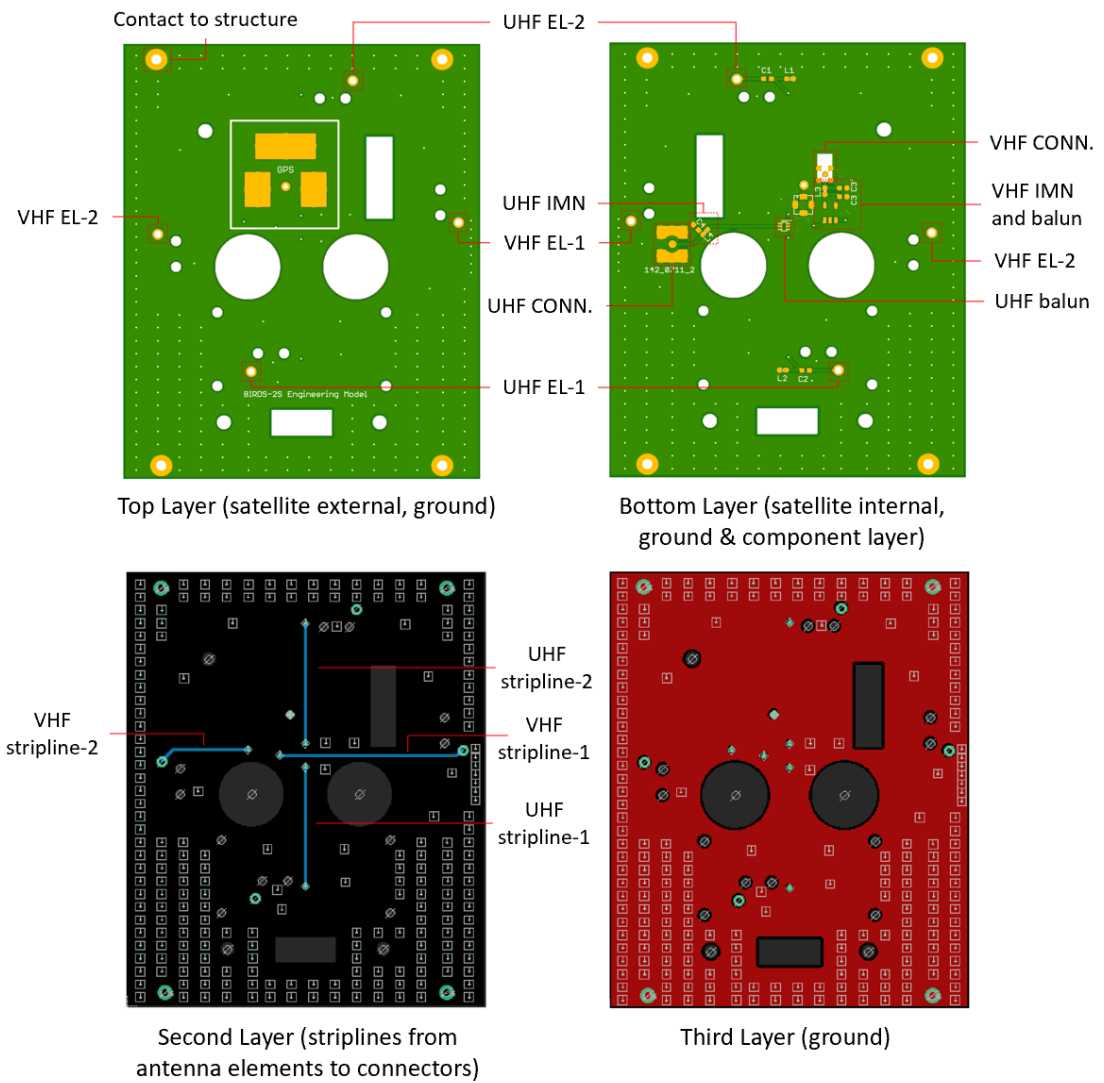


Figure 50. PCB layout of the four-layer antenna board for the BIRDS-2S CubeSat

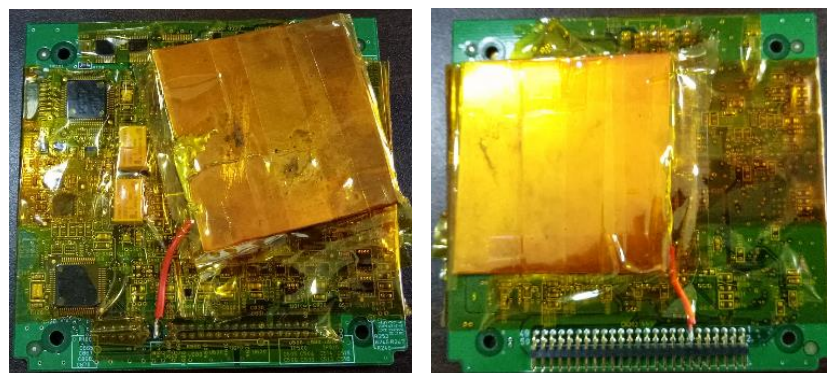


Figure 51. Photo of copper plate shielding on the OBC/EPS board of BIRDS-2S satellite: front side (left), back side (right)

5.4 Design Improvements Implemented on the BIRDS-4 CubeSat's APRS-DP/SF-WARD Mission Payload

The design modifications implemented on BIRDS-4 APRS-DP/SF-WARD mission payload are like that of BIRDS-2S. There are two slight differences, though. First, instead of using the already assembled product for TT4, a kit version was used so that the components could be soldered directly on the mission board (instead of using an adaptor board, which was done in BIRDS-2 and BIRDS-2S). Second, the orientation between UHF and VHF dipole antenna elements are different: perpendicular in BIRDS-2S and non-perpendicular in BIRDS-4. A perpendicular arrangement is the most ideal, but it was not possible to implement in BIRDS-4 due to space constraint (other parts need to be put on the board such as perovskite solar cell). Also, the UHF antenna elements' feed points are beside each other so they are connected to UHF balun without stripline. In addition to these two differences, the BIRDS-4 satellite has a modified OBC/EPS board design and it implemented an aluminum plate shielding. Figures 52 and 53 show BIRDS-4 CubeSat's APRS-DP/SFWARD mission payload and antenna design, respectively. As mentioned above, the OBC/EPS board of BIRDS-4 CubeSat was covered with an aluminum plate shielding to reduce the possible EMI noise (see Figure 52, lower).

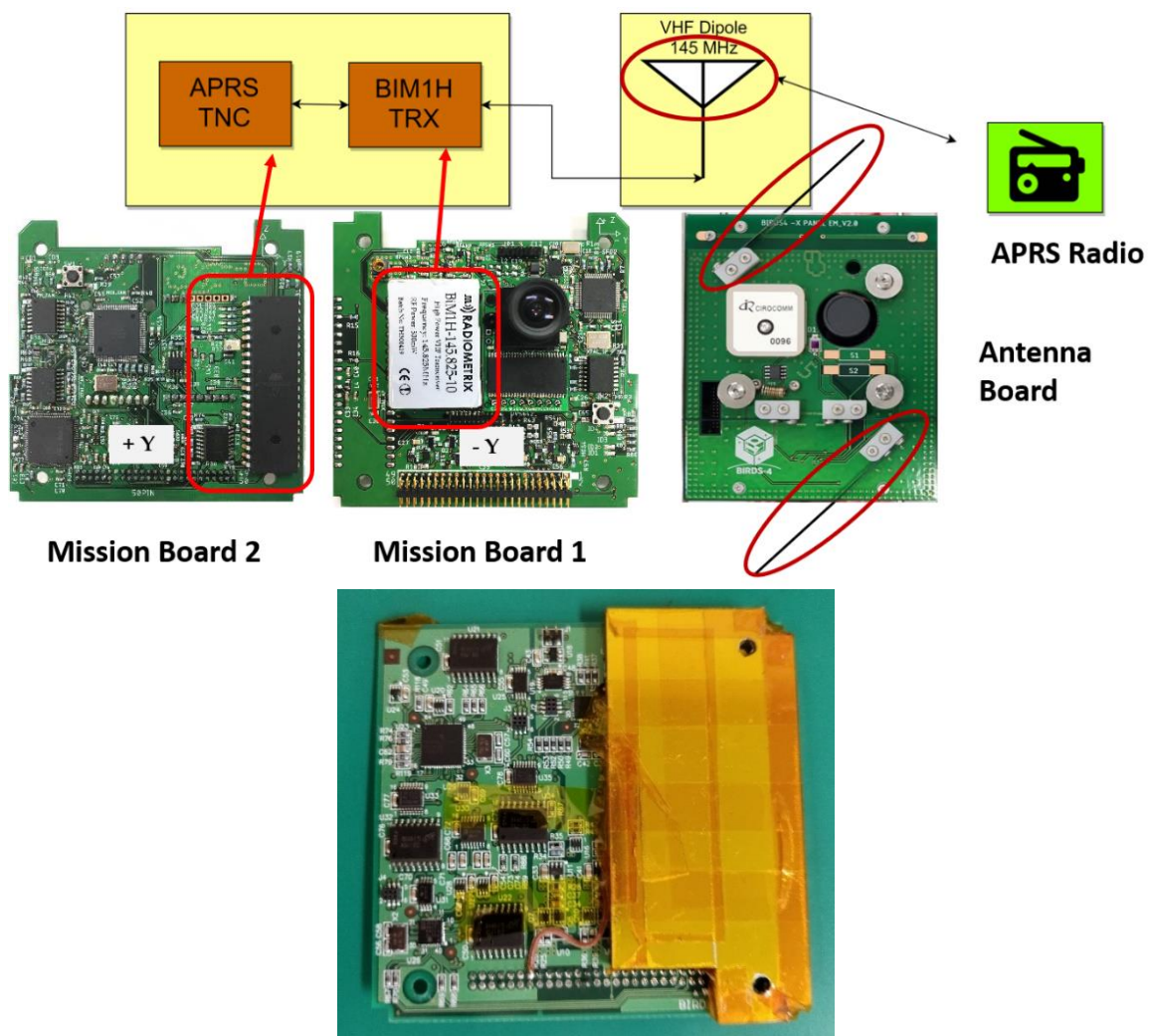


Figure 52. BIRDS-4 CubeSat's APRS-DP/SFWARD mission payload (top) and aluminum plate shielding method employed for BIRDS-4 OBC/EPS board (bottom)

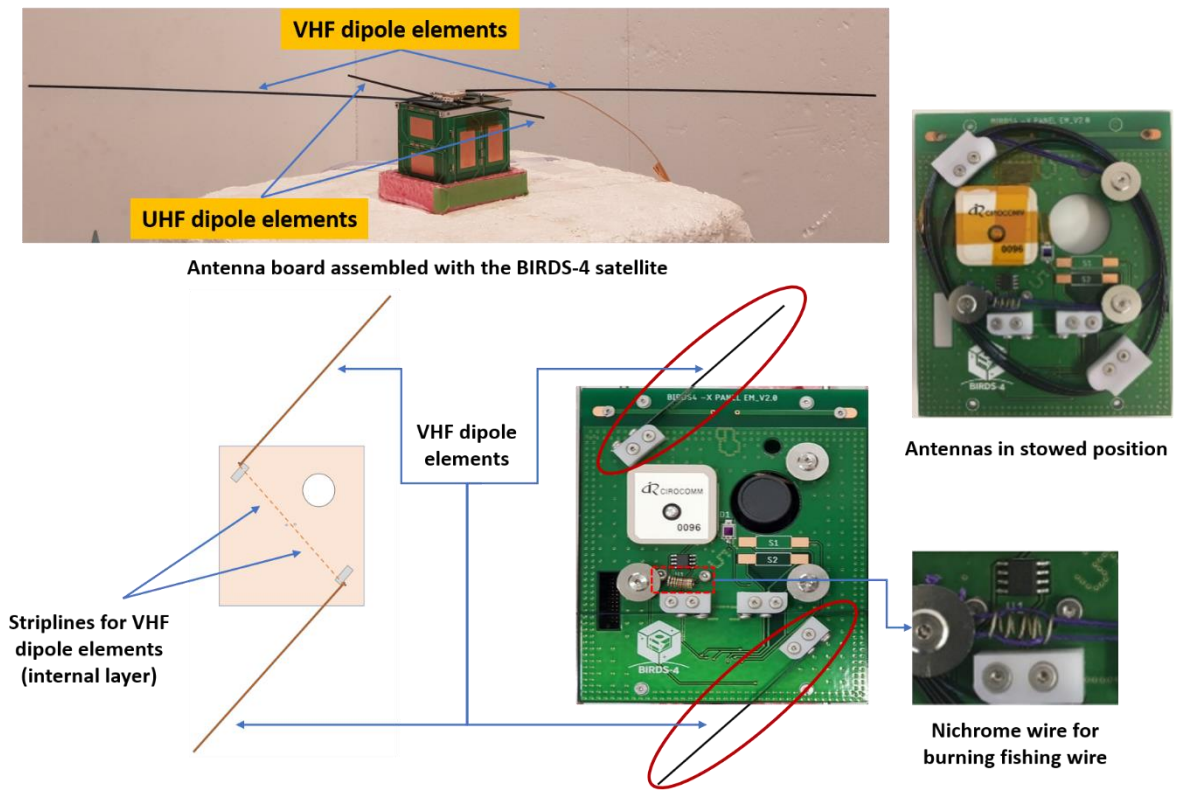


Figure 53. BIRDS-4 CubeSat's VHF dipole antenna for the APRS-DP/SFWARD payload

5.5 Antenna Reflection Coefficient Measurement and Tuning

The previous approach of measuring the antenna's reflection coefficient (S_{11}) using a VNA involved disconnecting the MMCX male connector of VHF cable from the MMCX female connector on the VHF transceiver (TRX) board (refer to Figure 17 bottom left) and connecting it to the VNA probe. This produced inaccurate measurement during BIRDS-2 antenna board testing because the VHF TRX board's ground would be part of the satellite's overall RF grounding in the real operation condition. To measure S_{11} more accurately, this time for the BIRDS-2S antenna board, we utilized a VHF TRX test board that is similar to the VHF TRX board but with another MMCX connector mounted at the point where the BIM1H transceiver's RF pin would be soldered (note: VHF TRX not mounted on the test board).

The test diagram is shown in Figure 55, wherein Z_m is the measured impedance just at the point representing the RF port of the transceiver. This enabled us to measure the S_{11} effectively at the transceiver's RF port, with the VNA substituting for the transceiver in the test. Also, the VNA was calibrated at the end of the probe cable. A photo of the actual measurement setup for the case of the BIRDS-2S antenna board is shown in Figure 54.

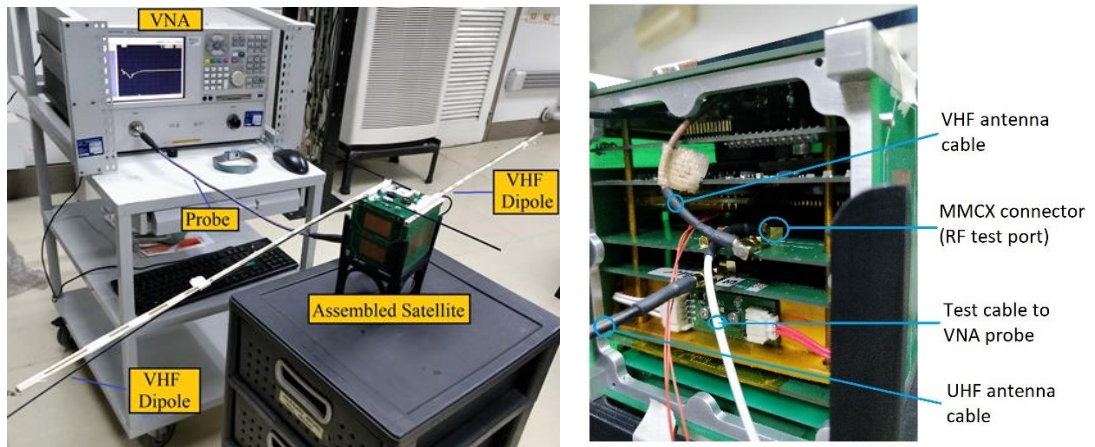


Figure 54. Actual setup for antenna S11 measurement and tuning

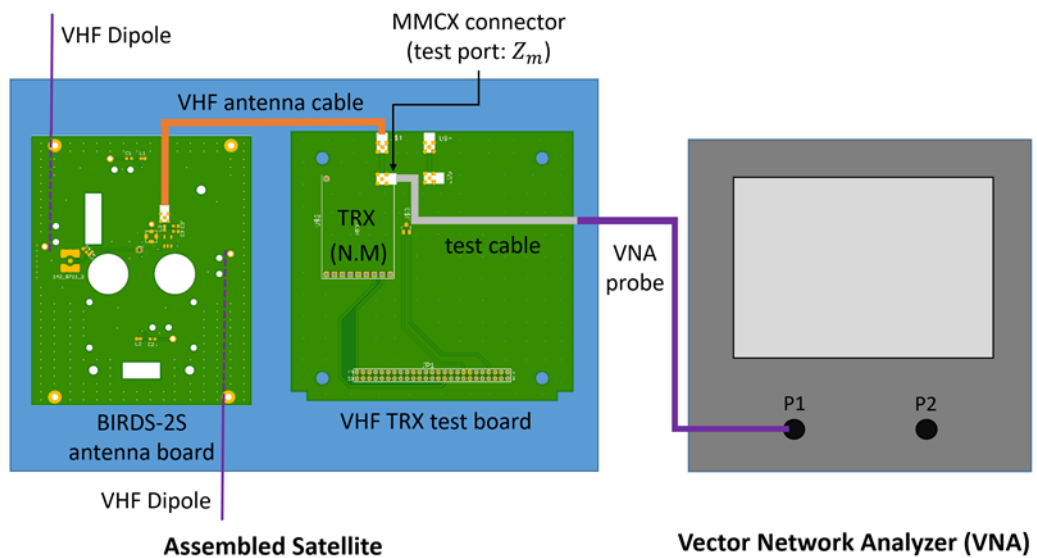


Figure 55. Setup diagram for antenna S11 measurement and tuning

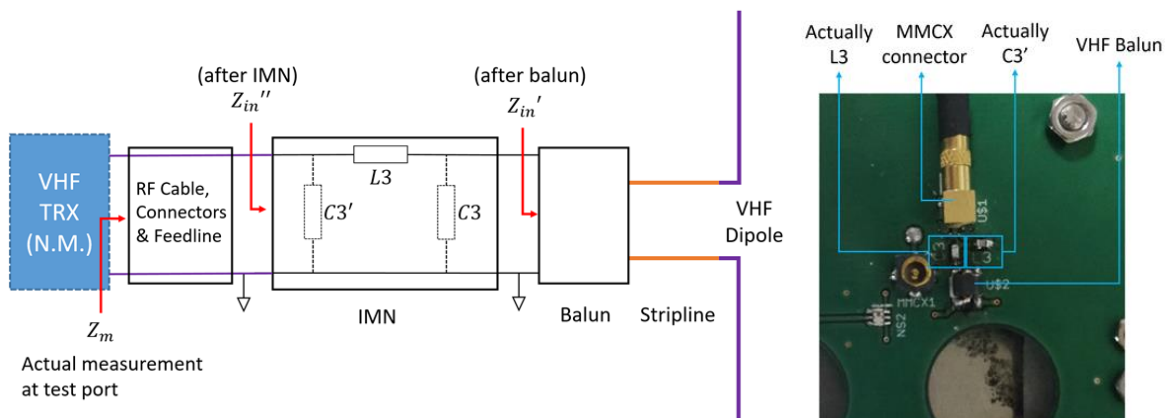


Figure 56. Circuit representation of the BIRDS-2S VHF dipole antenna parts and measurement setup (left) with a closer view of the actual antenna circuit implemented (right)

To better explain the antenna measurement, tuning and matching procedure, a circuit representation is provided in Figure 56 along with the actual circuit mounted on the antenna board. Tuning of the BIRDS-2S VHF antenna involved two steps. The first step entailed gradually cutting the antenna elements, starting from 65 cm on each element, until finding the length with maximum resistance R_m at 145.825 MHz. All

impedance measurements are done only for Z_m because it was difficult to perform direct measurements of Z'_{in} (impedance after the balun) and Z''_{in} (impedance after the matching network). This was done without the impedance matching network (IMN) components connected (i.e., with $L3$ pins shorted and $C3/C3'$ pins left open). For every reduced length, the center frequency, reflection coefficient (S11), real and imaginary components of input impedance $Z_m = R_m + jX_m$ at 145.825 MHz were recorded. As the length was reduced, the center frequency increased and R_m at 145.825 MHz increased, but only until a length 52 cm, where a maximum $R_m = 61 \Omega$ was obtained. The Z_m at 145.825 MHz was equal to $61 - j45 \Omega$ but the center frequency was lower than 145.825 MHz at this length.

The second step required computing the values of IMN components and soldering them on the board. However, since we were left with a length of 50 cm (we cut 2 cm. more from 52 cm before realizing it was the best length) with a $Z_m = 54.2 - j25.3 \Omega$ at 145.825 MHz, the values of IMN components were calculated for this length. The $L3$ and $C3$ obtained were 30.88 nH and 1.64 pF, respectively, but the actual components used were 33 nH and 1.8 pF, respectively.

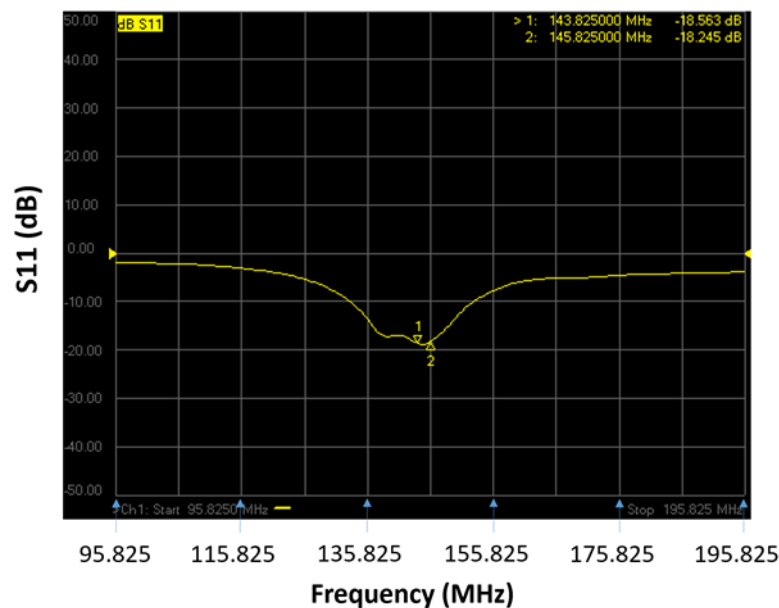


Figure 57. Measured S11 of the BIRDS-2S VHF dipole antenna after tuning

The 1.8 pF capacitor was mistakenly mounted on $C3'$ position. Nonetheless, since the calculated inductor and capacitor impedances at 145.825 MHz were $j30.2 \Omega$ and $-j606.3 \Omega$, respectively, the transformed impedance was expected to be $54.6 + j0.1 \Omega$. Thus, the supposed effect was simply to almost eliminate the reactive part and leaving a real part that would result in a very good S11 (< -20 dB). However, we actually obtained a $Z_m = 67.7 - j17.0 \Omega$ and $S11 = -13.9$ dB, which implies that the RF cable between antenna board and VHF TRX board and the feedline can change the impedance so that Z''_{in} and Z_m are actually different. Since our goal was to effectively match at the VHF TRX's RF port, we adjusted $L3$ and $C3'$ values and slightly reduced the antenna length to improve the S11. Finally, with 49.5 cm antenna length, $L3 = 22$ nH and $C3' = 1.5$ pF, we obtained $Z_m = 57.9 - j12.2 \Omega$ and $S11 = -18.2$ dB at 145.825 MHz, which are good enough. The resulting S11 plot is shown in Figure 57.

5.6 Antenna Radiation Pattern Test

Radiation pattern and gain measurement of BIRDS-2 antenna board was conducted during BIRDS-2 development. However, the data were found later to be unreliable because of the following reasons: (1) the BIRDS-2 satellite, with mounted antenna board as the antenna-under-test (AUT), acted in receive mode, and in order to measure the received power by the antenna, the VHF antenna cable had to be disconnected from the VHF TRX board, hence this does not represent the realistic grounding condition (important aspect especially for monopole antenna); (2) the internal 10 dB attenuator of dipole antenna used as reference antenna was overlooked, so in the calculation of gain, the resulting values were 10 dB higher than the actual values; (3) there was not sufficient distance inside the anechoic chamber in Kyutech to achieve far-field condition for the VHF antenna case, so the measurements were probably still in the near field to far field transition region.

Antenna radiation pattern measurement was conducted again at the UPD's newly established full anechoic chamber facility (FAC) that utilizes a state-of-the-art near-field-to-far-field transformation technology (i.e., near-field measurements are transformed into far-field radiation pattern data, so far-field distance is not necessary). Also, as previously mentioned, we utilized a VHF TRX test board in this testing with another MMCX connector mounted at the point where the BIM1H transceiver's RF pin would be soldered. This allowed us to measure the effective gain that would be seen exactly at the transceiver's RF port. For direct comparison, radiation pattern measurement was performed on both BIRDS-2 antenna board and BIRDS-2S antenna board.

Figure 58 shows the actual radiation pattern measurement setup. On one side, the AUT (antenna under test, which refers to the commercial dipole antenna used as reference, or BIRDS-2 antenna or BIRDS-2S antenna) was attached to an L-bracket positioner and on the other side, the probe antenna (yagi) was fixed to a stand. The probe antenna and the AUT were connected to RF cables leading to the two RF ports of the VNA outside chamber, which measured the total attenuation coefficient (S_{21}) in terms of magnitude and phase. The system recorded the S_{21} values while rotating the positioner about the theta and phi axes with the probe antenna fixed in co-polarization (horizontal) position in the first scan. This step was repeated in the second scan with the probe antenna fixed in cross-polarization (vertical) position.

After scanning, the system applied a near-to-far-field transformation algorithm and provided the 3D far-field data in various elevation (EL) and azimuthal (AZ) planes defined with respect to the AUT. However, due to the blocking effect of absorbers on the positioner, the resulting far-field data was inaccurate in the region of the AUT facing toward the positioner. Therefore, five strategically selected initial AUT positions were tested (following the procedure just described here) and only the far-field data on the narrow region facing toward the probe (about 90°) was extracted for each position. Then, the data extracted from the five positions were concatenated to obtain the radiation patterns on the antenna's E-plane and H-plane. A simple averaging filter was applied near the concatenation points to smoothen out the plots. Gain comparison method was used to estimate the gain in various directions, hence the radiation pattern in dB.

The resulting radiation patterns are presented in Figures 59 and 60 (the +z and other axes are the same as defined in Figure 58). Both BIRDS-2 and BIRDS-2S VHF antennas exhibit an omnidirectional pattern on the H-plane (perpendicular to the antenna element) and have nulls on the E-plane in the directions where the antenna elements are pointing. From the plots, the gain of the BIRDS-2 VHF monopole antenna is about -3 dB while the gain of the BIRDS-2S VHF dipole antenna is about 0.5 dB (note that the reference dipole antenna gain was assumed to be only 1.2 dB). These results demonstrate better gain performance of the new BIRDS-2S antenna design over the previous BIRDS-2 antenna design.

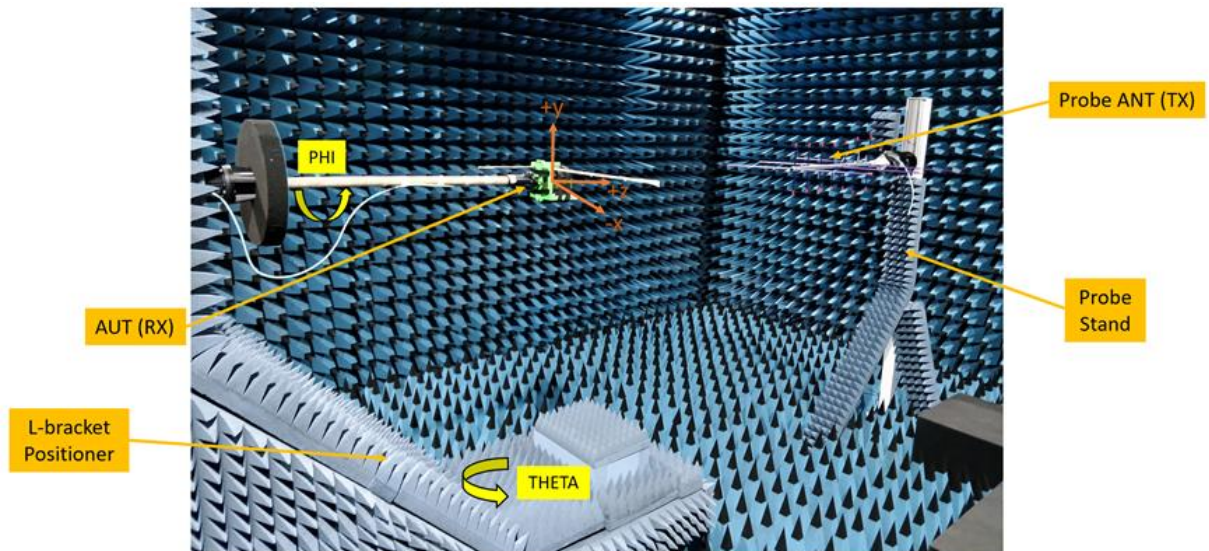


Figure 58. Antenna radiation pattern measurement setup at UPD's full-anechoic chamber (FAC) facility

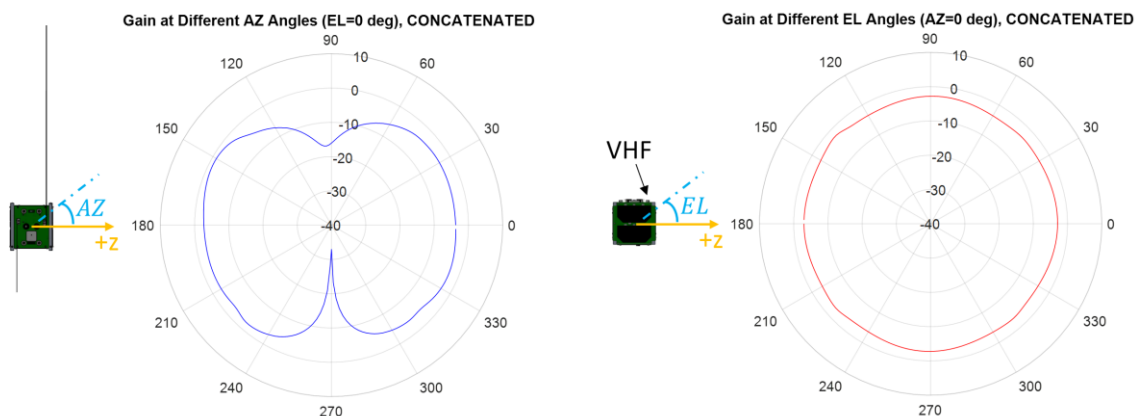


Figure 59. Radiation pattern of BIRDS-2 VHF monopole antenna on E-plane (left) and H-plane (right). Gain is shown in dB

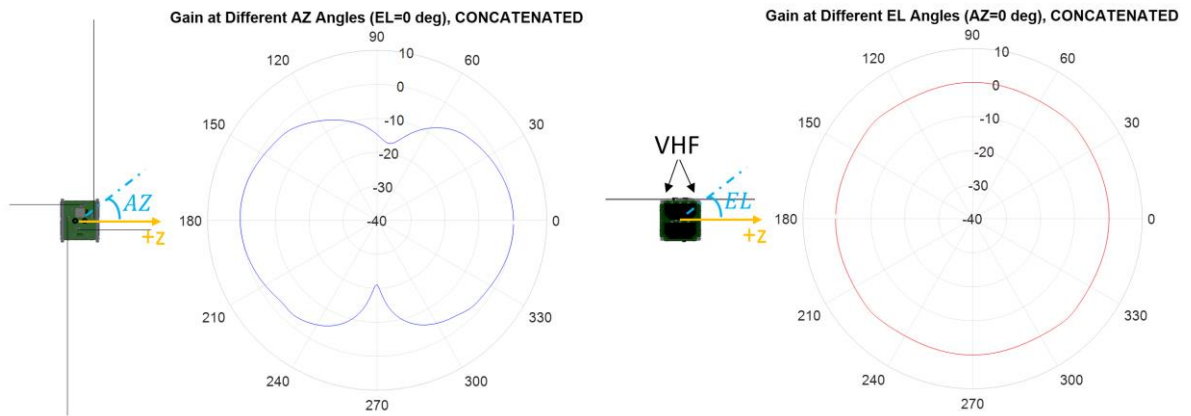


Figure 60. Radiation pattern of BIRDS-2S VHF dipole antenna on E-plane (left) and H-plane (right). Gain is shown in dB

5.7 Wireless Communication Tests Inside the Anechoic Chamber

To determine the actual payload receiver sensitivity in satellite-integrated and wireless condition, communication test between the satellite (with the payload and BIRDS-2S antenna board) and handheld radio (acting as an APRS user) was performed inside the FAC, with test setup shown in Figure 61. The distance between the satellite and dipole antenna (attached to attenuators and handheld radio outside the chamber) was confirmed to be about four meters. The received RF power at the payload receiver input was to be controlled by varying the attenuator value and then the uplink packet success rate would be recorded for each resulting receiver input power.

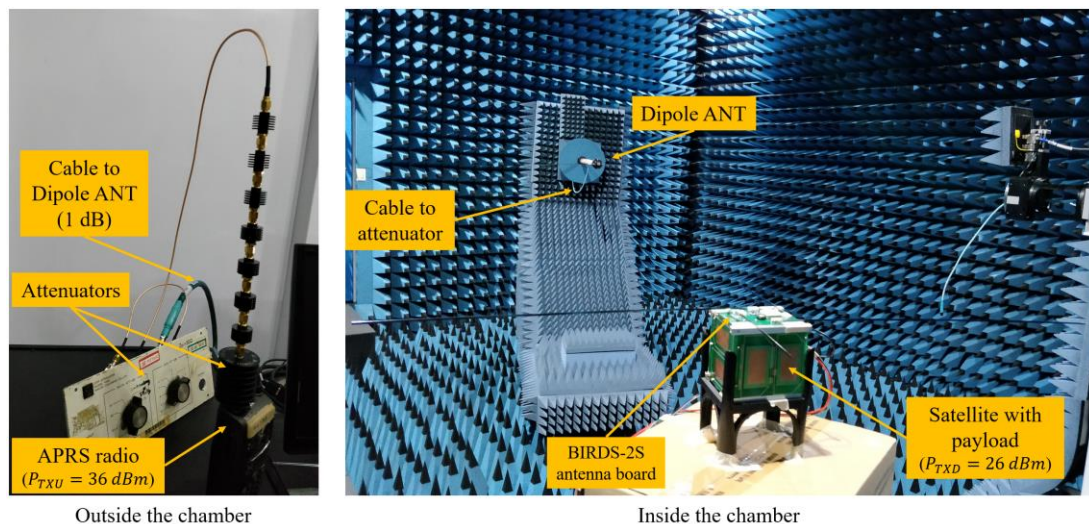


Figure 61. Wireless communication test setup at UPD FAC for testing the payload receiver sensitivity using BIRDS-2S dipole antenna (APRS-DP communication test)

Before communication test, the setup was carefully checked and calibrated by measuring the transmitters' output powers, cable losses and free space path loss, considering the antenna gains obtained from previous tests. When the attenuator was initially set to 40 dB, the measured received power from the satellite antenna (using spectrum analyzer) was -30 dBm. Considering radio output power of 36 dBm, 1 dB cable loss, 1.2 dB transmit antenna gain, and 0.5 dB receive antenna gain, the free-space path loss was estimated to be about 26.7 dB (compared to theoretical value of 27.8 dB, assuming far-field free-space

condition). Nonetheless, as part of the calibration procedure, the received power from the satellite antenna (equal to received power at the payload receiver input) was measured and recorded for each attenuator value. The measurement values confirmed that the receiver input power could be linearly (in dB) controlled by adjusting the attenuator value. To test the uplink communication, an APRS message (total packet length of about 50 bytes) was transmitted from the handheld radio.

The experimental results for uplink success rate are tabulated in Table 14, which suggests an uplink receiver sensitivity of about -79 dBm for a packet success rate of 70%. This wireless uplink receiver sensitivity result is 35 dB worse than the corresponding cabled test result of -114 dBm (refer to Figure 45). This worse payload receiver sensitivity is due to the radiated EMI from the satellite that is captured by the dipole antenna and goes into the receiver, thereby increasing the effective “noise” floor. The increased noise floor also raises by the same amount the required threshold input RF power for successful demodulation. This is explained further in the next section.

Table 14. Experimental values for APRS packet success rate at different payload receiver input power using BIRDS-2S dipole antenna (whole satellite assembled)

Attenuator Value (dB)	Expected Receiver Power (dBm)	Measured Receiver Power (dBm)	Uplink Packet Success Rate
40	-30	-30	~10/10 (full success)
65	-55	-54	~10/10 (full success)
90	-80	-79	7/10
93	-83	-82	2/10
96	-86	-86	fail
99	-89	-88	-
102	-92	-92	-
105	-95	-94	-
108	-98	-97	-

Prior to the wireless communication test at the UPD FAC described above, a similar test procedure had been conducted at Kyutech’s full anechoic chamber involving BIRDS-2 satellite flight spare but using a commercial dipole antenna. The test setup is shown in Figure 62. Instead of using the handheld radio to transmit an APRS message, it was used to transmit a 100-byte S&F packet for 100 trials. The results are given in Table 15, indicating a payload receiver sensitivity of about -77 dBm (for a 65% success rate) when using a commercial dipole antenna. This is comparable to the payload receiver sensitivity of -79 dBm (for a 50-byte APRS packet, 7/10 success rate) when using the BIRDS-2S dipole antenna in the UPD FAC communication test. This suggests roughly equal communication performance of the BIRDS-2S dipole antenna when benchmarked against the commercial dipole antenna.

Even earlier than this, a similar wireless communication test had been conducted at Kyutech’s full anechoic chamber using the same commercial dipole antenna but involving only the satellite’s mission board, VHF TRX, and an external power supply (other boards not connected). Also, the dipole antenna was positioned a little farther away from the satellite and instead of handheld radio, MTT4B transceiver was connected on the GST side. The test setup is shown in Figure 63 and the recorded average uplink success rate is given in Table 16. The S&F receiver sensitivity obtained in this test was about -95 dBm (for ~70% success rate), which is better than the other two tests with the whole satellite assembled. Although it is possible to say that the better sensitivity might be due to lower EMI, noting that other boards (e.g. OBC/EPS board) were not connected and the satellite was placed a little farther compared to the one in Figure 62, there are other significant differences between the test conditions in Figures 62 and 63. Thus, it is not right to assert this claim just by comparing the results of the tests in Figures 62 and 63. It would have been better if the same test as in Figure 62 was repeated but with only the satellite’s mission board, VHF TRX, and an external power supply (the same satellite distance and GST transmitter).

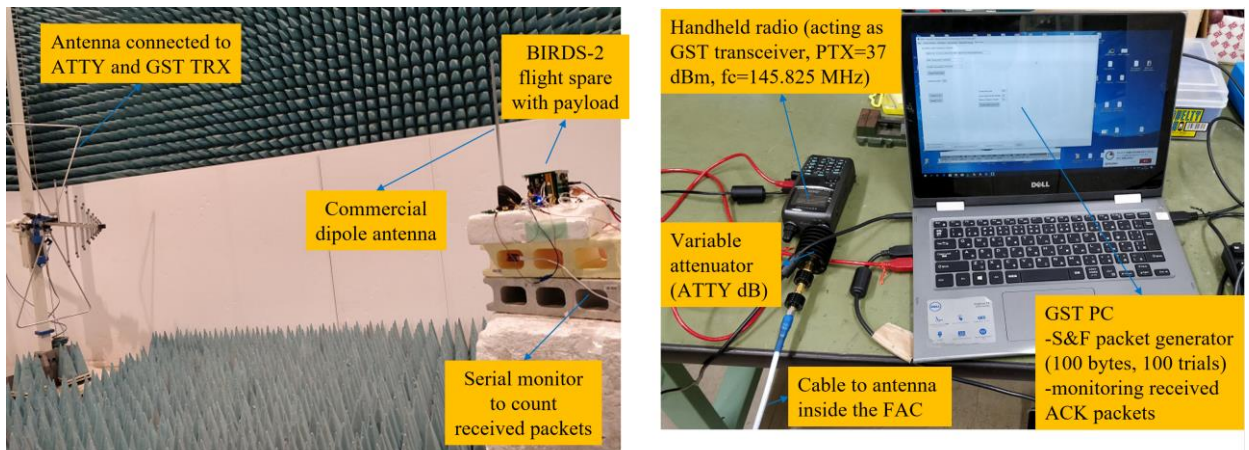


Figure 62. Wireless communication test setup at Kyutech FAC for testing the payload receiver sensitivity using a commercial dipole antenna (S&F communication test)

Table 15. Experimental values for S&F packet success rate at different payload receiver input power using a commercial dipole antenna (whole satellite assembled)

Attenuator Value (dB)	Received Power (dBm)	Uplink Packet Success Rate (out of 100 trials)
40	-32	-
70	-62	-
75	-67	100%
81	-73	98%
83	-75	96%
85	-77	65%
87	-79	39%

89	-81	12%
----	-----	-----

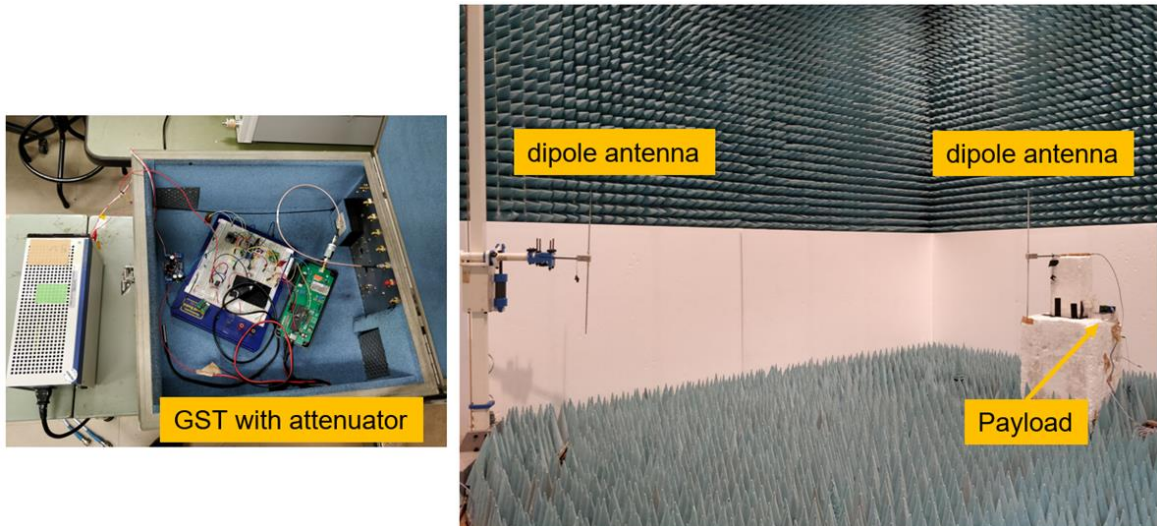
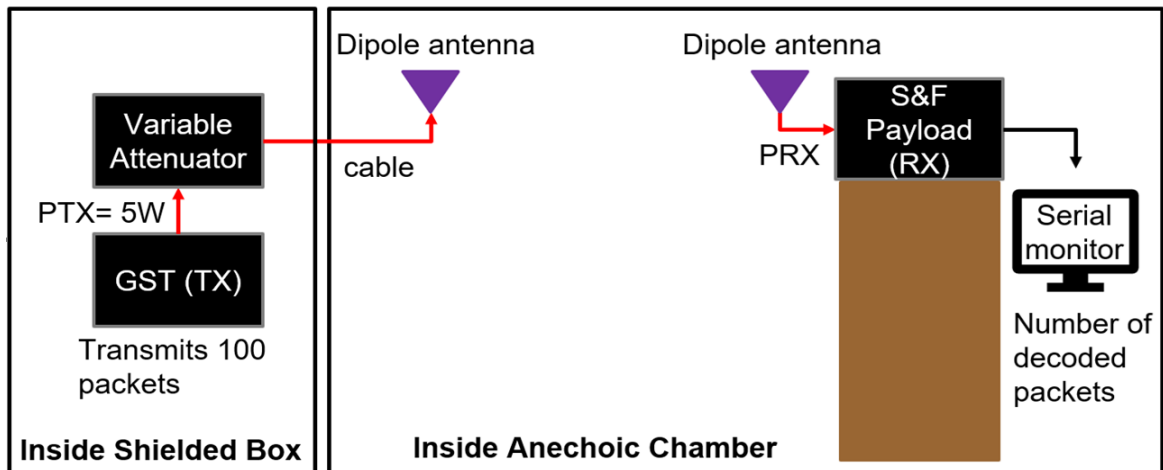


Figure 63. Wireless communication test setup at Kyutech FAC for testing the payload receiver sensitivity using a commercial dipole antenna (S&F communication test, with only mission board, VHF TRX and external power supply)

Table 16. Experimental values for S&F packet success rate at different payload receiver input power using a commercial dipole antenna (with only mission board, VHF TRX, and external power supply)

Received Power (dBm)	Average Packet Success Rate (over 100%)		
	L=50 bytes	L=100 bytes	L=150 bytes
-84	96.5	98.5	95
-87	98	96.5	95.3
-90	98	97	97
-94	85.5	86.5	92.3
-97	59	55	60
-101	8	3	18
-103	0.5	0	1

5.8 BIRDS-2S Payload Receiver Noise Level Measurements

The 35 dB worse uplink receiver sensitivity in wireless (antenna connected to satellite) test condition from its optimum value in cabled test condition can be accounted on the increased noise level in the payload receiver due to the radiated EMI from the satellite that is captured by the dipole antenna. To confirm this, we measured the received signal strength indicator (RSSI) voltage of the VHF TRX (BIM1H transceiver) in two conditions (RSSI voltage is an indicator of the receiver RF power estimate that is provided on an analog pin of BIM1H transceiver). In the first condition, the BIRDS-2S dipole antenna was disconnected from the transceiver RF port (open). Then, in the second condition, the dipole antenna was connected to the transceiver RF port. The test was conducted with the assembled BIRDS-2S satellite inside the anechoic chamber, as shown in Figure 64. The receiver input RF power level or the noise level in this test, could be estimated from the plot of the RSSI voltage vs RF level that is provided on BIM1H datasheet (which we had confirmed to be a good indicator of RF power level in a previous calibration test).

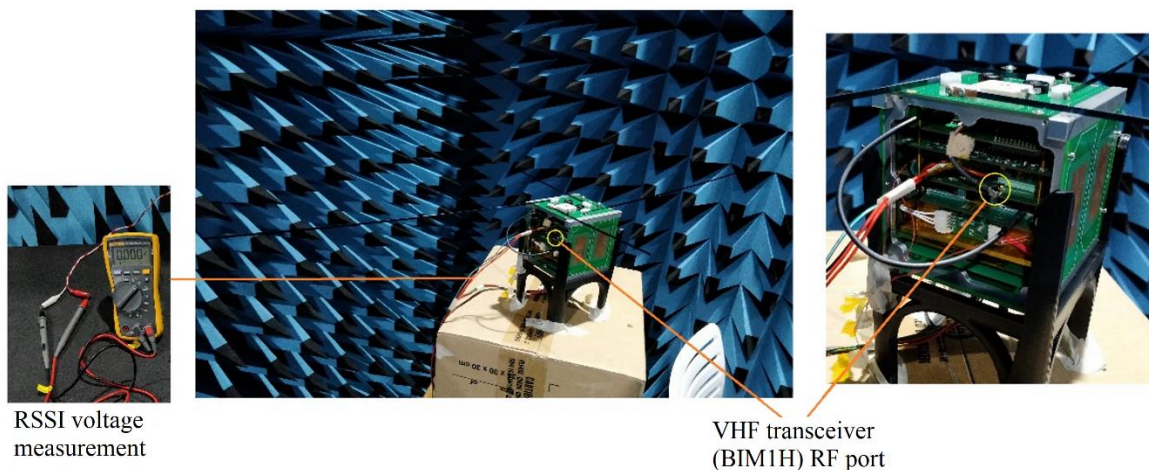


Figure 64. Test setup for detecting noise level increase in the payload receiver due to satellite-radiated EMI captured by the antenna. This was done inside UPD FAC.

The first condition represents the case wherein the satellite-radiated EMI is present but does not go into the receiver, hence the RSSI voltage indicates only the thermal noise level in the receiver in this condition. The second condition represents the case wherein the satellite-radiated EMI captured by the dipole antenna is transferred to the payload receiver, hence the RSSI voltage indicates the total noise level in the receiver (thermal noise and radiated EMI) in this condition. For comparison, the same procedure was performed with the BIRDS-2 monopole antenna. Finally, we put the copper plate shielding previously described to test its effectiveness and repeated the whole procedure.

The measurement results for the case before putting the copper plate shielding are provided in Table 17. With either antenna board integrated to the satellite but the VHF antenna disconnected from the VHF TRX port, an RSSI voltage of about 0.4 V was recorded, corresponding to an estimated noise level of -135 dBm. This value happens to be the minimum RF level detectable by the RSSI voltage (in the RSSI voltage vs RF level plot) and is not far from the theoretically estimated thermal noise power of about -130 dBm. Thus, it is very likely that thermal noise is the dominant noise present in the payload receiver when no

antenna is connected. When either VHF antenna is connected, however, one can clearly see a large increase in RSSI voltage and estimated RF level: 39 dB increase for the case of BIRDS-2S dipole antenna and 53 dB increase for the case of BIRDS-2 monopole antenna. Note that the 39 dB increase in receiver noise level for the BIRDS-2S dipole antenna case may account for the 35 dB worsening of uplink receiver sensitivity observed during the wireless communication test. The measurements for the case after putting the copper plate shielding are given in Table 18 and demonstrates that this shielding approach is not effective in attenuating the satellite-radiated EMI (in the case of the BIRDS-2S).

Table 17. BIRDS-2S payload receiver noise level from RSSI voltage without copper plate shielding

Condition	BIRDS-2 VHF Monopole Antenna (BIRDS-2 antenna board integrated)		BIRDS-2S VHF Dipole Antenna (BIRDS-2S antenna board integrated)	
	RSSI Voltage (V)	Estimated RX Power (dBm)	RSSI Voltage (V)	Estimated RX Power (dBm)
Satellite and payload on, BIM1H RF port open	0.40	-135	0.39	-135
Satellite and payload on, BIM1H RF port connected to antenna	1.55	-82	1.22	-96

Table 18. BIRDS-2S payload receiver noise level from RSSI voltage with copper plate shielding

Condition	BIRDS-2 VHF Monopole Antenna (BIRDS-2 antenna board integrated)		BIRDS-2S VHF Dipole Antenna (BIRDS-2S antenna board integrated)	
	RSSI Voltage (V)	Estimated RX Power (dBm)	RSSI Voltage (V)	Estimated RX Power (dBm)
Satellite and payload on, BIM1H RF port open	0.37	-135	0.38	-135
Satellite and payload on, BIM1H RF port connected to antenna	1.43	-87	1.22	-96

5.9 BIRDS-4 Payload Receiver Noise Level Measurements

As shown in Figure 65, the test setup for measuring the receiver noise level of BIRDS-4 payload is like that of BIRDS-2S but the test was done inside a cleanroom (instead of anechoic chamber). Also, due to unavailability of BIRDS-4’s own dipole antenna, a commercially available dipole antenna was used as substitute and attached to the satellite’s antenna board. The objective of this test is to measure the RSSI voltage of payload receiver – that would correspond to its noise power level – in different shielding

conditions with dipole antenna connected/disconnected to/from the payload RF port. The three OBC board shielding conditions were: (1) without shielding, (2) Aluminum shielding (Figure 52b), (3) commercial EMI shielding/absorber sheet (Figure 66). Before proceeding, calibration was performed by applying a CW signal output with settable power from a signal generator and recording the RSSI voltages for different input RF powers at 145.825 MHz.

The RSSI voltage measurements and their corresponding receiver noise level estimates are tabulated in Table 19. Without antenna connected to receiver input port, the RSSI voltage is 0.71 V for all three shielding conditions. This implies that without antenna, the receiver noise level is -135 dBm (or only the normal thermal noise was mainly present). When the antenna was connected, for all three shielding conditions, the RSSI voltage increased to about 1.47-1.49 V, corresponding to receiver noise level of -96 dBm to -93 dBm. Therefore, the results of this test demonstrated that in fact, like the case of BIRDS-2/BIRDS-2S satellite, receiver noise level is very low when no dipole antenna is connected to receiver port but receiver noise increases dramatically when dipole antenna is connected. Also, the increase in receiver noise level is neither affected nor mitigated by the two shielding methods. Therefore, all the shielding methods or configurations explored so far (copper plate shielding on BIRDS-2S, aluminum plate shielding on BIRDS-4, non-metallic EMI absorber/shielding sheet) were determined to be ineffective.

The test procedure described in this section was performed long after doing the long-range test for BIRDS-4 described in Section 5.10.

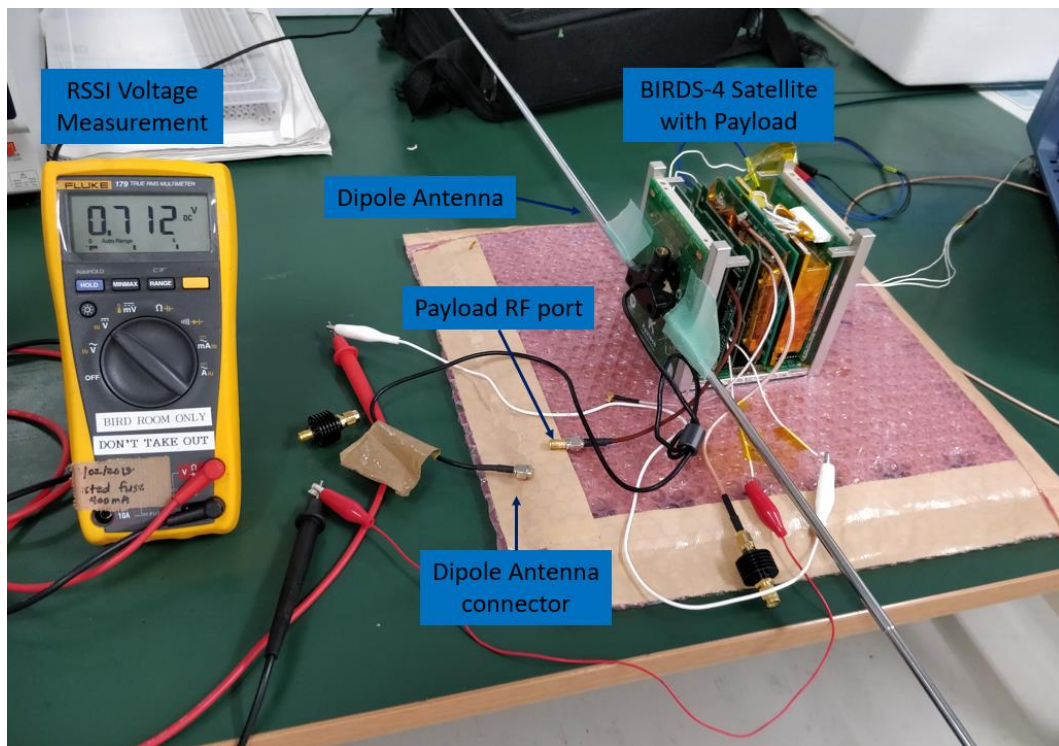


Figure 65. BIRDS-4 SFWARD payload receiver noise measurement by RSSI voltage



Figure 66. BIRDS-4 OBC board wrapped with commercially available EMI shielding/absorber sheet

Table 19. BIRDS-4 payload receiver noise level from RSSI voltage measurements under three shielding conditions

OBC Board Shielding Condition	Antenna disconnected		Antenna connected	
	RSSI Voltage (V)	Estimated RX Power (dBm)	RSSI Voltage (V)	Estimated RX Power (dBm)
Without shielding	0.71	-135	1.49	-93
With Aluminum shielding	0.71	-135	1.49	-93
With commercial EMI absorber/shielding sheet	0.71	-135	1.47	-96

5.10 BIRDS-4 Range Communication Test (LRT)

A long-range communication test (LRT) was conducted between a fully integrated BIRDS-4 EM satellite (with APRS-DP/S&F payload) and an APRS user radio (Kenwood TH-D72). The same test was repeated with a fully integrated BIRDS-4 FM satellite. A similar test will be conducted on the BIRDS-2S satellite after a better shielding approach is implemented. The objective of the LRT is to confirm the link budget in a test setup emulating ground-satellite distance. It is similar to that of the wireless test inside the FAC but since it is done in an outdoor environment, it has the following main differences: (a) the large distance between satellite and APRS user radio antennas ensures that the two sides communicate in very

far-field condition (much more than what could be achieved inside the FAC); (b) the channel between the two sides is not free-space so there are reflections and other propagation effects, but the lumped attenuation due to these could be determined during calibration procedure; (c) external devices in the vicinity (e.g., noise and interference sources) could impact the test, hence, the satellite is subjected to more noisy environment in this condition than inside an FAC or in space.

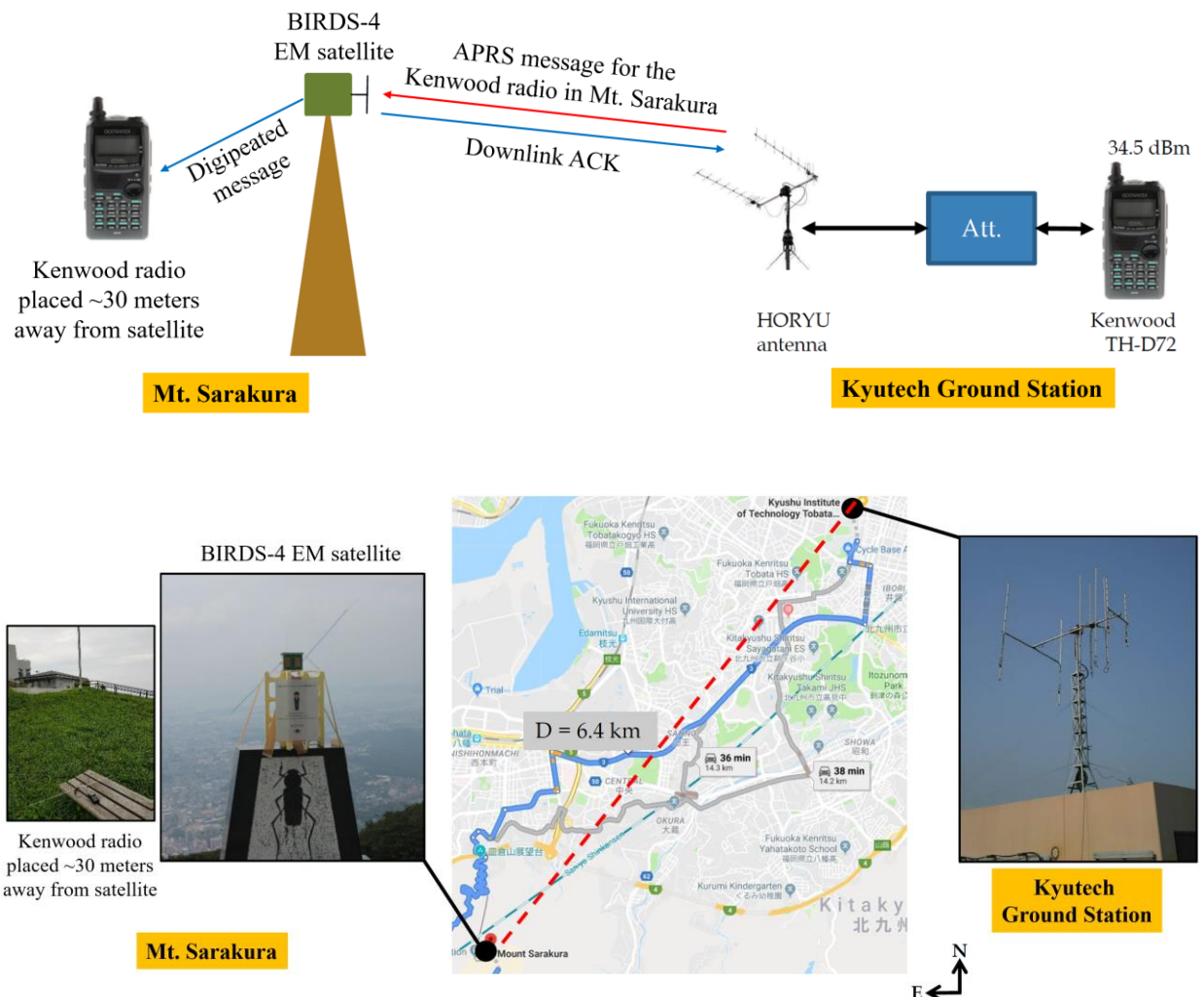


Figure 67. BIRDS-4 long-range communication test setup involving the BIRDS-4 EM satellite

The BIRDS-4 LRT setup is shown in Figure 67. The satellite and an APRS radio were placed in Mt. Sarakura that is located 6.4 km away from Kyutech. At Kyutech, another APRS radio with transmit power of 34.5 dBm was connected to the ground station’s yagi antenna with an attenuator in between. The attenuator value was gradually increased, and communication was tested for each attenuator value. In the LRT involving BIRDS-4 EM satellite, uplink success was achieved up to 130 dB effective attenuation (channel, antenna, cable, attenuator), implying a payload receiver sensitivity of about -95 dBm. On the other hand, a very close value of -96 dBm was obtained in the LRT involving BIRDS-4 FM satellite. This BIRDS-4 payload receiver sensitivity obtained in outdoor long-range wireless condition is 16-17 dB better than the BIRDS-2S payload receiver sensitivity (-79 dBm) obtained in wireless communication test inside the FAC. However, the BIRDS-4 payload receiver sensitivity of about -95 dBm obtained in long-range test does not quite make sense considering that the BIRDS-4 payload receiver noise floor obtained by RSSI

method (as discussed in Section 5.9) is about -93 dBm. This puts into question the validity of the BIRDS-4 receiver sensitivity result obtained in long-range test. At this point, the exact reason for obtaining better result is not certainly determined and it is better to perform the long-range test again. Also, it would have been better to perform long-range test with the BIRDS-2S satellite (this will be performed by the BIRDS-2S team in UPD).

5.11 Communication Link Budget Analysis

The link margin in uplink and downlink paths were calculated based on the parameters summarized in Table 20 for two cases of GS (GST or APRS user) antenna: (a) 16 dBi directive (cross-Yagi) antenna with pointing, and (b) 5.6 dBi omnidirectional antenna (“Eggbeater” antenna [27]) with fixed position and 120° beamwidth. Both GS antennas are circularly polarized. The main lobe of the omnidirectional antenna is assumed to be pointing upward (90° elevation) and so the GS antenna pointing error depends on satellite elevation. For the link margin calculations, we assumed the experimental uplink receiver sensitivity of -95 dBm (obtained from BIRDS-4 LRT) and downlink receiver sensitivity of -105 dBm (obtained from actual RF power measurements on regular beacon signals received from BIRDS-2 satellites).

Table 20. Parameters used in link margin calculation

Parameter	Value
Orbit altitude	400 km
Center frequency	145.825 MHz
GS transmit power (uplink)	Kenwood TH-D72 handheld radio: 5 W (37 dBm)
Satellite transmit power (downlink)	0.5 W (27 dBm)
GS antenna gain	directive: 16 dB (yagi antenna), omnidirectional: 5.6 dB (Eggbeater antenna)
Cable loss at GS side	2 dB
GS antenna pointing error, APE_{GS}	directive antenna (with pointing): 5°, omnidirectional (fixed): $APE_{SC} = 90^\circ - \text{elevation}$
GS antenna pointing error loss (APE_{LGS})	directive antenna: 1 dB, omnidirectional antenna: $APE_{LGS} = -10\log(\cos(APE_{GS}))$
Polarization loss	3 dB
Atmospheric and ionospheric losses	1.8 dB
Satellite antenna pointing error loss (APE_{LSC})	3 dB
Satellite antenna gain & cable loss	0.5 dB

Free-space path loss (FSPL)	127.8 dB (at EL=90°) to 143.0 dB (at EL=0°)
Received power (dBm)	<u>Uplink</u>
	Omnidirectional: -118.2 (at EL=5°) to -94.5 (at EL=90°)
	Directive: -98.2 (at EL=5°) to -85.1 (at EL=90°)
	<u>Downlink</u>
	Omnidirectional: -128.0 (at EL=5°) to -104.5 (at EL=90°)
	Directive: -108.2 (at EL=5°) to -95.1 (at EL=90°)
Receiver sensitivity (dBm)	Uplink: -95 (payload receiver), Downlink: -105 (GS receiver)

The plots of the uplink and downlink margins vs elevation angle are given in Figure 68, for the two GS antenna cases. Although the downlink transmit power is 10 dB lower than the uplink transmit power, the required minimum receiver power is 10 dB lower in downlink than in uplink. This is the reason why overall, the uplink margin and downlink margin plots for a given GS antenna appear the same. These plots indicate the required minimum elevation angles of 15° and 75° for the directive and omnidirectional GS antenna cases, respectively. Therefore, only amateur stations with 16 dB or higher gain circularly antennas can be expected to effectively communicate with the payload. The uplink margin may be improved once the satellite noise problem is more effectively addressed but the limited downlink transmit power will remain a bottleneck for the downlink margin.

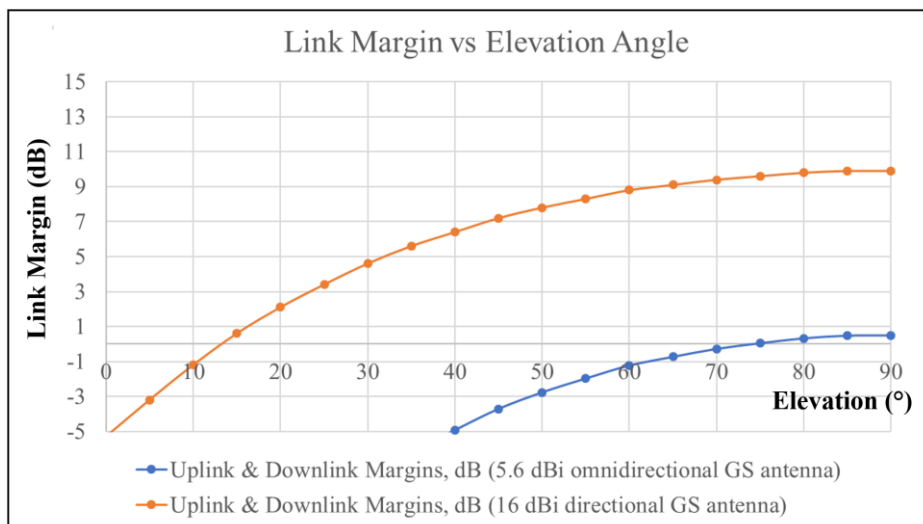


Figure 68. Uplink and downlink margins for the two GS antenna cases

5.12 Lessons Learned and Recommendations from Investigation on Communication Issues

From the investigation we conducted and our experiences in BIRDS-2 Project and succeeding BIRDS projects in the matter of communication design for our CubeSat-onboard amateur radio payload (i.e., the APRS-DP/S&F payload), we summarize the following lessons learned and recommendations:

1) Since the antenna characteristics (tuning, grounding, performance) and EMI/EMC aspects (coupling, grounding, shielding, etc.) are intricately related to one another, as well as to the whole satellite structural and electrical power design considerations, these aspects must be altogether examined and verified through practicable methods during the preliminary design phase of satellite development. As the parts are closely positioned inside a CubeSat, it is crucial to consider the potential EMI/EMC issues in the design of the whole satellite. For the case of BIRDS-2 Project, the design issues related to these aspects were overlooked and lately diagnosed (even beyond the development time), so we could not address them proactively. On hindsight, the BIRDS-2 CubeSat bus design was adopted from a previous design without careful consideration of these issues.

2) Optimum receiver sensitivity performance must be verified in transceiver unit level, first in a cabled condition and then in a wireless (antenna-connected) condition in the early phase of development, that is, before integrating with other satellite subsystems.

3) Also, during the early phase of development, antenna reflection coefficient (and tuning) and radiation pattern tests must be done with pre-existing or mock-up satellite structure and boards. Similarly, subsystem boards, such as EPS board, must be tested to check if they might contribute significant EMI levels, whether conducted or radiated type. In the case of BIRDS-2, we found out later by using small loop antenna that the switching inductors on the OBC/EPS board emit significantly higher EMI levels compared to other parts of the boards and the satellite.

4) Then, antenna and EMI/EMC designs must be verified as soon as possible through antenna performance and EMI/noise measurement tests with the fully integrated satellite (for example, during activities leading to CDR). Aside from design verification, this is also necessary to diagnose potential design problems and mechanisms previously unconsidered and to find ways to mitigate these issues (e.g., adding EMI absorbers or shielding, filtering, modify signal routing and grounding, etc.).

5) Antenna tuning, S11 and radiation pattern measurements should be done as close as possible to the real operational condition, that is, how the antenna will be connected to a cable, transceiver board, grounding, satellite, etc.

6) In terms of antenna design, if the space constraints allow, dipole antenna is recommended over monopole antenna as the former's tuning and performance characteristics are less vulnerable to grounding issues. From our own experience in BIRDS-2 antenna development, we found that a monopole antenna is highly sensitive to size and configuration of grounding, which is especially difficult to optimize in a 1U CubeSat due to limited space. Also, from our own measurement data, the antenna's susceptibility to

Nanosatellite S&F Communication Systems for Remote Data Collection Applications

satellite-radiated EMI (or the amount of EMI coupled to the antenna) seems to be intricately related the quality of grounding of a monopole antenna. While we could have modified the BIRDS-2 monopole antenna design to mitigate the grounding and EMI vulnerability issues, we think that a dipole antenna design is the more conservative and less risky design choice to begin with because in principle, its performance is independent of a ground plane, unlike monopole antenna. Still, even if one uses a dipole antenna, one must still consider (5) because the matching network on the antenna board is connected after the unbalanced side of the balun, so the actual impedance itself and the measurement may be affected by the grounding and the cable from the antenna board to the VHF TRX board.

7) Wireless communication test inside a full-anechoic chamber and long-range communication test – between the fully integrated satellite and a ground station or user radio – must be done as final confirmation of end-to-end performance and the link budget analysis.

Chapter 6: E-SSA-based Nanosatellite IoT/M2M Communication System Model and Signal Processing Algorithm

This chapter first describes the nanosatellite IoT/M2M communication model based on enhanced spread spectrum Aloha (E-SSA) and derives the mathematical definitions of packet loss rate (PLR), throughput (THR) and energy efficiency (EE) metrics. Then, it tackles the formulated baseband signal processing algorithm for E-SSA, including packet detection, channel estimation, demodulation and decoding.

6.1 Communication Scenario Overview

As illustrated in Figure 69, the communication scenario under investigation consists of K active ground sensor terminals (GSTs) in the satellite footprint during a short time window (i.e., several packet durations). Note that there may be other terminals in the same footprint but only the K terminals are sending data during the said time window. The K terminals independently and time-asynchronously transmit packets to the satellite that arrive at the receiver after each experiencing a different propagation channel. In notation, the received packet from a terminal k has a random time delay τ_k , carrier phase offset ϕ_k , amplitude A_k , frequency shift f_k and frequency (change) rate d_k . Terminals transmit at a common frequency channel centered at $f_c = 402$ MHz but because only baseband representation is considered, it is assumed f_c becomes 0 after signal has been converted to baseband. The packets add up and combine with a complex additive white Gaussian noise (AWGN).

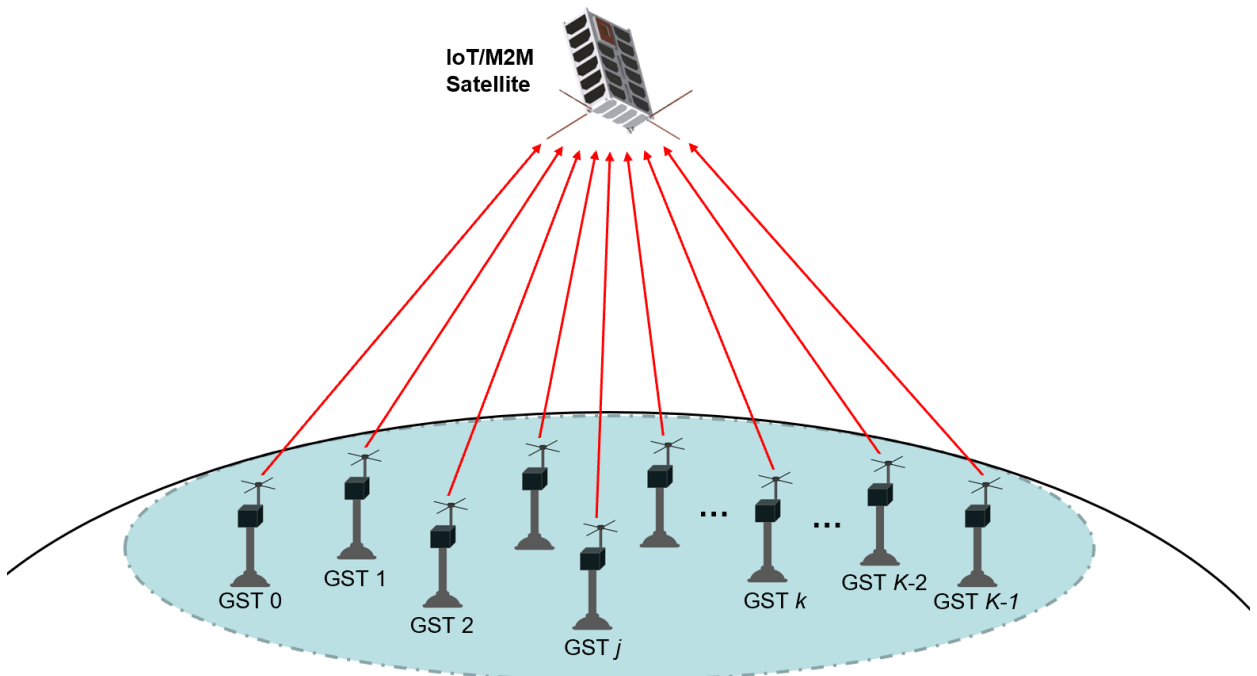


Figure 69. Satellite IoT/M2M Communication Scenario

Consider a processing time window defined at the receiver consisting of 11 packet durations $[0, 11T_p]$, during which the K packets are received. According to a Poisson distribution described in Section 6.4, K

is determined in a simulation run and each time delay τ_k is randomly selected within $[0, 10T_p]$. Each carrier phase offset ϕ_k is uniformly distributed within $[0, 2\pi]$. Amplitude A_k , frequency shift f_k and frequency rate d_k values depend on the satellite's elevation and azimuth angles with respect to terminals' positions, as discussed in Section 6.3. A_k is considered constant throughout the whole packet duration. Although f_k is mainly due to Doppler frequency shift, it can be considered to also account for any carrier frequency errors at the terminals and satellite receiver. Packets are generated at the terminals following a format and spread-spectrum modulation described in Section 6.2.

6.2 Packet Generation at Terminal Side and Received Signal at the Satellite

Preamble and Postamble Parts

Each terminal asynchronously transmits a packet to the satellite anytime it has data to send, independently of others, following the packet format in Figure 70. Preamble aids the receiver detect the presence and start of a packet (i.e., time delay τ_k) and to roughly estimate the amplitude, ϕ_k , and f_k at packet start. Similarly, postamble indicates the end of a packet and is used to roughly estimate the amplitude and frequency shift at packet end. A coarse estimate for d_k can be obtained from the difference of end and start frequency estimates over packet duration. Preamble and postamble have similar formats shown in Figure 71 but use different sequences. Each is a composite of a complex outer sequence and a real inner sequence with similar features inferred from the limited descriptions in [9], but not necessarily the same. The composite preamble/postamble sequence, consisting of $\{(\pm 1) + (\pm 1j)\}$, can be mathematically expressed as

$$p_{pre/pos}(n_{c,pre/pos}) = s_1 \left(\lfloor n_{c,pre/pos} \rfloor_{N_c} \right) s_2 \left(\lfloor n_{c,pre/pos} \rfloor_{N_c} \right) \quad (1)$$

where:

$$\lfloor n_{c,pre/pos} \rfloor_{N_c} = \text{integer}\{n_{c,pre/pos}/N_c\}$$

$$\lfloor n_{c,pre/pos} \rfloor_{N_c} = n_{c,pre/pos} \text{ modulus } N_c$$

$$n_{c,pre/pos} = 0, 1, 2, \dots, N_{pre} \cdot N_c - 1.$$

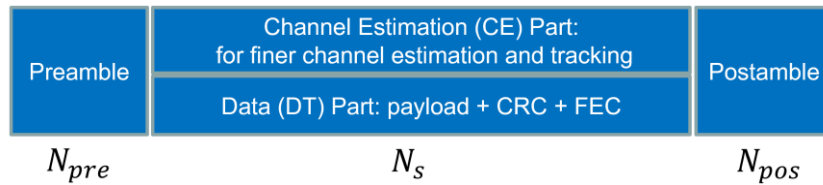
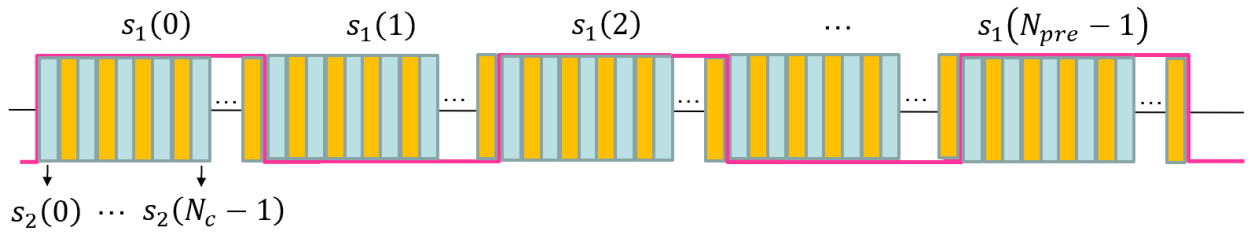


Figure 70. Uplink packet format



$s_1(i)$ = complex outer sequence (complex Gold) with length $N_{pre} = N_{pos} = 96$ symbols
 $s_2(i)$ = real inner sequence (complementary Golay) with length $N_c = 128$ chips

Figure 71. Preamble and postamble formats

The complex outer sequence can be expressed as

$$s_1(i) = z_n(i) + jz_n(i + 256) \quad (2)$$

where $z_n(i)$ is a real-valued Gold sequence with length of 511 chips and $i = 0, 1, 2, \dots, N_{pre} - 1$. The sequence $z_n(i)$ is generated using a built-in Matlab function *comm.GoldSequence* with the parameters summarized in Table 21. The inner sequence is a 128-element complementary Golay sequence consisting of $\{-1, +1\}$ elements; identical sequences are used for preamble and postamble. Hence, preamble and postamble lengths are both equal to $N_{pre} \cdot N_c = 96 \cdot 128 = 12888$ chips. The same preamble and postamble sequences are commonly used by all terminals.

Table 21. Parameters for Generating the Gold Sequences for Preamble/Postamble using a Matlab Function

Parameters	Preamble	Postamble
First generator polynomial ('FirstPolynomial')	Degree $n=9$: P1 = [9 4 0]	
Second generator polynomial ('SecondPolynomial')	Degree $n=9$: P2 = [9 6 4 3 0]	
'FirstInitialConditions'	I1 = [0 0 0 0 0 0 0 1]	
'SecondInitialConditions'	I2 = [0 0 0 0 0 0 0 1]	
'Index'	0	1
'SamplesPerFrame'	$N = 2^n - 1 = 511$	
z_n	goldseq = comm.GoldSequence(...); $z_n = 2 * \text{goldseq} - 1$	

Finer Channel Estimation (CE) and Data (DT) Parts

Figure 72 shows the block diagram for generating baseband signal on terminal side. The CE and DT parts are carried in parallel by two multiplexed channels which follow the preamble and precede the postamble. The two channels are I-Q multiplexed using two Orthogonal Variable Spreading Walsh sequences C_E and C_D , each with length equal to spreading factor SF=128 chips and consists of $\{-1, +1\}$ elements. The sum of $C_E \cdot C_D$ over SF chips (or within one modulated symbol) is 0, a property which will facilitate separation of CE and DT symbols at the processor (demodulator) side. In the DT part, user

payload bits are appended with a 16-bit Cyclic Redundancy Code (CRC) following the CRC-16 method for error detection. The CRC-encoded bits are in turn encoded for forward error correction (FEC) using a rate $\sim 1/3$ Turbo encoder. The encoded bits are converted to BPSK modulated symbols and then each symbol is spread (i.e., multiplied) by C_D . In the CE part, all fixed +1 symbols are spread by C_E and scaled down by a channel gain $\beta_{CE} = 1/3$. Once the DT and CE parts have been I-Q multiplexed, the resulting sequence is multiplied by a repeating scrambling code with a period of 255 chips, with the same chip rate as C_E and C_D . The scrambling code is a Gold sequence generated by the *comm.GoldSequence* function but using two $n = 8$ degree polynomials $P1 = [8\ 7\ 6\ 5\ 2\ 1\ 0]$, $P2 = [8\ 7\ 6\ 1\ 0]$, initial conditions $I1 = I2 = [0\ 0\ 0\ 0\ 0\ 0\ 0\ 1]$ and index = 0. Finally, the spread sequence will be passed to a digital-to-analog converter (DAC) to produce the analog input to RF circuitry part, which is omitted in our baseband-only model. To simplify the succeeding analysis, the CRC bits will be treated as lumped with the pre-FEC-coded payload bits.

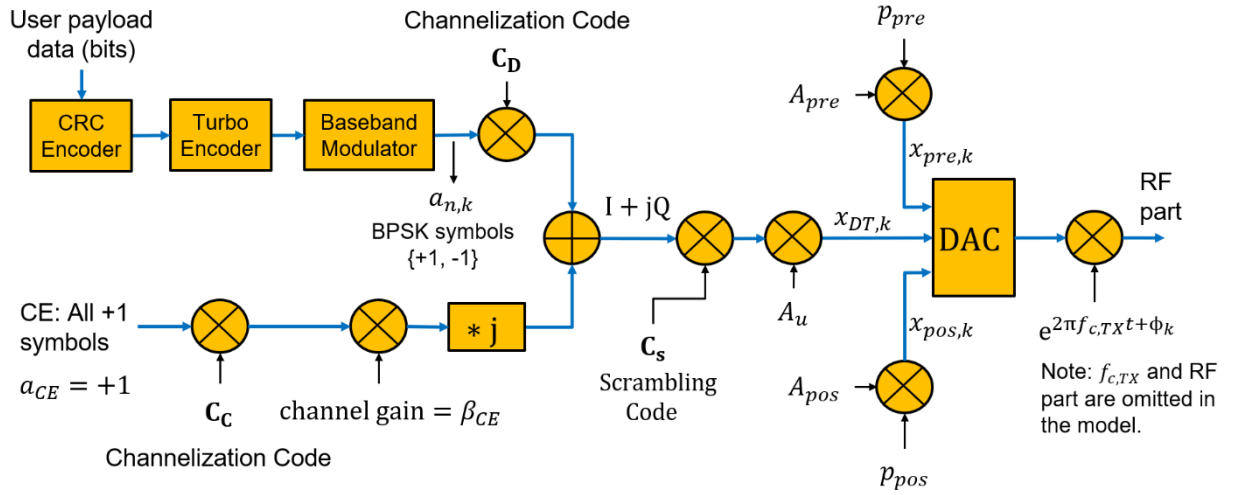


Figure 72. Block diagram of baseband signal generation on terminal side

The preamble and postamble parts of the baseband sequence of terminal k can be expressed as

$$x_{k,pre}(n_{c,pre}) = A_{pre}p_{pre}(n_{c,pre}) \quad (3)$$

$$x_{k,pos}(n_{c,pos}) = A_{pos}p_{pos}(n_{c,pos}) \quad (4)$$

where $A_{pre} = A_{pos} = 1/\sqrt{2T_s}$ makes the symbol energy of the corresponding analog baseband signal equal to unity. The DT and CE parts of the baseband sequence of terminal k can be expressed as

$$x_{k,DC}(n_{c,DC}) = A_u C_s \left(|n_{c,DC}|_{255} \right) \left[a_k \left(n = \lfloor n_{c,DC} \rfloor_{SF} \right) C_D \left(|n_{c,DC}|_{SF} \right) + j a_{CE} \beta_{CE} C_C \left(|n_{c,DC}|_{SF} \right) \right] \quad (5)$$

where $a_k(n)$ is the n -th modulated symbol of terminal k , $n = 0, 1, 2, \dots, N_s - 1$, $n_{c,DT} = 0, 1, 2, \dots, SF \cdot N_s - 1$. Amplitude $A_u = 1/\sqrt{(1 + a_{CE}^2 \beta_{CE}^2) T_s}$ makes the symbol energy equal to unity. The overall baseband sequence of terminal k is composed by concatenating the preamble, DT+CE and

postamble sequences

$$x_k(n_c) = [x_{k,pre} \ x_{k,DC} \ x_{k,pos}], \quad (6)$$

$$n_c = 0, 1, 2, \dots, (2N_{pre} \cdot N_c + SF \cdot N_s - 1).$$

The corresponding analog baseband signal of terminal k , assuming rectangular chip pulse shape, is given by

$$x_k(t) = x_k(n_c) \cdot \Pi(t - n_c T_c) \quad (7)$$

$$\Pi(\tau) \triangleq \begin{cases} 1 & 0 < \tau < T_c \\ 0 & \tau < 0, \tau > T_c \end{cases} \quad (8).$$

Then, the baseband signal arriving at the receiver due to packet from terminal k can be described in the form

$$r_k(t) = x_k(t - \tau_k) A_k e^{j\varphi_k(t)} \quad (9)$$

$$\varphi_k(t) = \phi_k + 2\pi f_k(t - \tau_k) + \frac{2\pi d_k(t - \tau_k)^2}{2} \quad (10).$$

where $\varphi_k(t)$ is the instantaneous phase error due to propagation channel experienced by the packet from terminal k . The total received baseband signal is the sum of K packet signals and a complex additive white Gaussian (AWGN) noise, $n(t)$, with independent real and imaginary components each normally distributed with zero mean ($\mu_N = 0$) and variance $\sigma_N^2/2$ (corresponding to an E_b/N_0 value):

$$r(t) = \sum_{k=0}^{k=K-1} r_k(t) + n(t) = \sum_{k=0}^{k=K-1} x_k(t - \tau_k) A_k e^{j\varphi_k(t)} + n(t) \quad (11).$$

6.3 LEO Channel Model

Consider a satellite flying on a circular LEO orbit with altitude h km above the ground, as illustrated in Figure 73. The K active terminals are assumed to be uniformly distributed on the earth's surface with area density ρ_A (number of active terminals per unit area). The satellite footprint changes as the satellite moves so the terminal population being served at different time windows also changes. We are focusing

on a representative short time window during which only the K terminals are sending packets to the satellite. Specifically, a footprint is defined as a portion of a spherical surface on which the K terminals are located from the satellite at different positions with $\varepsilon_{\min} = 5^\circ$ to $\varepsilon_{\max} = 90^\circ$ and from $\alpha = 0^\circ$ to $\alpha = 360^\circ$. Hence, terminal position may be expressed in (ε, α) . Note that in the left illustration of Figure 73, ε, β and γ are actual direction angles, $\vec{v}_{s\parallel}$ is in true direction, but \vec{v}_s and \vec{v}_{sJ} may not be in true directions (since \vec{v}_s is generally in a different plane as triangle OTE). In the right illustration, α is defined as a projection angle (as viewed from the top) and \vec{v}_s is in true direction. By applying the law of sines and noting that $\beta = 90^\circ - \varepsilon - \gamma$, it can be shown that

$$\beta = \cos^{-1}\left(\frac{R_E}{R_E+h} \cos \varepsilon\right) - \varepsilon \quad (12)$$

$$s = \frac{(R_E+h)\sin\beta}{\cos \varepsilon} = \frac{(R_E+h) \sin\left[\cos^{-1}\left(\frac{R_E}{R_E+h} \cos \varepsilon\right) - \varepsilon\right]}{\cos \varepsilon} \quad (13).$$

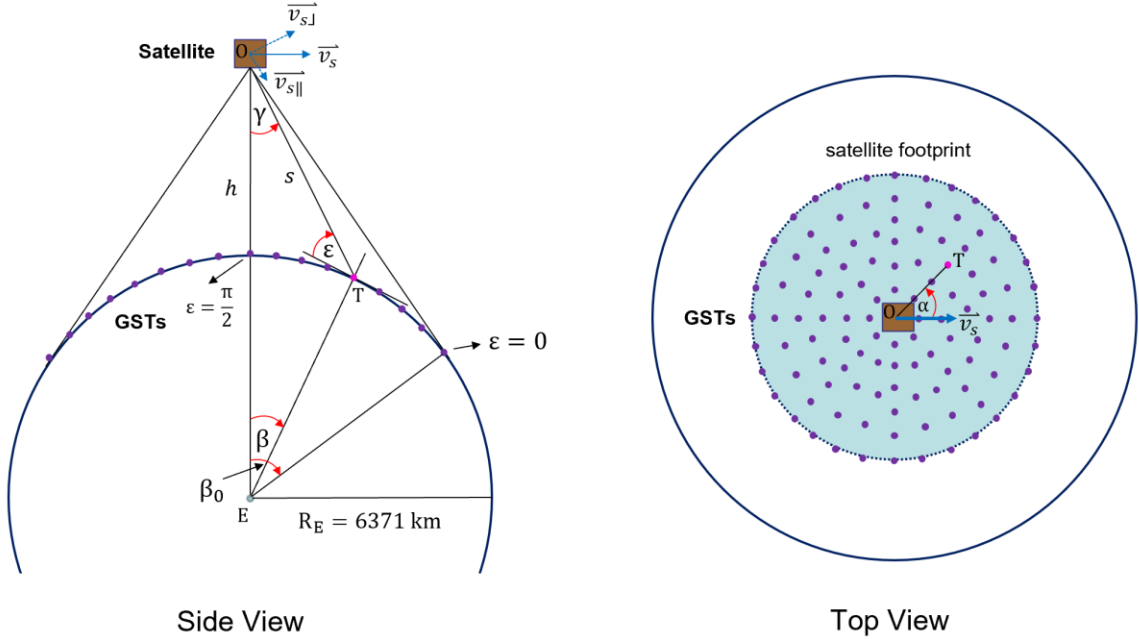


Figure 73. A snapshot of satellite orbit and footprint

Now we want to determine the spatial distribution function (sdf) of terminals. It is noted that terminal sdf is uniform with respect to α and non-uniform with respect to ε because more terminals are located at lower ε . By considering a differential area da containing dn_k terminals, relations (14) to (23) in Appendix 1 can be derived. The resulting terminal sdfs in terms of ε and α are given here in equations (22) and (23) and plotted in Figure 74 for a 600-km orbit, which shows that 80% of the terminals see the satellite at elevations below 26° .

$$p_\varepsilon(\varepsilon) \triangleq \frac{1}{K} \frac{dn_k}{d\varepsilon} \Big|_{\Delta\alpha=2\pi} = \frac{2\pi R_E^2}{C} \sin\left[\cos^{-1}\left(\frac{R_E}{R_E+h} \cos \varepsilon\right) - \varepsilon\right] \delta_\beta(\varepsilon) \quad (22)$$

$$p_\alpha(\alpha) \triangleq \frac{1}{K} \frac{dN_k}{d\alpha} = \int_{\varepsilon=\varepsilon_{\min}}^{\varepsilon=\pi/2} p_{\varepsilon\alpha}(\varepsilon, \alpha) d\varepsilon = \frac{1}{2\pi} \quad (23).$$

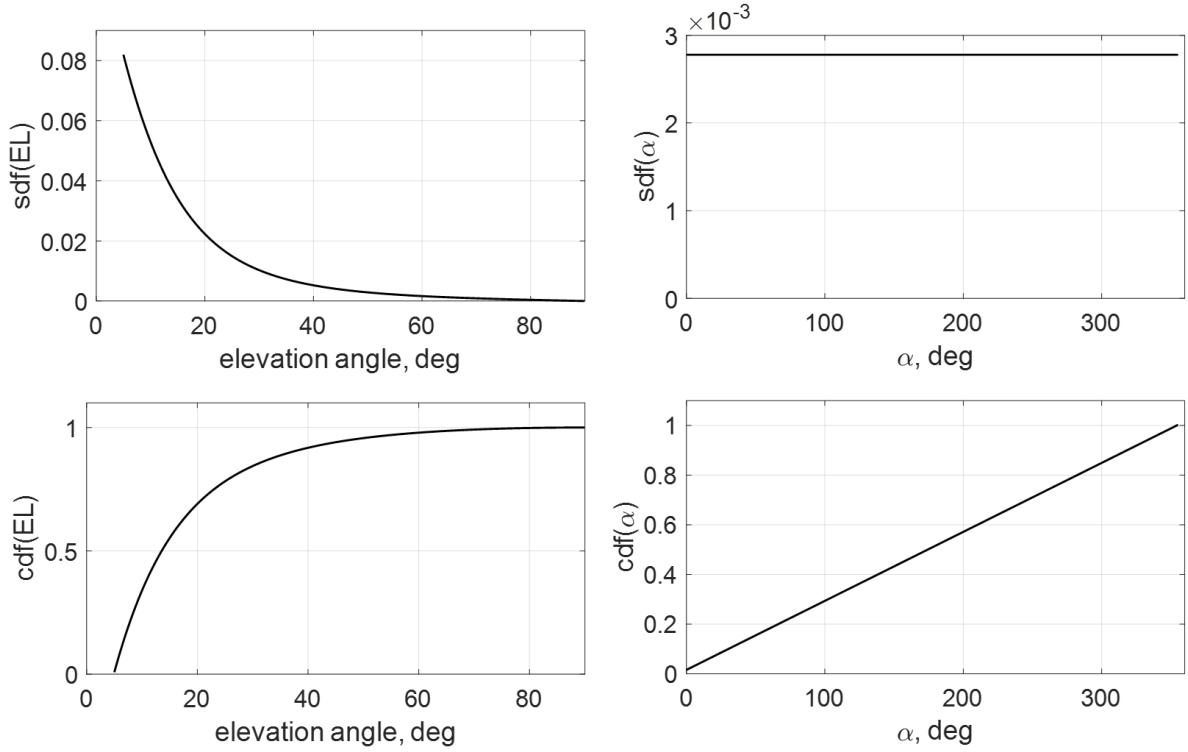


Figure 74. Terminal spatial and cumulative distribution functions in terms of ε and α ($h=600$ km)

The Doppler frequency shift f and rate d can be derived as follows (see Appendix 2 for derivation of dA/dt):

$$f(\varepsilon, \alpha) = \left(\frac{\vec{v}_s \cdot \vec{OT}}{|\vec{OT}|} \right) \frac{f_c}{c} = \frac{v_s f_c}{c} \cos A = \frac{v_s f_c}{c} \sin \gamma \cos \alpha = \frac{v_s f_c}{c} \frac{R_E}{R_E + h} \cos \varepsilon \cos \alpha \quad (24)$$

$$d(\varepsilon, \alpha) = \frac{d}{dt} (f(\varepsilon, \alpha)) = \frac{-v_s f_c}{c} (\sin A) \frac{dA}{dt} = -\frac{v_s^2 f_c \sin^2 A}{cs} = -\frac{v_s^2 f_c}{cs} \left(1 - \left(\frac{R_E}{R_E + h} \cos \varepsilon \cos \alpha \right)^2 \right) \quad (25)$$

where $v_s = \sqrt{Gm_E/(R_E + h)}$, $A \triangleq \angle OT$ is the direction angle between \vec{v}_s and \vec{OT} .

To generate a set of channel values for the K active terminals, first we generate random ε_k, α_k following the spatial distributions $p_\varepsilon(\varepsilon)$ and $p_\alpha(\alpha)$ in (22) and (23). The corresponding f_k and d_k values are then computed using (24) and (25). The carrier phase offset values ϕ_k are randomly selected from within $[0, 2\pi]$. For generating the A_k values, we consider two main factors causing the received signal amplitudes variation. First, there is amplitude variation in line-of-sight (LOS) condition due to having different satellite elevations as seen from terminals. Since the received signal power in LOS condition is proportional to $1/s^2$, the amplitudes due to satellite elevations are computed by (26) and (27). The probability distribution functions (pdfs) for $A_{k,dB}$ (LOS condition), f_k and d_k are obtained by generating

many samples. The resulting pdfs are shown in Figure 75. The standard deviation of LOS amplitudes due to elevation differences alone is $\sigma_{LOS} \approx 3\text{dB}$.

$$A'_{k,\text{dB}} = 20 \log_{10} \left(\frac{s_{\text{mean}}}{s(\varepsilon_k)} \right) \quad (26)$$

$$A_k = 10^{(A'_{k,\text{dB}} - A'_{k,\text{dB,mean}})/20} \quad (27).$$

Second, even among terminals with equal elevations, there will be additional power fluctuations around the line-of-sight (LOS) value due to land-mobile satellite (LMS) channel fading/shadowing statistics. In [6], it is assumed that the received power fluctuation is caused by uplink LMS channel fading/shadowing statistics, conditioned to the terminals transmit power control algorithm (based on downlink signal strength). Considering a GEO satellite and a fixed elevation, the amplitude variation due to joint effect of shadowing, fading and imperfect power control is modeled as a log-normal distribution with mean μ_{LN} (dB) and standard deviation σ_{LN} (dB). Their simulations show that σ_{LN} is about 2 dB but can be as high as 3 dB with power control, and 6.4 dB without power control.

In this work, assuming a LEO orbit, we model the received amplitude A_k to be the product of LOS amplitude generated by the elevation random variable (RV) with pdf described above and another amplitude RV generated by a lognormal pdf with mean μ_{LN} and standard deviation σ_{LN} . Albeit quite simplified, the said lognormal pdf may be considered to account in lump for the variations due to LMS fading/shadowing, as well as actual antenna patterns, which will be captured by considering σ_{LN} up to 9 dB. With this model, the resulting pdfs and cdfs are shown in Figure 76 for $\sigma_{LN} = 0, 3, 6, 9$ dB.

We can look at the case with $\sigma_{LN} \approx 3$ dB as representing the scenario with a rough (non-tight) power control. This condition gives amplitudes with overall standard deviation of 4.2 dB. The case with $\sigma_{LN} \approx 6$ dB might represent the situation without power control but with a perfectly omnidirectional antenna (overall standard deviation of 6.7 dB). Finally, the case with $\sigma_{LN} \approx 9$ dB can represent the scenario without power control, using practical circularly polarized antennas with wide beamwidths (overall standard deviation of 9.5 dB). For the case without power control, noting the previous findings in [6], it is expected that more amplitude variation may increase the maximum achievable throughput, although this also results in higher PLR. On the other hand, too much variation would reduce the throughput due to more frequent occurrence of packets with power below the demodulation threshold.

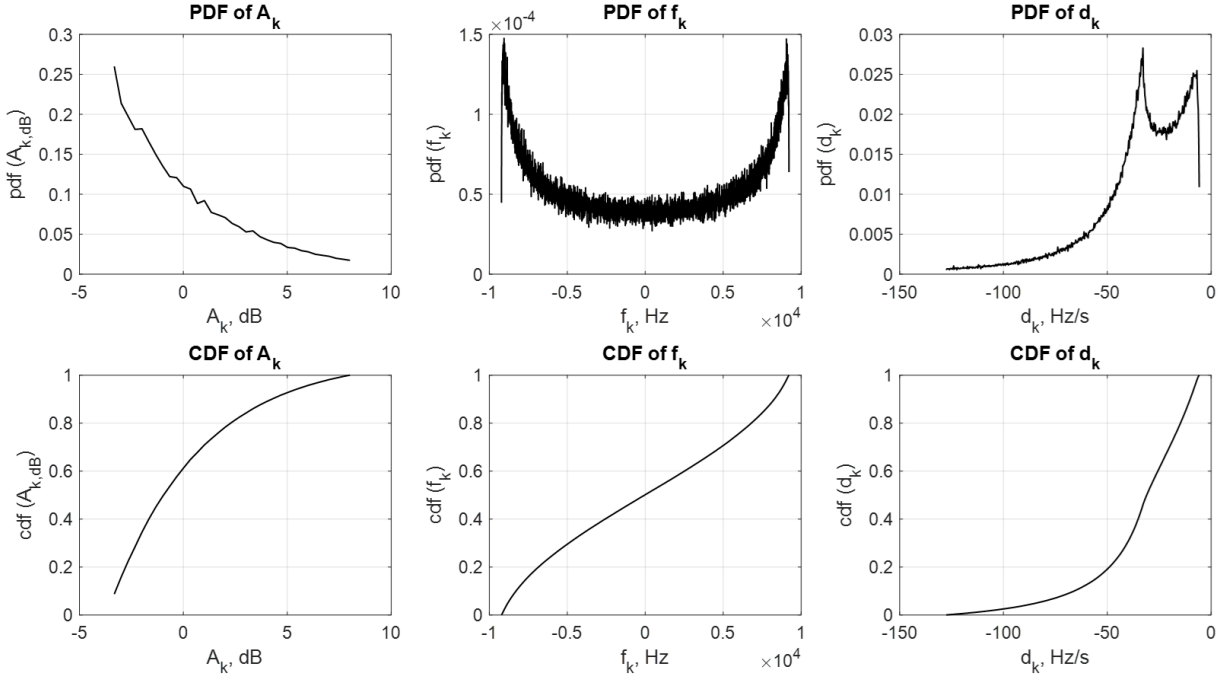


Figure 75. Pdfs and cdfs for $A_{k,dB}$, f_k and d_k due to LEO channel without lognormal fading/shadowing or $\sigma_{LN} = 0dB$ ($h=600$ km, $f_c=402$ MHz, $\mu_{LN} = 0dB$)

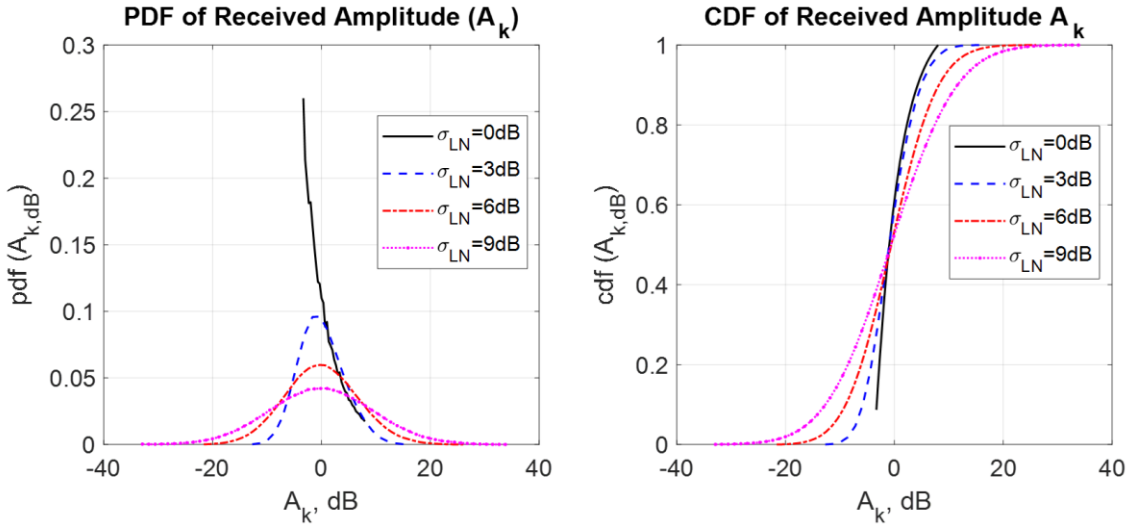


Figure 76. Pdfs and cdfs for $A_{k,dB}$ due to LEO channel with and without lognormal fading/shadowing for different σ_{LN} ($h=600$ km, $f_c=402$ MHz, $\mu_{LN} = 0dB$)

6.4 Packet Arrival Model

We assume packets arrive at the receiver following a Poisson distribution such that the number of packet arrivals within one packet duration T_p is a Poisson RV with intensity $\lambda_{rp} = GG_p$, where G is defined as the MAC load expressed in information bits/s/Hz. The processing gain G_p is defined as $G_p = R_{chip}/R_b = SF/(R_c \log_2 M)$, where R_{chip} is the channel chip rate, R_b is the information bit rate, SF is the spreading factor, R_c is the FEC coding rate, and M is the modulation order. The Poisson RV discrete pdf is given by

$$p_{PRV}(k_r; \lambda_{rp}) = \frac{\lambda_{rp}^{k_r} e^{-\lambda_{rp}}}{k_r!} \quad (28)$$

where $p_{PRV}(k_r; \lambda_r)$ expresses the probability of k_r packet arrivals within one packet duration T_p given λ_{rp} , which is also the expected (average) number of packet arrivals within T_p . In the simulation model, the number of packet arrivals within every symbol duration T_s is randomized at every symbol according to an equivalent Poisson RV with intensity $\lambda_{rs} = \lambda_{rp}/(N_{pre} + N_s + N_{pos})$. Any arriving packets within a symbol duration assume random delays between 0 and $(SF - 1)$ chips from beginning of the symbol. All arriving packets also assume the channel parameters generated as described above.

For our analysis and signal processing, we consider a time processing window illustrated in Figure 77 that has a total duration of $11T_p$ and wherein packets arriving between $t_0 = 0$ to $t_{10} = 10T_p$ should be decoded. Thus, K is a random variable whose value is determined during simulation run (with expectation value of $10\lambda_{rp}$ packets arriving within $10T_p$). The simulation parameters are given in Table 22.

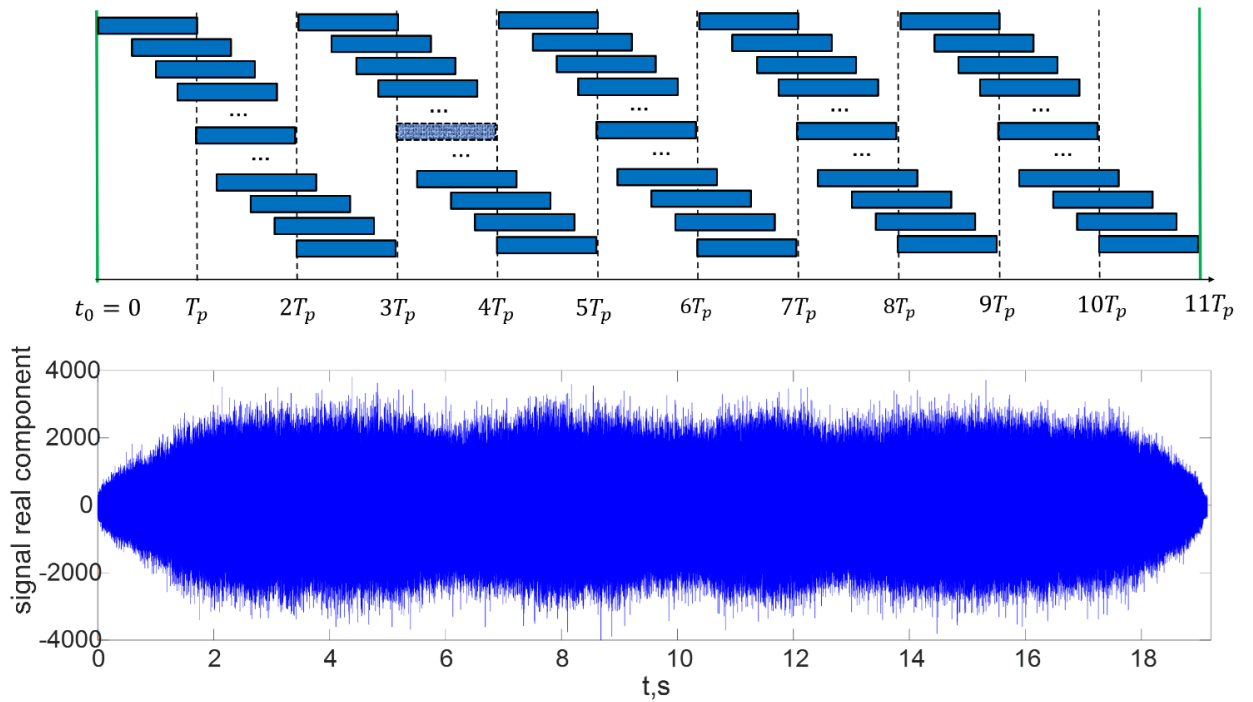


Figure 77. Illustration of time processing window with total duration $T_w=11T_p$ (top); an example of received baseband signal for $G = 1.0$ (bottom)

Table 22. Simulation Parameters

Parameter Symbol	Description/Meaning	Value
h	Satellite orbit altitude above the ground	600 km
$N_{pre} = N_{pos}$	Preamble/postamble length in symbols	96
N_b	Pre-FEC-coded payload length in bits (including 16-bit CRC with generator polynomial $z^{16} + z^{15} + z^2 + 1$)	512

$N_{b,coded}$	FEC-coded packet length in bits (Turbo code with rate $R_c \sim 1/3$)	1548
M , type	Modulation order and type	BPSK ($M = 2$)
$SF (= N_c)$	Spreading factor	128
N_{Ts}, N_{Tc}	Total packet length in symbols; in chips	1740; 222720
R_b	Information bit rate (including CRC)	333.33 bps
$R_s = R_b/R_c$	Symbol rate	1000 symbols/s
$R_{chip} = SF \cdot R_s$	Chip rate (\approx signal bandwidth)	128000 chips/s
$T_p = N_{Tc}/R_{chip}$	(One) packet duration	1.74 s
G_p	Processing gain	384
G	MAC load (bps/Hz, or more appropriately bits/chip for spread spectrum)	Variable
$\lambda_{rp} = GG_p$	Poisson RV intensity for packet arrivals, expected (average) number of arrivals per T_p	Variable (38.4 at $G = 0.1$, 384 at $G = 1.0$, 768 at $G = 2.0$)
T_w	Time processing window (total observation duration for signal processing)	$11T_p$
K	Number of packets arriving within $T_w - T_p$ (packets that should be decoded within T_w)	Average values: 1920 at $G = 0.5$, 3840 at $G = 1.0$, 7680 at $G = 2.0$
$\gamma_b = \frac{E_b}{N_0}$	Information bit energy to noise power spectral density (defined at the receiver)	Variable
$\mu_{LN} = 0\text{dB}, \sigma_{LN}$	Mean and standard deviation (in dB) of log-normal Gaussian distribution accounting for received power fluctuations due to LMS channel fading/shadowing statistics, imperfect power control, and antenna patterns (simplified)	σ_{LN} : 3 dB (with rough power control (PC)), 6 dB (w/o PC, perfectly omnidirectional antenna), 9 dB (w/o PC & with wide beamwidth antennas)

6.5 Throughput (THR), Packet Loss Rate (PLR) and Energy Efficiency (EE) Metrics

We define packet loss rate (PLR) as the number of decoded packets $N_{decoded}$ over the total number of received packets K within the time processing window T_w , as mathematically expressed in equation (29). As commonly defined in literature, we define throughput (THR) according to equation (30).

$$PLR = 1 - PSR = 1 - \frac{N_{decoded}}{K} \quad (29)$$

$$THR = G \cdot PSR = G \cdot (1 - PLR) \quad (30)$$

Here we derive a definition for energy efficiency metric appropriate for later discussion. First, at the transmitter, the average energy per successfully transmitted information bit (ESB) is defined by (31). The total energy consumption for packet transmission E_{TX} , which includes that of RF power amplifier, is calculated by (32), where P_{TX} is the RF output power and α expresses the ratio of amplifier overhead power consumption over output RF power. The value of α depends on type of amplifier used, that is, appropriate for a modulation scheme. For a class-A amplifier normally used for BPSK modulation, $\alpha = 1.8571$ [133]. Packet transmission time T_{TX} , neglecting the preamble and postamble overheads, is calculated by (33). Considering PLR, equation (34) computes the average number of successfully transmitted (decoded) bits per transmission attempt, $N_{b,ave}$. Incorporating (32) to (34) into (31) results to equation (35) for ESB_{TX} . After end-to-end signal attenuation (which can be analyzed separately in detail), a corresponding energy per information bit $E_{b,RX}$ is obtained at the receiver and equation (36) expresses a similar ESB metric at the receiver, ESB_{RX} .

Finally, by normalizing ESB_{RX} to the noise PSD N_0 , and taking the reciprocal, equation (37) defines a new energy efficiency metric η_{EE} in decoded bits per normalized energy (J/(W/Hz) or unit-less). This metric will be useful to evaluate the impact of PHY layer parameters (choice of modulation scheme, FEC scheme, etc.) on energy efficiency. In (37), γ_b serves as a shorthand notation for $E_{b,RX}/N_0$, which indicates extent of input energy chosen for a given modulation to achieve a certain PLR in the presence of both noise and MUI. Note that PLR is a confluence of effects of several variables, including PHY layer design choices, γ_b , extent of MUI due to MAC load G , and the MAC scheme itself. Altogether, PLR , THR and η_{EE} , will be used to assess the performance and energy efficiency trade-offs of the designed PHY-MAC scheme. Note that since P_{TX} accounts for the transmission of total signal including the CE part, all derived parameters ($E_{b,TX}$, ESB_{TX} , $E_{b,RX}$, ESB_{RX} , γ_b , η_{EE}) include the CE symbol energy as part of the energy needed to successfully transmit an information bit (preamble and postamble energies, whose sum is about 1/10 of the total, are neglected).

$$ESB_{TX} \triangleq \frac{E_{TX}}{N_{b,ave}} \quad (31)$$

$$E_{TX} = (1 + \alpha)P_{TX}T_{TX} \quad (32)$$

$$T_{TX} = N_b \cdot T_b = \frac{N_b}{R_b} \quad (33)$$

$$N_{b,ave} = N_b \cdot PSR + 0 \cdot PLR = N_b \cdot (1 - PLR) \quad (34)$$

$$ESB_{TX} = \frac{(1+\alpha) \cdot P_{TX}}{N_b(1-PLR)} \cdot \frac{N_b}{R_b} = \frac{(1+\alpha) \cdot E_{b,TX}}{1-PLR} \quad (35)$$

$$ESB_{RX} \triangleq \frac{(1+\alpha) \cdot E_{b,RX}}{1-PLR} \quad (36)$$

$$\eta_{EE} \triangleq \left(\frac{ESB_{RX}}{N_0} \right)^{-1} = \left[\frac{(1+\alpha)}{(1-PLR)} \cdot \frac{E_{b,RX}}{N_0} \right]^{-1} = \frac{1-PLR}{(1+\alpha)\gamma_b} \quad (37)$$

6.6 Overview of Signal Processing Algorithm

We formulated a detailed baseband signal processing algorithm by adopting with modifications the basic procedure outlined in [7] and [8]. An overview of our detailed baseband signal processing algorithm is shown in Figure 78. The algorithm begins with baseband signal samples within a time processing window illustrated in Figure 77. The first step is packet detection which involves correlating a chip-wise swept signal portion (with length equal to preamble) to the known preamble sequence, thus determining the start of suspected packets. Secondly, channel parameters are roughly estimated from preamble and postamble portions of detected packets. Next, by applying the knowledge of the known fixed CE symbols (shown in Figure 72), finer channel estimates are obtained, and suspected packets are further screened. At every iteration i , K_i suspected packets are detected (remaining as packet candidates after screening), depending on a computed amplitude threshold value. Because there is no prior knowledge of the number of transmitting terminals, K_i is determined upon execution. Then, detected packets are arranged from highest power ($k = 1$) to lowest power ($k = K_i$). Note that in the first E-SSA iteration, only K_1 out of K total received packets are detected, that is, those with relatively higher powers are likely to come out first.

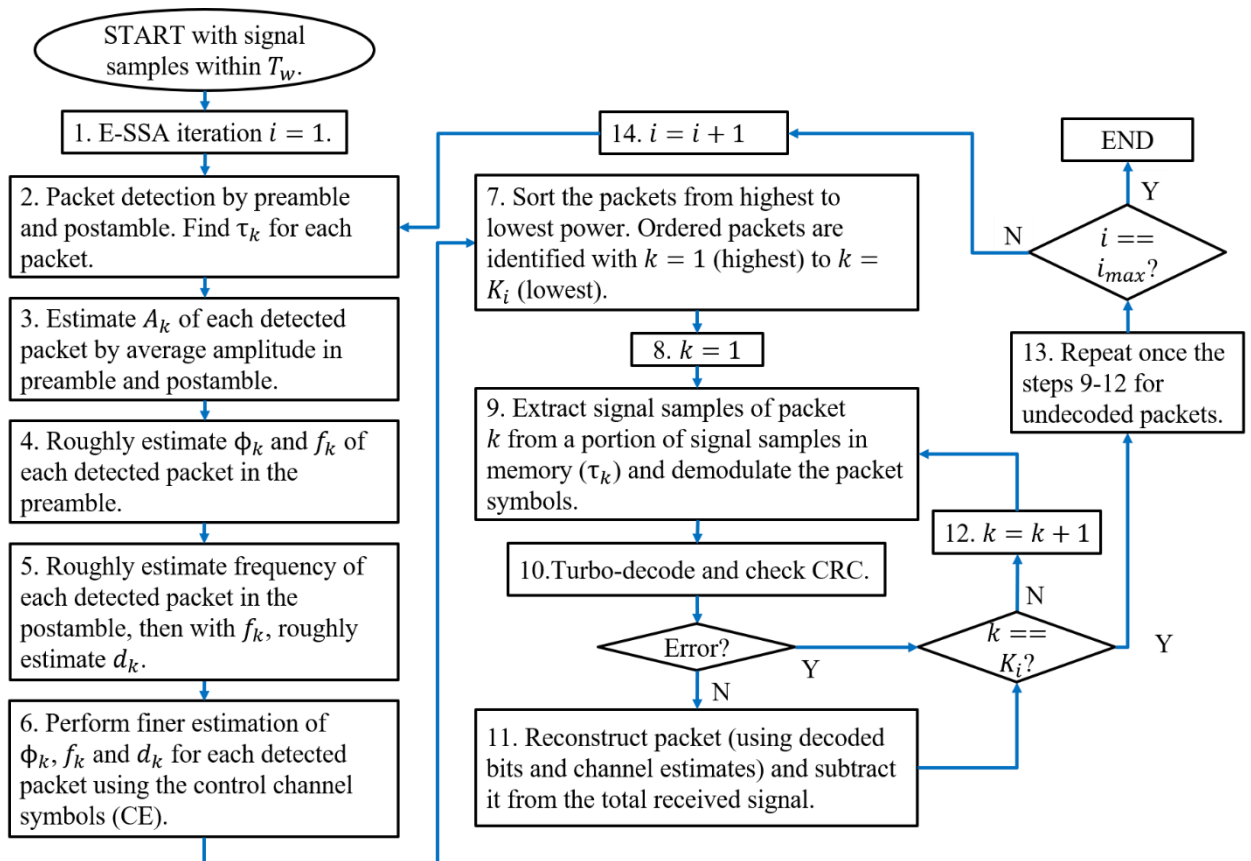


Figure 78. Signal processing algorithm overview

Once sorted, each packet signal k undergoes BPSK demodulation, Turbo-decoding and CRC checking process. A completely decoded (error-free) packet is reconstructed using the decoded bits and

estimated channel parameters and then it is subtracted from the (running) total signal saved in memory. These steps are repeated in the subsequent E-SSA iterations, until the maximum number of allowed iterations i_{max} is reached. The value of i_{max} was set to five based on the general observation that after the fifth iteration, there is only marginal PLR improvement. Details of packet detection, channel estimation and decoding algorithms are described below.

6.7 Packet Detection and Coarse Channel Estimation

The relevant working equations referred here are placed in Appendix 3. Preamble match-detection is performed on every preamble-long signal portion $r_{pre,\kappa}$ expressed in (38), wherein $\kappa = 0, 1, 2, \dots, (10N_{Tc} - 1)$ indicates the chip-wise offset value. This is done by correlating $r_{pre,\kappa}$ to the complex conjugate of preamble sequence and computing the discrete Fourier transform (DFT) of correlation, $r_{pre,\kappa,corr}$, as in (39) to (40). The DFT result $\mathcal{R}_{pre,\kappa}(\Omega_l)$ provides the frequency spectrum of $r_{pre,\kappa,corr}$ such that existence of a peak in the magnitude spectrum $|\mathcal{R}_{pre,\kappa}|$ indicates a likely occurrence of a packet. The peak appears at a normalized frequency $\Omega_l = 2\pi l / (N_{pre}N_c)$ corresponding to the channel frequency shift. Peak magnitude $V_{\kappa,pre}$ estimates the packet signal amplitude in the preamble. When $V_{\kappa,pre} > V_{th}$, the same calculations are applied on the postamble-long signal portion $r_{pos,\kappa}$ and if $V_{\kappa,pos} > V_{th}$, a positive detection is decided at $\tau_k = \kappa$. Coarse channel estimates are computed according to the set of equations (50a-f). V_{th} is decided for a good balance between false alarm rate and misdetection rate in every E-SSA iteration. Figure 79 provides illustrative plots for detected amplitude A_κ vs time delay in 1st to 5th iterations.

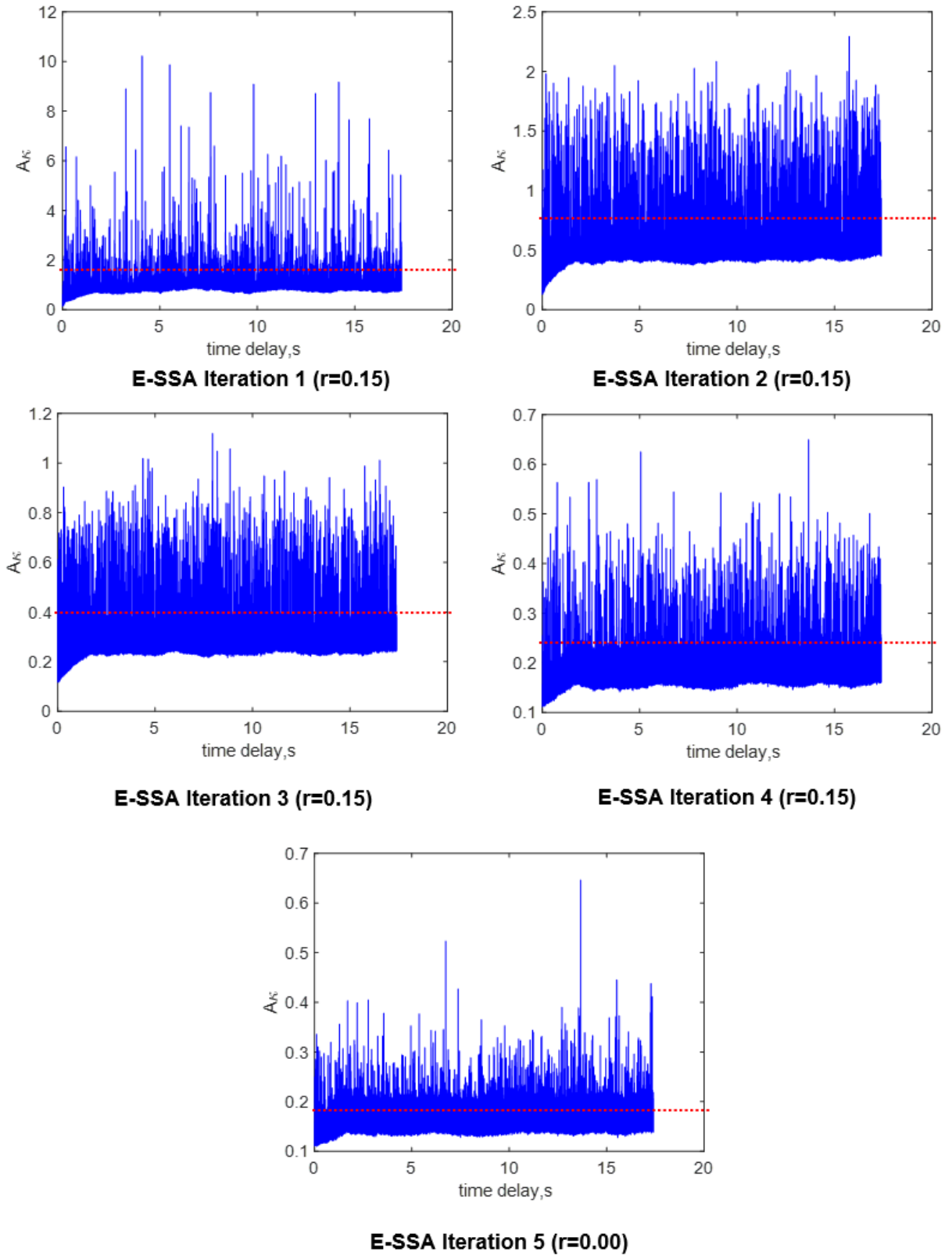


Figure 79. Packet detection decision, shown for E-SSA iterations 1-5 (red line: detection threshold, $\sigma_{LN} = 6dB$, $G = 0.7$)

6.8 Fine Channel Estimation

The relevant working equations referred here are placed in Appendix 4. For finer channel estimation, the known fixed symbols of CE part are used. The following is the procedure for each detected packet k .

A signal portion after preamble and before postamble is taken from the signal memory, i.e., $r_{k,DC}$ in (51). Then, equation (52) removes from the signal the effects of coarse channel estimates $\phi_k^{(1)}$, $f_k^{(1)}$ and $d_k^{(1)}$. The resulting signal $y_{k,DC}^{(1)}$, which takes the form of equation (54), still contains the effects of remaining channel estimation error $\theta_{k,err}(n_{c,DC})$, multiuser interference (MUI) and noise.

To extract the channel estimation information, the DT part is removed by multiplying C_C to each of real and imaginary components of $y_{k,DC}^{(1)}$ and taking the average over every SF chips (noting sum of $C_D \cdot C_C$ over SF chips is 0). These operations are expressed in (55) and (56), wherein $a'_{CE}(n)$ and $a''_{CE}(n)$ are subsequently used in (57) and (58), thereby obtaining very “noisy” cosine and sine plots of the estimate of remaining channel estimation error, with resolution of $1/R_s$. The channel estimation error cosine and sine plots are smoothed by a simple moving average function (MAF), as in (59) and (60). However, because the plots are still “noisy” due to MUI, candidate frequency ψ_k and rate δ_k values within narrow search ranges are tried to find the values which give the strongest correlation with the noisy estimate, as in (61). The selected ψ_k and δ_k values are used in (62a-c) to obtain better channel estimates, $\phi_k^{(2)}$, $f_k^{(2)}$ and $d_k^{(2)}$. These steps are executed recursively three times, obtaining fine channel estimates $\phi_k^{(2)}$, $f_k^{(2)}$ and $d_k^{(2)}$.

The broken plot in Figure 80 is an example of *candidate* channel estimation error cosine plot which is derived from the selected ψ_k and δ_k values. This plot visualizes the estimate for the coarse channel estimation error $\theta_{k,err}$, noting that ψ_k and δ_k are used to improve the previous (coarse) estimation. In addition, the highest correlation value obtained for each k is compared to a threshold to further decide whether the suspected packet is considered a valid candidate. Since absence of a packet would give a weak correlation with any candidate channel parameters, falsely detected packets in preamble match would be filtered out in this screening. After this screening, there would be K_i remaining suspected packets in the current E-SSA iteration, out of K total received packets.

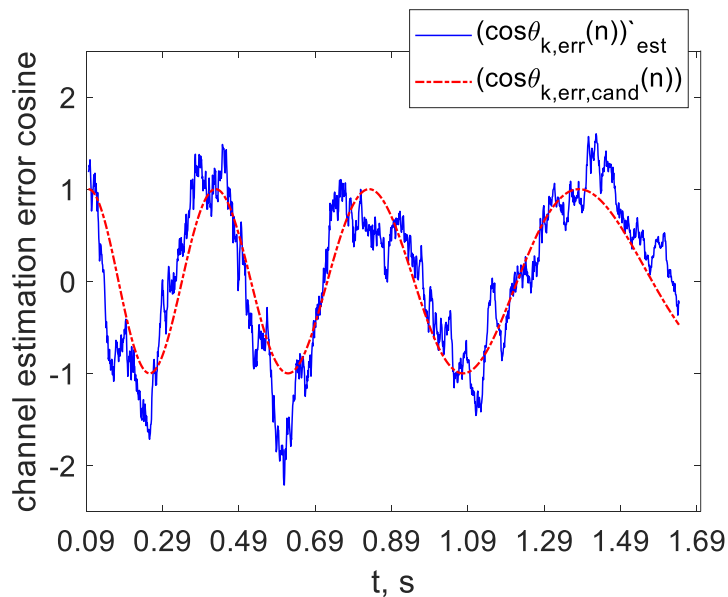


Figure 80. Fine channel estimation illustrative example

6.9 Demodulation and Decoding

After fine channel estimation, the K_i detected packets are arranged from highest to lowest powers and they are demodulated and decoded in that order, each according to the following steps. Like (52), equation (63) removes from packet k signal $r_{k,DC}$ the effect of channel parameters $\phi_k^{(2)}$, $f_k^{(2)}$ and $d_k^{(2)}$. Equation (65) extracts the DT part information from the resulting signal $y_{k,DC}^{(2)}$, where $a'_k(n)$ are used in (66) to obtain the symbol decision statistics $a_{k,est}(n)$, which serve as input to the Turbo decoder. It is noted that in (65), $\cos(\theta_{k,err}^{(2)}(n)) \approx 1$ if fine channel estimates are accurate (that is, $\theta_{k,err}^{(2)}(n) \approx 0$). However, practically there will be small channel estimation errors. Note that even small errors in f_k and d_k estimates will cause phase reversal of the packet's latter symbols when packet duration T_p is comparable to coherence time T_{coh} dictated by channel estimation error (as expressed in (67)). For example, assuming $\phi_{k,err}$ is small (<0.3 rad), the total frequency error from frequency shift and rate estimation errors must be less than ~ 0.3 Hz so that coherence time $T_{coh} > T_p = 1.74$ s. This means we must, conservatively, target each of f_k and d_k to be accurate within ~ 0.15 Hz. As we will see in Chapter 7, these channel estimation accuracy targets are very difficult to attain even with fine channel estimation method described in Section 6.8.

Nonetheless, errors due to phase reversals, MUI and noise can still be corrected even if T_p slightly exceeds T_{coh} , thanks to rate 1/3 Turbo-code's powerful error-correcting capability and interleaving features. Turbo-decoded bits are CRC-checked and if error-free, correctly transmitted symbols are derived by passing the decoded bits to a Turbo coder and BPSK modulator (in the same way as in the terminal side). Comparing the received symbols to the correctly transmitted symbols allows compensation, to some extent, of remaining instantaneous phase estimation error. The entire packet is reconstructed from the preamble, postamble, reproduced symbols and estimated channel parameters. Then, it is subtracted from the (running) total received signal. If packet decoding fails using the fine channel estimates, the above procedure is repeated reactively for another f_k and d_k candidates around the fine estimates (with 0.2 Hz and 0.2 Hz/s increments/decrements within ± 1.4 Hz and ± 1.2 Hz/s in iteration 1; ± 2.0 Hz and ± 2.0 Hz/s in iterations 2-3; ± 3.0 Hz and ± 3.0 Hz/s in iterations 4-5). After doing these steps on all the K_i detected packets, these are repeated one more time on undecoded packets (to take advantage of resulting lower MUI) before proceeding to the next E-SSA iteration.

$$y_{k,DC}^{(2)} = r_{k,DC} \cdot c_k^{(2)} \cdot (1/A_u) \text{conj}(C_s) \quad (63)$$

$$c_k^{(2)}(n_{c,DC}) = \exp\left(-j \left[\phi_k^{(2)} + 2\pi f_k^{(2)}(N_{pre}N_c + n_{c,DC})/R_{chip} + \frac{2\pi d_k^{(2)}((N_{pre}N_c + n_{c,DC})/R_{chip})^2}{2} \right]\right) \quad (64)$$

$$a'_k(n) = \text{average over every } SF \text{ chips of } \left[\text{Re} \left\{ y_{k,DC}^{(2)} \right\} \cdot C_D \right] = A_k a_k(n) \cos \left(\theta_{k,err}^{(2)}(n) \right) + ERR_3 \quad (65)$$

$$a_{k,est}(n) = \frac{a'_k(n)}{A_k} \quad (66)$$

$$\phi_{k,err} + 2\pi f_{k,err} T_{coh} + \frac{2\pi d_{k,err} T_{coh}^2}{2} = \pm\pi \quad (67)$$

Chapter 7: Simulation Results and Discussion for E-SSA-based Nanosatellite IoT/M2M Communication System

This chapter discusses the simulation results for packet detection and channel estimation algorithms, as well as the packet loss rate (PLR), throughput (THR) and energy efficiency η_{EE} of the overall PHY-MAC scheme with the baseband signal processing algorithm.

7.1 Target Values for Evaluation Metrics

PLR serves as a quality-of-service (QoS) metric, which indicates the probability of successfully decoding a transmitted packet from a GST. As such, the threshold PLR constraints the maximum MAC load G and THR in which the system can be operated. Similarly, maximum EE also follows from the threshold PLR. The target PLR really depends on the application requirements so it can be set based on the serviced applications. Since we are considering applications where there is no need for high reliability (or guarantee of successful uplink), a target value of $PLR < 5\%$ should be reasonable, thus it is chosen for succeeding discussions. Table 22 lists the target values for the evaluation metrics.

Table 23. Target Values for the Evaluation Metrics

Metric	Target
PLR	<5%
MAC load G	The higher the better – the highest value wherein $PLR < 5\%$
THR	
EE	

7.2 Packet Detection

Figure 81 shows the iteration false alarm rate (IFAR), iteration misdetection rate (IMDR) and cumulative misdetection rate (CMDR) results for different MAC loads at a constant $\sigma_{LN} = 6\text{dB}$, while Figure 82 shows the results for different σ_{LN} values at a constant $G = 1.0$. IFAR, IMDR and CMDR results are plotted vs E-SSA iteration number to see performance trend as the recursive algorithm progresses. Also, results for non-filtered (Section 6.7 method) and filtered (Section 6.8 method) are given, which show that further screening by correlation in the CE part effectively filters out most of falsely detected packets while keeping most of the correct ones. IFAR progressively drops within 1st to 4th iterations then starts increasing in the 4th iteration. This is because in later iterations, only fewer remaining packets – those with lower power – are left to be detected. Also, the accumulated residue power from imperfect interference cancellations becomes comparable to the lower power desired signal. An exception is noted when σ_{LN} is low (e.g., 3 dB) because having relatively small amplitude variation, most packets can be already detected and decoded during 1st to 2nd iterations. IFAR tends to decrease with higher G due to greater probability of packet occurrence at any instant, rather than MUI + noise. On the other hand, IFAR tends to increase with higher σ_{LN} but we do not have a straightforward or intuitive explanation for this. Again, the exception at later iterations when $\sigma_{LN} = 3\text{dB}$ is noted.

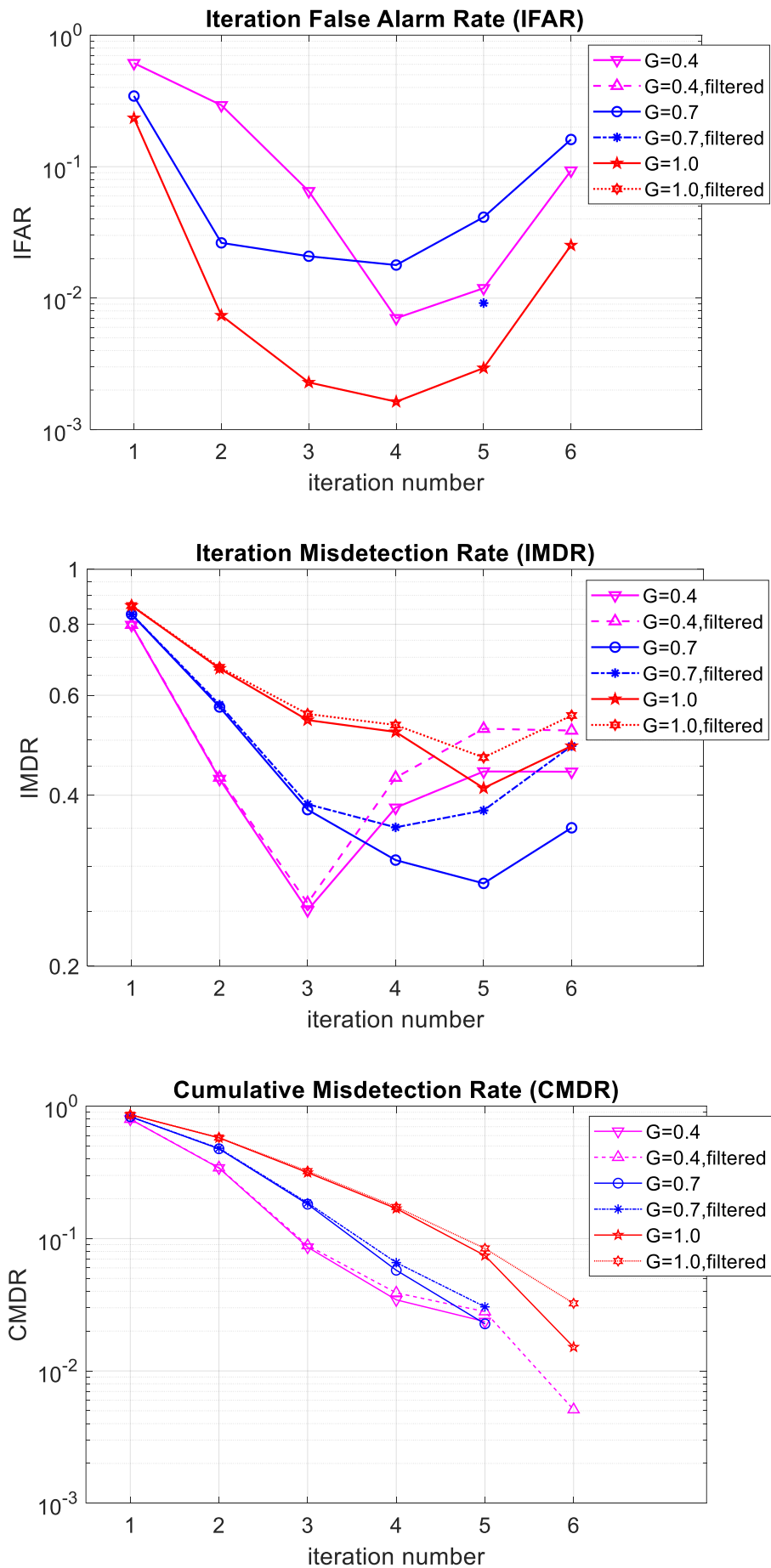


Figure 81. IFAR, IMDR and CMDR for different G values ($\sigma_{LN} = 6\text{dB}$, $E_b/N_0 = 14\text{dB}$)

IMDR, and consequently CDMR, tend to be higher with higher MAC load G or higher σ_{LN} . With higher G , this is expected due to greater MUI in earlier iterations and greater residue interference power in later iterations. Both MUI and residue interference power make it more difficult to detect lower power packets. With higher σ_{LN} , IMDR is expected to be higher because more power variation increases chance of having packets falling below the detection threshold at a given iteration. Although residue interference power accumulates for any given G and σ_{LN} , IFAR and IMDR still tend to decrease in succeeding iterations because as more and more packets have been already decoded (and cancelled), power variation among the remaining packets becomes smaller. Note that it is important to attain as low CDMR as possible in the last iteration because it dictates the lower bound for PLR (packets must be detected before they can be decoded).

We can also notice some trends in the IMDR and CDMR vs iteration number. IMDR drops more rapidly in successive iterations (i.e., as the E-SSA algorithm progresses) when G is lower than when G is higher. However, when G is lower, IMDR starts to increase at an earlier iteration number. Increase in IMDR starting from an iteration number indicates a significant number of packets have already been decoded in the preceding iterations. Since packets are more quickly decoded in earlier iterations when G is lower, this explains the earlier increase of IMDR when G is lower. The same trend applies for CDMR vs iteration number across different G values. CDMR drops more quickly in successive iterations when G is lower than when G is higher, but this decreasing trend breaks earlier (i.e., CDMR's reduction slows down) when G is lower. The slowdown of CDMR's decrease occurs when IMDR starts to increase.

We also examine the trends in the IMDR and CDMR vs iteration number for different σ_{LN} values. When σ_{LN} is only 3 dB (low), IMDR drops progressively in successive iterations. However, when σ_{LN} is 6 dB or 9 dB (high), IMDR also reduces but rather stagnates in successive iterations. Meanwhile, CDMR drops more quickly in successive iterations when σ_{LN} is lower than when σ_{LN} is higher. In the case when σ_{LN} is 9 dB, the reduction of CDMR in successive iterations is rather very slow and the CDMR value in the 6th iteration is still quite high at about 0.12.

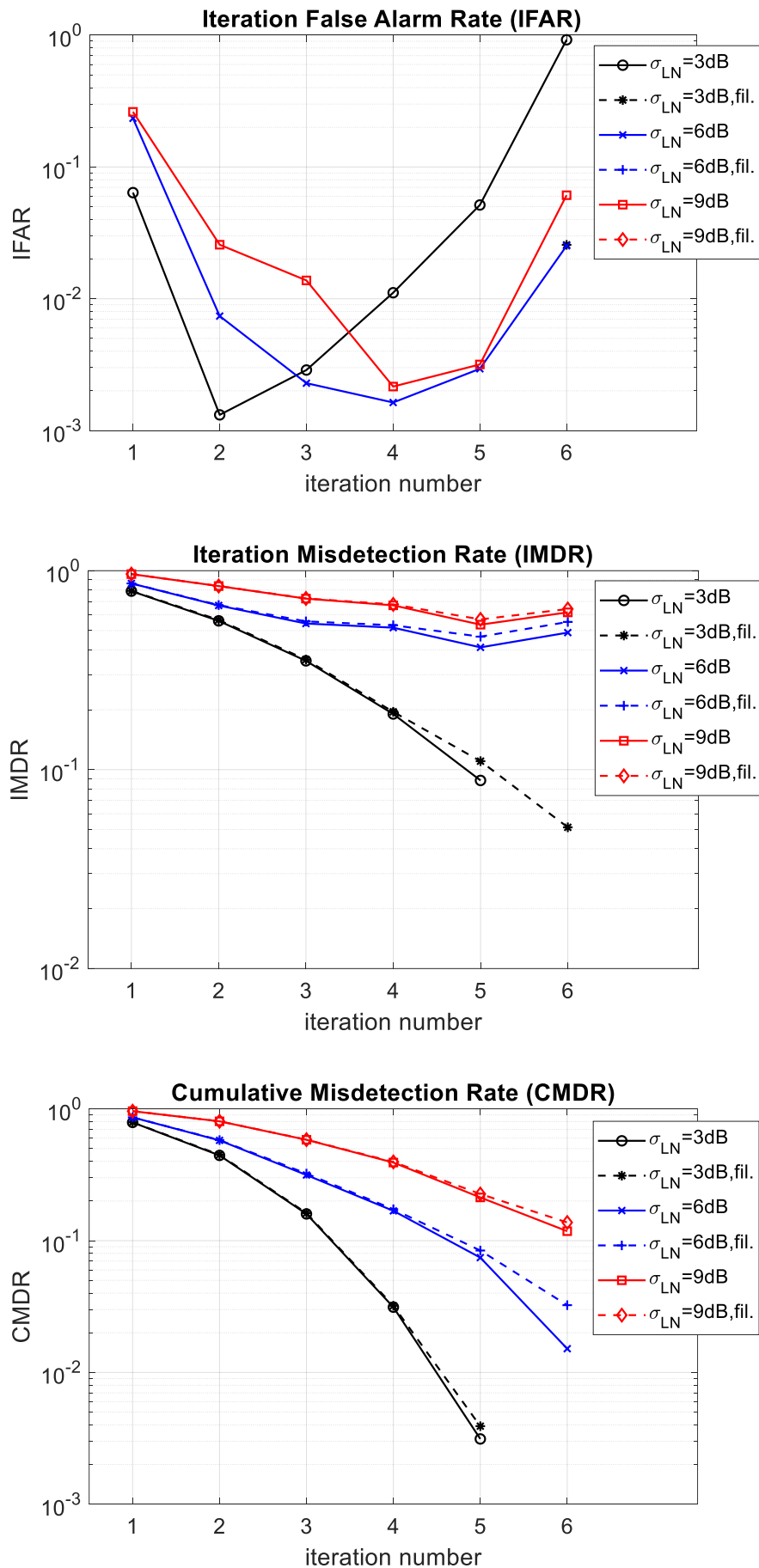


Figure 82. IFAR, IMDR and CMDR for different σ_{LN} values ($G = 1.0$, $E_b/N_0 = 14\text{dB}$)

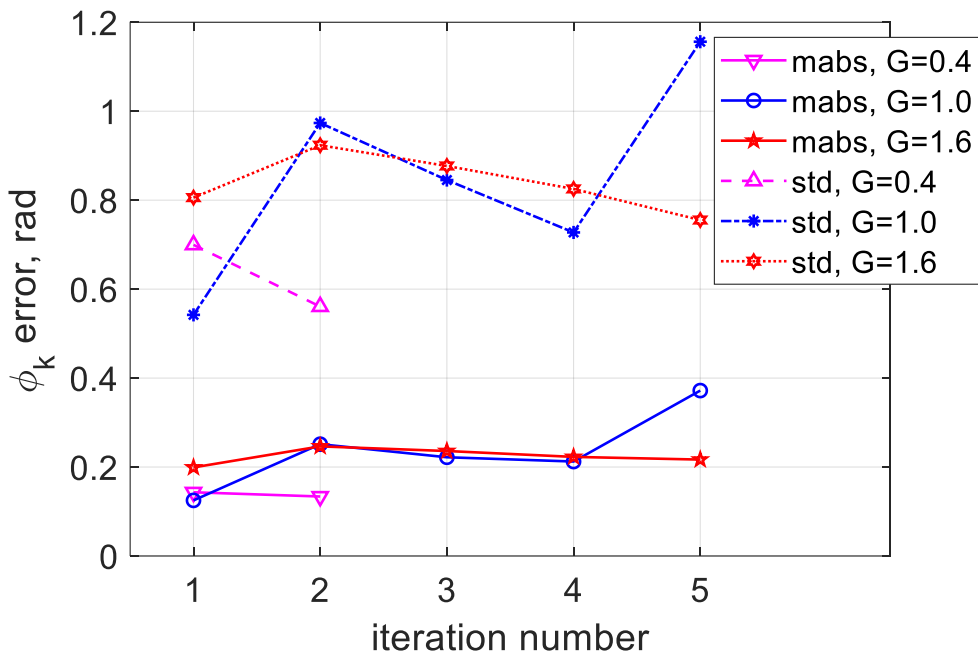
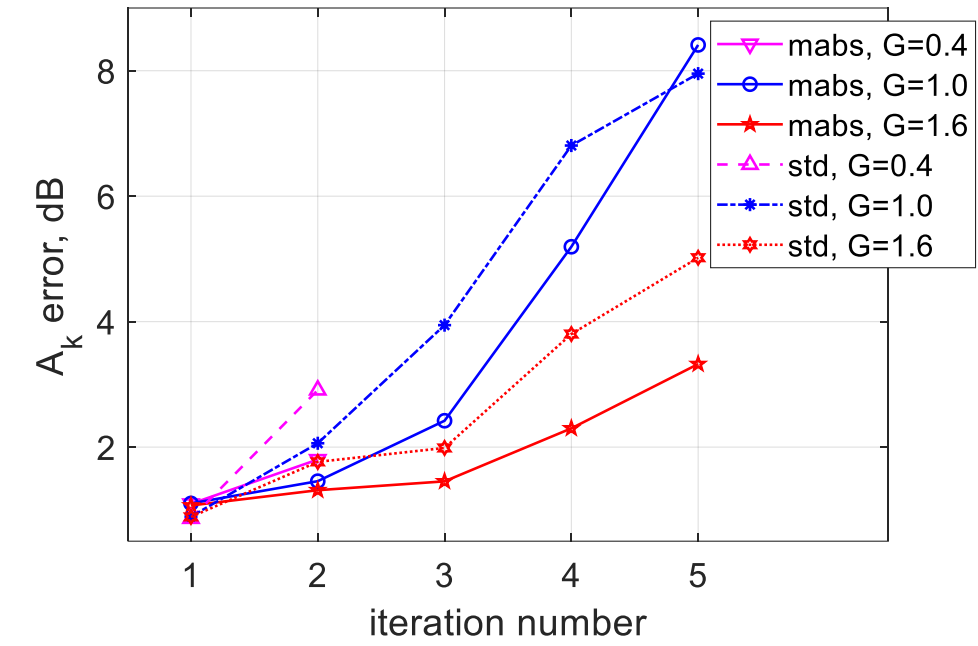
7.3 Channel Estimation

Figure 83 shows the fine channel estimation error results for different G values at constant $\sigma_{LN} = 6\text{dB}$, while Figure 84 shows the results for different σ_{LN} values at constant $G = 1.0$. Plots are given for mean absolute (mabs) and standard deviation (std) errors. In general, a gap in the data in an iteration means that for that specific case, there are no valid (previously undecoded) packets detected (so no data for averaging is available for that iteration). The trends described in the following consider the observations on other plots (for other σ_{LN} and G values).

Amplitude estimation mabs and std errors decrease with higher G , increase with higher σ_{LN} and increase with later iteration. Frequency shift estimation mabs and std errors increase with higher G and decrease with higher σ_{LN} . Frequency rate estimation mabs and std errors increase with higher G and decrease with higher σ_{LN} . Phase estimation mabs and std errors generally (or slightly) increases with higher G , and generally (or slightly) decreases with higher σ_{LN} , although the trends are not so consistent compared to those of frequency shift and rate estimation errors. Unlike amplitude estimation error, which apparently increases with later iterations, there are not obvious trends for phase, frequency shift and rate estimation errors vs iteration number. This is because amplitude estimation accuracy significantly depends on the desired signal level relative to the combined levels of MUI, accumulated residue power from imperfect interference cancellations and noise. In first iteration, MUI is high but higher power packets come out first. In later iterations, MUI is reduced but accumulated residue power (plus noise) becomes comparable to lower power packets. The range of mabs and std errors across $G = 0.1$ to 2.5 and $\sigma_{LN} = 3, 6, 9$ dB are summarized in Table 24.

Table 24. Typical range of channel estimation mean absolute (mabs) and standard deviation (std) errors across different G and σ_{LN} (5 iterations)

Parameters	Rough Channel Estimation		Fine Channel Estimation	
	mabs	std	mabs	std
$A_{k,dB}$	0.8~1.2 (it=1); 1.0~9.0 (it=3); 1.0~13.3 (it=5);	0.8~1.2 (it=1); 1.0~7.2 (it=3); 1.0~10.3 (it=5);	same	same
ϕ_k (rad)	0.3~1.7	0.7~2.5	0.03~0.60	0.06~1.30
f_k (Hz)	3.0~5.1	2.8~4.3	0.09~0.60	0.13~0.94
d_k (Hz/s)	1.8~2.9	2.1~3.5	0.10~0.64	0.13~0.94



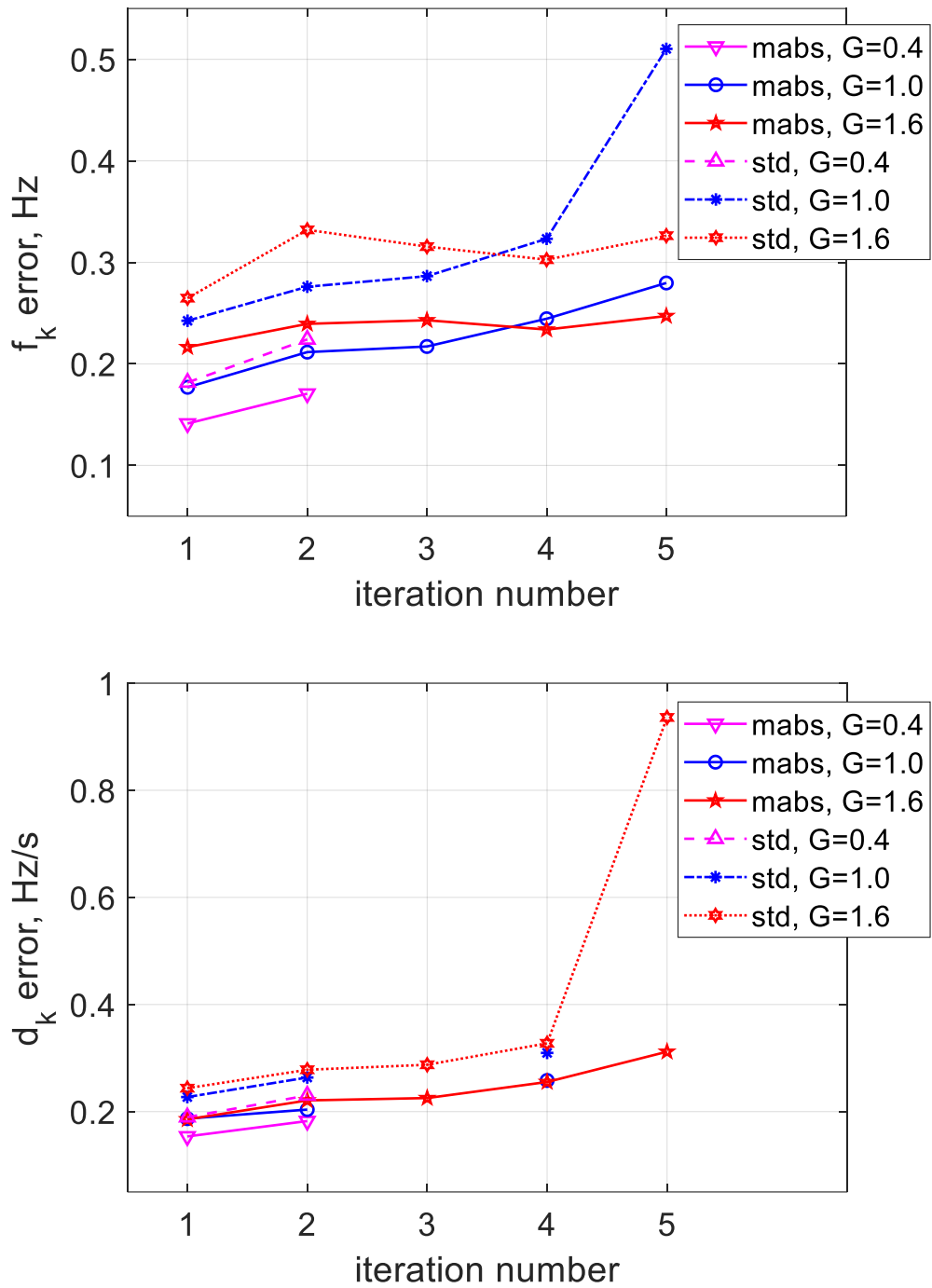
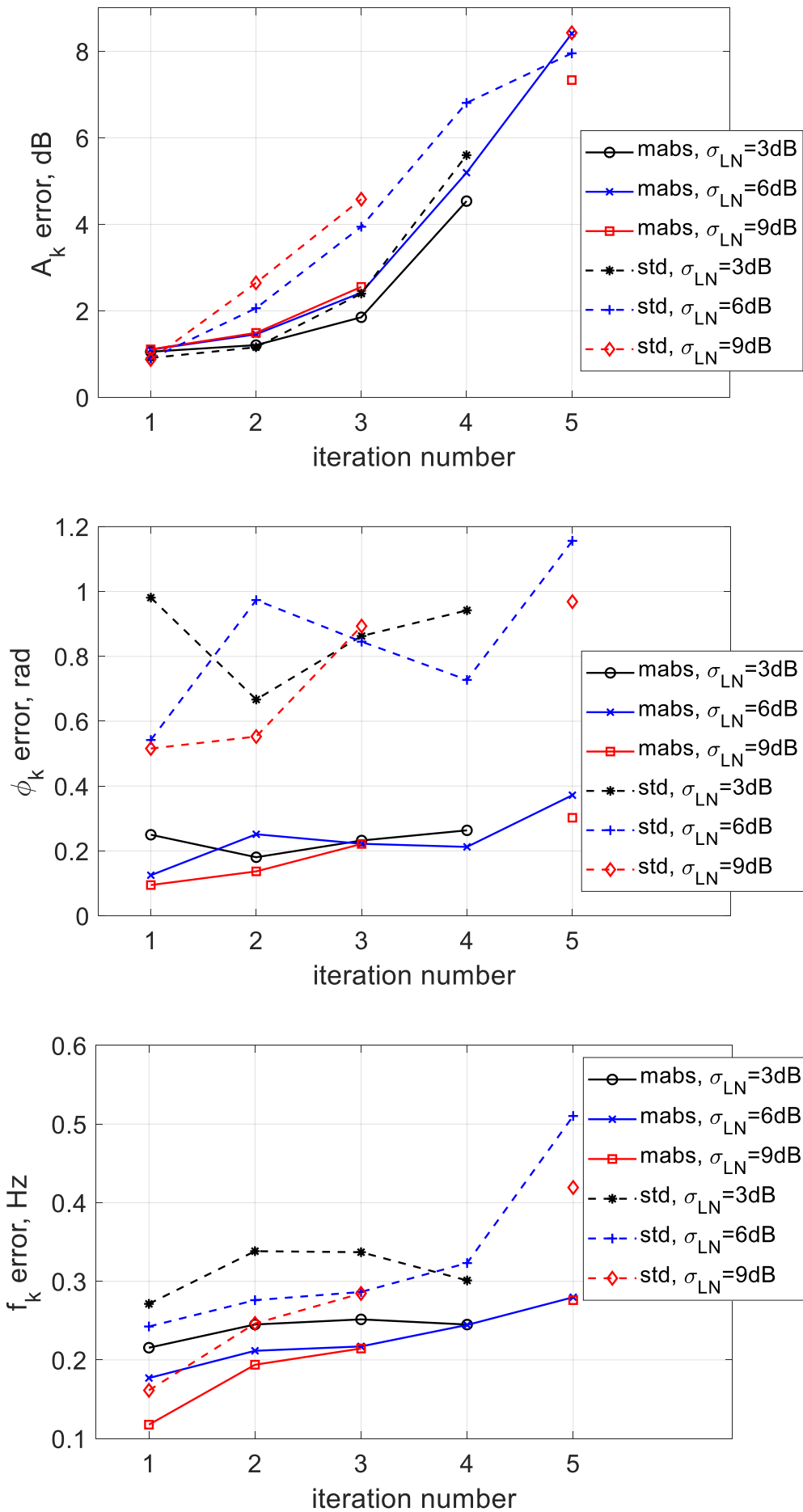


Figure 83. Fine channel estimation mean absolute (mabs) and standard deviation (std) errors for different G values ($\sigma_{LN} = 6\text{dB}$, $E_b/N_0 = 14\text{dB}$)



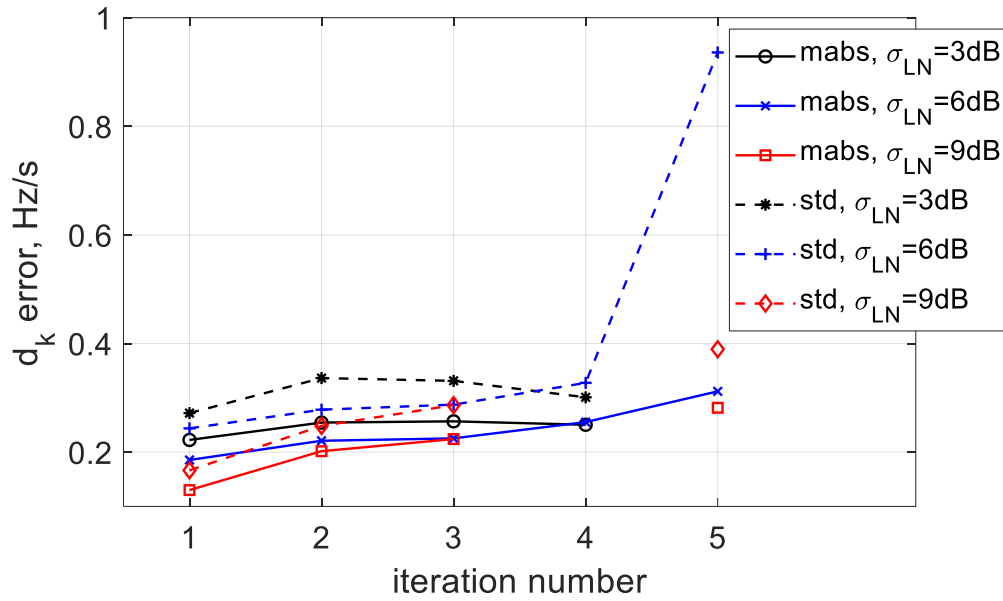


Figure 84. Fine channel estimation mean absolute (mabs) and standard deviation (std) errors for different σ_{LN} values ($G = 1.0$, $E_b/N_0 = 14$ dB)

7.4 THR, PLR and EE Assuming Perfect Detection and Channel Estimation

Figure 85 shows the PLR , THR and η_{EE} plots vs MAC load G for different σ_{LN} values at fixed $E_b/N_0 = 14$ dB with five iterations, assuming perfect packet detection and channel estimation (i.e., the ideal case where packet delays and channel parameters are known exactly). With higher σ_{LN} , that is, more received signal power variation, the maximum G in which the system can be operated before saturation is higher, although at the expense of higher PLR . As a result, the maximum achievable throughput is higher with higher σ_{LN} . At $\sigma_{LN} = 3$ dB (representing the case with non-tight power control), the maximum G is about 1.9 bps/Hz, giving a maximum THR of 1.9 bps/Hz with $PLR < 10^{-3}$. This result is quite close to the result in [6] at $\sigma_{LN} = 3$ dB (GEO orbit, fixed elevation). At $\sigma_{LN} = 6$ dB (representing the case without power control, with perfectly omnidirectional antennas), the maximum G is about 2.8 bps/Hz, giving a maximum THR of 2.6 bps/Hz with PLR of about $(3\sim 5)\times 10^{-2}$.

With even more signal variation, that is, at $\sigma_{LN} = 9$ dB (representing the case without power control, with wide beamwidth antennas), the maximum G is about 3.4 bps/Hz, giving a maximum THR of 2.9 bps/Hz with PLR of about 10^{-1} . Meanwhile, η_{EE} remains constant with increasing G below the saturation value and only slightly decreases with higher σ_{LN} . Thus, energy efficiency is barely affected by MAC load and received power variation when one operates below the saturation region. Operating in the saturation region or beyond gives very bad PLR , much lower energy efficiency and THR . This is because the extremely high MUI in such condition causes too many symbol errors beyond the error-correction capability of Turbo code.

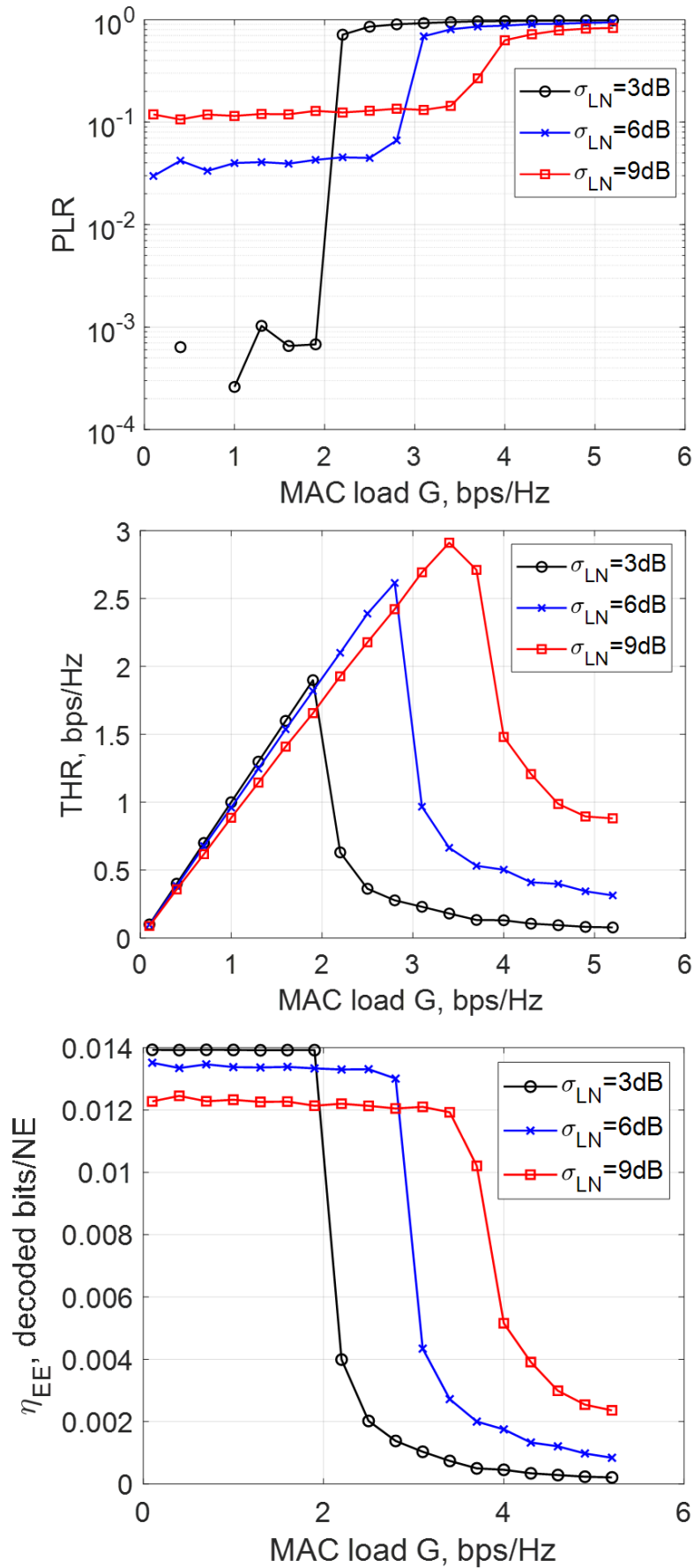


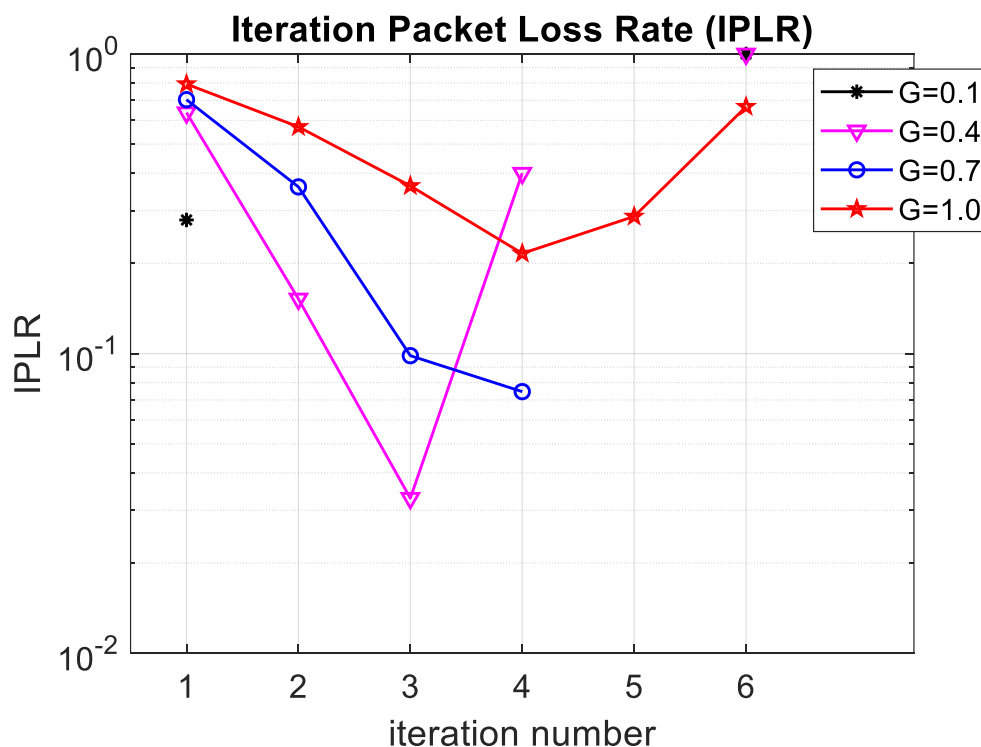
Figure 85. Simulation PLR, THR and η_{EE} for different G and σ_{LN} values ($E_b/N_0 = 14\text{dB}$, perfect detection and channel estimation, 5 iterations)

7.5 THR, PLR and EE Considering Actual Processing Algorithm

Figures 86-88 show the plots of iteration PLR (IPLR) and cumulative PLR (CPLR) vs iteration number for different G values (at constant $\sigma_{LN} = 3\text{dB}, 6\text{dB}, \text{ or } 9\text{dB}$, $E_b/N_0 = 14\text{dB}$), when applying the signal processing algorithm described in Chapter 6. Figures 89-90 show the corresponding plots for different σ_{LN} values (at constant $G = 0.4$ or 1.0 , $E_b/N_0 = 14\text{dB}$).

It can be noticed that CPLR appears to approach to a final value and reaches very close to this final value at a certain iteration number, which generally depends on the values of G and σ_{LN} . When $\sigma_{LN} = 3\text{dB}$ and G is low, it is possible that all packets can be decoded by the 4th iteration or earlier so that CPLR becomes 0 from that iteration (this is the reason for gaps in data in some figures). Otherwise, CPLR approaches a non-zero final value. The lower G is, the lower is the final CPLR value and the earlier it is to get to this value (i.e., CPLR drops more quickly when G is lower). Meanwhile, the lower σ_{LN} is, the lower is the CPLR value (at any iteration and the final value) and the faster CPLR drops.

Considering the CPLR plots across various G and σ_{LN} conditions, it can be fairly said that overall, there is only marginal CPLR improvement from 5th to 6th iteration. Comparing with the CMDR plots in Figures 81-82 – where it is evident that the reduction of CMDR from 5th to 6th iteration is still rather significant –, it can be said that although lower power packets (that have not been previously undetected) can be newly detected in the 6th iteration, those packets can no longer be decoded effectively. Therefore, five is evidently the optimum maximum number of iterations for running the formulated E-SSA algorithm, even without knowledge of G and σ_{LN} conditions or to be able to accommodate various conditions.



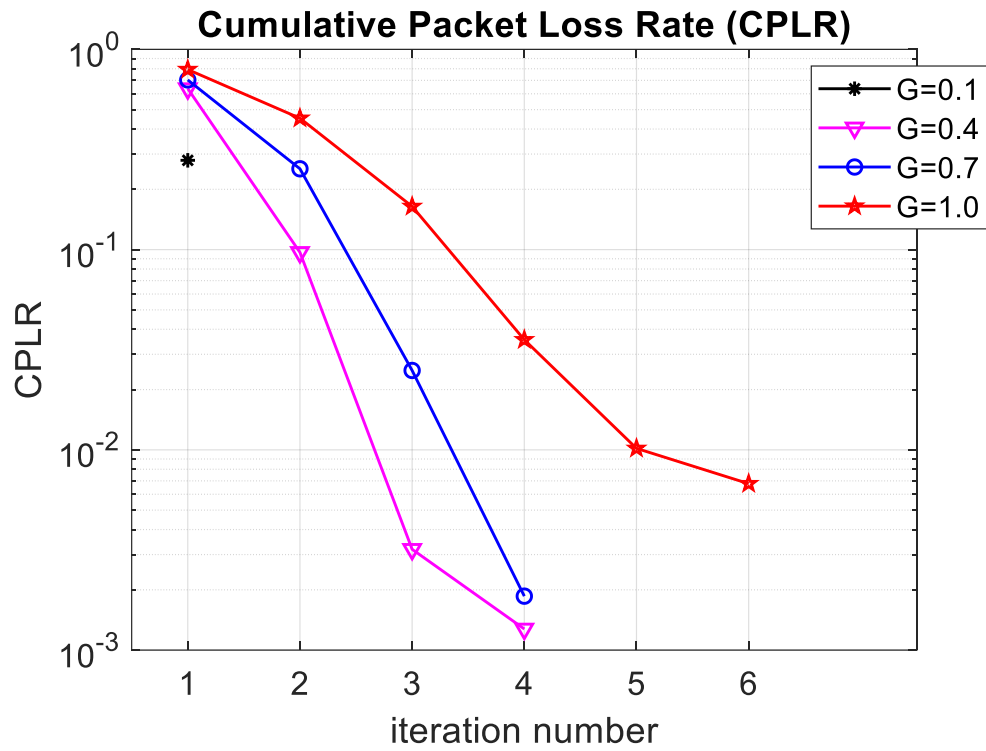
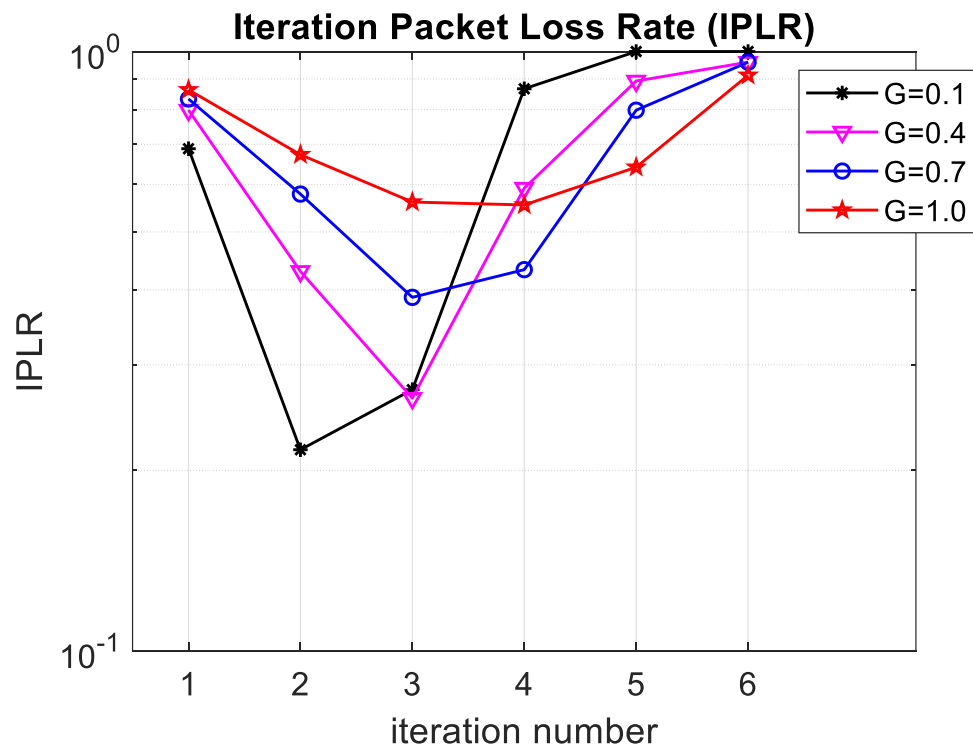


Figure 86. IPLR and CPLR for different G values ($\sigma_{LN} = 3\text{dB}$, $E_b/N_0 = 14\text{dB}$, actual algorithm)



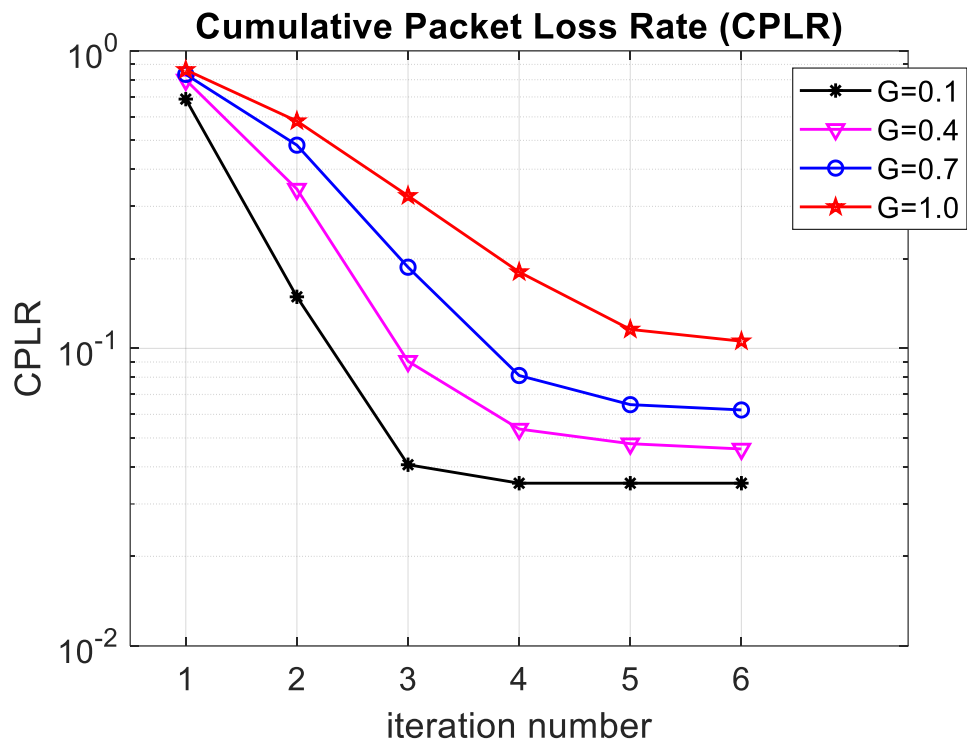
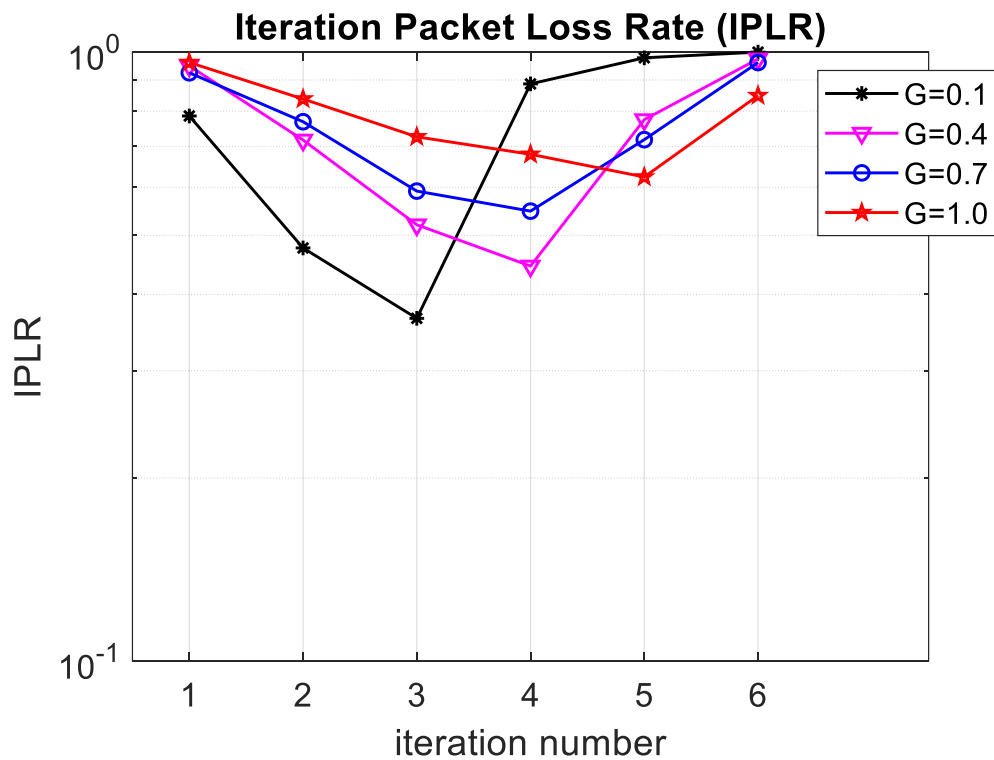


Figure 87. IPLR and CPLR for different G values ($\sigma_{LN} = 6\text{dB}$, $E_b/N_0 = 14\text{dB}$, actual algorithm)



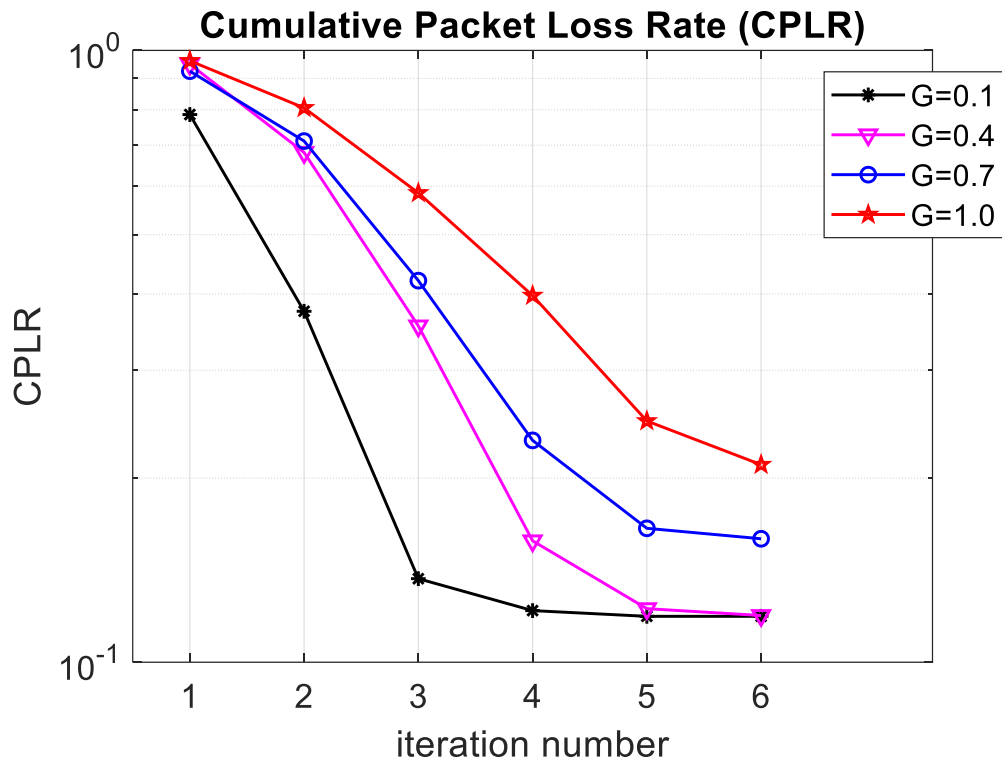
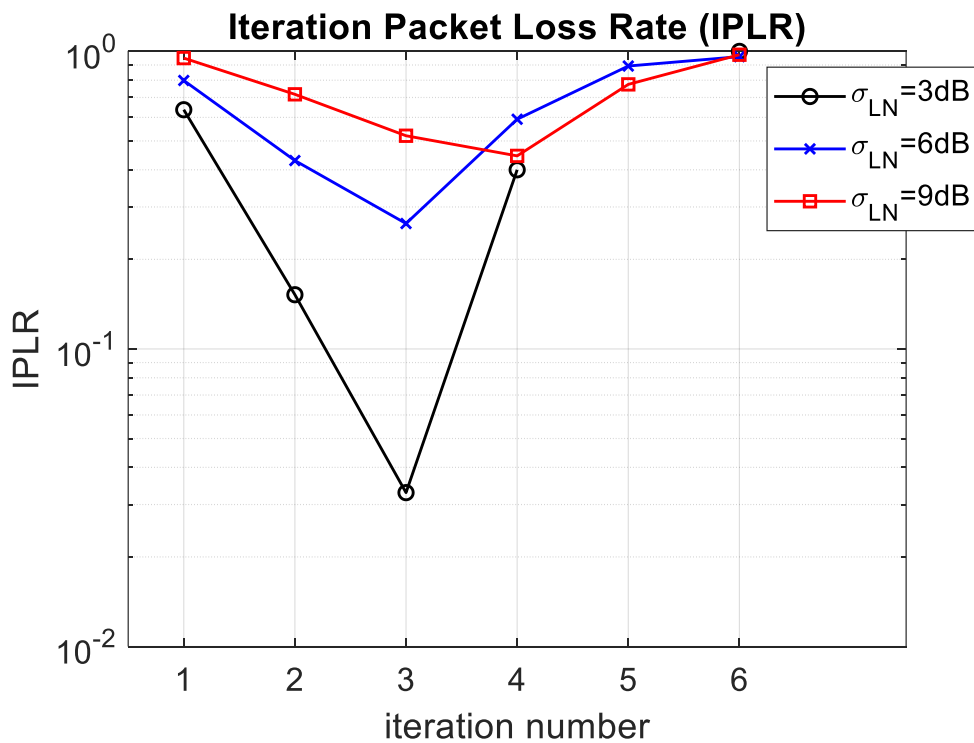


Figure 88. IPLR and CPLR for different G values ($\sigma_{LN} = 9\text{dB}$, $E_b/N_0 = 14\text{dB}$, actual algorithm)



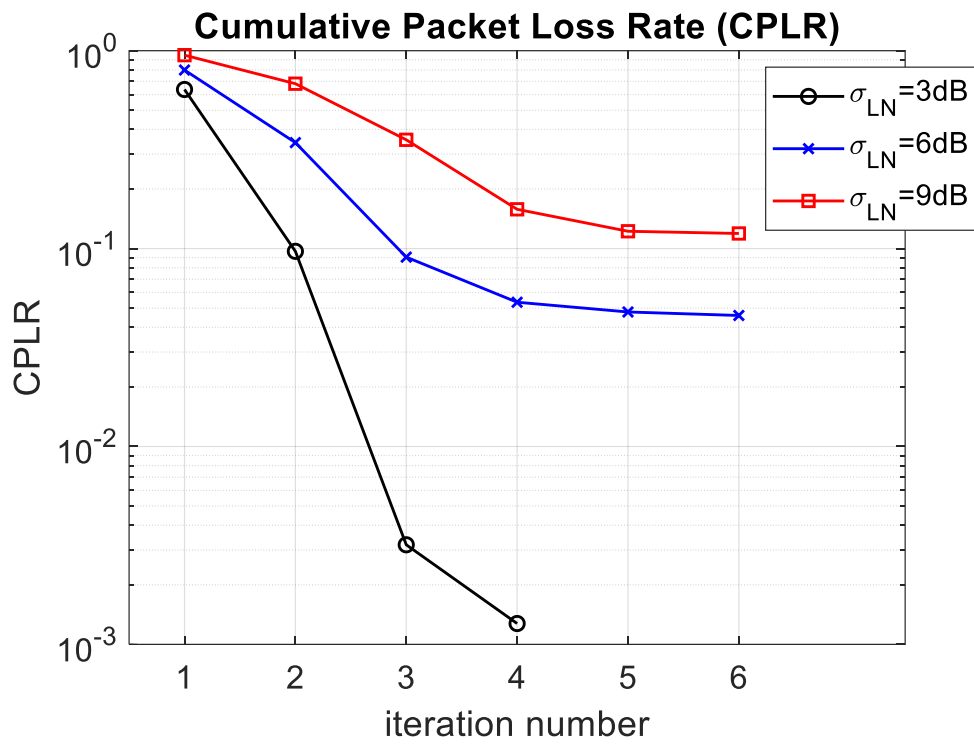
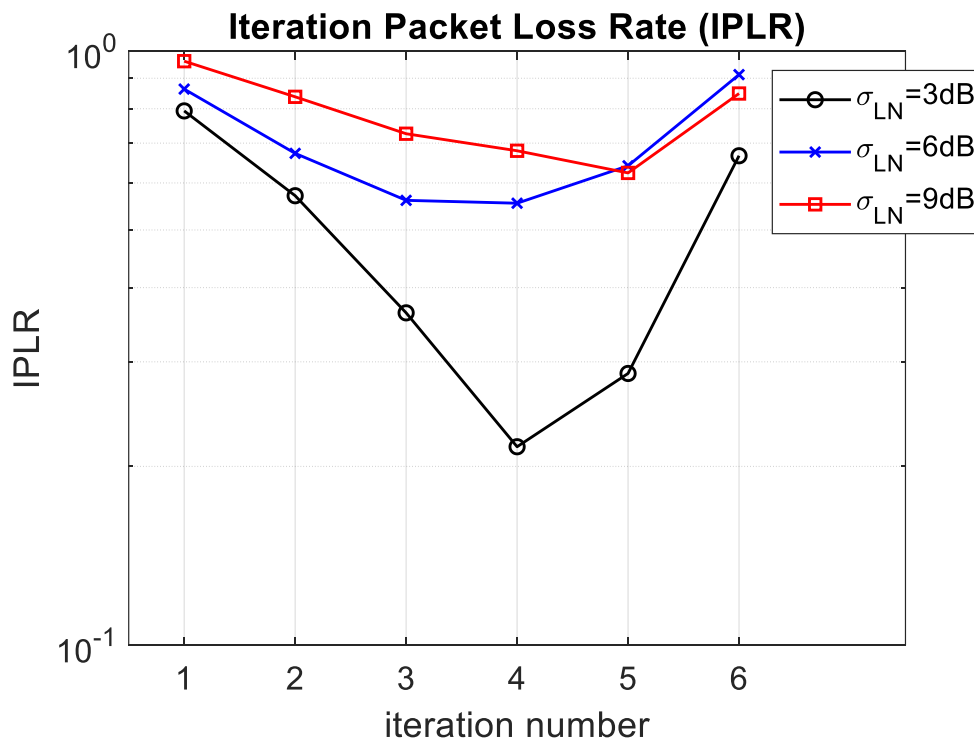


Figure 89. IPLR and CPLR for different σ_{LN} values ($G = 0.4, E_b/N_0 = 14\text{dB}$, actual algorithm)



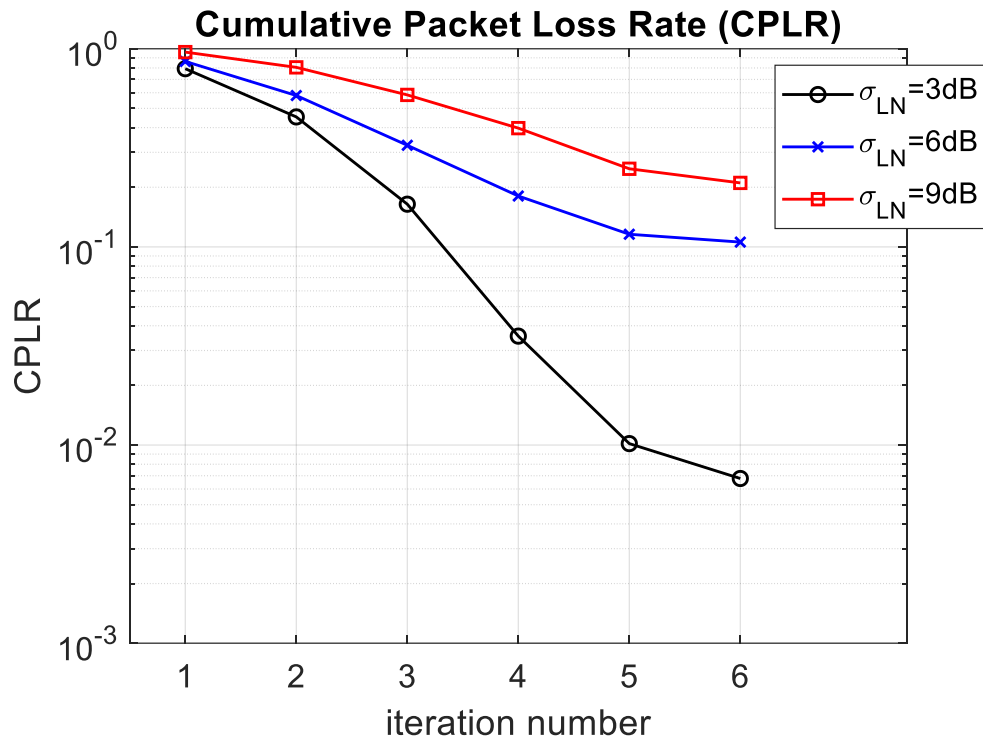
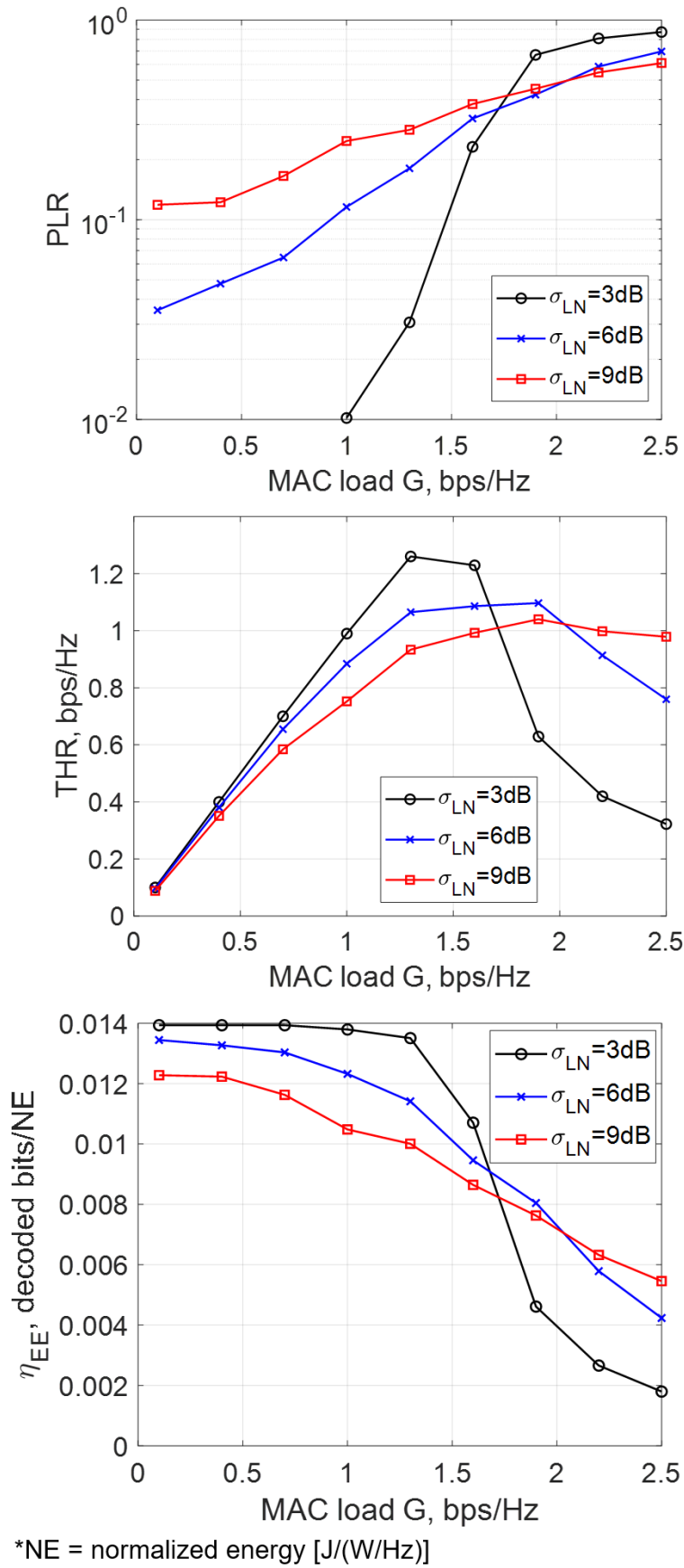


Figure 90. IPLR and CPLR for different σ_{LN} values ($G = 1.0$, $E_b/N_0 = 14\text{dB}$, actual algorithm)

Figure 91 shows the corresponding PLR , THR and η_{EE} plots vs MAC load G for different σ_{LN} values at fixed $E_b/N_0 = 14\text{dB}$ and five iterations, after applying the signal processing algorithm described in Chapter 6. With the actual processing algorithm, for a given G , PLR increases, THR decreases and η_{EE} decreases with higher σ_{LN} . However, here it is noticeable that G and σ_{LN} more adversely affect the three metrics. As a result, the linear region, which is the maximum MAC load G in which the system can be operated before saturation, is much smaller. At $\sigma_{LN} = 3\text{ dB}$ (representing the case with non-tight power control), the maximum G decreases to 1.3 bps/Hz, giving a maximum THR of 1.25 bps/Hz with $PLR < 0.03$. For both $\sigma_{LN} = 6\text{ dB}$ and 9 dB (representing the cases without power control), the saturation value for G also drops to 1.3 bps/Hz, THR plots have much more limited and less linear region, and PLR values are worse compared to those in perfect detection and channel estimation condition.

Moreover, for all three σ_{LN} values, PLR , THR and η_{EE} are more sensitive to MAC load such that even for $G < 1.3\text{ bps/Hz}$, we see increasing PLR and decreasing η_{EE} with increasing G (compared with relatively constant plots in Figure 85). Considering the said limits for G , the maximum THR for $\sigma_{LN} = 6\text{ dB}$ and 9 dB are about 1.1 bps/Hz and 0.9 bps/Hz, respectively. However, if we consider the target $PLR < 5\%$, it is impossible to meet this with any G when $\sigma_{LN} = 9\text{ dB}$. For $\sigma_{LN} = 6\text{ dB}$, it is possible to meet PLR requirement when $G < 0.5$. For $\sigma_{LN} = 3\text{ dB}$, it is possible to meet PLR requirement when $G < 1.4$.



*NE = normalized energy [J/(W/Hz)]

Figure 91. Simulation PLR, THR and η_{EE} for different G and σ_{LN} values ($E_b/N_0 = 14\text{dB}$, actual algorithm, 5 iterations)

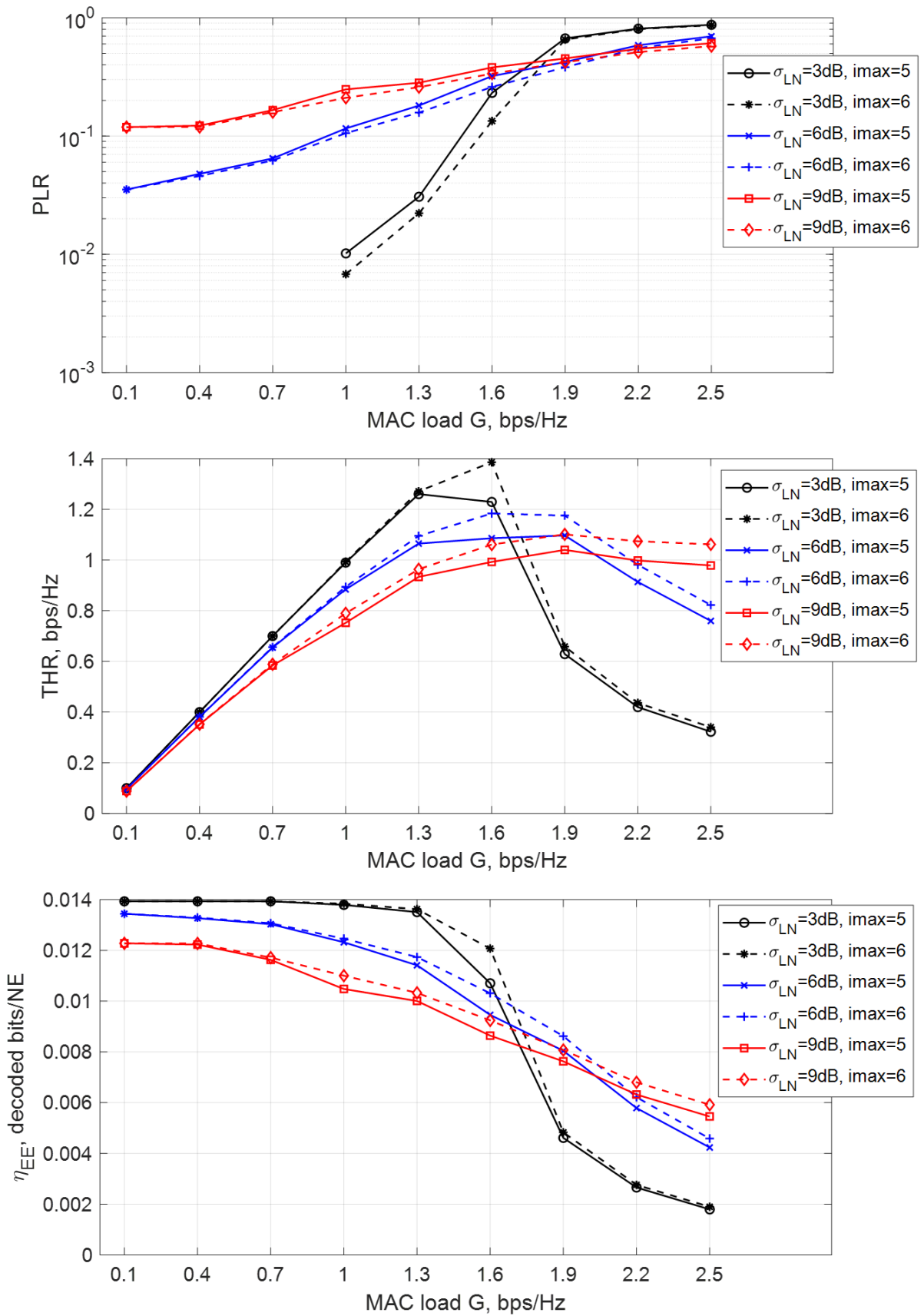
Figure 92 compares the corresponding plots for five and six iterations, which suggests that there is only very small improvement gained in proceeding to 6th iteration after 5th iteration. Since there is very little benefit from six iterations, five iterations can be considered to be the optimum number of iterations for running the formulated E-SSA algorithm. The worse *PLR* and *THR* results can be explained by the imperfect packet detection and channel estimation algorithms whose performance are discussed in Sections 7.1 and 7.2. Firstly, cumulative misdetection rates (*CMDR*), even after 5 or 6 iterations, are quite high.

For example, at $G = 1.0$ and $\sigma_{LN} = 6$ dB, after 5 iterations, *CMDR* is ~ 0.08 and *PLR* is ~ 0.11 . Meanwhile, at $G = 1.0$ and $\sigma_{LN} = 9$ dB, after 5 iterations, *CMDR* is ~ 0.20 and *PLR* is ~ 0.23 . On the other hand, at $G = 1.0$ and $\sigma_{LN} = 6$ dB, after 6 iterations, *CMDR* is ~ 0.03 while *PLR* is ~ 0.10 . Similarly, at $G = 1.0$ and $\sigma_{LN} = 9$ dB, after 6 iterations, *CMDR* is ~ 0.13 while *PLR* is ~ 0.20 . If we only observed the data after five iterations, we might be tempted to say that majority of packet losses are caused by packets being not yet detected and the remaining smaller portion are due to demodulation/decoding error. However, since we also examined the data after six iterations, we realized that while *CMDR* can be reduced by proceeding to 6th iteration, those lower power newly detected packets can no longer be decoded effectively. Therefore, we can say that overall, packet losses can be attributed – in mutually significant proportions – to both packet misdetections and demodulation/decoding errors.

As previously mentioned, two factors cause packet misdetections. First is received amplitude variations such that at every iteration, higher σ_{LN} increases occurrence probability of packets having amplitudes lower than detection threshold. Second, although these lower power packets are supposed to be detectable in succeeding iterations, a higher MAC load G leads to greater residue interference power whose level may be enough to obscure some of the lower power packet signals. In fact, it is observed that re-detection of already decoded packets becomes more frequent in later iterations, with residual power still enough for the previously decoded (and supposedly cancelled) packet to be still decodable. This is further complicated by the worsening amplitude estimation accuracy in later iterations.

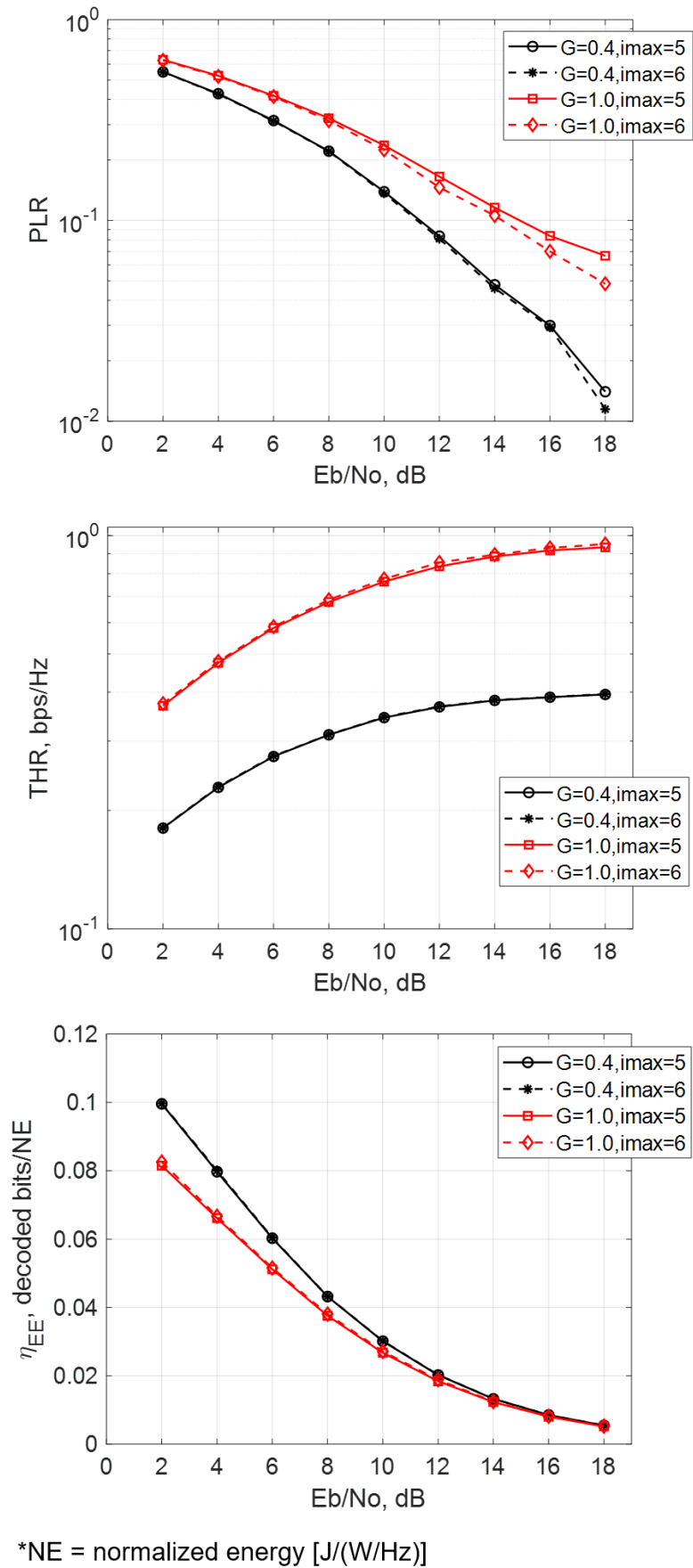
As for demodulation/decoding, although MUI power should decrease after cancelling the decoded packets, accumulated residue power from imperfect interference cancellation hampers not only detection of lower power packets in later stages (as described above), but also demodulation/decoding of detected lower power packets. Therefore, even small channel estimation errors can adversely impact packet detection and demodulation/decoding, and consequently the *PLR*, especially when σ_{LN} is high.

The *PLR* and *THR* can be improved by operating with higher E_b/N_0 (i.e., increasing transmit power) as shown in Figure 93, although of course this sacrifices energy efficiency. Plots in Figure 93 show the trade-offs between performance and energy efficiency.



*NE = normalized energy [J/(W/Hz)]

Figure 92. Simulation PLR, THR and η_{EE} for different G and σ_{LN} values ($E_b/N_0 = 14\text{dB}$, actual algorithm, 5 vs 6 iterations)



*NE = normalized energy [J/(W/Hz)]

Figure 93. Simulation PLR, THR and η_{EE} for different E_b/N_0 values ($\sigma_{LN} = 6\text{dB}$, actual algorithm, 5 vs 6 iterations)

Chapter 8: Nanosatellite Constellation for Global Coverage

In this chapter, we tackle the problem of designing a S&F nanosatellite constellation that provides a global communication coverage to ground sensor terminals (GSTs) deployed in any remote location on the planet. We use AGI's Systems Tool Kit (STK) software to simulate a selection of constellations in terms of communication coverage, which is computed based on satisfaction of link budget. Link budget analysis applies the results on E-SSA protocol obtained in the previous chapter. The goal is to come up with a small constellation size (i.e., low-cost) that only requires a low transmit power from GSTs to meet the link budget requirement.

8.1 Constellation Design Considerations

There are several interrelated factors that must be considered when designing a communication satellite constellation: (a) constellation type or configuration, (b) number of planes, (c) number of satellites per plane, (d) orbital altitude, (e) other orbital parameters e.g. inclination, right ascension of the ascending node (RAAN), phasing (argument of periapsis and true anomaly), and (f) communication link budget constraints. Factors (a) to (e) are orbit-related that have practical implications on the cost and logistics for realizing the constellation. Factor (f) is directly related to GST transmit power and has practical implications on the cost and complexity of GSTs. Setting the GST transmit power high would normally involve a more costly and complex GST design (e.g., RF amplifier, higher capacity electrical power system). Doing this would reduce the required number of satellites (since as a result, each satellite can cover a wider area due to lower minimum required elevation) or permit higher altitude (which would increase coverage area per satellite). On the other hand, with more satellites flying on a lower altitude, a lower GST transmit power and thus simpler GST design would be needed.

The cost of realizing a constellation heavily depends on too detailed project management and logistical considerations (e.g., contracts with one or more launch providers, timing of launches, etc.) so it is not straightforward to relate the cost to the orbit-related factors. However, it would be reasonable for cost and logistical purposes to target a fewer number of planes, then a lower altitude, and lastly, fewer satellites per plane. Aside from considering the number of planes and satellites per plane, to achieve a global coverage it would be necessary to distribute the satellites in multiple planes which have either different inclinations or RAANs or both.

In terms of constellation type, Walker constellation, wherein all satellites are distributed in multiple planes with the same inclinations but different RAANs, is commonly employed for earth observation and telecommunications missions. For example, a high-inclination Walker constellation can cover all latitudes (and all longitudes at different times depending on the number of planes) but the percent time coverage in lower absolute latitude regions (closer to the equator) would be less than those in near polar regions (which would enjoy more frequent revisits and access times). Meanwhile, a low-inclination Walker constellation would provide better percent time coverage to lower absolute latitude regions than near polar regions (or no coverage at all). Nonetheless, with sufficiently high number of planes and number of satellites, a 98°

inclination Walker constellation can always provide a fully global coverage. On the other hand, a hybrid constellation, that is consisting of multiple planes with different inclinations and RAANs, can provide a more balanced (or less skewed) percent time coverage across all latitudes on the planet.

Again, determining which is the better option would also require very detailed project management and logistical plans involving comparison of available options for nanosatellite launches. Recently, already operational, soon-to-be-operational and under development commercial small launchers provide customers with two possible options: dedicated launch or ride-share launch. Some surveys on the status of operational and under development small launchers are given in references [171] and [172]. The burgeoning industry in small launchers (or so-called “micro-launchers”) has been driven particularly by the potential offered by small satellite deliveries [173][174]. While small launcher development has been happening, more than a thousand nanosatellites have been launched. Figures 94 and 95 show the distribution of the number of launched nanosatellites in terms of orbit and launchers. For obvious reasons, deployment by release from the ISS has been the most predominant means, which explains why the 400 km 51.6° orbit has the largest share. Besides that, there is also a significant portion of the population of launched nanosatellites with 470km-780 km altitude, 97.5°-98.2° inclination. Although less common, there have been nanosatellites with lower inclination orbits.

As for nanosatellites, rideshare launches are likely (and still going to be) the more affordable option (being secondary payloads of small launchers primarily booked for mini-satellites or other larger small satellite classes). Rather than booking dedicated launches, a nanosatellite project is likely to seek multiple rideshare launch opportunities from one or more launch providers. For instance, it is possible to book several scheduled rideshare launches from one launch provider: one inclination but perhaps different RAANs. One can also imagine booking several scheduled rideshare launches from several launch providers: different inclinations and RAANs. In either case, though, it might be difficult to get the desired exact inclinations and RAANs. To simplify the constellation design and simulation process in this work, we assume the designed inclinations and RAANs are met. If constellation size is quite large, the results may still approximate the characteristics of the case with inexact or with-error inclinations and RAANs. On the other hand, considering a “constellation” with randomly generated orbital parameters, as done in a previous work, will produce results that might be difficult to replicate or make sense of.

Also, as there is no explicit mathematical relationship between GST transmit power vs GST cost and complexity, arbitrarily low transmit powers less than or equal to 100 mW are tried.

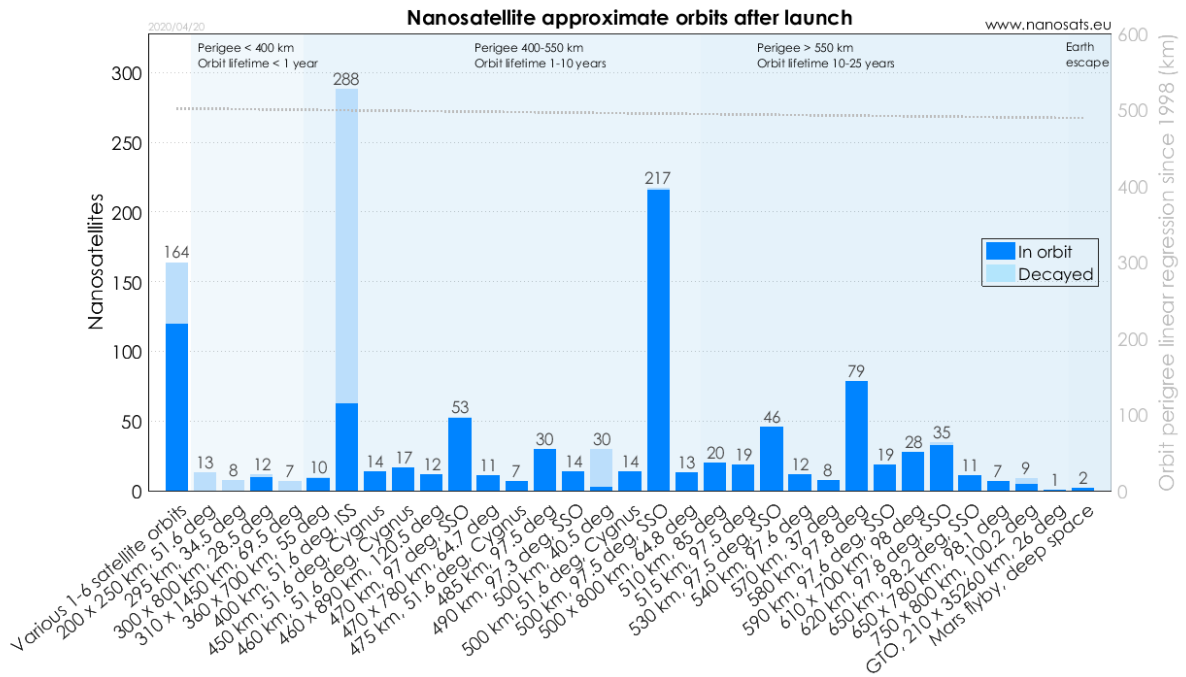


Figure 94. Nanosatellite approximate orbits after launch (source: www.nanosats.edu)

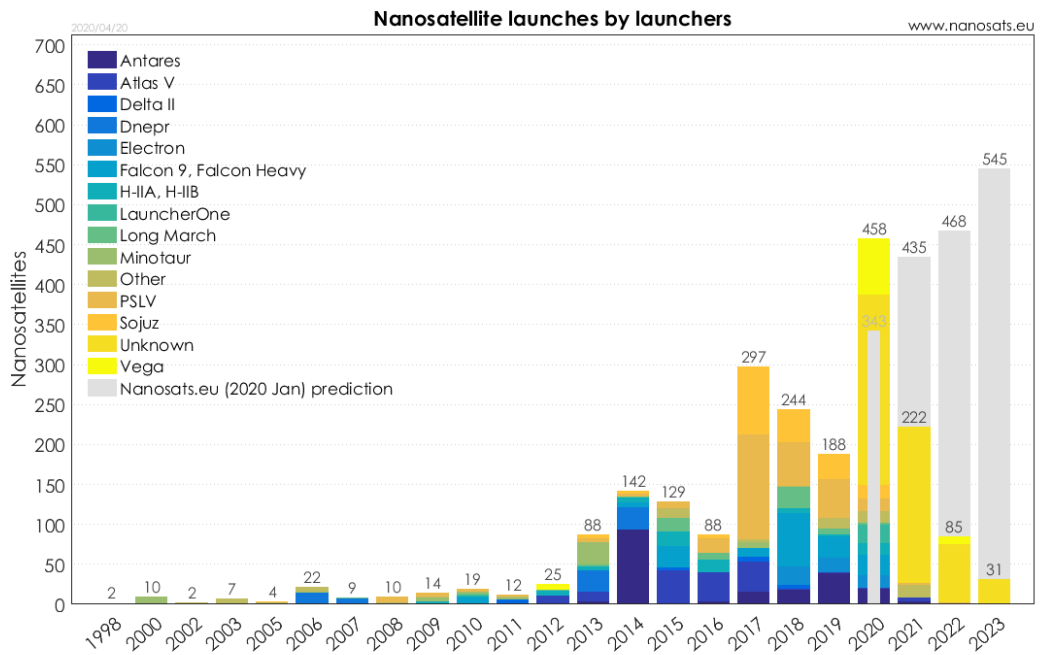


Figure 95. Nanosatellite launches by launchers (source: www.nanosats.edu)

8.2 Constellation Simulation Setup and Design Procedure

In the following, we consider two types of constellations: Walker Delta and Hybrid. The number of planes is denoted by N_p , the number of satellites per plane by N_s , and the total number of satellites by $N_{sat} = N_p \times N_s$. In Walker Delta constellation, inclination is fixed to 98° and RAAN is spread between 0° and 360° with offset between two consecutive planes. In Hybrid constellation, inclinations and RAANs are spread in the ranges of 0° - 100° and 0° - 360° , respectively. Details for the GST transmitter model, satellite

receiver model and satellite orbit are listed in Table 25 below. In addition to meeting the link budget requirement, a minimum satellite elevation of 5° must be met to establish communication access from a GST to any satellite in the constellation. A 3D illustration of the system model in STK is given in Figure 96.

To facilitate the evaluation of communication coverage, representative GSTs are placed at various latitudes from -90° to $+90^\circ$ with 10° intervals (longitude fixed to 0°). STK then computes all accesses from each GST to any constellation member. There is access from a GST when there is at least one satellite meeting the link budget and minimum elevation requirements. The assumed value of E_b/N_0 for demodulation is set to 15 dB and link margin requirement is set to 5 dB, which means the required threshold value for E_b/N_0 is 20 dB. For each test latitude, the *percent coverage time (PCT)* is evaluated. In addition, *percent area coverage (PAC)* is evaluated. PAC is computed by the software at any time instant as the total global area wherein a satellite is visible (not necessarily communicable, i.e., satellite elevation is $\geq 0^\circ$) over the total global area, although we look at the minimum, maximum and mean PAC.

The following summarizes the overall sequence of steps:

- (1) Start with a 3 x 3 Hybrid constellation. Given a fixed $P_{TX} = 20$ dBm (100 mW), compute the AD, ATG, PCT at all latitudes and the PAC for different orbit altitudes: 500 km, 600 km, 700 km, 800 km and 900 km. Do the same for fixed $P_{TX} = 17$ dBm (50 mW) and $P_{TX} = 14$ dBm (25 mW). For each P_{TX} , choose the optimum altitude that gives the highest PCT. For a given P_{TX} , we can expect that with low altitude, visibility area is smaller and coverage area is mainly constrained by the minimum required elevation; with high altitude, visibility area is bigger but coverage area is mainly constrained by the link budget requirement (i.e., GST-satellite distance). With a higher P_{TX} , a higher altitude is possible, thus providing a wider coverage area and consequently, when scaling up, smaller constellation size would be needed for full global coverage. With a lower P_{TX} , altitude must be lowered, thus providing a smaller coverage area and larger constellation size would be needed for full global coverage. While a higher altitude is advantageous for achieving full global coverage with a smaller constellation size, it would require higher P_{TX} and possibly more costly satellite launcher. Therefore, we select a P_{TX} and altitude that provides a good balance among higher PCT (determines the upscaled constellation size), lower P_{TX} and lower altitude (if possible, <800 km).
- (2) Fixing the P_{TX} and altitude to the selected values in (1), try out bigger size Walker Delta and Hybrid constellations. Compute the AD, ATG, PCT at all latitudes and the PAC.
- (3) Determine the minimum constellation sizes for both Walker Delta and Hybrid constellations that provide a **minimum PCT of 95% across all latitudes** and **minimum PAC of 100%**.

Table 25. GST Transmitter, Receiver and Satellite Constellation Models in STK AGI

Parameter	Value
Transmitter (GST)	
Object type and model	Complex Transmitter model, Transmitter object attached as a child to a Place object
Center Frequency	402 MHz
Transmit Power, P_{TX}	To be determined (nominal: 50 mW, unless otherwise specified)
Data Rate	333 bps
Antenna	$\lambda/2$ dipole, right-hand circular polarization
Modulator	BPSK-Conv-3-1-6, with CDMA spreading (substitute model for BPSK, rate 1/3 Turbo code, SSA)
Cable loss	2 dB
Positions	Longitude: 0° Latitude: $\pm 90^\circ$, $\pm 80^\circ$, $\pm 70^\circ$, $\pm 60^\circ$, $\pm 50^\circ$, $\pm 40^\circ$, $\pm 30^\circ$, $\pm 20^\circ$, $\pm 10^\circ$, 0°
Receiver (onboard satellite)	
Object type and model	Complex Receiver model, Receiver object attached as a child to a Satellite object
Center Frequency	402 MHz (auto-track)
Eb/No threshold for demodulation	15 dB
Link margin threshold	5 dB
Antenna	$\lambda/2$ dipole, right-hand circular polarization
Demodulator	Same as above (auto-select)
Filter + implementation losses	3 dB
System noise temperature	1000 K
Satellite Orbit	
Orbit type	circular
Argument of perigee	0° in all cases
Altitude	To be determined (nominal: 700 km unless otherwise specified)
Inclination	98° (for Walker Delta constellation); spread between 0° and 100° (for Hybrid constellation)
RAAN	Uniformly spread between 0° and 360°
True anomaly	Uniformly spread between 0° and 360°
Minimum elevation requirement for communication access	5°

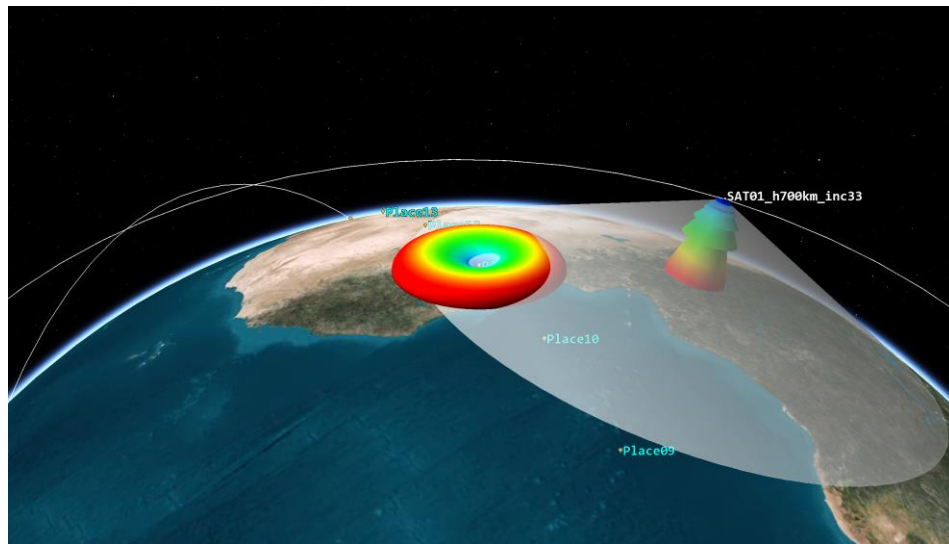


Figure 96. 3D illustration of the system model in STK showing the GST and satellite antenna radiation patterns and visibility area

8.3 Selecting Transmit Power and Orbital Altitude

Figure 97 shows a snapshot of the 3x3 hybrid nanosatellite constellation as simulated in STK. There are three planes with three satellites per plane: Plane 1 (inclination = 33°, RAAN = 0°, TA = 0°, 120°, 240°); Plane 2 (inclination = 67°, RAAN = 120°, TA = 0°, 120°, 240°); and Plane 3 (inclination = 100°, RAAN = 240°, TA = 0°, 120°, 240°).

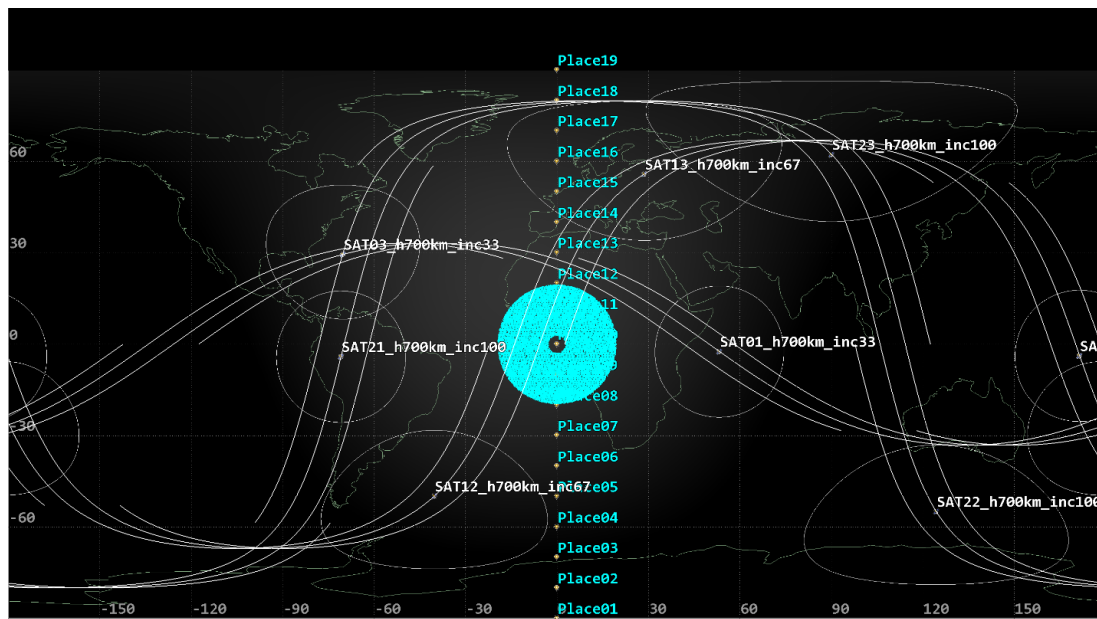


Figure 97. 3x3 Hybrid constellation simulated in STK

Figure 98 shows the average PCT (percent coverage time) results plotted vs orbital altitude for P_{TX} equal to 14 dBm (25 mW), 17 dBm (50 mW) and 20 dBm (100 mW). For $P_{TX} = 14$ dBm, coverage area is constrained by the link budget requirement so access can be made only if satellite altitude is low (<600 km). Optimum altitude is somewhere below 500 km, giving an average PCT of about 16%. For $P_{TX} = 17$ dBm, the optimum altitude is 700 km, giving an average PCT of about 28%. Below 700 km, coverage area

is limited by the minimum elevation requirement; and above 700 km, coverage is limited by the link budget requirement. For $P_{TX} = 20$ dBm, coverage area is not constrained by the link budget requirement when altitude is between 500 km and 900 km; it is limited only by the minimum elevation requirement. Average PCT increases linearly with altitude and the optimum altitude is somewhere above 900 km, giving an average PCT of more than 35%. For upscaling the constellation, P_{TX} and satellite altitude equal to 17 dBm and 700 km, respectively, are selected.

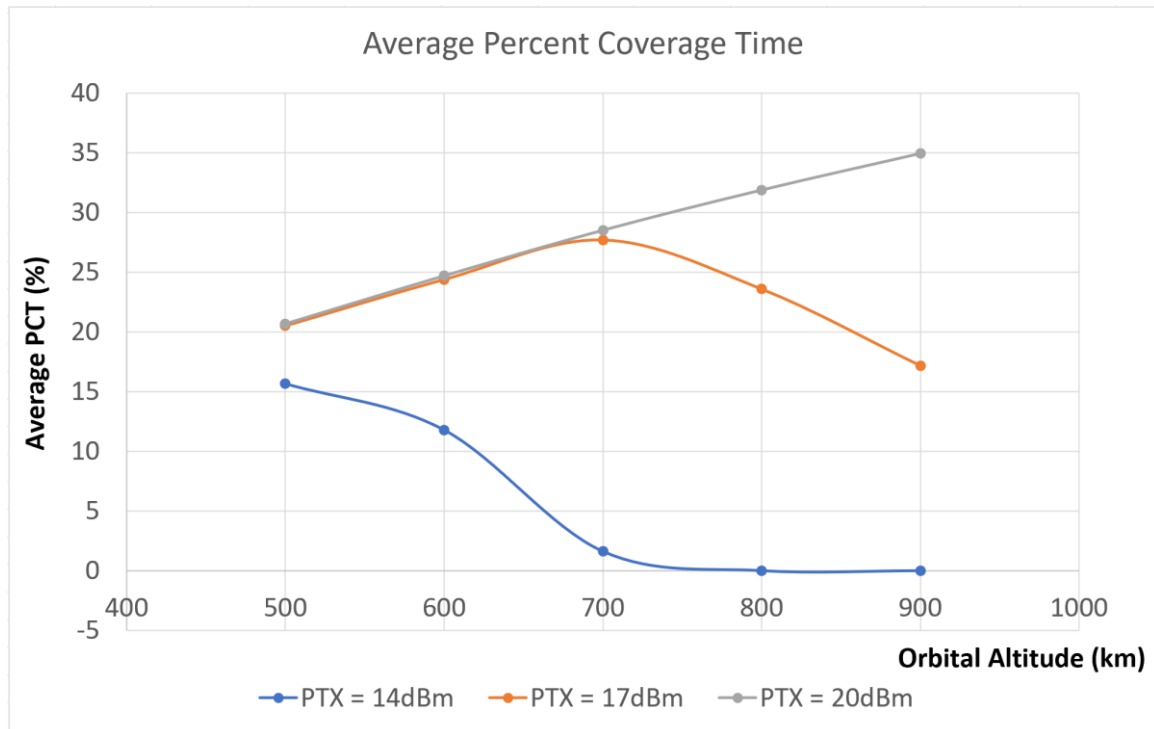


Figure 98. Average percent coverage time (across all latitudes) vs orbital altitude for different P_{TX}

8.4 Coverage for Larger Constellations

Table 37 in Appendix 6 provides the orbital parameters of the Walker Delta and Hybrid constellations that were simulated. Figure 99 shows the PCT across different latitudes for Walker Delta constellations while Figure 100 shows for Hybrid constellations. Figure 101 compares the PCT plots for larger Walker Delta and Hybrid constellations. Compared to Walker Delta constellations, Hybrid constellations provide more even coverage across all latitudes. For the Walker Delta constellations, because of high inclination used, near polar regions (higher absolute latitudes) enjoy more frequent revisits and satellite passes than near equatorial regions (lower absolute latitudes). This explains why near polar regions have higher PCT than near equatorial regions. A close examination of Figure 101 will reveal that to achieve the target PCT of more than 95% across all latitudes, a 9x10 Hybrid constellation or a 10x10 Walker Delta constellation would be required (although for the latter, PCT is slightly below 95% at $\pm 10^\circ$ latitudes). Table 26 provides the PAC for different constellations. Both the 9x10 Hybrid constellation and the 10x10 Walker Delta constellation meet the 100% minimum PAC requirement.

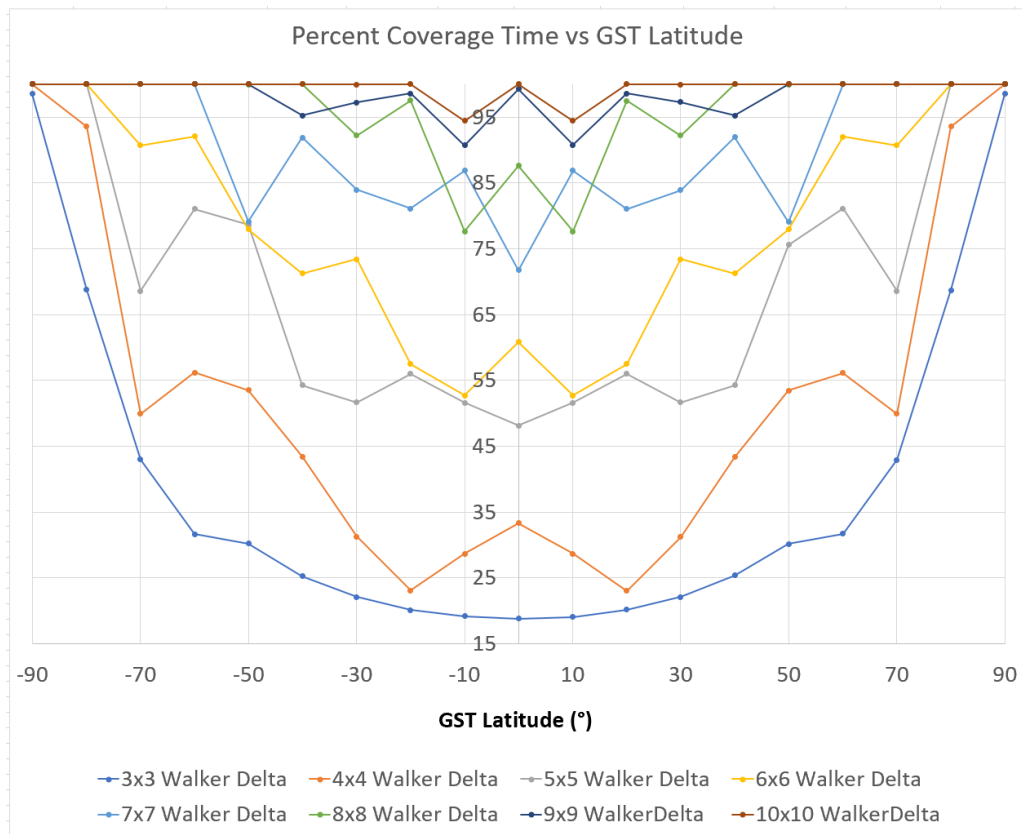


Figure 99. Percent coverage time across different latitudes for Walker Delta constellations ($h=700$ km, $P_{TX}=50$ mW)

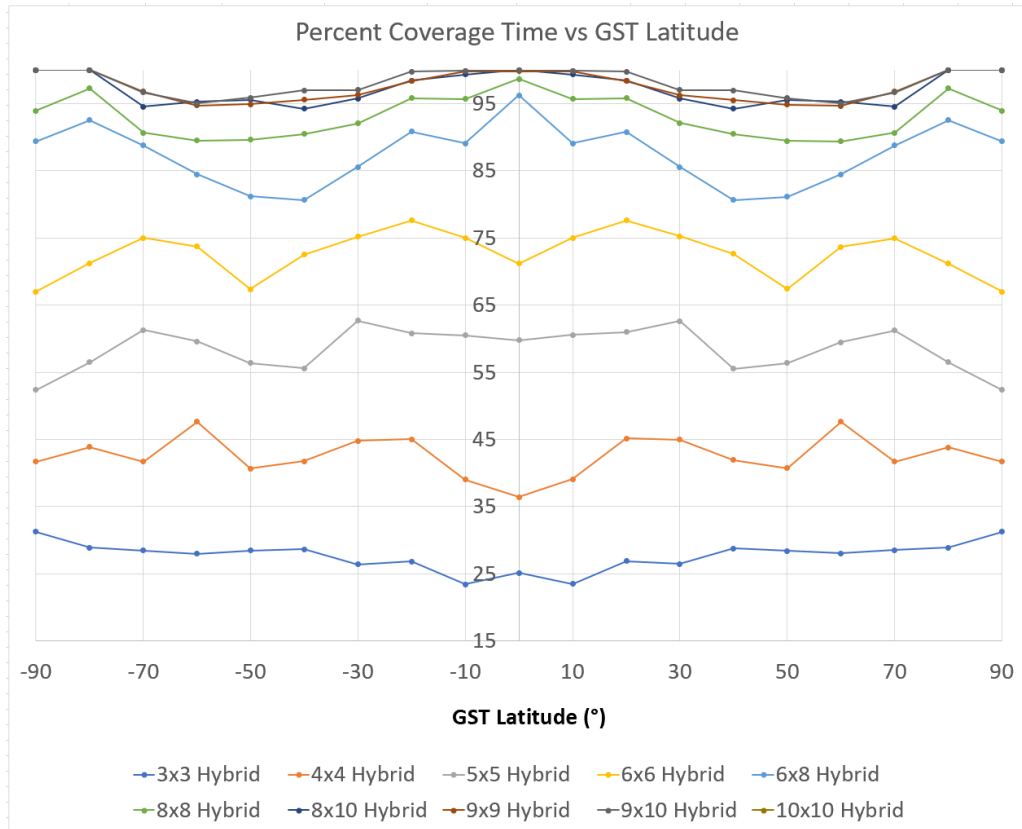


Figure 100. Percent coverage time across different latitudes for Hybrid constellations ($h=700$ km, $P_{TX}=50$ mW)

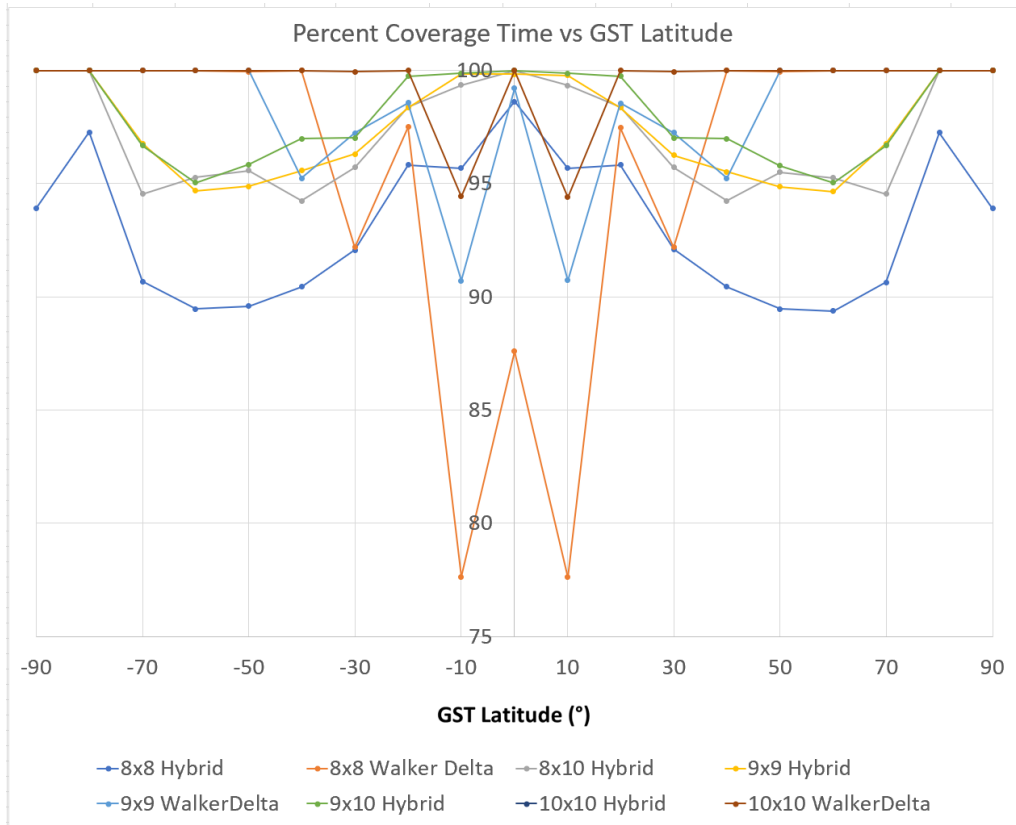


Figure 101. Percent coverage time across different latitudes for Walker Delta and Hybrid constellations ($h=700\text{ km}$, $P_{TX}=50\text{ mW}$)

Table 26. Percent Area Coverage (PAC) of Different Constellations

Constellation Size	Percent Area Coverage		
	Min	Max	Mean
3 x 3 (Hybrid)	36.16	42.93	39.61
3 x 3 (Walker Delta)	36.76	41.11	38.91
4 x 4 (Hybrid)	43.49	69.64	59.64
4 x 4 (Walker Delta)	50.13	58.33	54.91
5 x 5 (Hybrid)	74.95	81.31	78.02
5 x 5 (Walker Delta)	77.87	82.32	79.8
6 x 6 (Walker Delta)	85.99	91.58	88.84
6 x 6 (Hybrid)	83.53	96.32	90.76
6 x 8 (Hybrid)	96.07	100	97.97
7 x 7 (Walker Delta)	98.38	100	99.12
8 x 8 (Hybrid)	98.76	100	99.81
8 x 8 (Walker Delta)	98.09	99.52	99.25
8 x 10 (Hybrid)	99.56	100	100
9 x 9 (Hybrid)	99.75	100	100
9 x 9 (Walker Delta)	100	100	100
9 x 10 (Hybrid)	100	100	100
10 x 10 (Walker Delta)	100	100	100

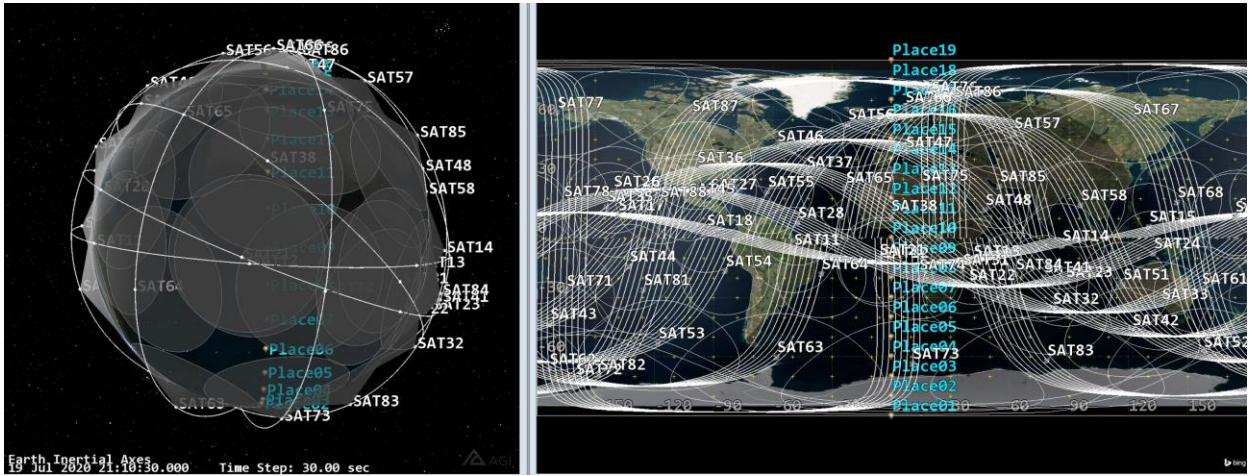


Figure 102. 8x8 Hybrid constellation simulated in STK

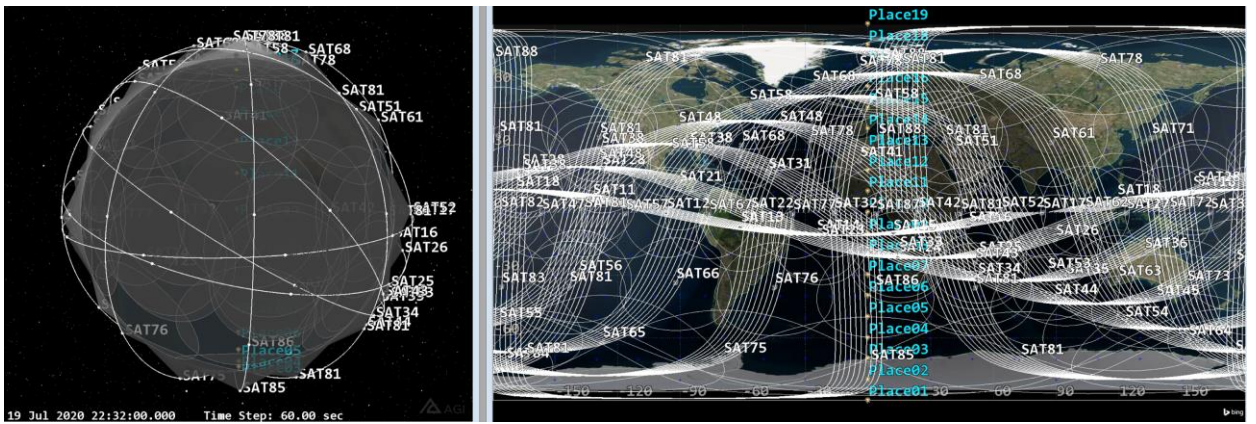


Figure 103. 9x10 Hybrid constellation simulated in STK

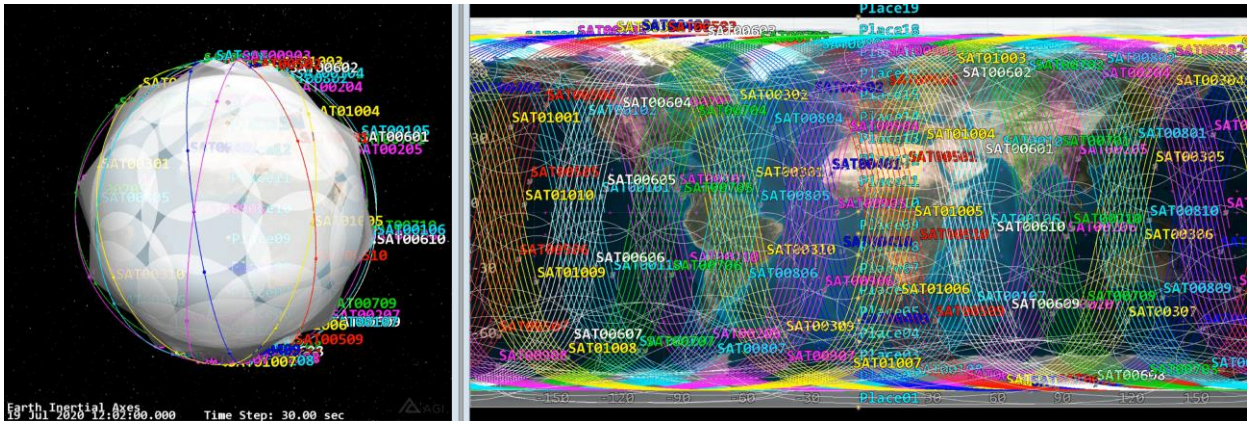


Figure 104. 10x10 Walker Delta constellation simulated in STK

Chapter 9: Experimental Laboratory Validation for E-SSA Protocol, Research Summary, Conclusions and Recommendations

The E-SSA protocol simulated as described in Chapter 6 and whose simulation results are discussed in Chapter 7 accounts only for the channel attenuations and received amplitudes variation among terminals, Doppler frequency shifts, Doppler frequency rates and phase offsets between each terminal and the payload receiver. The MATLAB simulation does not account for other impairments such as phase noise, errors in transmitters' and receiver's LO carrier frequencies (static and dynamic – instabilities), and clock (timing) errors.

In this chapter, we describe our experimental laboratory validation setup for the E-SSA protocol. Then, we present the experimental results and compare them with simulation results. The end of this chapter also provides the dissertation summary, conclusions, recommendations and plans for future work.

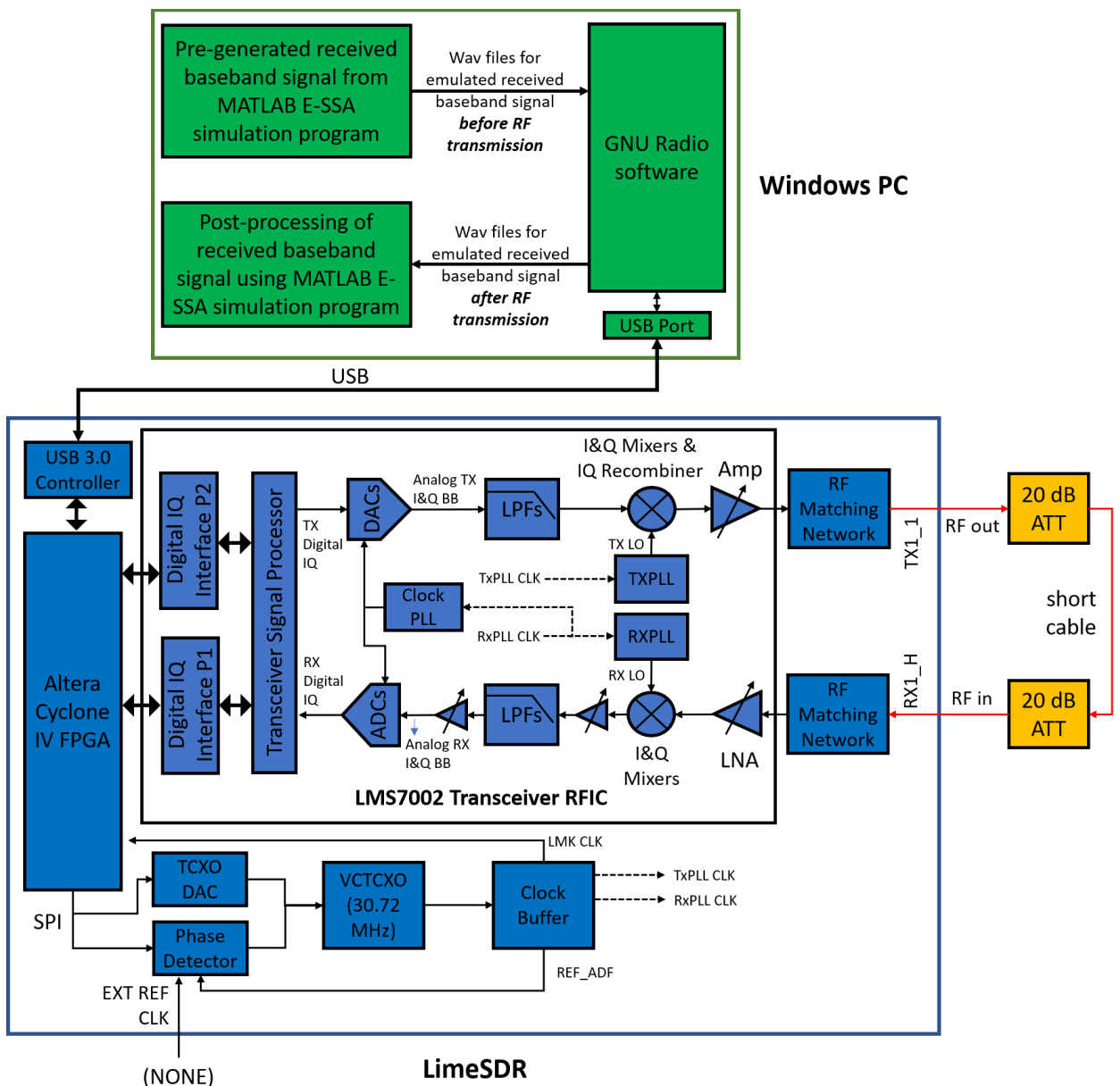
9.1 Four Laboratory Setups for E-SSA Protocol Validation

In simulation, the MATLAB program generates the received baseband signal at satellite receiver as a sum of received signals from numerous GSTs and noise. Then, the MATLAB program executes the formulated baseband signal processing algorithm including packet detection, channel estimation, decoding and successive interference cancellation. To validate the simulation results while also emulate the additional impairments in various degrees (albeit not fully equivalent to the real scenario), four laboratory setups were considered, as illustrated in Figures 105 to 108.

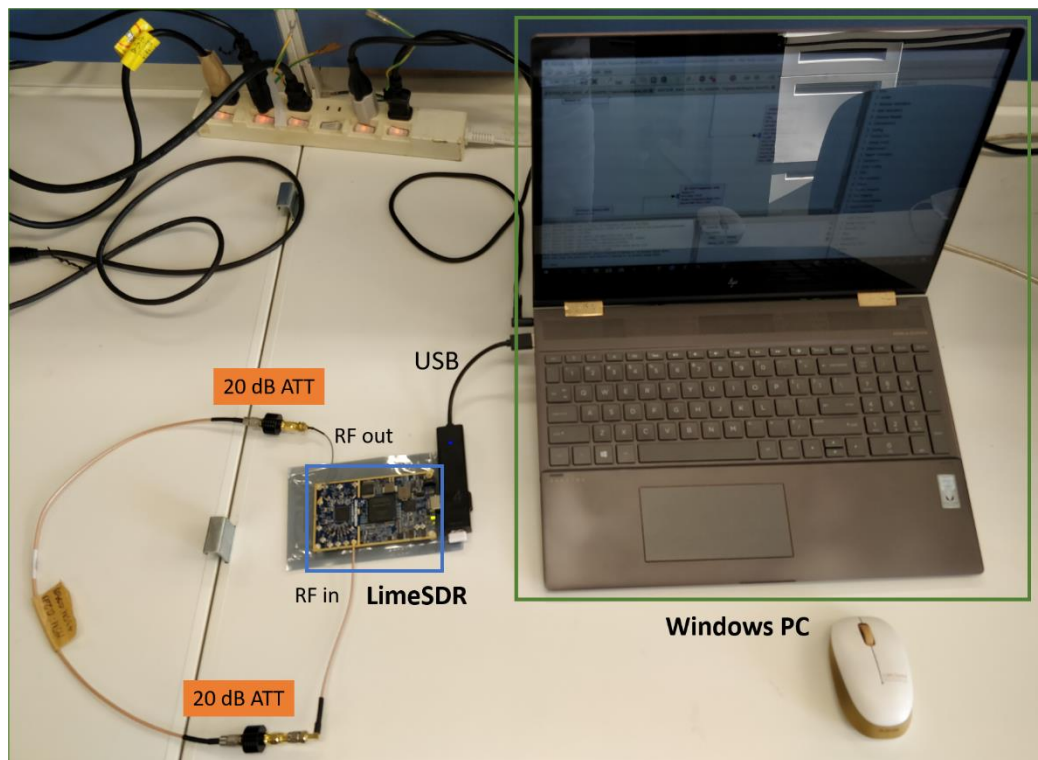
In the laboratory setup, we allow the received baseband signal pre-generated by the MATLAB program to be transmitted through the digital, analog baseband, and RF blocks of a real software-defined radio (SDR) transmitter. The transmitted signal is then received by RF, analog baseband, and digital blocks of an SDR receiver. Finally, digitized samples of the received baseband signal are later post-processed by the MATLAB program. In transmit side, the pre-generated received baseband signal's I and Q components are normalized and saved in separate .wav files, which are subsequently read by a GNU Radio software running on a computer that is communicating with the SDR transmitter module via USB interface. GNU Radio is tasked with exchanging data with the SDR's FPGA, as well as compiling and loading program into FPGA for controlling its computational resources. The FPGA in turn directly communicates with and partly controls the transceiver RFIC inside the SDR module. In receive side, the reverse process happens, that is, the received baseband signal's I and Q components are recorded and saved in separate .wav files for post-processing.

Figure 105 shows the Lab Setup 1 diagram, which involves only one PC running the GNU Radio software and a single LimeSDR whose transmitter and receiver sections are utilized for our purpose. The data and signal flow are described as follows. In the transmit side, GNU Radio first reads the MATLAB program-pre-generated received baseband signal I and Q .wav files in the PC and transfers the data to

LimeSDR's FPGA (Altera Cyclone IV) via USB interface. The FPGA interfaces with the LMS7002 transceiver RFIC – including sending of I-Q data and configuration data for component blocks inside the transceiver (e.g., DACs, analog filters, and RF blocks such as TX/RX PLLs, mixers, amplifiers). The FPGA sends the I&Q data to the LMS7002 through the Digital IQ Interface, which are then forwarded to the Transceiver Signal Processor (TSP). Next, inside LMS7002, digital baseband I and Q data are converted to analog baseband signals by two separate DAC channels and passed through low pass filters (LPFs). Then, the I and Q LPFs' outputs are each directly upconverted to the desired RF frequency by mixing them with TX LO chain through the I&Q mixers. At this point, the upconverted I and Q outputs are recombined and then amplified. External to LMS7002, impedance matching networks are connected to RF input and output ports. The final RF output of LimeSDR (TX1_1) is fed into a 20 dB attenuator, which in turn is connected to a short cable and another 20 dB attenuator whose output is fed back into the RF input of LimeSDR (RX1_H).



(a) Diagram



(b) Photo of actual setup

Figure 105. Laboratory setup 1 for validating E-SSA protocol with additional impairments

In the receive side, after passing through the matching network, the input RF signal is amplified by LNA before downconverted by I&Q mixers. At this point, the mixers' outputs constitute the analog baseband I and Q signals which then are each fed into two separate branches each consisting of low pass filter, analog voltage amplifier and ADC. The ADCs' outputs now constitute the digital baseband I and Q data which are cached in the TSP and forwarded to the FPGA through the Digital IQ Interface. Then, I & Q .wav files are created by FPGA and forwarded to the PC via USB interface for later post-processing by the MATLAB program.

Note that the pertinent component blocks of LimeSDR – more importantly those of LMS7002 and clock generation – shown in the figure are illustrated based on the descriptions provided in product datasheets and documentations. It is important to investigate how the several clocks in the system, including those in the DACs/ADCs, TX LO and RX LO, are generated beginning with the built-in reference clock (VCTCXO) and any external reference clock. It can be noticed in setup 1 that LimeSDR's TX PLL, RX PLL, Clock PLL and LMK CLK are driven by clocks coming from the same clock buffer. The input of this clock buffer is the built-in 30.72 MHz VCTCXO which is either tuned by the TCXO DAC (by default) or calibrated by an external reference clock through a phase detector (if selected, but which is not selected for Lab Setup 1). This means that in Lab Setup 1, there is only very small additional carrier phase offset between TXLO and RXLO within a single RFIC. There can be significant static frequency errors and instabilities in the VCTCXO output, and consequently in the individual outputs of TXLO and RXLO PLLs. However, since a common clock source drives the TXLO and RXLO PLLs, these LO PLLs' outputs will have small frequency difference. Any small difference in LOs' frequencies would be due to

imperfections in individual PLLs within a single RFIC. Similarly, although there will be significant sampling timing errors within the DACs and ADCs themselves – mainly due to inaccurate built-in reference clock – their effect will not be noticeable in the received samples (i.e., inexact sampling timing with respect to transmitted samples) due to a common clock source triggering the TX DACs and RX ADCs. Therefore, in Lab Setup 1, we expect the impairments would be phase noise and small difference between TX and RX LOs' frequencies.

Figure 106 shows the Lab Setup 2 diagram, which is like Lab Setup 1 but uses another PC and USRP B200mini SDR for the transmit side. Lab Setup 2 uses only the receive branch of LimeSDR and only the transmit branch of USRP B200mini SDR. Also, notice the use of Agilent N9310 signal generator as a common external reference clock for both LimeSDR and USRP B200mini SDR. The 10 MHz 16 dBm output from Agilent N9310 is split into two by a 3 dB splitter, whose outputs are separately fed into external reference clock inputs of the SDRs. Note that the pertinent component blocks of USRP B200mini SDR – more importantly those of AD9364 RFIC and clock generation – shown in the figure are illustrated based on the descriptions provided in product datasheets and documentations. By default, without an external reference clock, a built-in 40 MHz VCTCXO – which is tuned by a TCXO DAC controlled by the FPGA (Xilinx Spartan 6) – is used as the clock source for the data CLKs, sample CLKs and LOs inside AD9364 and CLK-40M-FPGA for the FPGA. With an external reference clock, although it is not explicitly described, it is inferred that the input clock is used for the programmable clock generators inside FPGA (which might be subsequently used to control TCXO DAC through some feedback circuit analogous to the phase detector in LimeSDR).

In Lab Setup 2, if the PLLs in both SDRs are properly working, there should be only very small additional carrier phase offset between USRP B200mini SDR TXLO and LimeSDR RXLO. The difference from setup 1, though, is that a more accurate common external reference clock is used by the PLLs but the PLLs' specifications themselves might deviate more depending on the varying design/component selection choices by different SDR and RFIC manufacturers. The different RFICs, built-in VCTCXOs and calibration circuits involved in Lab Setup 2 might produce greater overall difference in TXLO and RXLO PLL outputs. Meanwhile, due to use of a common external reference clock, the USRP B200mini SDR TXLO and LimeSDR RXLO PLL outputs themselves should be individually more accurate than the outputs in Lab Setup 1. Still due to use of a common external reference clock, frequency difference between USRP B200mini SDR TXLO and LimeSDR RXLO should also be small – due to imperfections in TXLO and RXLO PLLs. However, compared to Lab Setup 1, different RFICs, built-in VCTCXOs and calibration circuits are involved, which might produce more overall frequency offset. In terms sampling timing accuracy, again due to a common external reference clock, the individual ADCs/DACs sampling accuracies in TX and RX sides should be better than in Lab Setup 1, but due to separate clocks (that trigger sampling), even small sampling timing errors in the RX side ADCs (with respect to the TX side DACs) can lead to noticeable errors in the received samples (i.e., inexact sampling timing with respect to transmitted samples).

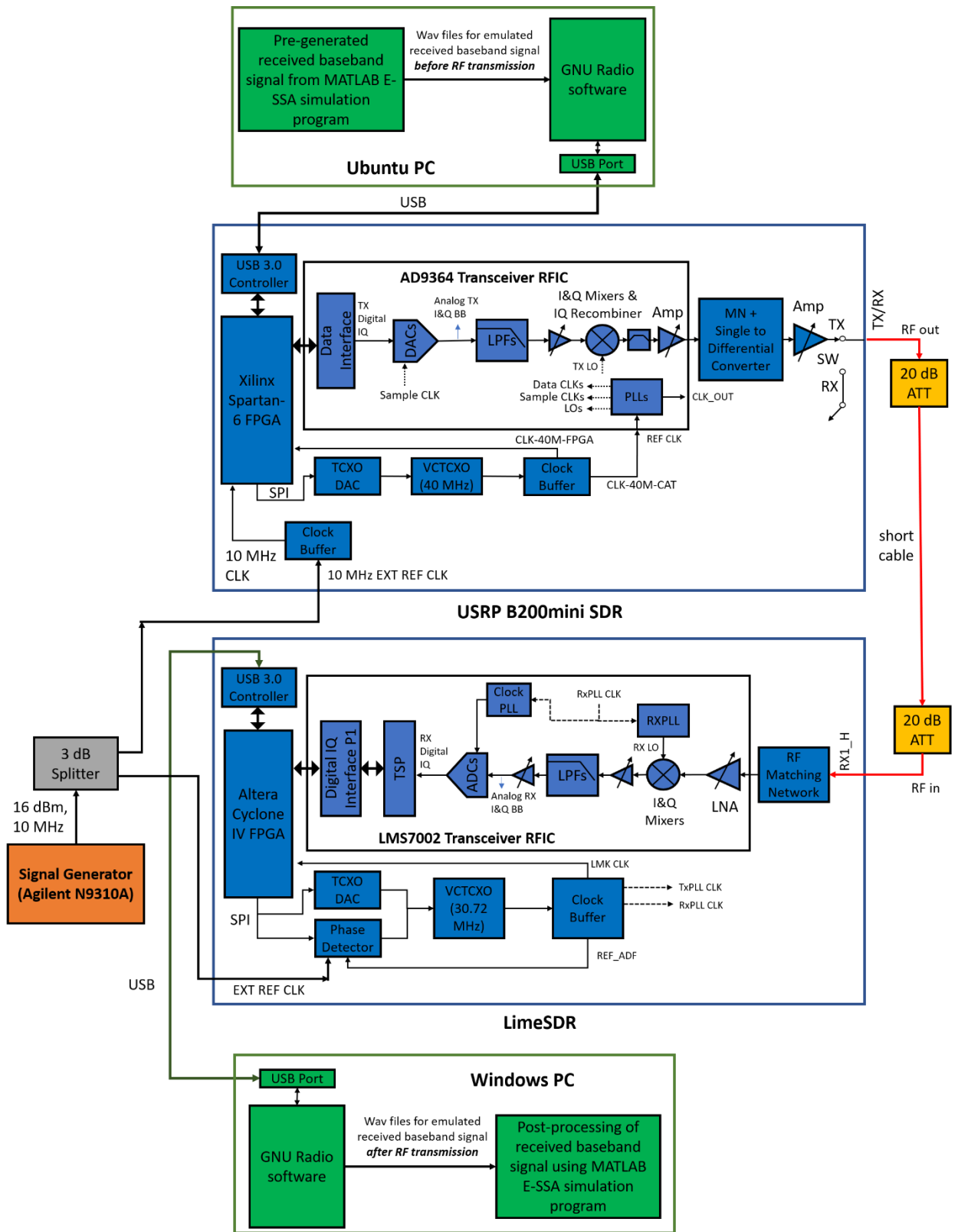
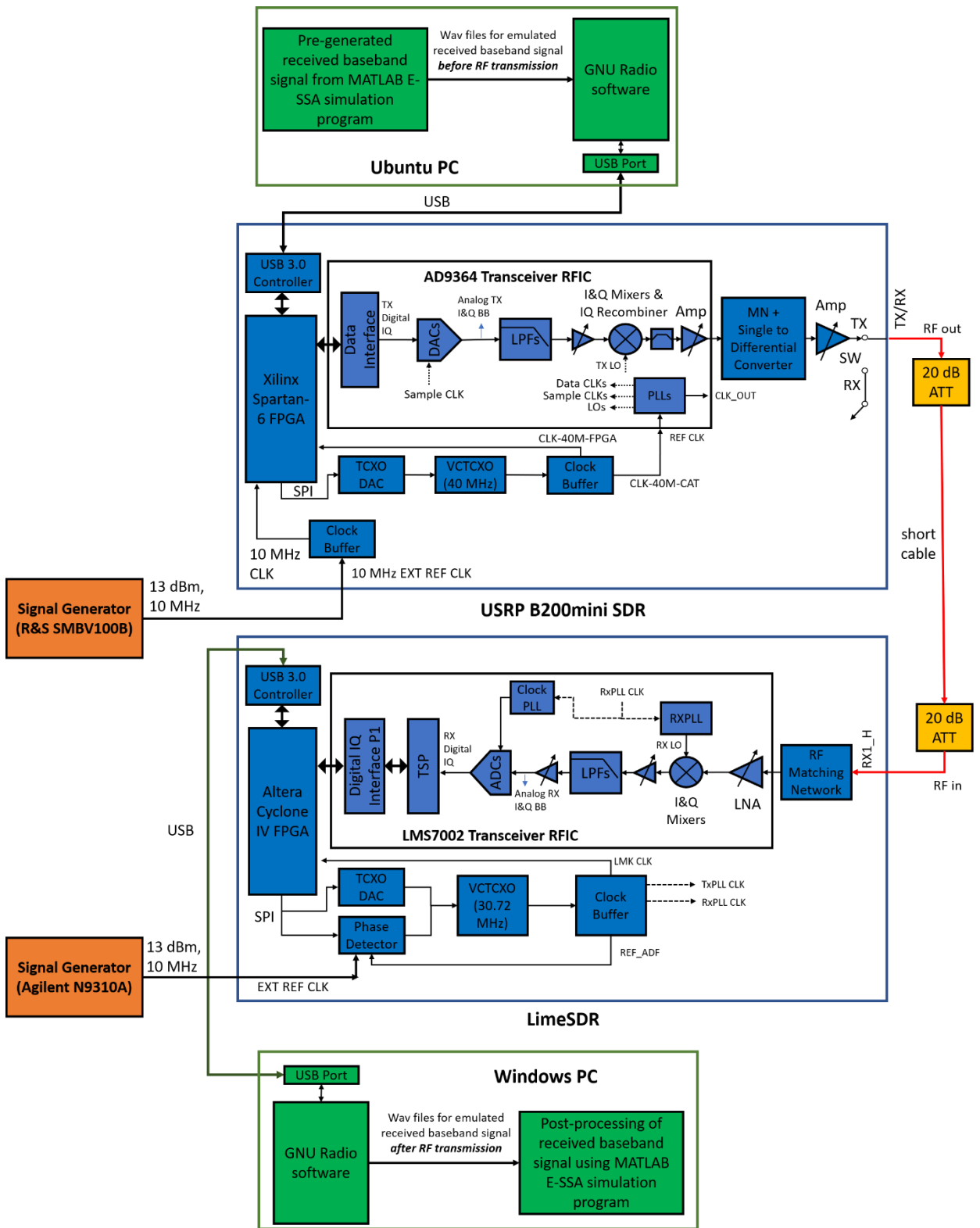
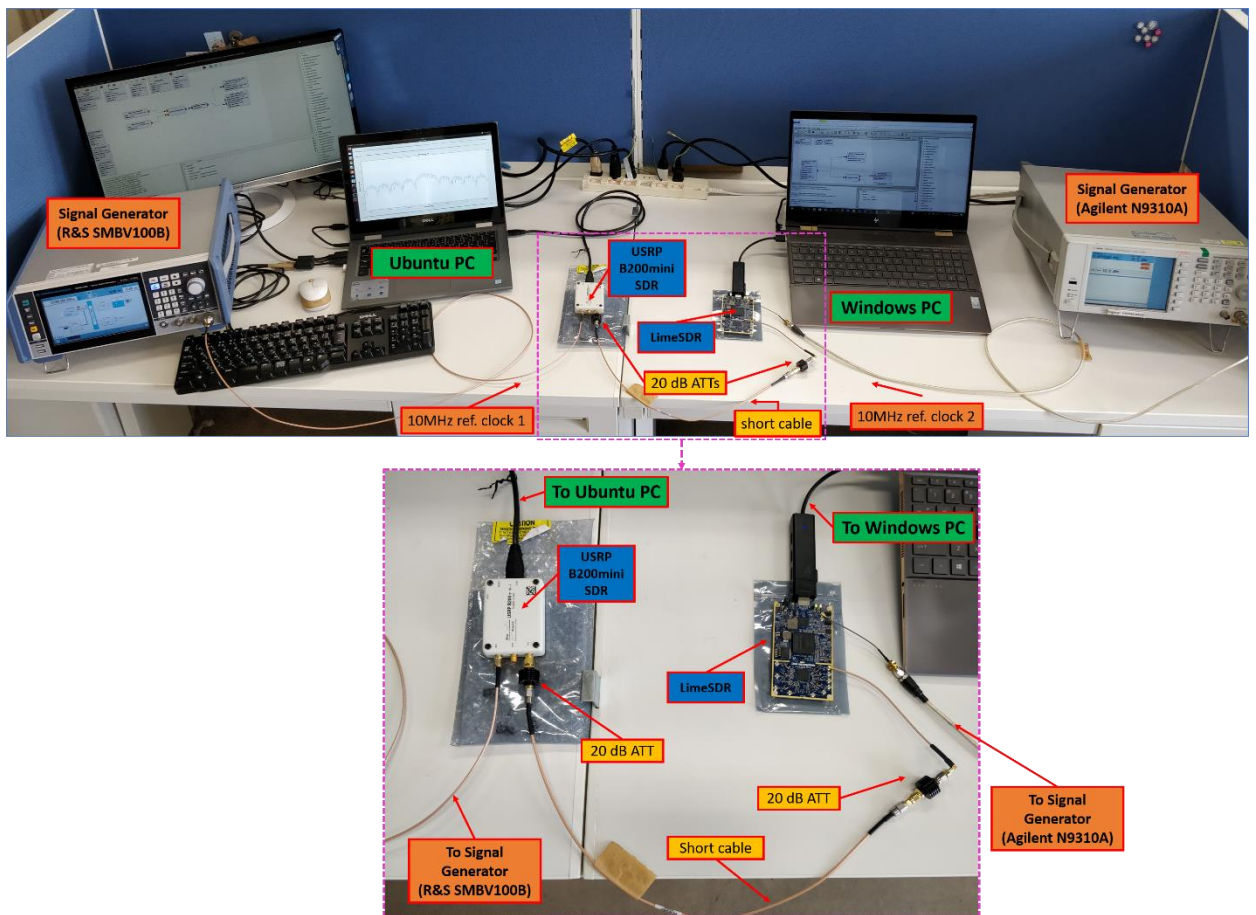


Figure 106. Laboratory setup 2 for validating E-SSA protocol with additional impairments (diagram)



(a) Diagram



(b) Photo of actual setup

Figure 107. Laboratory setup 3 for validating E-SSA protocol with additional impairments

Figure 107 shows the diagram for Lab Setup 3, which is very similar to Lab Setup 2 except that another signal generator (R&S SMBV100B) is used as external reference clock for the TX side. Unlike Lab Setups 1 and 2, since the two signal generators are independent, there can be large/small and random (in every test trial) additional carrier phase offset between USRP B200mini SDR TXLO and LimeSDR RXLO. If the two signal generators are both accurate, the frequency difference between USRP B200mini SDR TXLO and LimeSDR RXLO should also be small due to the same errors in Lab Setup 2. Practically, however, there is additional small errors due to difference in the signal generators' output frequencies. The ADCs/DACs individual and relative sampling timing errors are like those in Lab Setup 2 but will be (slightly) higher due to difference in the signal generators' output frequencies and the random carriers' phase offset. Note that if there are several samples per chip, then the effect in increased timing error relative to setup 2 should only be slightly 'felt' in the received samples.

Finally, Figure 108 shows the diagram for Lab Setup 4, which among the four setups most represents the realistic scenario of having inaccurate reference clocks in the GSTs. It involves the greatest extent of additional carrier phase offset between USRP B200mini SDR TXLO and LimeSDR RXLO, difference in their TX and RX LOs' frequencies, and sampling timing errors. The differences among the simulation and laboratory setups are summarized in Table 28. For a rough quantitative comparison, the specifications of the reference clocks involved in the four setups are provided in Table 27. Note that in all four laboratory

setups, the baseband and RF gains in the TX and RX sides are adjusted so that the recorded baseband signal amplitudes do not saturate the ADCs (not exceeding the ± 1 amplitude limits but not too low). Further details on SDR TX and SDR RX settings, as well as the RF spectrum measurements, are provided in Tables 29 and 30 and Figures 109 to 113 (note that the spectrum analyzer used for measurement may also have limited accuracy for the purpose).

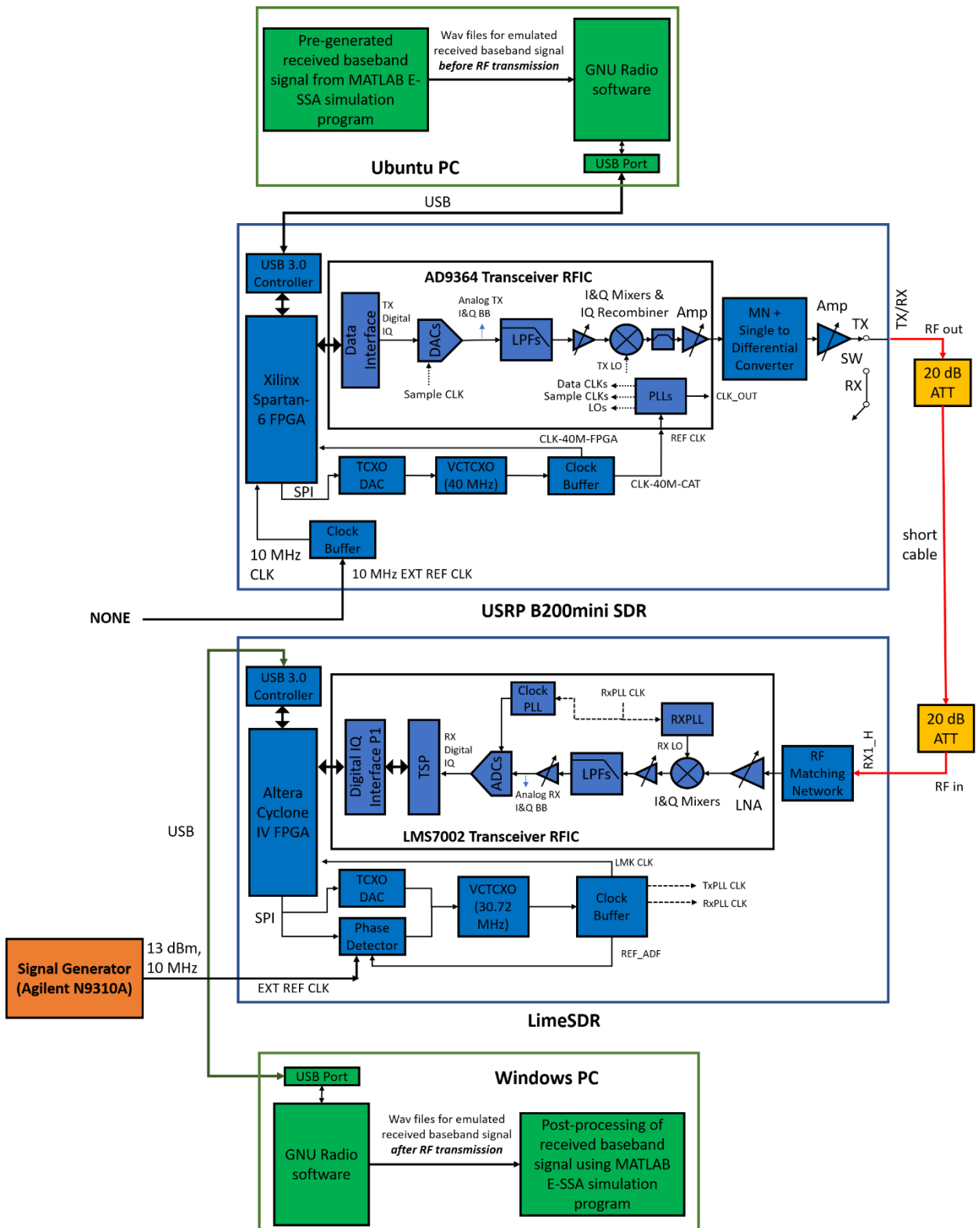


Figure 108. Laboratory setup 4 for validating E-SSA protocol with additional impairments (diagram)

Table 27. Reference Clocks Accuracies in Different Setups

Laboratory Setup	Description	Reference Clocks Settings and Accuracies	
		TX Side	RX Side
Lab Setup 1 (LS1)	Single internal reference clock, single SDR module for TX and RX sides	± 1 ppm initial, ± 4 ppm stable (built-in VCTCXO)	
Lab Setup 2 (LS2)	Single external reference clock, separate SDR modules for TX and RX sides	$\sim \pm 0.2$ ppm (Agilent N9310A)	
Lab Setup 3 (LS3)	Separate external reference clocks, separate SDR modules for TX and RX sides	$\pm ?$ ppm (R&S SMBV100B)	$\sim \pm 0.2$ ppm (Agilent N9310A)
Lab Setup 4 (LS4)	Internal reference clock on TX side, external reference clock on RX side, separate SDR modules for TX and RX sides	± 2 ppm (built-in VCTCXO)	$\sim \pm 0.2$ ppm (Agilent N9310A)

Table 28. Expected Signal Impairments in Different Setups

Setup	Impairments				
	Doppler shifts, rates, carrier phase offset between each GST TX and satellite payload RX	Phase Noise	Additional <i>initial</i> carrier phase offset due to SDR TX and RX	TX and RX LO frequency errors and instability*	Sampling timing errors
Simulation	Yes	No	No	No	No
Lab Setup 1 (LS1)	Yes	Yes	Small [1]	Small [1]	Large [2], but not noticeable effect in received samples* due to common clock for TX and RX
Lab Setup 2 (LS2)	Yes	Yes	Small [3] (LS2 > LS1)**	Small [3] (LS2 > LS1)**	Small [4], but effect in received samples* may be noticeable (LS2 > LS1)**
Lab Setup 3 (LS3)	Yes	Yes	Large/small and random in every test trial [5] (gen. LS3 > LS2)**	Small [6] (LS3 > LS2)**	Small [7], but effect in received samples* may be noticeable (LS3 > LS2)**
Lab Setup 4 (LS4)	Yes	Yes	Large/small and random in every test trial [5] (gen. LS4 > LS2)**	Large [8] (LS4 >> LS3)	Large [8] and noticeable effect in received samples* (LS4 >> LS3)

- [1] Due to imperfect TXLO and RXLO PLLs in TX and RX sides within a single transceiver RFIC
- [2] Mainly due to inaccurate built-in reference clock in a single TX/RX SDR module
- [3] Due to imperfect TXLO and RXLO PLLs in TX and RX sides (in different RFICs), as well as well as different built-in VCTCXOs and their calibration circuits (in different SDR modules)
- [4] Due to imperfect sampling clock PLLs in TX and RX sides (in different RFICs), as well as well as different built-in VCTCXOs and their calibration circuits (in different SDR modules)
- [5] Due to independent/separate external reference clocks
- [6] Due to imperfect TXLO and RXLO PLLs in different RFICs, different built-in VCTCXOs and their calibration circuits (in different SDR modules), and in addition to LS2 are small relative errors between SGs RF outputs
- [7] Due to imperfect sampling clock PLLs in TX and RX sides (in different RFICs), different built-in VCTCXOs and their calibration circuits (in different SDR modules), and in addition to LS2 are small relative errors between SGs RF outputs
- [8] Mainly due to inaccurate built-in reference clock in SDR TX side (among all setups, this most represents realistic situation of GSTs having inaccurate reference clocks)

*With respect to transmitted samples

**In terms of overall TX-RX difference or net effect

Table 29. SDR TX and RX Settings for Laboratory Setup 1

Parameter	Value or Setting
TX Side (LimeSDR)	
Center frequency	402 MHz
Sampling rate	1.28M samples/sec
Channel	'A' (=TX1_1)
Oversample	Default
NCO frequency	'0' (default)
Calibration BW	5x10 ⁶ (default)
PA Path	'Auto(Default)'
Analog filter BW	'0' (default)
Digital filter BW	1.28 MHz (=sampling rate)
Gain	72 dB
Allow TCXO DAC control	Yes (use DAC tuner with built-in VCTCX0)
Measured output RF power (by spectrum analyzer, for $\sigma_{LN}=9\text{dB}$, $G=0.4$)	~-8 dBm to ~-3 dBm (similar reading for 250 kHz and 500 kHz bandwidth)
RX Side (same LimeSDR module used in TX Side)	
Center frequency	402 MHz
Sampling rate	1.28M samples/sec
Channel	'A' (=RX1)
Oversample	Default
Measured input RF power (after 40 dB total attenuators, by spectrum analyzer, for $\sigma_{LN}=9\text{dB}$, $G=0.4$)	~-48 dBm to ~-44 dBm (similar reading for 250 kHz and 500 kHz bandwidth)
NCO frequency	'0' (default)
Calibration BW	5x10 ⁶ (default)
LNA path	'H' (use RX1_H as RF input port)

Analog filter BW	'0' (default)
Digital filter BW	1.28 MHz (=sampling rate)
Gain	60 dB
Allow TCXO DAC control	Yes (use DAC tuner with built-in VCTCX0)
Wav File Sink	1.28M samples/sec, 16 bits/sample

Table 30. SDR TX and RX Settings for Laboratory Setups 2-4

Parameter	Value or Setting
TX Side (USRP B200mini SDR)	
Center frequency	402 MHz
Sampling rate	1.28M samples/sec
Sync	'don't sync'
Mb0 clock source	External/Internal
Mb0 time source	Default
Gain value	68 dB
Ch0 antenna (RF port)	TX/RX
Ch0 bandwidth	'0' (default)
Measured output RF power (by spectrum analyzer, unrecorded σ_{LN} and G setting)	~-12 dBm to ~-9 dBm (similar reading for 250 kHz and 500 kHz bandwidth)
RX Side (LimeSDR)	
Center frequency	402 MHz
Sampling rate	1.28M samples/sec
Channel	'A' (=RX1)
Oversample	Default
Measured input RF power (after 40 dB total attenuators, by spectrum analyzer, unrecorded σ_{LN} and G setting)	~-52 dBm to ~-49 dBm (similar reading for 250 kHz and 500 kHz bandwidth)
NCO frequency	'0' (default)
Calibration BW	5×10^6 (default)
LNA path	'H' (use RX1_H as RF input port)
Analog filter BW	'0' (default)
Digital filter BW	1.28 MHz (=sampling rate)
Gain	60 dB
Allow TCXO DAC control	No (use phase detector with external reference clock)
Wav File Sink	1.28M samples/sec, 16 bits/sample

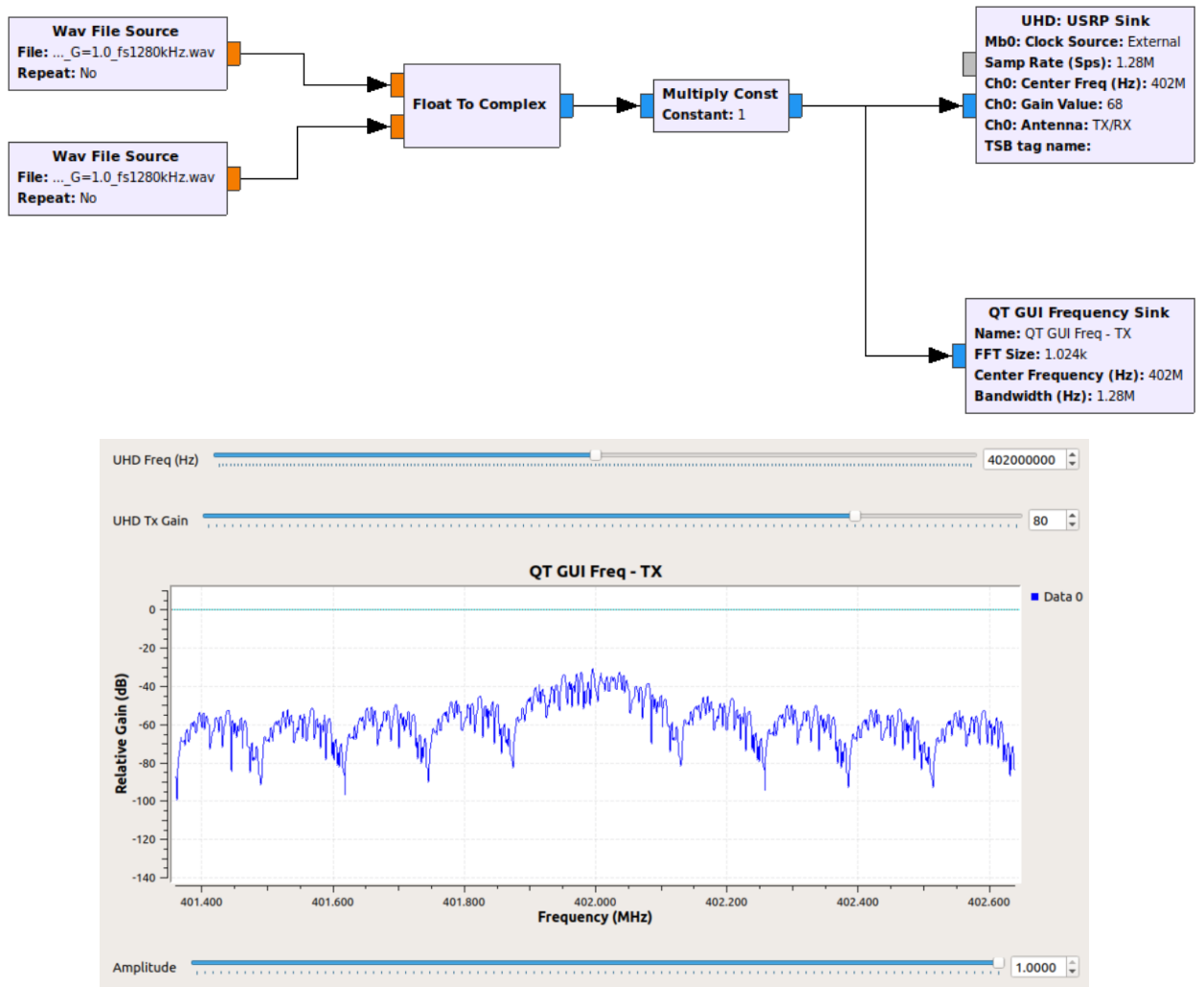
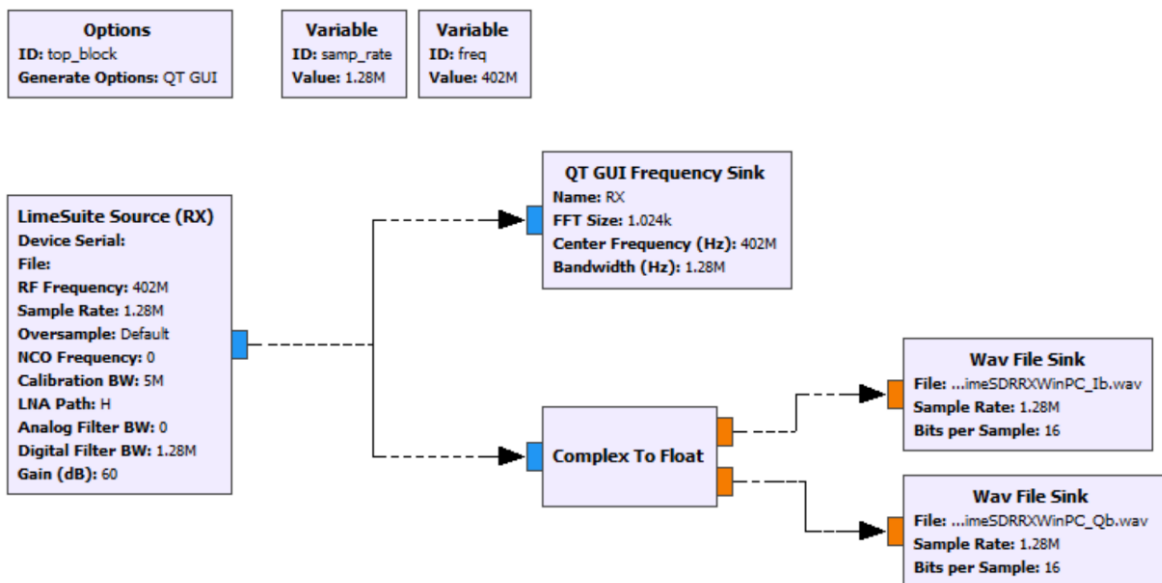


Figure 109. USRP B200mini SDR TX side GNU Radio program for laboratory setups 2-4



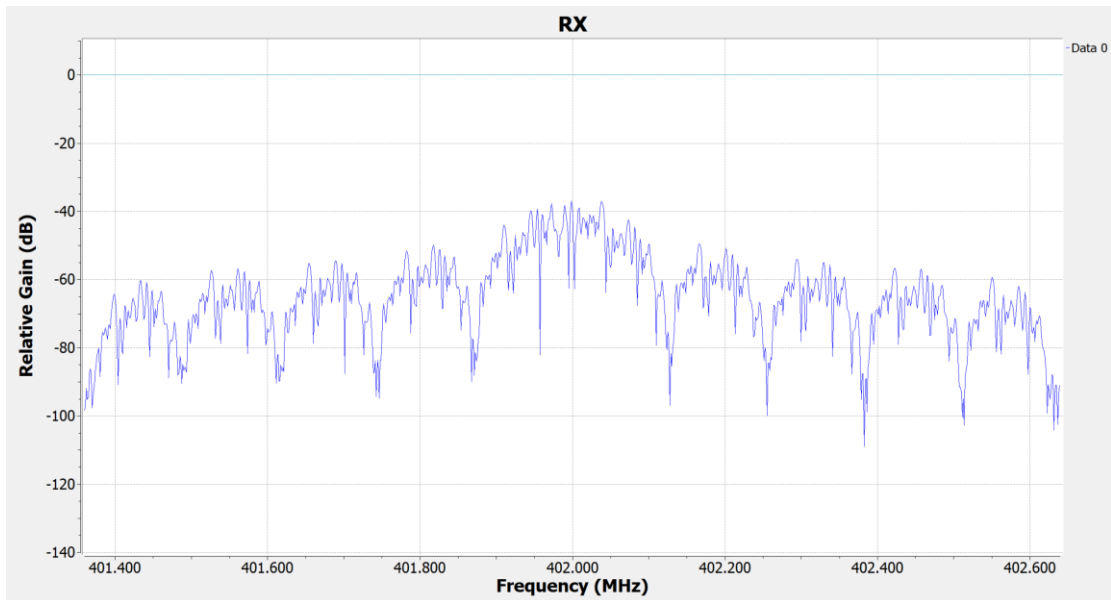


Figure 110. LimeSDR RX side GNU Radio program for laboratory setups 2-4

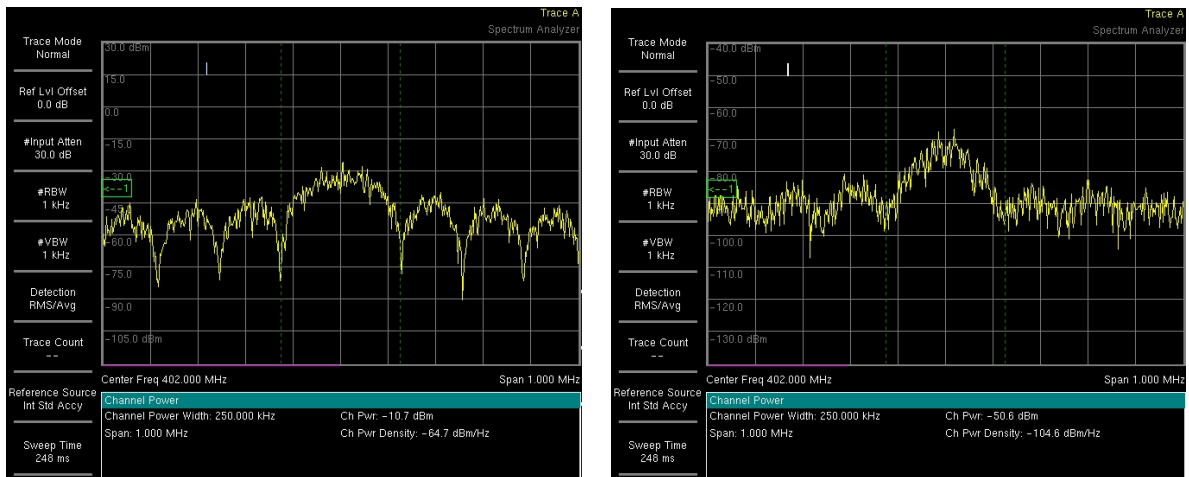


Figure 111. RF spectrum measurements of SDR TX output (left) and SDR RX input (right) for laboratory setup 1 (different σ_{LN} , G and gain settings as in Table 27)

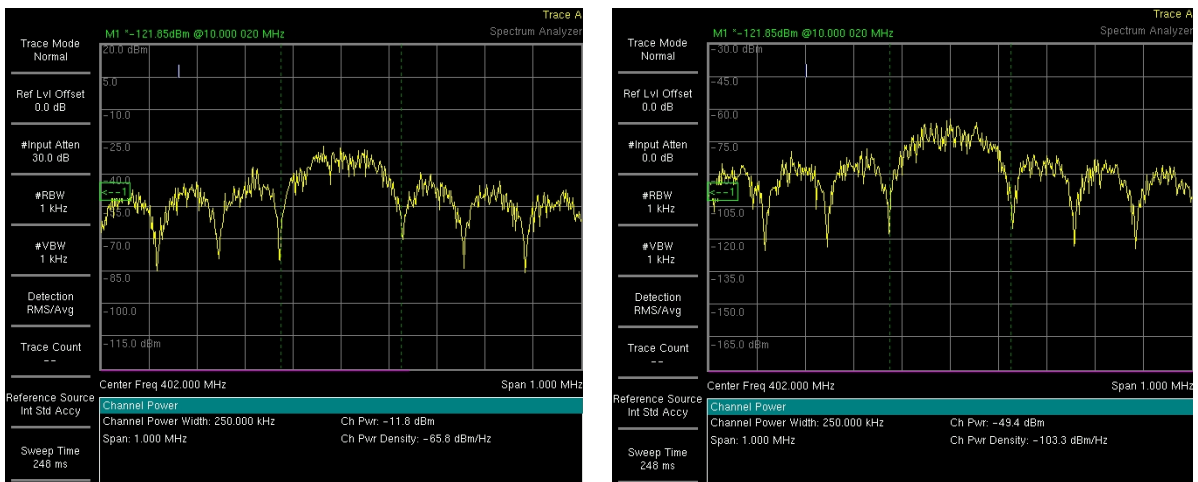


Figure 112. RF spectrum measurements of SDR TX output (left) and SDR RX input (right) for laboratory setups 2-4 (same σ_{LN} , G and gain settings as in Table 28)

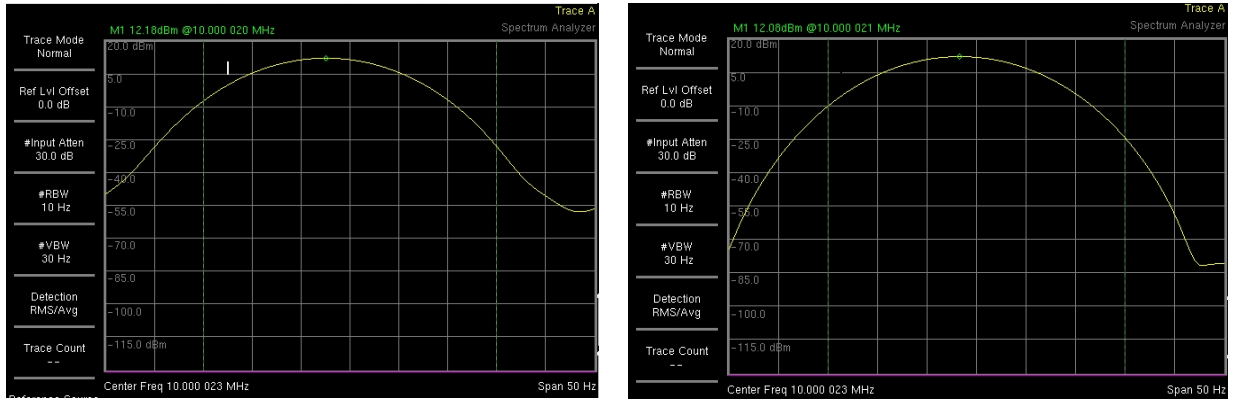


Figure 113. RF spectrum measurements of signal generators’s RF outputs: (left) Agilent N9310A, set to 9.999998 MHz, 13 dBm; (right) R&S SMBV100V, set to 10.000000 MHz, 13 dBm

9.2 Examination of Received Baseband Signal Recorded at RX Side

To evaluate the impairments in the signal caused by the real propagation medium (in this case, the electronics inside SDRs, cables, attenuators) – beyond what have been modeled in MATLAB program for artificial generation of received baseband signal –, we need to compare the actually recorded received signal $y(t)$ with that of the originally generated received signal $x(t)$. As mentioned above, the MATLAB-generated signal is normalized to a maximum value before it is transmitted so the $x(t)$ we are concerned with from now on is this normalized signal. Also, since here we are not concerned with the attenuation caused by the real medium, the recorded signal $y(t)$ is also a re-scaled version such that its total power is equal to that of $x(t)$.

In the real medium, the transmitted and received RF signals have carrier frequencies, carrier phase errors, and possibly other noises and distortion effects. However, since we only have the pre-RF-transmitted $x(t)$ and the recorded down-converted signal $y(t)$, we can express them in the following:

$$x(t) = A_1(t)e^{j(\omega_1 t + \phi_1(t))} = A_1(t) \quad (1)$$

$$y(t) = kA_1(t) = A_2(t)e^{j(\omega_2 t + \phi_2(t))} = A_2(t)e^{j(\Delta\omega t + \Delta\phi(t))} \quad (2)$$

$$A_2(t) = kA_1(t) + E(t) \quad (3).$$

Generally, $y(t)$ contains amplitude noise $E(t)$ but this should be negligible since the actual RF input power at the SDR RX was set to be much higher than SDR RX noise floor. Thus, $A_2(t) \approx kA_1(t)$. Then, the baseband signal $y(t)$ contains the effects of frequency error $\Delta\omega$ and phase error $\Delta\phi(t)$. The TXLO and RXLO output frequencies will have long-term and short-term instabilities but for $\Delta\omega$, we assume long-term stability (throughout the recording duration of ~20 s) so that $\Delta\omega$ can be considered only as the fixed frequency offset between TXLO and RXLO. Time-varying $\Delta\phi(t)$ includes the short-term frequency offset changes, as well as the initial carrier phase offset $\Delta\phi_0$ and the random phase errors (so-called, “phase noise” or “jitter”).

We compare $y(t)$ with $x(t)$ using the following cross-correlation operations (where $x^*(t)$ is the complex conjugate of $x(t)$):

$$R(t) \triangleq y(t) \cdot x^*(t) = k|A_1(t)|^2 e^{j(\Delta\omega t + \Delta\phi(t))} \quad (4)$$

$$r(t) \triangleq \frac{R(t)}{|A_1(t)|^2} = k e^{j(\Delta\omega t + \Delta\phi(t))} \quad (5)$$

$$r(\Omega) = r_{FFT} \triangleq FFT\{r(t)\} \quad (6).$$

Plotting $R(t)$ vs time will show not only the dynamic frequency and phase errors, but also the amplitude variation inherent in the “message” signal $A_1(t)$. To see only the dynamic frequency and phase errors due to the real medium – removing the effect inherent amplitude changes in MATLAB-generated signal –, we must instead plot the cross-correlation $r(t)$ vs time. Finally, plotting vs frequency the magnitude of the result of FFT operation on $r(t)$, $|r(\Omega)|$, will reveal several important things:

- *Center frequency shift (Δf):* the frequency where the maximum $|r(\Omega)|$ is located is where the power of the signal $y(t)$ is concentrated. This is also the center-to-center frequency offset between TXLO and RXLO.
- *Distribution of frequency errors around the center frequency shift (W_1, W_2):* the power will “leak” around the center frequency shift when there are short-term frequency instabilities in TXLO and RXLO and phase noise. On the other hand, if these errors are very small, we will see in the frequency plot a very narrow “impulse” located at the center frequency shift.
- *Signal-to-phase-noise ratio estimate (A_{dB}):* This is the $|r(\Omega)|$ level at center frequency shift relative to the level away from the center frequency shift. Away from the center frequency shift, the $|r(\Omega)|$ plot is generally flat across wide frequencies, and this part is attributed to phase noise due to random phase errors. The $|r(\Omega)|$ level away from the center frequency shift, relative to the level at the center frequency shift, indicates an estimate of the phase noise power relative to the frequency-shifted non-phase-noise signal power. Note that the total power of $y(t)$ is (made) equal to that of $x(t)$, but in the former, phase noise takes some of this power and distributes it across wide frequencies away from the center frequency shift. Of course, the dynamic frequency errors around the center frequency shift also takes another part of this power.

In the succeeding figures, for the four laboratory setups, we present and compare the cross-correlation time plots and $|r(\Omega)|$ plots after being *normalized to their respective maximum value*. As reference for comparison, we also show the corresponding plots for the reference hypothetical case, that is, wherein $y(t)$ in equation (4) is replaced with $x(t)$. Note that the minimum level of the normalized $|r(\Omega)|$ plot for the reference case is only a pseudo-phase noise level (not a real phase noise since by default, $x(t)$ does not have phase noise). It only indicates the minimum magnitude limit of the FFT operation. Plots for the reference case are shown first – in Figures 114-115. Plots for the laboratory setups are shown next in Figures 116-123. Table 31 provides a summary of the observations.

The actual observations as listed in Table 31 fairly match the expectations laid down in Section 9.1 (as summarized in Table 28), although there are slight deviations. As for carrier phase offset, the values for Lab Setups 3 and 4 are expected to be random for each trial (can be large or small), and the large results

for both are consistent with this. For both Lab Setups 1 and 2, the carrier phase offset is expected to be low, with that of the latter expected to be greater than that of the former. The observed carrier phase offsets for Lab Setups 1 and 2 agree with this expectation, although the actual result for Lab Setup 2 is rather not small. As for observed frequency offsets, the trend from Lab Setup 1 to Lab Setup 4 is toward increasing, and notably, frequency offset for Lab Setup 4 is much greater than those of other three – these also match with the expectations. Again, note that the frequency errors in Lab Setup 1 is actually large but cannot be noticed because of common circuitries and clocks in TX and RX sides.

As for distribution of frequency errors around the center frequency shift, all laboratory setups have wider distributions than the reference case, which is expected. It is remarkable, though, that the frequency error distributions of Lab Setups 2 and 3 are much greater than those of Lab Setups 1 and 4. Also, Lab Setups 2 and 3 produced many frequency shifts during the 20-second transmission and recording duration, unlike the single frequency shift in Lab Setups 1 and 4. These can be attributed to the fact that Lab Setups 2 and 3 both involved an external reference clock for SDR TX, but the other two setups only involved the internal reference clock for SDR TX. Thus, there is a basis to believe that for SDR TX (USRP B200mini), using an external reference clock would provide a more accurate but less stable (i.e., varies with time) frequency output. On the other hand, using internal reference clock would provide a less accurate but more stable frequency output.

The same might be true for SDR RX (LimeSDR), which can be inferred (but not certainly) by comparing between results for Lab Setups 2 and 3. Lab Setup 3 involved two independent external reference clocks, whereas Lab Setup 2 involved only one common external reference clock. This explains, as expected, why there is greater frequency offset in Lab Setup 3. Moreover, as inferred in the preceding paragraph, this also explains the wider frequency error distribution in Lab Setup 3 than in Lab Setup 2.

As for the relative phase noise increase, Lab Setup 1 has the highest signal-to-phase-noise ratio (SPNR) of 30 dB, followed by Lab Setups 2 and 3 with roughly equal SPNR of 21/22 dB, and lastly, Lab Setup 4 with the lowest SPNR of 11 dB. Note that these SPNR values are only estimates and should not be treated as absolute or direct phase noise measurements. These should only be considered as rough indications of the phase noise added introduced to the original signal. The relative increase in phase noise (which is not present in the MATLAB-generated signal) should be accounted when evaluating the result of E-SSA performance in laboratory setups compared to simulation setup, in which phase noise was not included. Note that in E-SSA simulation results, performance of E-SSA has been found to be sensitive to E_b/N_0 or equivalently to noise level (or SNR). Although phase noise might be different in nature to the AWGN modeled in simulation, phase noise due to random phase errors still raises up the total noise level.

Therefore, phase noise, along with sampling timing errors, frequency errors and phase offset, will increase the difficulty of detecting and/or demodulating/decoding the packets. These additional signal impairments will expose the weakness or limitation of the formulated signal processing algorithm. While the channel estimation algorithm can compensate for constant frequency offset and phase offset errors, it

cannot mitigate the distortions in the signal caused by dynamic frequency errors and phase noise. Lab Setup 4 has smaller dynamic frequency errors than Lab Setups 2 and 3 but it has higher phase noise.

Table 31. Observed Additional Signal Impairments in Recorded Received Baseband Signal

Case	A_{dB}	Frequency Offset Δf (Hz)	W_1 (Hz)	W_2 (Hz)	Carrier Phase Offset (radians)	Sampling Timing Errors observed in chips-level?*
Reference	33	0	0.1	2	≈ 0	No (default)
Lab Setup 1 (1 SDR for TX/RX, 1 common int. ref.)	30	0	0.1	13	-0.21	No
Lab Setup 2 (2 SDRs, 1 common ext. ref.)	21	≈ 0 (average); -19; -7; -2; 2; 5; 12; 20	16	280	-0.90	No
Lab Setup 3 (2 SDRs, 2 ext. refs.)	22	≈ 46 (main); -340; -140; -20; 10; 38; 51; 63; 220	8	700	-2.35 (instance of random var.)	No
Lab Setup 4 (2 SDRs, 1 int. ref. on TX, 1 ext. ref. on RX)	11	≈ -854	4	13	2.20 (instance of random var.)	Yes (0, +1, +2, +3, +4, +5 chips)

*This was evaluated by comparing the observed chip delays of detected packets (applying the packet detection algorithm) with the correct chip delays (set within the MATLAB program that generated the received baseband signal). Note that timing errors rawly can occur in the samples-level but tedious to check. Examined only the data for first iteration of signal processing.

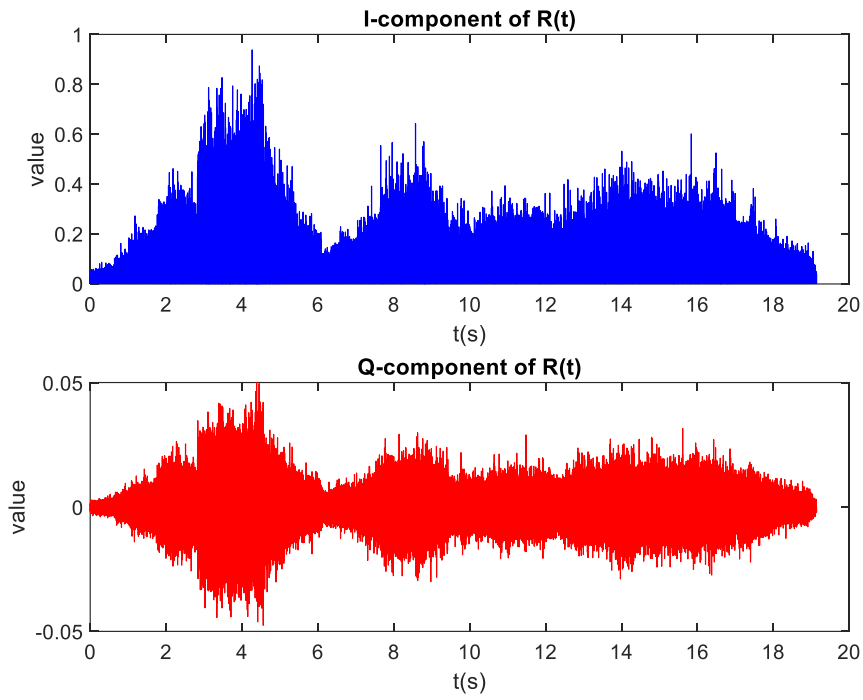


Figure 114. Plot of I and Q components of $R(t)$ vs time for reference case

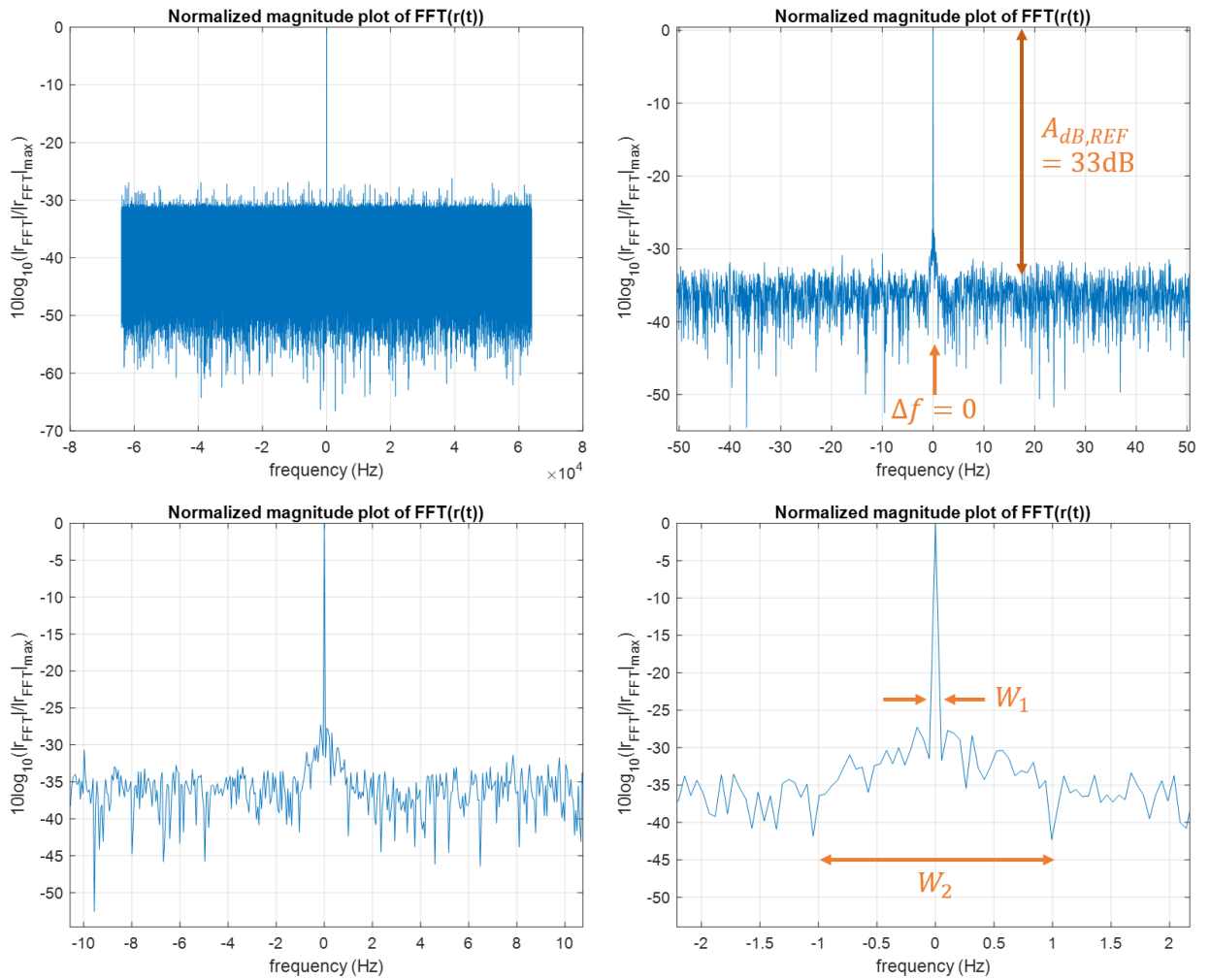


Figure 115. Normalized magnitude plot of $r(\Omega)$ for reference case

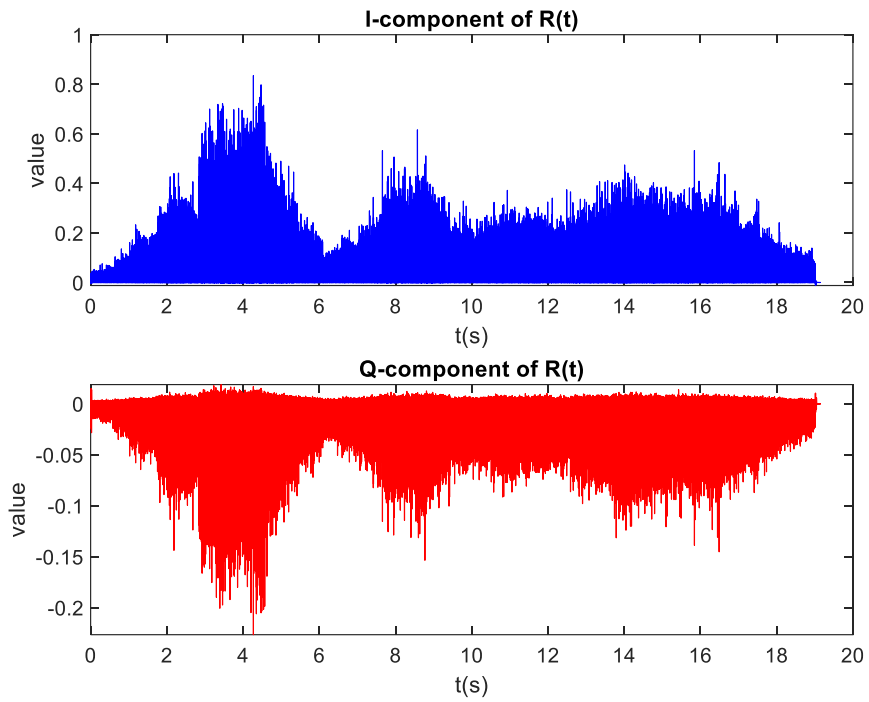


Figure 116. Plot of I and Q components of $R(t)$ vs time for Lab Setup 1

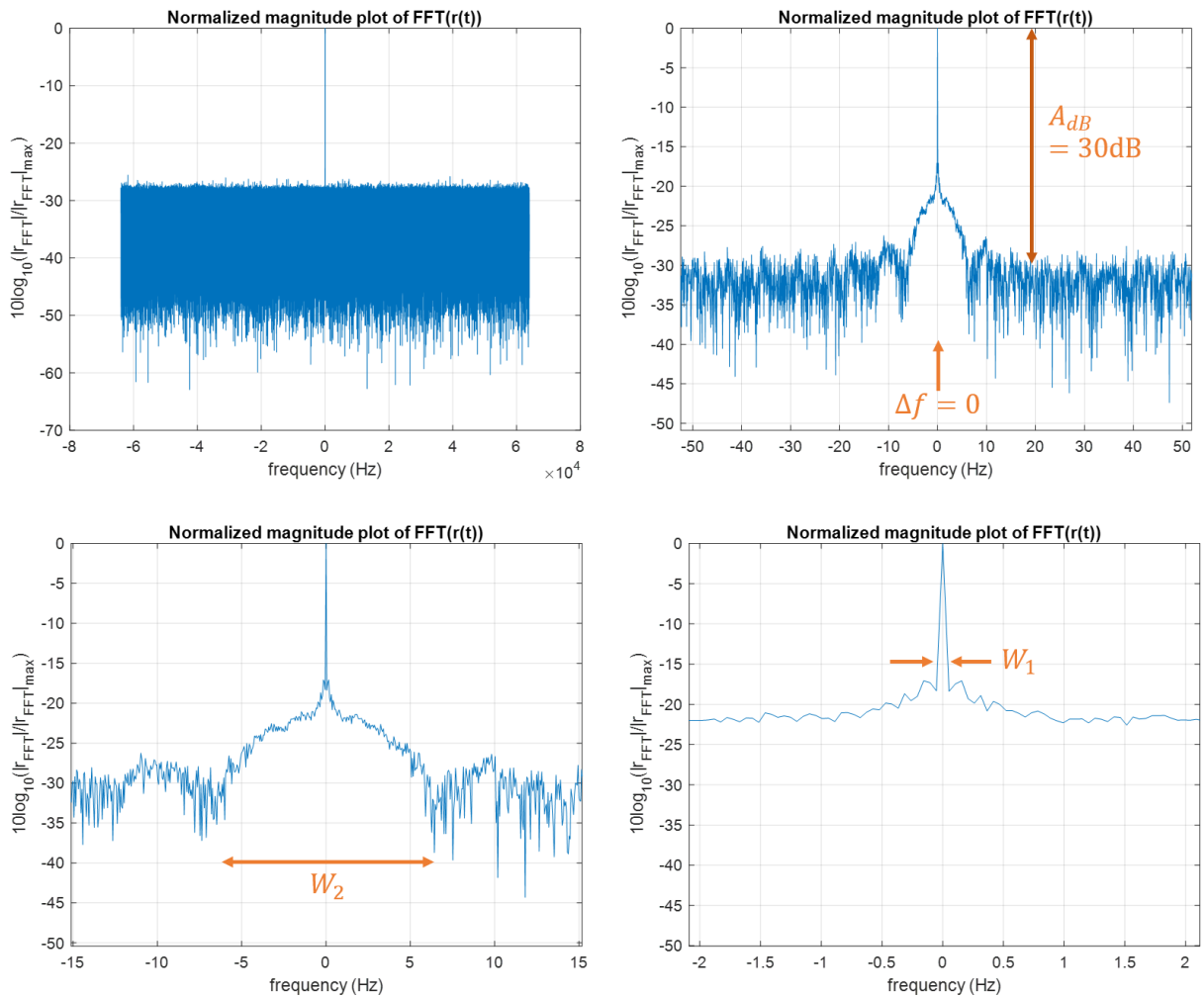


Figure 117. Normalized magnitude plot of $r(\Omega)$ for Lab Setup 1

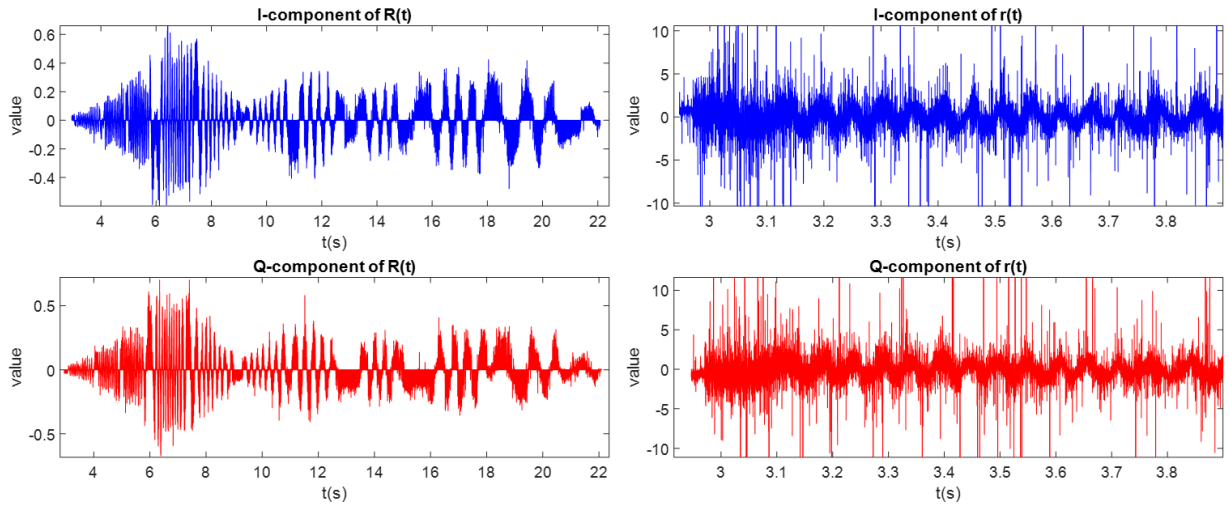


Figure 118. Plot of I and Q components of $R(t)$ vs time for Lab Setup 2

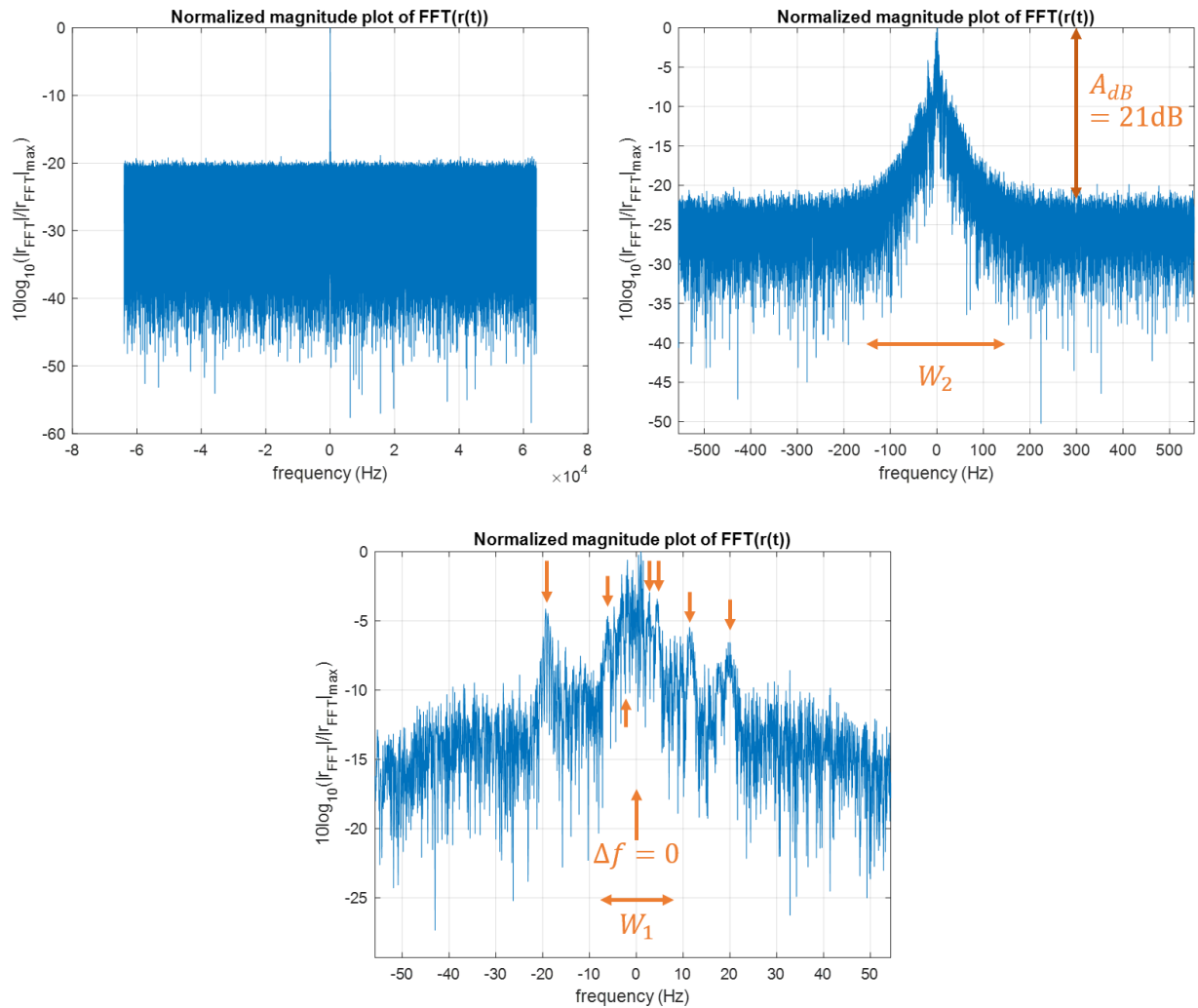


Figure 119. Normalized magnitude plot of $r(\Omega)$ for Lab Setup 2

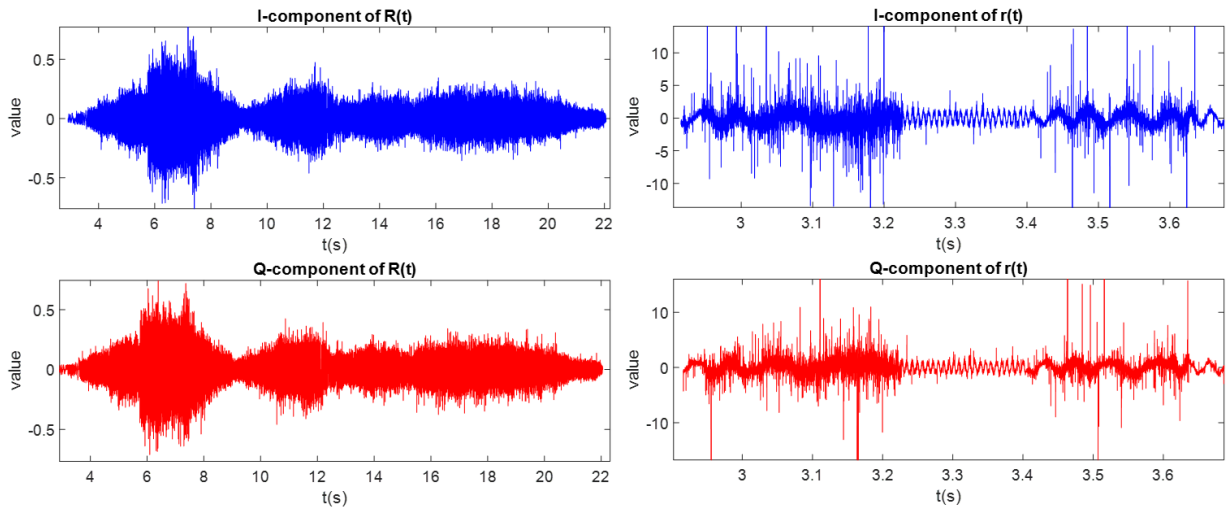


Figure 120. Plot of I and Q components of $R(t)$ and $r(t)$ vs time for Lab Setup 3

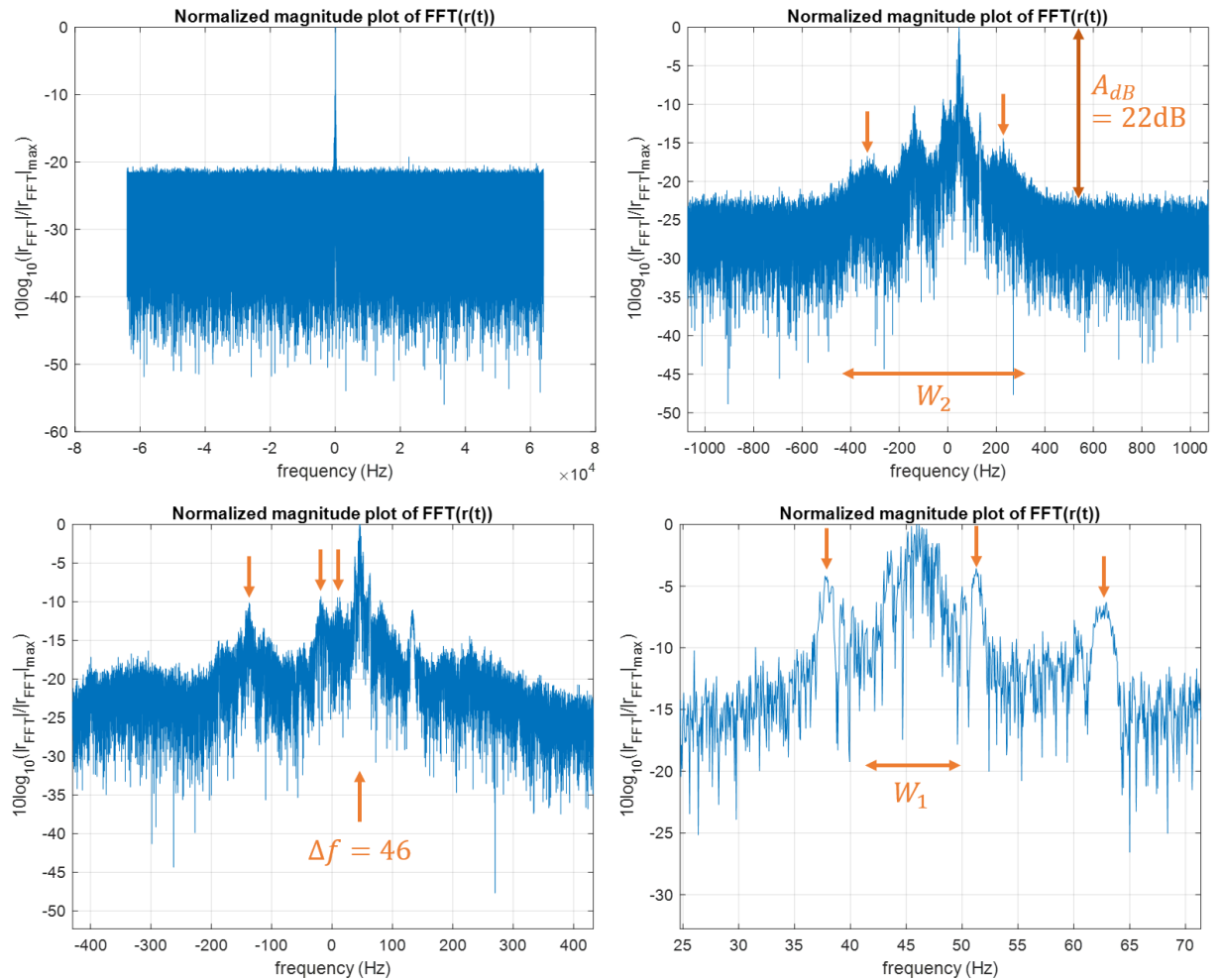


Figure 121. Normalized magnitude plot of $r(\Omega)$ for Lab Setup 3

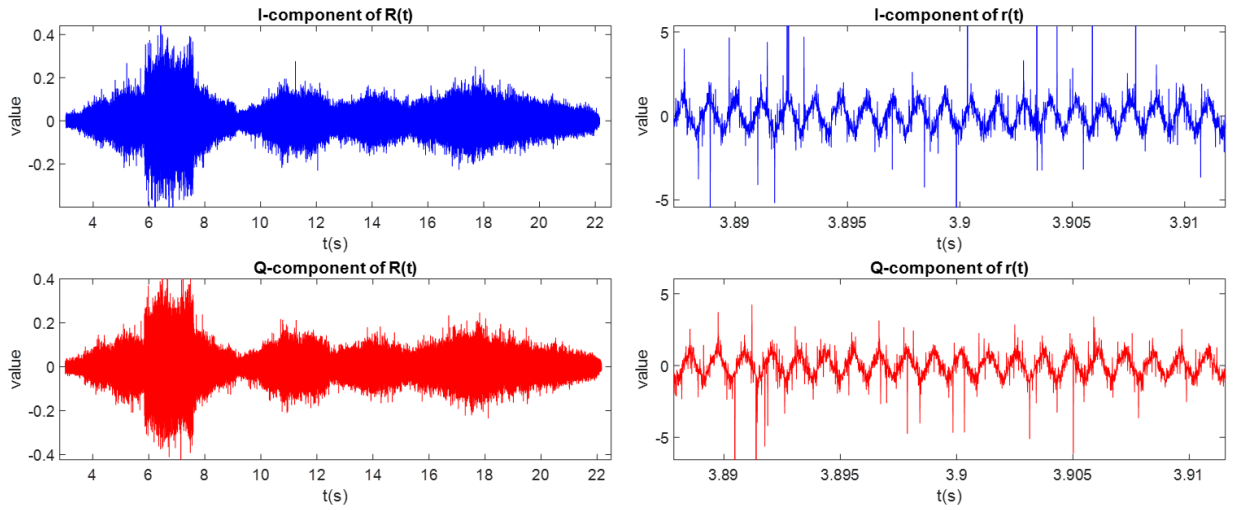


Figure 122. Plot of I and Q components of $R(t)$ and $r(t)$ vs time for Lab Setup 4

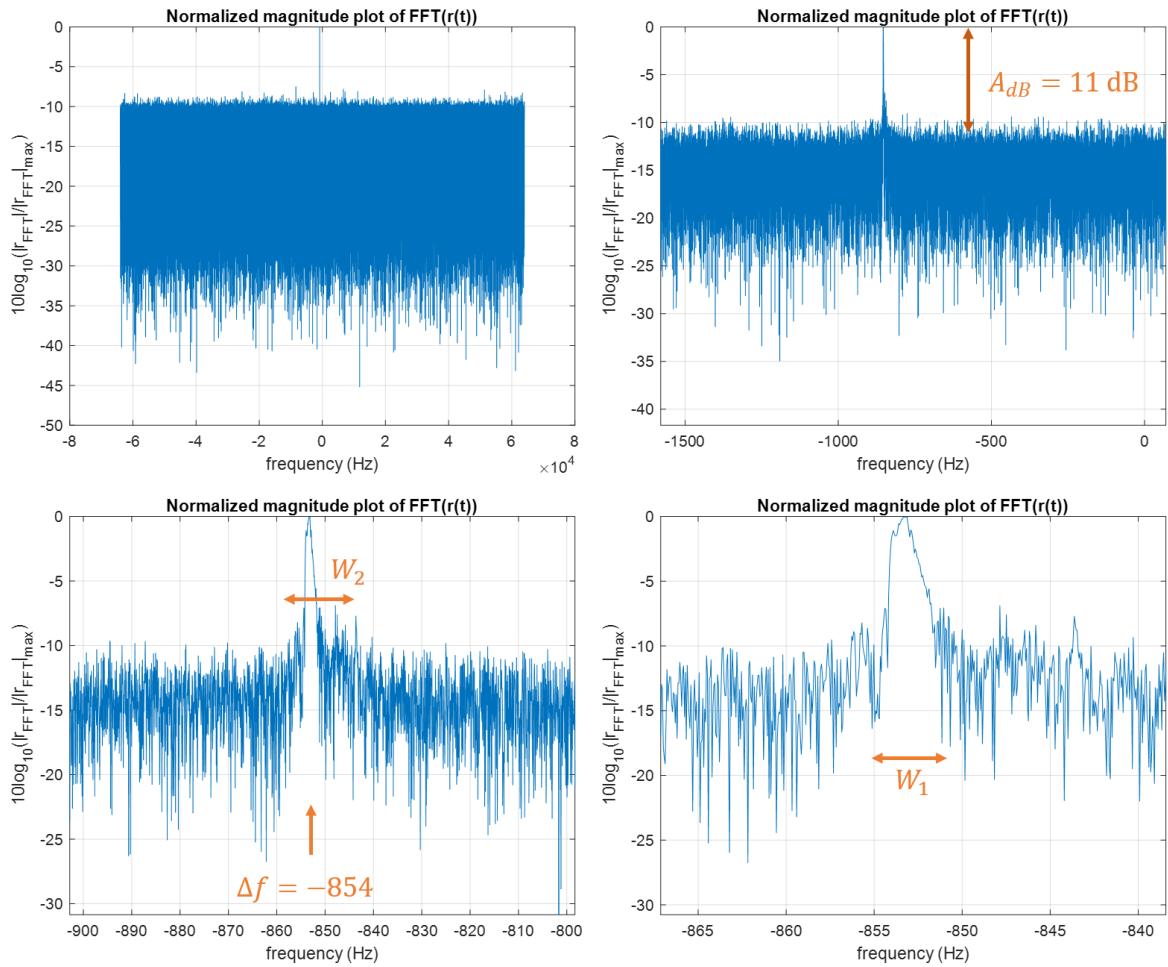


Figure 123. Normalized magnitude plot of $r(\Omega)$ for Lab Setup 4

9.3 Experimental Performance Results For E-SSA Protocol

Tables 32 and 33 provide the cumulative PLR vs iteration number for $G=0.1$, $E_b/N_0 = 14\text{dB}$, $\sigma_{LN} = 6\text{dB}$. Table 32 gives the data for the first attempt in which it was not noticed that there was an error in the program so that the threshold level in the 4th iteration was fixed (hardcoded) to 1.3×10^{-4} . Table 33 gives the data corresponding to the corrected program. Comparing the data for the mistaken program (Table 32) and corrected program (Table 33) let us notice that if we use the same packet detection threshold settings as in the simulation, cumulative PLR “stagnates” (or remains roughly the same) at a high value starting from 2nd or 3rd iteration. This is because the remaining packets could not be effectively detected as was in the simulation case. In Table 32, noting that cumulative PLR significantly dropped in the 4th iteration (in which threshold level was fixed to a very low value), gave us an idea that threshold levels must be lowered to improve the detection rate and thus lower the cumulative PLR.

Table 32. Experimental Cumulative PLR for $G=0.1$, $E_b/N_0 = 14\text{dB}$, $\sigma_{LN} = 6\text{dB}$ (with mistake in iteration 4)

Setup	Cumulative PLR				
	Iteration 1	Iteration 2	Iteration 3	Iteration 4	Iteration 5
Simulation	0.6883	0.1491	0.0407	0.0352	0.0352
Lab Setup 1	0.6938	0.1572	0.0271	0.0244	-
Lab Setup 2	0.8482	0.8347	0.8347	- (too long)	-
Lab Setup 3	0.8482	0.8455	0.8455	0.2114	0.2114
Lab Setup 4	0.8347	0.5501	0.4959	0.2304	0.2304

Simulation: threshold ratios are $r_1=r_2=r_3=r_4=0.15$, $r_5=0.00$

Lab Setups: threshold ratios are $r_1=r_2=r_3=0.15$, $\text{threshold_iteration4}=1.3 \times 10^{-4}$ (hardcoded, mistake), $r_5=0.00$

Table 33. Experimental Cumulative PLR for $G=0.1$, $E_b/N_0 = 14\text{dB}$, $\sigma_{LN} = 6\text{dB}$ (corrected iteration 4)

Setup	Cumulative PLR				
	Iteration 1	Iteration 2	Iteration 3	Iteration 4	Iteration 5
Simulation	0.6883	0.1491	0.0407	0.0352	0.0352
Lab Setup 1	0.6938	0.1572	0.0271	0.0190	0.0163
Lab Setup 2	0.8482	0.8347	0.8347	0.8347	0.7534
Lab Setup 3	0.8482	0.8455	0.8455	0.8455	0.7669
Lab Setup 4	0.8347	0.5501	0.4959	0.4905	0.3875

Simulation: threshold ratios are $r_1=r_2=r_3=r_4=0.15$, $r_5=0.00$

Lab Setups: threshold ratios are $r_1=r_2=r_3=r_4=0.15$ (corrected), $r_5=0.00$

Similarly, Tables 34 and 35 provide the cumulative PLR vs iteration for $G=0.1$, $E_b/N_0 = 26\text{dB}$, $\sigma_{LN} = 6\text{dB}$. However, it seems that no matter what E_b/N_0 was set in the Matlab program generating the received baseband signal, the phase noise is added on top of the phase noise-less signal. In other words,

even if the MATLAB-generated program has zero AWGN, since phase noise is always added on top of the generated signal, a very high E_b/N_0 value will not matter much in the recorded received baseband signal (i.e., in this case, phase noise dominates instead of AWGN). Thus, if we want to control E_b/N_0 after phase noise, we would have to generate noise-less $x(t)$, allow it to propagate in RF and then add AWGN to whatever signal is received at SDR RX based on desired E_b/N_0 .

Table 36 provides the cumulative PLR vs iteration for $G=0.1$, $E_b/N_0 = 14\text{dB}$, $\sigma_{LN} = 6\text{dB}$ after trying out two arrangements for lowering the packet detection thresholds. Note that detection threshold value in each iteration is normally computed as $\text{threshold_iteration}_i = \text{low} + (\text{high}-\text{low}) \cdot \text{ratio}$. Data under Lab Setup 4A correspond to the arrangement in which all ratios $r_1=r_2=r_3=r_4=r_5$ are set to zero, while data under Lab Setup 4B correspond to the arrangement in which the formula for threshold computation is changed from $\text{threshold_iteration}_i = \text{low} + (\text{high}-\text{low}) \cdot \text{ratio}$ to $\text{threshold_iteration}_i = 0.5 \cdot \text{low} + (\text{high}-\text{low}) \cdot \text{ratio}$. Doing this further lowered the detection threshold, thus allowing more packets (even lower powered) to be detected and decoded at earlier iterations, at the expense of higher false alarm rate. This resulted in lower cumulative PLR but took significantly longer processing time.

Table 34. Experimental Cumulative PLR for $G=0.1$, $E_b/N_0 = 26\text{dB}$, $\sigma_{LN} = 6\text{dB}$ (with mistake in iteration 4)

Setup	Cumulative PLR				
	Iteration 1	Iteration 2	Iteration 3	Iteration 4	Iteration 5
Simulation	-	-	-	-	-
Lab Setup 1	0.7154	0.2276	0.0108	-	-
Lab Setup 2	0.8103	0.7832	0.7832	0.4878	0.4444
Lab Setup 3	0.8753	0.8699	0.8672	0.3713	-
Lab Setup 4	0.8455	0.5393	0.4959	0.1924	-

Simulation: no data for $E_b/N_0=26\text{ dB}$

Lab Setups: threshold ratios are $r_1=r_2=r_3=0.15$, $\text{threshold_iteration}_4=1.3 \times 10^{-4}$ (hardcoded, mistake), $r_5=0.00$

Table 35. Experimental Cumulative PLR for $G=0.1$, $E_b/N_0 = 26\text{dB}$, $\sigma_{LN} = 6\text{dB}$ (corrected iteration 4)

Setup	Cumulative PLR				
	Iteration 1	Iteration 2	Iteration 3	Iteration 4	Iteration 5
Simulation	-	-	-	-	-
Lab Setup 1	0.7154	0.2276	0.0108	0	0
Lab Setup 2	0.8103	0.7832	0.7832	0.7832	0.6504
Lab Setup 3	0.8753	0.8699	0.8672	0.8645	0.7832
Lab Setup 4	0.8455	0.5393	0.4959	0.4932	0.4011

Simulation: no data for $E_b/N_0=26\text{ dB}$

Lab Setups: threshold ratios are $r_1= r_2=r_3=r_4=0.15$ (corrected), $r_5=0.00$

Table 36. Experimental Cumulative PLR for $G=0.1$, $E_b/N_0 = 14\text{dB}$, $\sigma_{LN} = 6\text{dB}$ (thresholds lowered to improve packet detection rate)

Setup	Cumulative PLR				
	Iteration 1	Iteration 2	Iteration 3	Iteration 4	Iteration 5
Simulation	0.6883	0.1491	0.0407	0.0352	0.0352
Lab Setup 4A	0.7425	0.4309	0.3875	0.3740	0.3713
Lab Setup 4B	0.7425	0.4309	0.1978	0.1491	0.0650

Simulation: threshold ratios are $r_1=r_2=r_3=r_4=0.15$, $r_5=0.00$

Lab Setups 4A: $r_1=r_2=r_3=r_4=r_5=0.00$ (ratios lowered to improve detection rate)

Lab Setups 4B: same as Lab Setup 4A but in iterations 3-5, changed threshold computation formula from $\text{threshold_iteration}_i = \text{low} + (\text{high}-\text{low}) * \text{ratio}$ to $\text{threshold_iteration}_i = 0.5 * \text{low} + (\text{high}-\text{low}) * \text{ratio}$

9.4 Summary, Conclusion and Recommendations on APRS-DP/S&F Payload Development

This work developed a CubeSat-onboard amateur radio payload that supports both APRS Digipeater and S&F communication for remote data collection. The aim was to leverage on CubeSat platform’s simple architecture, short development time and low cost for these applications, while dealing with tight constraints on space, power, and link budget. The APRS-DP/S&F payload was designed to operate at the VHF amateur frequency (145.825 MHz) to make it easily available for use by the global amateur radio community. The reason for choosing an amateur radio payload implementation is practicality: the opportunity to develop a payload that would be launched and operated in the context of the hands-on BIRDS-2 project and would be easily accessible for use by amateur radio users. Nonetheless, the findings will find relevance to nanosatellite communication design issues regardless of frequency or type of service – beyond amateur radio.

This thesis tackled the design, development, and testing of the APRS-DP/S&F payload onboard the BIRDS-2 CubeSat constellation, as well as the findings from the investigation on uplink communication failure. The developed payload can be accommodated on a 1U CubeSat platform for limited operation time or on a 3U CubeSat platform for full-time operation. It consists of very low-cost COTS components selected for having small form factor, low power consumption, ease of interfacing and little programming work required for the development. Overall, the payload occupies about ¼ of the space on the mission board (which also hosts other subsystems and mission payloads), except for the VHF transceiver placed on a separate board and the dipole antenna mounted on an external board. The payload itself consumes only about 0.29 W while in receive or standby mode and 1.4 W during active RF signal transmission. It underwent various functionality, communication, and space environment verification tests during development.

After the satellites’ deployment into 400km 51° inclination orbit, it was confirmed that receiving the beacon messages regularly transmitted by the payload was working, but full two-way communication

failed due to uplink communication problem. Our post-development investigation through ground-based communication tests found that the uplink failure was caused by two design problems that were overlooked during development, namely, the poor antenna performance and increased payload receiver noise floor due to satellite-radiated EMI coupled to the antenna. The latter problem increased the required receiver input RF power by over 50 dB in the original BIRDS-2 design, thus degrading the receiver sensitivity by a tremendous amount.

In efforts to improve the design and performance of the payload for implementation in the next iteration of BIRDS projects (BIRDS-2S Project at UPD and BIRDS-4 Project at Kyutech), we (1) changed the antenna design from monopole to dipole, and (2) explored on different shielding methods and configurations. Reflection coefficient (S11) measurements and radiation pattern tests on the dipole antennas of BIRDS-2S and BIRDS-4 satellites EM models demonstrated significant improvements in terms of tuning, radiation pattern omnidirectionality and gain. To try to mitigate the effects of satellite-radiated EMI on the payload receiver noise floor, we experimented three shielding methods: (a) copper plate shielding (on BIRDS-2S), (b) aluminum plate shielding (on BIRDS-4) and (c) commercially available non-metallic EMI absorber/shielding sheet. The idea was to wrap the suspected EMI source, that is, OBC/EPS board, with the shielding material, to reduce the amount of EMI captured by the antenna and prevent the receiver noise level from increasing. Unfortunately, all the three methods to date failed to resolve the EMI problem.

The experimental results demonstrated that receiver noise floor increases dramatically (from -135 dBm to about -96 dBm~-93 dBm) whenever a dipole antenna is connected to the receiver RF port. This observation persisted without shielding or with any of the three shielding methods. On the other hand, the BIRDS-4 team performed long-range communication test on the payload twice and reported a receiver sensitivity of about -95 dBm on both occasions. However, this result does not agree with the receiver noise floor measurements inside the laboratory and therefore must be investigated further in the future. The long-range test and receiver noise floor measurement results cannot be correct at the same time. Moreover, although a very good receiver sensitivity was consistently obtained in cabled setup, it must be verified again in wireless setup in isolated condition (i.e., without other satellite parts).

Our experience and investigation emphasize four important recommendations. Firstly, since the antenna characteristics and EMI/EMC aspects are intricately related to one another in a 1U CubeSat with compactly positioned parts, these aspects and altogether with the satellite's structural and EPS designs, must be carefully examined during the preliminary design phase of satellite development. Secondly, the optimum cabled condition receiver sensitivity and the antenna (with pre-existing or mock-up satellite structure and boards) performance must each be tested in early phase of development. In terms of antenna design, if the space constraints allow, dipole antenna is recommended over monopole antenna as the former's characteristics are less dependent on grounding. Similarly, subsystem boards, such as EPS board, must be checked if they might contribute significant EMI levels, whether conducted or radiated form. Thirdly, antenna performance, EMI and receiver noise measurement tests must be performed with the fully

integrated satellite as soon as possible. Mitigation approaches such as adding EMI absorbers or shielding may be experimented upon diagnosis of previously unconsidered problems. Lastly, wireless communication tests inside a full-anechoic chamber and in outdoor very long-distance condition must be done as final confirmation of end-to-end performance and the link budget analysis. For further work, we also recommend to conduct a more comprehensive and systematic study that will examine the EMI/EMC related design issues on CubeSat platforms and provide guidelines to proactively address or mitigate issues that usually arise in very compact CubeSat platforms.

9.5 Summary, Conclusion and Recommendations on E-SSA Protocol-based Nanosatellite S&F Communication System for IoT/M2M Applications

This thesis investigated using E-SSA protocol for nanosatellite IoT/M2M uplink communication and analyzed the packet loss rate (PLR), throughput (THR) and energy efficiency (EE) considering different multiple access (MAC) load, E_b/N_0 and received power imbalance conditions expected in LEO. The E-SSA protocol had been previously proposed and investigated in prior works in literature considering GEO satellite. Our research focused on investigating suitability of E-SSA protocol for the said application considering a nanosatellite platform with hardware, processing capability and energy constraints, as well as ground sensor terminals (GSTs) with low-cost, simple hardware and limited energy budget. Our study assumes a nanosatellite constellation in LEO so that it must face several physical communication layer constraints and characteristics of a LEO communication channel (Doppler shift, rate, phase offset, and received amplitudes variation) involving a large population of GSTs. Although it is true that E-SSA requires a tremendous signal processing power to be able to decode a large number of overlapping packets, we think of a practical work-around in which nanosatellites only record received baseband signals and on-ground post-processing is performed on downloaded signal samples.

We modeled the communication scenario in a MATLAB simulation program, considering physical communication layer details in the baseband domain. To reflect the different Doppler frequency shifts, rates, and amplitudes among received packets in realistic condition, channel parameters of individual terminals were randomly generated based on terminals' spatial distribution. The received amplitude was modeled as the product of a random variable (RV) due to terminal spatial distribution and a lognormally distributed RV accounting for the joint effect of land mobile service (LMS) channel fading/shadowing statistics, antenna radiation patterns and with/without power control. We then described details of an iterative baseband signal processing algorithm having random-access resolution and packet decoding capabilities (E-SSA protocol-based). The formulated E-SSA protocol-based algorithm involves packet detection, channel estimations, demodulation/decoding and successive interference cancellation. The algorithm was optimized to obtain a good balance between high packet detection rate and low false alarm rate, very accurate channel estimation, and overall, obtain low packet loss rates even with ultra-low data rate transmissions from GSTs (<333 bps). Rate $\sim 1/3$ Turbo code was employed to completely recover packets even with several bit errors due to imperfect channel estimation, multi-user interference, and noise.

Simulation results across different MAC load G and received amplitude variation σ_{LN} conditions showed that at $E_b/N_0=14$ dB, the channel estimation algorithm can estimate amplitude with mean absolute (mabs) error of 0.8~1.2 dB in 1st iteration, 1.0~9.0 dB in 3rd iteration, and 1.0~13.3 dB in 5th iteration. Phase estimation mabs error of 0.03~0.60 rad., frequency shift estimation mabs error of 0.09~0.60 Hz, and frequency rate estimation mabs error of 0.10~0.64 Hz/s, were attained. However, because these estimation error ranges would still result in coherence times shorter than the packet duration, these estimates alone would not be enough for successful packet decoding. Thus, when decoding each packet, other frequency shift and rate candidates around the fine estimates were tried with 0.2 Hz and 0.2 Hz/s increments/decrements within limited trial ranges. Doing this would give 0.2 Hz and 0.2 Hz/s minimum average final estimation errors. With the rate $\sim 1/3$ Turbo code, these limited accuracies could still allow complete packet recovery despite erroneous symbols caused by combined effects of multiuser interference (MUI), imperfect interference cancellation residue power, noise, and phase reversals, as PLR results showed.

Simulation results showed that with the actual baseband signal processing algorithm, THR, PLR and EE metrics are sensitive to MAC load G , received power variation σ_{LN} , and E_b/N_0 . With loose power control ($\sigma_{LN} = 3$ dB), at $E_b/N_0=14$ dB, the system can be operated up to a maximum load of 1.3 bps/Hz, achieving a maximum THR of 1.25 bps/Hz with $PLR < 0.03$. Without power control (higher $\sigma_{LN} = 6$ dB, 9 dB), at $E_b/N_0=14$ dB, maximum load is also 1.3 bps/Hz, but achievable THR is lower than ~ 1 bps/Hz and PLR values can be as high as ~ 0.23 . Moreover, for all three σ_{LN} values, PLR , THR and η_{EE} are more sensitive to MAC load such that even for $G < 1.3$ bps/Hz, we see increasing PLR and decreasing η_{EE} with increasing G (compared with relatively constant plots in ideal case with perfect packet detection and channel estimation). Considering the said limits for G , the maximum THR for $\sigma_{LN} = 6$ dB and 9 dB are about 1.1 bps/Hz and 0.9 bps/Hz, respectively. However, if we consider the target $PLR < 5\%$, it is impossible to meet this with any G when $\sigma_{LN} = 9$ dB. For $\sigma_{LN} = 6$ dB, it is possible to meet PLR requirement when $G < 0.5$. For $\sigma_{LN} = 3$ dB, it is possible to meet PLR requirement when $G < 1.4$.

The worse PLR results are due to imperfect packet detection and channel estimation algorithms. Firstly, cumulative misdetection rates (CMDR), even after 5 or 6 iterations, are quite high. Had we only observed the data after five iterations, we might be tempted to say that majority of packet losses are caused by packets being not yet detected and the remaining smaller portion are due to demodulation/decoding error. However, since we also examined the data after six iterations, we realized that while $CMDR$ can be reduced by proceeding to 6th iteration, those lower power newly detected packets can no longer be decoded effectively. Therefore, we can say that overall, packet losses can be attributed – in mutually significant proportions – to both misdetections and demodulation/decoding errors. Both are caused by the combined effects of MUI, channel estimation errors, imperfect interference cancellation residue power, and noise. Also, imperfect channel estimation causes accumulated residue interference power which can hamper detection and/or demodulation/decoding of lower power packets in later iterations. The PLR and THR can

be improved by operating with higher E_b/N_0 (i.e., higher transmit power) at the expense of lower energy efficiency.

Finally, we experimentally validated the simulation results through four laboratory setups representing various extents of additional signal impairments not accounted for in simulation model, including frequency errors, phase noise and sampling timing errors. These impairments arise in practical scenarios wherein GSTs employ low-cost oscillators but with output frequency uncertainties (limited accuracies), instability (dynamically varies, with time) and random phase errors (phase noise). Thus, the goal is not only to validate the simulation results but also to confirm whether the formulated algorithm for E-SSA protocol can still perform well even with additional signal impairments caused by employing low-cost oscillators on the GSTs. Using software-defined radio (SDR) modules, the MATLAB-generated received baseband signal (emulating numerous GST transmissions, each experiencing different Doppler shift, rate, amplitude and carrier phase offset) was allowed to go through data conversion circuits (DACs/ADCs), analog filters and RF frontends (TX/RX PLL and mixers). The RF output signal on the SDR TX side propagated to the SDR RX side through RF cable and attenuators. Then, the recorded received baseband signal at SDR RX side was post-processed by the same MATLAB simulation program.

Among the four laboratory setups, Lab Setup 4 represents most closely the realistic scenario because it uses only the reference oscillator built-in the SDR TX. Experimental results for cumulative PLR (CPLR) in Lab Setup 4 (with $G=0.1$, $E_b/N_0 = 14\text{dB}$, $\sigma_{LN} = 6\text{dB}$) were bad, reaching only 0.3875 after five iterations, compared to simulation result of 0.0352. It was noticed that CPLR stagnates at a still high value after 2nd or 3rd iteration due to high packet misdetection rate, and that only high-power packets could be detected and decoded (in the 1st and 2nd iterations). Packet detection rate was improved by lowering the detection threshold values, thus lowering the experimental CPLR result to 0.0650, although still slightly worse than simulation result. However, false alarm rate increased, thus leading to significantly longer processing time. With the given $G=0.1$, $E_b/N_0 = 14\text{dB}$, $\sigma_{LN} = 6\text{dB}$ conditions considered so far, we can conclude that the formulated algorithm for E-SSA protocol can still work even with inaccurate oscillator (± 2 ppm), but this requires lowering the detection thresholds and takes significantly longer processing time.

For future work, other G and σ_{LN} conditions will be considered in the laboratory setup. Also, for further work, it is recommended to perform the laboratory validation in a wireless condition. Other recommendations include: (1) further optimizing the signal processing algorithm so that it takes shorter time, and (2) implementing a computing hardware to execute the algorithm at faster speed (e.g. computing hardware supporting parallel or distributed processing).

9.6 Summary, Conclusion and Recommendations on S&F Nanosatellite Constellation Design

S&F nanosatellite constellation design applied the findings from E-SSA protocol simulation in computing the coverage in terms of meeting the link budget requirement ($E_b/N_0 > 15\text{ dB}$, link margin $> 5\text{ dB}$), in addition to the minimum satellite elevation requirement (5°). We considered a communication scenario

Nanosatellite S&F Communication Systems for Remote Data Collection Applications

with operation frequency of 402 MHz and information transmission rate of 333 bps. For a given constellation size, there are optimum values for satellite altitude and GST transmit power that can provide the highest percent coverage time (PCT). The optimum values for satellite altitude and GST transmit power were determined by first considering a small constellation (3x3 Hybrid constellation). The optimum values were found to be altitude=700 km and $P_{TX}=17$ dBm, which were selected for upscaling the constellation.

Compared to Walker Delta constellations, Hybrid constellations provide more even coverage across all latitudes. For the high-inclination Walker Delta constellations, near polar regions have higher PCT than near equatorial regions. To achieve the target PCT of more than 95% across all latitudes, a 9x10 Hybrid constellation or a 10x10 Walker Delta constellation would be required (although for the latter, PCT is slightly below 95% at $\pm 10^\circ$ latitudes). Both the 9x10 Hybrid constellation and the 10x10 Walker Delta constellation meet the 100% minimum percent area coverage (PAC) requirement.

To achieve the minimum PCT requirement, a large constellation is required, thus it becomes unavoidable that multiple satellites will be visible to GSTs at any time. We recommend investigating the improvement it brings to the PLR since the computation of PLR in the simulation assumes the GSTs always communicate only to a single satellite.

References

- [0] “Definition and Requirements of Small Satellites Seeking Low-Cost and Fast-Delivery”, edited by Mengu Cho and Filippo Graziani, International Academy of Astronautics, Code ISBN/EAN IAA: 978-2-917761-59-5, 2017.
- [1] Adriano Camps, Satellites Missions and Technologies for Geosciences (book title, edited by Prof. Vladislav Demyanov and Dr. Jonathan Becedas), *Nanosatellites and Applications to Commercial and Scientific Missions* (chapter title) by Adriano Camps, November 2019, DOI: 10.5772/intechopen.90039.
- [2] K.K. Pradhan and M. Cho, “Shortening of Delivery Time for University-Class Lean Satellites”, *Journal of Small Satellites (JoSS)*, Vol. 9, No. 1, pp. 881-896, <https://jossonline.com/letters/shortening-of-delivery-time-for-university-class-lean-satellites/>
- [3] Erik Kulu, Nanosats Database, <https://www.nanosats.eu/#figures> , Accessed: July 31, 2020.
- [4] London Economics, “Nanosatellite Telecommunications: A Market Study for IoT/M2M applications”, August 2017, Available: https://londoneconomics.co.uk/wp-content/uploads/2017/10/LE-CSL-IoT-M2M-Market-Sizing-Requirements-Report-FINAL_PUBLIC-S2C310817_FOR-WEBSITE_v2.pdf.
- [5] PSAT2 - Amateur Radio Communications Transponders, <http://aprs.org/psat2.html>
- [6] Improving Mission Success of CubeSats, U.S. Space Program Mission Assurance Improvement Workshop, June 2017. https://www.nasa.gov/sites/default/files/atoms/files/improving_mission_success_of_cubesats_-_tor-2017-01689.pdf
- [7] O. del Rio Herrero and R. De Gaudenzi, “High Efficiency Satellite Multiple Access Scheme for Machine-to-Machine Communications”, *IEEE Transactions on Aerospace and Electronics Systems*, Vol. 48, No. 4, October 2012.
- [8] R. De Gaudenzi, O. del Herrero and G. Gallinaro, “Enhanced spread Aloha physical layer design and performance”, *Int. J. Satell Commun Network*, Vol. 32, Issue 6, May 2014, pages 457-473, <https://doi.org/10.1002/sat.1078>.
- [9] M. Andrenacci, G. Mendola, F. Collard, D. Finocchiaro and A. Recchia, “Enhanced spread spectrum aloha demodulator implementation, laboratory tests and satellite validation”, *Int. J. Satell Commun Network*, Vol. 32, Issue 6, November 2014, pages 521-533, <https://doi.org/10.1002/sat.1086>.
- [10] IBM, “What is the Internet of Things (IoT)?”, <https://www.ibm.com/blogs/internet-of-things/what-is-the-iot/>, November 17, 2016.
- [11] The M2M (wireless M2M: The Wireless M2M) meaning, <https://mono-wireless.com/jp/tech/M2M.html>
- [12] R. Diersing, G. Jones, *Low Earth-Orbit Store-And-Forward Satellites in the Amateur Radio Service*, *IEEE AES Systems Magazine*, 8 1 (1993) 21–30.
- [13] M.N. Allery, H.E. Price, J.W. Ward, R.A. Da Silva Curiel, *Low Earth orbit microsattellites for data communications using small terminals*, 10th International Conference on Digital Satellite

Communications, 1995, October.

- [14] M. Antonini, et. al., “Satellite Data Collection & Forwarding Systems”, IEEE A&E Systems Magazine, September 2005.
- [15] D. Abbasi and M. Abolghasemi., “Store & Forward Communication Payload Design for LEO Satellite Systems”, Majlesi Journal of Electrical Engineering, Vol. 10, No. 3, September 2016.
- [16] V. Vaidehi, S. Muthuselvam, et.al., “Software Design of Store and Forward Payload for a Microsatellite”, Dept. Electronics Engineering, Madras Institute of Technology, Anna University, India.
- [17] T. Matsumoto, M. Matsui, S. Nakasuka, et. al., “Development of Store and Forward System for Hodoyoshi-3&4 Microsatellites”, Trans. JSASS Aerospace Tech. Japan, Vol. 14, No. ists30, 2016.
- [18] SkyscraperCity “Le satellite marocain : MAROC-TUBSAT (زرقاء اليمامة)”,
<https://www.skyscrapercity.com/showthread.php?t=1100887>, April 1, 2020.
- [19] The Satellite Encyclopedia “Maroc-Tubsat”, https://www.tbs-satellite.com/tse/online/sat_maroc_tubsat.html, August 30, 2020.
- [20] E.B. Zantou, A. Kherras, Small Mobile Ground Terminal Design for a Microsatellite Data Collection System, Journal of Aerospace Computing, Information, and Communication, 1 (2004) 364–371.
- [21] eoPortal Directory, “ANUSat (Anna University Microsatellite)”,
<https://earth.esa.int/web/eoportal/satellite-missions/a/anusat>.
- [22] T. Matsumoto, M. Matsui, S. Nakasuka, et. al., “Development of Store and Forward System for Hodoyoshi-3&4 Microsatellites”, Trans. JSASS Aerospace Tech. Japan, Vol. 14, No. ists30, 2016.
- [23] H.E. Price, J.W. Ward, “PACSAT Protocol Suite - An overview”, TAPR, Available:
<https://web.tapr.org/pdf/CNC1990-PacSatOverview-NK6K-K8KA.pdf>.
- [24] R.J. Twigg, H. Heidt, J. Puig-Suari, A.S. Moore, S. Nakasuka, A CubeSat: a new generation of Picosatellite for education and industry low-cost space experimentation, Proceedings of the 14th Annual AIAA/USU Conference on Small Satellites, SSC00-V-5, Logan, Utah, USA, 2000, August.
- [25] J. Guzman, G. Comina, H. Bedon, et. al., Global water pollution monitoring using a nanosatellite constellation (chapter 1), in: R. Sandau, S. Nakasuka, R. Kawashima, J. Sellers (Eds.), Novel Ideas for Nanosatellite Constellation Missions Edition 1, International Academy of Astronautics, 2012. pp. 144-155.
- [26] A. Addaim, A. Kherras, Z. Gennoun, Design of WSN with Relay Nodes Connected Directly with a LEO Nanosatellite, Int. J. of Computer and Communications Engineering, 3 5 (2014). 310–316.
- [27] H. Bedon, C. Miguel, A. Fernandez, J.S. Park, A DTN System for Nanosatellite-based Sensor Networks using a New ALOHA Multiple Access with Gateway Priority, Smart Computing Review, 3 5 (2013), 383–396.
- [28] M. De Sanctis, E. Cianca, G. Araniti, et. al., Satellite Communications Supporting Internet of Remote Things, IEEE Internet of Things Journal, 3 1 (2016) 113–123.
- [29] T. Koritza, J.M. Bellardo, Increasing cubesat downlink capacity with store-and-forward routing and

- data mules, July 2010,
https://www.researchgate.net/publication/229018687_Increasing_CubeSat_Downlink_Capacity_With_Store-and-Forward_Routing_and_Data_Mules, (accessed 10.09.18).
- [30] W. Colitti, K. Steenhaut, N. Descouvemont, A. Dunkels, “Poster Abstract: Satellite Based Wireless Sensor Networks – Global Scale Sensing with Nano- and Pico-Satellites”, SenSys 2008.
- [31] A. Addaim, E.B. Zantou, A. Kherras, Design and Analysis of Store-and-Forward Data Collection Network using Low-cost LEO Small Satellite and Intelligent Terminals, *Journal of Aerospace Computing, Information, and Communication*, 5, (2008), 35–46.
- [32] A. Addaim, A. Kherras, Z. Guennoun, Enhanced MAC protocol for designing a wireless sensor network based on a single LEO Picosatellite, *Int. J. of Sensor Networks*, 23 3 (2017) 143–154.
- [33] E.B. Zantou, A. Kherras, A. Addaim, Performance Evaluation of a Single Microsatellite Data Collection System using Small Ground Terminals, *Journal of Aerospace Computing, Information, and Communication*, 3 (2006) 63–72.
- [34] A. Castro, R. Walker, F. Emma, F. Aguado, R. Tubio, W. Balogh, “Hands-on Experience: The HumSAT system and the ESA GEOID Initiative”, *ESA Bulletin*, No. 149, February 2012, pp. 45-50.
- [35] M.G. Jenkins, J.C. Alvarado, A.J. Calvo, A.C. Jimenez, et. al., Project Irazu: Advances of a Store & Forward CubeSat Mission for Environmental Monitoring in Costa Rica, 68th International Astronautical Congress (IAC), Adelaide, Australia, 2017, 25–29 September.
- [36] Q. Verspiepren, T. Obata, S. Nakasuka, Innovative Approach to Data Gathering in Remote Areas Using Constellations of Store & Forward Communications Cubesats, 31st International Symposium on Space and Technology (ISTS), Matsuyama, Japan, 2017, 3–9 June.
- [37] HumSat, “HumSat payload”, Available: <https://www.humsat.org/humsat-d-mission/space-segment/humsat-payload/>.
- [38] Q. Verspiepren, T. Matsumoto, Y. Aoyanagi, T. Fukuyo, T. Obata, S. Nakasuka, G. Kwizera, J. Abakunda, “Store and Forward 3U CubeSat Project TRICOM and Its Utilizations for Development and Education: the cases of TRICOM-1R and JPRWASAT”, 32nd International Symposium on Space Technology and Science, Fukui, Japan, June 2019.
- [39] Q. Verspiepren, Y. Aoyanagi, T. Matsumoto, T. Hamada, S. Nakasuka, “CubeSat-Based Low-Cost Communication Network and its Utilisation for Capacity Building in Developing Countries”, 70th International Astronautical Congress (IAC), Washington D.C. United States, October 2019.
- [40] PCSAT-1, Amateur Radio Satellite NO-44, <http://aprs.org/pcsat.html>
- [41] LAPAN-A2 microsatellite of Indonesia, <https://directory.eoportal.org/web/eoportal/satellite-missions/l/lapan-a2>
- [42] Diwata-2, <https://phl-microsat.upd.edu.ph/diwata2>
- [43] PSAT-ARPS and a new PSK31 Approach, <http://aprs.org/psat.html>
- [44] PSAT-2 - Standardizing Cubesat APRS Transponders USNA Student Satellite Project 2016!, <http://aprs.org/psat-2.html>

- [45] BRICSAT2 (USNAP1) - The first APRS Satellite with Thrusters, <http://aprs.org/bricsat2.html>
- [46] Automatic Packet Reporting System (APRS), 2002, www.aprs.org.
- [47] US Naval Academy, “BRICSAT2 (USNAP1) - The first APRS Satellite with Thrusters”, <http://aprs.org/bricsat2.html>.
- [48] US Naval Academy, “PSAT2 - Amateur Radio Communications Transponders”, <http://aprs.org/psat2.html>.
- [49] A.C. Salces, S.B.M. Zaki, S. Kim, H. Masui, M. Cho, “Design, Development, Testing and On-Orbit Performance Results of a Low-cost Store-and-Forward Payload Onboard a 1U CubeSat Constellation for Remote Data Collection Applications”, Proceedings of the 69th International Astronautical Congress (IAC), October, 2018.
- [50] US Naval Academy, “PCSAT-1, Amateur Radio Satellite NO-44”, <http://aprs.org/pcsat.html>.
- [51] Astrocast, <https://www.astrocast.com/>
- [52] SpaceNews, “Astrocast raises \$9.2 million, grows target IoT constellation size to 80 satellites” by Caleb Henry, September 4, 2019, <https://spacenews.com/astrocast-raises-9-2-million-grows-target-iot-constellation-size-to-80-satellites/>
- [53] Gunter’s Space Page, “Astrocast 0.1, 0.2 (Kiwi, Hawaii)”, https://space.skyrocket.de/doc_sdat/astrocast-0.htm
- [54] Electronics Weekly, “Astrocast preps launch of IoT nanosatellite constellation”, by Alun Williams, February 6, 2020, <https://www.electronicsweekly.com/news/astrocast-preps-launch-iot-nanosatellite-constellation-2020-02/>
- [55] <https://hiber.global/>
- [56] Gunter’s Space Page, “Hiber 1, 2”, https://space.skyrocket.de/doc_sdat/hiber-1.htm
- [57] NewSpace Index, “Hiber”, <https://www.newspace.im/constellations/hiber>
- [58] Space IT Bridge, “Hiber launches commercial IoT satellite trials worldwide”, by Doug Mohny, November 6, 2019, <https://www.spaceitbridge.com/hiber-launches-commercial-iot-satellite-trials-worldwide.htm>.
- [59] Kepler, <https://www.kepler.space>
- [60] TechCrunch, “Kepler will build its small satellites at a new manufacturing facility in Toronto”, by Darrell Etherington, January 29, 2020, <https://techcrunch.com/2020/01/28/kepler-will-build-its-small-satellites-at-a-new-manufacturing-facility-in-toronto/>
- [61] Gunter’s Space Page, “KIPP, CASE (Kepler 1, 2)”, https://space.skyrocket.de/doc_sdat/kepler-1.htm
- [62] Gunter’s Space Page, “TARS (Kepler 3, IOD 5)”, https://space.skyrocket.de/doc_sdat/kepler-3.htm
- [63] Space Daily, “Space Flight Laboratory and Kepler Communications team up for nanosatellite constellation”, February 4, 2020, https://www.spacedaily.com/reports/Space_Flight_Laboratory_and_Kepler_Communications_announce_collaboration_on_fully_operational_nanosatellite_constellation_999.html
- [64] Fleet Space, <https://www.fleet.space/>

- [65] SpaceNews, “Fleet details 100 nanosat constellation for Internet of Things connectivity”, by Caleb Henry, December 6, 2017, <https://spacenews.com/fleet-details-100-nanosat-constellation-for-internet-of-things-connectivity/>
- [66] IT News, “Fleet Space Tech to launch two commercial CubeSats”, by Juha Saarinen, October 30, 2018, <https://www.itnews.com.au/news/fleet-space-tech-to-launch-two-commercial-cubesats-514736>.
- [67] SpaceNews, “Fleet raises \$7.35 million to expand Internet of Things constellation”, by Jeff Foust, September 4, 2019, <https://spacenews.com/fleet-raises-7-35-million-to-expand-internet-of-things-constellation/>
- [68] Keneis, <https://www.kineis.com/en/>
- [69] SpaceNews, “Kinéis raises 100 million euros to build and launch 25 IoT cubesats”, by Caleb Henry, February 4, 2020, <https://spacenews.com/kineis-raises-100-million-euros-to-build-and-launch-25-iot-cubesats/>
- [70] Myriota, <https://myriota.com/>
- [71] Myriota, “Myriota Product Brief”, <https://myriota.com/wp-content/uploads/2019/04/Myriota-Product-Brief-Final.pdf>
- [72] NewSpace Index, “Myriota”, <https://www.newspace.im/constellations/myriota>
- [73] Space IT Bridge, “Satellite IoT: Myriota orders Tyvak cubesats; Fleet Space – \$2/device/year; Astrocast books launch”, by Dough Mohny, February 7, 2019, <https://www.spaceitbridge.com/satellite-iot-myriota-orders-tyvak-cubesats-fleet-space-2deviceyear-astrocast-books-launch.htm>
- [74] ComputerWorld, “Myriota touts IoT satellite service’s ability to scale, power-efficiency”, by Rohan Pearce, May 24, 2019, <https://www.computerworld.com/article/3487950/myriota-touts-iot-satellite-service-s-ability-to-scale-power-efficiency.html>
- [75] Swarm, <https://www.swarm.space/>
- [76] NewSpace Index, “Swarm Technologies”, <https://www.newspace.im/constellations/swarm-technologies>
- [77] Space IT Bridge, “Swarm lands \$25 million venture round for satellite IoT network”, by Dough Mohny, January 24, 2019, <https://www.spaceitbridge.com/swarm-lands-25-million-venture-round-for-satellite-iot-network.htm>
- [78] TechCrunch, “Swarm gets green light from FCC for its 150-satellite constellation”, by Devin Coldewey, October 18, 2019, <https://techcrunch.com/2019/10/17/swarm-gets-green-light-from-fcc-for-its-150-satellite-constellation/>
- [79] Via Satellite, “Swarm Receives FCC Approval to Launch 150 Satellites”, by Annamarie Nyirady, October 18, 2019, <https://www.satellitetoday.com/government-military/2019/10/18/swarm-receives-fcc-approval-to-launch-150-satellites/>
- [80] Lacuna Space, <https://lacuna.space/>
- [81] NewSpace Index, “Lacuna Space”, <https://www.newspace.im/constellations/lacuna-space>

- [82] Semtech, “Semtech and Lacuna Receiving Messages from Space”, February 15, 2018, <https://www.semtech.com/company/press/semtech-and-lacuna-receiving-messages-from-space>
- [83] NewSpace Index, “Helios Wire”, <https://www.newspace.im/constellations/helios-wire>
- [84] Space News, “EchoStar, fresh off Helios Wire acquisition, orders S-band smallsats from Tyvak”, by Caleb Henry, November 14, 2019, <https://spacenews.com/echostar-fresh-off-helios-wire-acquisition-orders-s-band-smallsats-from-tyvak/>
- [85] Gunter’s Space Page, “Helios-Wire 1, 2, 3”, https://space.skyrocket.de/doc_sdat/helios-wire.htm
- [86] Eutelsat, “LEO Fleet”, <https://www.eutelsat.com/en/satellites/leo-fleet>
- [87] Capacity Media, “Eutelsat to launch nano satellites in IoT partnership with Sigfox”, <https://www.capacitymedia.com/articles/3824281/eutelsat-to-launch-nano-satellites-in-iot-partnership-with-sigfox>, September 25, 2019.
- [88] SpaceWatch, “France’s Sigfox and Plastimo partner to provide satellite IoT maritime geolocation”, <https://spacewatch.global/2019/12/frances-sigfox-and-plastimo-partner-to-provide-satellite-iot-maritime-geolocation/>
- [89] Eutelsat, “Eutelsat kicks off ELO, its constellation of nanosatellites dedicated to the Internet of Things”, <https://news.eutelsat.com/pressreleases/eutelsat-kicks-off-elo-its-constellation-of-nanosatellites-dedicated-to-the-internet-of-things-2923247>, September 24, 2019.
- [90] Wireless, “Sigfox results in, Eutelsat plans global satellite coverage, says CEO”, <https://rethinkresearch.biz/articles/sigfox-results-in-eutelsat-plans-global-satellite-coverage-says-ceo/>, February 22, 2019.
- [91] Telecom TV, “Sigfox adds satellite connectivity to its low power IoT offering”, <https://www.telecomtv.com/content/satellite/sigfox-adds-satellite-connectivity-to-its-low-power-iot-offering-37223/>, December 13, 2019.
- [92] NewSpace Index, “Eutelsat (CubeSats)”, <https://www.newspace.im/constellations/eutelsat>
- [93] Space News, “Eutelsat taps Loft Orbital, AAC Clyde to lay cornerstone for ELO constellation”, by Caleb Henry, September 25, 2019, <https://spacenews.com/eutelsat-taps-loft-orbital-aac-clyde-to-lay-cornerstone-for-elo-constellation/>
- [94] Gunter’s Space Page, “ELO”, https://space.skyrocket.de/doc_sdat/elo.htm
- [95] Sky and Space (SAS), <https://www.skyandspace.global/>
- [96] NewSpace Index, “Sky and Space”, <https://www.newspace.im/constellations/sky-and-space-global>
- [97] NewSpace Index, “Sky and Space”, <https://www.newspace.im/constellations/sky-and-space-global>
- [98] Space News, “Sky and Space Global narrows immediate goal to eight satellites as funding remains elusive”, by Caleb Henry, December 4, 2019, <https://spacenews.com/sky-and-space-global-narrows-immediate-goal-to-eight-satellites-as-funding-remains-elusive/>
- [99] Wikipedia, “Sky and Space Global”, https://en.wikipedia.org/wiki/Sky_and_Space_Global
- [100] GomSpace, “Sky and Space Global”, <https://gomspace.com/sky-and-space-global.aspx>
- [101] Alén Space, “Sateliot selects Alén Space to design its satellite payloads”, January 29, 2020, <https://alen.space/sateliot-selects-alen-space-to-design-its-satellite-payloads/>

- [102] <https://www.spaceitbridge.com/sateliot-joins-the-5g-iot-satellite-wave.htm>
- [103] Space IT Bridge, “Sateliot joins the 5G IoT satellite wave”, Doug Mohny, November 21, 2019, <https://www.spaceitbridge.com/sateliot-joins-the-5g-iot-satellite-wave.htm>
- [104] NewSpace Index, “Sateliot”, <https://www.newspace.im/constellations/sateliot>
- [105] OQ Technology, <http://www.oqtec.space/>
- [106] Space News, “OQ Technology hoping to jump ahead in IoT race through GomSpace cubesat tests”, by Caleb Henry, October 16, 2019, <https://spacenews.com/oq-technology-hoping-to-jump-ahead-in-iot-race-through-gomspace-cubesat-tests/>
- [107] NewSpace Index, “OQ Technology”, <https://www.newspace.im/constellations/oq-technology>
- [108] Nanosats Database, “Finch-1 (MACSAT, MACHine SATellite)”, <https://www.nanosats.eu/sat/finch-1>
- [109] <https://lynk.world/home>
- [110] NewSpace Index, “Lynk”, <https://www.newspace.im/constellations/lynk>
- [111] Space IT Bridge, “UbiquitiLink gets \$5M seed, preps for second demo of satellite cellular tech”, by Doug Mohny, July 18, 2019, <https://www.spaceitbridge.com/ubiquitilink-gets-5m-seed-preps-for-second-demo-of-satellite-cellular-tech.htm>
- [112] SpaceWorks, <https://www.spaceworks.aero/>
- [113] Space IT Bridge, “Blink Astro second satellite IoT firm to sign with NanoAvionics”, by Doug Mohny, May 2, 2018, <https://www.spaceitbridge.com/blink-astro-second-satellite-iot-firm-to-sign-with-nanoavionics.htm>
- [114] SpaceWorks, “Blink Astro Announces the Successful Launch of its First Hosted Custom Radio Payload”, April 2, 2019, <https://www.spaceworks.aero/blink-astro-announces-the-successful-launch-of-its-first-hosted-custom-radio-payload/>
- [115] NewSpace Index, “Blink Astro”, <https://www.newspace.im/constellations/blink-astro>
- [116] P. Rawat, K.D. Singh, H. Chaouchi, J.M. Bonnin, “Wireless sensor networks: A survey on recent developments and potential synergies”, *The Journal of Supercomputing*, 2013.
- [117] N. Celandroni, E. Ferro, A. Gotta, et. al., “A survey of architectures and scenarios in satellite-based wireless sensor networks: system design aspects”, *Int. J. Satell. Commn. Network*. 2013.
- [118] M. De Sanctis, E. Cianca, G. Araniti, et. al., *Satellite Communications Supporting Internet of Remote Things*, *IEEE Internet of Things Journal*, 3 1 (2016) 113–123.
- [119] P. Weng, J. Zhang, X. Zhang, et. al., “Convergence of Satellite and Terrestrial Networks: A Comprehensive Survey”, *IEEE Access*, December 2019.
- [120] Inmarsat, “Inmarsat and Actility deliver world’s first global LoRaWAN™ IoT network empowering business applications”, February 8, 2017, Available: <https://www.inmarsat.com/press-release/inmarsat-actility-deliver-worlds-first-global-lorawan-iot-network-empowering-business-applications/>.
- [121] I. Lysogor, L. Voskov, A. Rolich and S. Efremov, “Study of Data Transfer in a Heterogeneous LoRa-Satellite Network for the Internet of Remote Things”, *MDPI Sensors*, Vol. 19, Issue 15,

August 2019.

- [122] CORDIS, “Internet of Things Everywhere on Earth: a satellite based M2M solution”, July 9, 2018. Available: <https://cordis.europa.eu/article/id/232842-space-iot-takes-off>.
- [123] SAT4M2M, “Global IoT Coverage: Always Stay Connected to Your IoT.”, <https://sat4m2m.com/wordpress/global-iot-coverage/>.
- [124] J. Fraire, S. Cespedes, and N. Accettura, “Direct-To-Satellite IoT – A Survey of the State of the Art and Future Research Perspectives, Backhauling the IoT Through LEO Satellites”, Springer Nature Switzerland AG 2019.
- [125] Lacuna Space, “Lacuna Space Technology”, Available: <https://lacuna.space/technology/>.
- [126] M. Palattella and N. Accettura, “Enabling Internet of Everything Everywhere: LPWAN with satellite backhaul”, 2018 Global Information Infrastructure and Networking Symposium (GIIS), October 2018, Thessaloniki, Greece.
- [127] Wikipedia, “Narrowband IoT”, Available: https://en.wikipedia.org/wiki/Narrowband_IoT.
- [128] S. Cluvel, L. Franck, J. Radzik, et. al., “3GPP NB-IoT coverage extension using LEO satellites”, IEEE, 2018.
- [129] Satnews Daily, “Narrow-Band IoT Successfully Tested by OQ Technology Using a Smallsat”, October 17, 2019, Available: <http://www.satnews.com/story.php?number=2029355696#>.
- [130] Z. Qu, G. Zhang, H. Cao, and J. Xie, “LEO Satellite Constellation for Internet of Things”, IEEE Access, August 2017.
- [131] N. Saeed, A. Elzanaty, H. Almorad, et. al., “CubeSat Communications: Recent Advances and Future Challenges”, IEEE Communications Surveys & Tutorials, April 2020. DOI: 10.1109/COMST.2020.2990499
- [132] V. Almonacid and L. Franck, “Extending the coverage of the internet of things with low-cost nanosatellite networks”, Acta Astronautica, Vol. 138, pages 95-101, September 2017.
- [133] J. Abouei, K.N. Plataniotis, S. Pasupathy, “Green modulations in energy-constrained wireless sensor networks”, IET Communications, Vol. 5, Issue 2, pp. 240-251, 2011. <https://doi.org/10.1049/iet-com.2010.0472>.
- [134] M. Holland, T. Wang, B. Tavli, A. Seyedi and W. Heinzelman, “Optimizing Physical Layer Parameters for Wireless Sensor Networks”, ACM Transactions on Sensor Networks, Vol. 7, Issue 4, Article No. 28, February 2011. <https://doi.org/10.1145/1921621.1921622>.
- [135] A. Gaysin, V. Fadeev, and M. Hennhöfer, “Survey of modulation and coding schemes for application in CubeSat systems”, 2017 Systems of Signal Synchronization, Generating and Processing in Telecommunications (SINKHROINFO), July 2017.
- [136] The Consultative Committee for Space Data Systems (CCSDS), “RADIO FREQUENCY AND MODULATION SYSTEMS—PART 1 EARTH STATIONS AND SPACECRAFT (CCSDS 401.0-B-30)”, CCSDS Recommendations for Space Data System Standards, February 2020.
- [137] I. VERTÁT and J. MRÁZ, “Hybrid M-FSK/DQPSK Modulations for CubeSat Picosatellites”, Radioengineering, Vol. 22, No. 1, April 2013.

- [138] W.A.C. Fernando and R.M.A.P. Rajatheva, "Performance of Turbo and Trellis Coded OFDM for LEO Satellite Channels in Global Mobile Communications", 1998 IEEE International Conference on Communications (ICC '98), June 1998.
- [139] "Bandwidth-efficient modulations: Summary of definition, implementation, and performance," CCSDS 413.0-G-3: Green Book, Washington, DC, USA, International report, Issue 3, Feb. 2018.
- [140] U. Raza, P. Kulkarni, M. Sooriyabandara, "Low Power Wide Area Networks: An Overview", IEEE, January 2017.
- [141] B. Reynders and S. Pollin, "Chirp Spread Spectrum as a Modulation Technique for Long Range Communication", 2016 Symposium on Communications and Vehicular Technologies (SCVT), November 2016.
- [142] M. Marchese, A. Moheddine and F. Patrone, "IoT and UAV Integration in 5G Hybrid Terrestrial-Satellite Networks", MDPI Sensors, Vol. 19, Issue 17, August 2019.
- [143] A. Doroshkin, A. Zadorozhny, O. Kus, V. Prokopyev and Y. Prokopyev, "Laboratory testing of LoRa modulation for CubeSat radio communications", MATEC Web Conf., Vol. 158, March 2018. <https://doi.org/10.1051/mateconf/201815801008>
- [144] A. Doroshkin, A. Zadorozhny, O. Kus, V. Prokopyev and Y. Prokopyev, "Experimental Study of LoRa Modulation Immunity to Doppler Effect in CubeSat Radio Communications", IEEE Access, Vol. 7, May 2019. <https://doi.org/10.1109/ACCESS.2019.2919274>.
- [145] Q. Verspiepren, T. Matsumoto, Y. Aoyanagi, T. Fukuyo, T. Obata, S. Nakasuka, G. Kwizera, J. Abakunda, "Store and Forward 3U CubeSat Project TRICOM and Its Utilizations for Development and Education: the cases of TRICOM-1R and JPRWASAT", 32nd International Symposium on Space Technology and Science, Fukui, Japan, June 2019.
- [146] A. Carlson and P. Crilly, "COMMUNICATION SYSTEMS – An Introduction to Signals and Noise in Electrical Communication", Fifth Edition, McGraw-Hill, 2010.
- [147] B. Omijeh and I. Eyo, "Comparative Study of Bit Error Rate of Different M-ary Modulation Techniques in AWGN Channel", American Journal of Networks and Communications, Vol. 5, Issue 5, October 2016, pages 82-90, doi: <https://doi.org/10.11648/j.ajnc.20160505.11>.
- [148] R. De Gaudenzi, O. del Rio Herrero, G. Gallinaro, S. Cioni and P. Arapoglou, "Random Access Schemes for Satellite Networks: from VSAT to M2M - A Survey", Int. J. Satell Commun Network, Vol. 36, Issue 1, December 2016, pages 66-107, <https://doi.org/10.1002/sat.1204>.
- [149] T. Ferrer, S. Céspedes and A. Becerra, "Review and Evaluation of MAC Protocols for Satellite IoT Systems Using Nanosatellites", MPDI Sensors, Vol. 19, Issue 8, April 2019, <https://doi.org/10.3390/s19081947>.
- [150] Y. Quian, L. Ma and X. Liang, "Symmetry Chirp Spread Spectrum Modulation used in LEO Satellite Internet of Things", IEEE Communications Letters, Vol. 22, Issue 11, November 2018, pages 2230-2233, <https://doi.org/10.1109/LCOMM.2018.2866820>.
- [151] Y. Quian, L. Ma and X. Liang, "The Acquisition Method of Symmetry Chirp Signal Used in LEO Satellite Internet of Things", IEEE Communications Letters, Vol. 23, Issue 9, July 2019, pages

1572-1575, <https://doi.org/10.1109/LCOMM.2019.2926262>.

- [152] Y. Quian, L. Ma and X. Liang, “The Acquisition Method of Symmetry Chirp Signal Used in LEO Satellite Internet of Things”, *IEEE Communications Letters*, Vol. 23, Issue 9, July 2019, pages 1572-1575, <https://doi.org/10.1109/LCOMM.2019.2926262>.
- [153] C. Hofmann and A. Knopp, “Ultra-Narrowband Waveform for IoT Direct Random Multiple Access to GEO Satellites”, *IEEE Internet of Things Journal*, Vol. 6, Issue 6, August 2019, pages 10134 - 10149, <https://doi.org/10.1109/JIOT.2019.2935909>.
- [154] V. Zamora, “Cross-layer design applied to small satellites for data collection”, PhD Thesis, Université Montpellier, October 2017. Available: <https://tel.archives-ouvertes.fr/tel-01951803>.
- [155] M. Anteur, N. Thomas, V. Deslandes and A. Beylot, “On the performance of UNB for machine-to-machine low earth orbit (LEO) satellite communications”, *Int. J. Satell Commun Network*, Vol. 37, Issue 1, October 2018, pages 56-71, <https://doi.org/10.1002/sat.1285>.
- [156] O. del Rio Herrero and R. De Gaudenzi, “High Efficiency Satellite Multiple Access Scheme for Machine-to-Machine Communications”, *IEEE Transactions on Aerospace and Electronics Systems*, Vol. 48, No. 4, October 2012.
- [157] R. De Gaudenzi, O. del Herrero and G. Gallinaro, “Enhanced spread Aloha physical layer design and performance”, *Int. J. Satell Commun Network*, Vol. 32, Issue 6, May 2014, pages 457-473, <https://doi.org/10.1002/sat.1078>.
- [158] M. Andrenacci, G. Mendola, F. Collard, D. Finocchiaro and A. Recchia, “Enhanced spread spectrum aloha demodulator implementation, laboratory tests and satellite validation”, *Int. J. Satell Commun Network*, Vol. 32, Issue 6, November 2014, pages 521-533, <https://doi.org/10.1002/sat.1086>.
- [159] F. Collard, A. Recchia, N. Antip, et. al., “Performance Analysis of an Enhanced Spread Spectrum Aloha System”, *Personal Satellite Services, PSATS 2012, Lecture Notes of the Institute for Computer Sciences, Social Informatics and Telecommunications Engineering*, Vol 52. Springer, Berlin, Heidelberg, 2013. https://doi.org/10.1007/978-3-642-36787-8_4.
- [160] M. Zhao, H. Li, Y. Li, L. Fang and P. Chen, “Non-orthogonal Multi-carrier Technology for Space-Based Internet of Things Applications”, *ChinaCom 2017, LNICST 236*, pp. 37–45, 2018, https://doi.org/10.1007/978-3-319-78130-3_5.
- [161] T. Xu and I. Darwazeh, “Non-Orthogonal Narrowband Internet of Things: A Design for Saving Bandwidth and Doubling the Number of Connected Devices”, *IEEE Internet of Things Journal*, Vol. 5, No. 3, June 2018, <https://doi.org/10.1109/JIOT.2018.2825098>.
- [162] H. Bedon, C. Miguel, A. Fernandez and J.S. Park, “A DTN System for Nanosatellite-based Sensor Networks using a New ALOHA Multiple Access with Gateway Priority”, *Smart Computing Review*, Vol. 3, No. 5, October 2013.
- [163] H. Bedon, C. Miguel, R. Alcarria, A. Fernandez and F.J. Ruiz, “Message fragmentation assessment in DTN nanosatellite-based sensor networks”, *Ad Hoc Networks*, March 2016.
- [164] A. Addaim, E.B. Zantou, A. Kherras, Design of Store and Forward Data Collection Low-cost

Nanosatellite, IEEE Aerospace Conference, MT, USA, 2007, 3–10 March.

- [165] A. Addaim, E.B. Zantou, A. Kherras, DSP implementation of integrated store-and-forward APRS payload and OBDH subsystems for low-cost small satellite, *Aerospace Science and Technology*, 12 4 (2008) 308–317.
- [166] A. Addaim, A. Kherras, E.B. Zantou, Design of Low-cost Telecommunications CubeSat-class Spacecraft, in: T. Arif (Ed.), *Aerospace Technologies Advancements*, InTech, 2010. pp. 294–318.
- [167] W.A. Beech, D.E. Nielsen, J. Taylor, AX.25 Link Access Protocol for Amateur Packet Radio Version 2.2, Tucson Amateur Packet Radio Corporation, 1997,
<https://www.tapr.org/pdf/AX25.2.2.pdf>
- [168] Nagai Giken, Types, characteristics, terms, etc. of steel (metal materials) stipulated by JIS, 2018,
https://www.hamadashokai.co.jp/goods/detail.php?match_code=4906365066865
- [169] Hamadashokai Co., Ltd., GOHSEN PE Hunter Lock (100 m connection), 2018,
<https://www.nagai-giken.com/snonfm18.html>
- [170] J.A. King, AMSAT/IARU Annotated Link Model System Version 2.4.1, 22 October 2006,
<https://amsat-uk.org/tag/link-budget/>
- [171] D. Lim, “Small launcher market survey”, *ROOM Space Journal of Asgardia*, Issue #3(9), 2016.
<https://room.eu.com/article/small-launcher-market-survey>
- [172] C. Niederstrasser, “Small Launch Vehicles – A 2018 State of the Industry Survey”, 32nd Annual AIAA/USU Conference on Small Satellites, 2018.
<https://digitalcommons.usu.edu/cgi/viewcontent.cgi?article=4118&context=smallsat>
- [173] D. Dy, Y. Perrot and R. Pradal, “Micro-launchers: what is the market?” , PricewaterhouseCoopers, February 2017, <https://www.pwc.fr/fr/assets/files/pdf/2018/11/space/pwc-micro-launchers-what-is-the-market.pdf>
- [174] M. Puteaux and A. Najjar, “Analysis | Are smallsats entering the maturity age?”, *SpaceNews*, August 6, 2019. <https://spacenews.com/analysis-are-smallsats-entering-the-maturity-stage/>

Appendix 0: BIRDS-2 S&F Packet Format

Sensor Data Packet (Uplink)

	Start	Destination Callsign	Source Callsign	Control	PID	Information Field				FCS	End
Byte #	1	2-8	9-15	16	17	18	19-20	21-50	51-172 (up to 122 bytes)	173-174	175
Content	Start flag	Satellite callsign	GST callsign or ID	Control (0x3E)	PID (0xF0)	Packet type (0x01)	Data Packet sequence #	Time packet transmitted, time packet generated, AZ and EL during packet transmission	Time data logged, sensor data, etc.	FCS	End flag
Format	HEX	ASCII string	ASCII string	HEX	HEX	HEX	HEX	ASCII string	ASCII string	HEX	HEX

Fig. 10. Format of sensor data packet sent by the GST (AX.25 protocol-compliant packet format)

Byte #	Content	Example	Remarks
18	Packet type	0x01	Will be used by the Payload to identify sensor data packet
19-20	Data packet sequence number	0x2A 0x01	16-bit, 0 to 65535
21-32	Time packet is <i>first</i> generated (i.e., when satellite appears on the horizon) ASCII string format: YYMMDDHHMMSS	180710131505 (2018 July 10 13:15:05)	Not necessarily part of the sensor data, included only for the purpose of delay performance evaluation
33-44	Time (just before) packet is transmitted ASCII string format: YYMMDDHHMMSS	180710131520 (2018 July 10 13:15:20)	

Byte #	Content	Example	Remarks
45-50	3-digit AZ and EL angles in degrees of the satellite just before packet transmission ASCII string format (AZ followed by EL): XXXXYY	225015 (AZ=225°, EL=15°)	
51-62*	Time packet is logged ASCII string format: YYMMDDHHMMSS	180710131400 (2018 July 10 13:14:00)	
63-172*	Measured data from one or more sensors separated by ';' ASCII string format: WW;XX.XXX;Y.YY;Z ZZ.ZZZZZ	<i>Ex. 1:</i> 45;-12.345;6.78;901.23456 <i>Ex. 2:</i> 45%;-12.345°C;6.78kPa;901.23456nT	The content in between ';' is user-defined. For example, the user may decide to indicate the unit of measurement (e.g. Ex. 2).

51-172	18071013150545%;-12.345°C;6.78kPa;901.23456nT_18071013450532%;+11.234°C;8.19kPa;803.78912nT
--------	---

Fig. 12. Packet format for sending multiple sets (logged at different times) of sensor data (for bytes 50 and below, same as in Fig. 11)

Acknowledgment Packet (Downlink)

	Start	Destination Callsign	Source Callsign	Control	PID	Information Field		FCS	End
Byte #	1	2-8	9-15	16	17	18	19-20	21-22	23
Content	Start flag	GST callsign or ID	Satellite callsign	Control (0x3E)	PID (0xF0)	Packet type (0x04)	16-bit packet sequence # of last received data packet	FCS	End flag
Format	HEX	ASCII string	ASCII string	HEX	HEX	HEX	HEX	HEX	HEX

Fig. 15. Format of ACK packet sent by the Payload (AX.25 protocol-compliant packet format)

TLE Packet (Downlink)

	Start	Destination Callsign	Source Callsign	Control	PID	Information Field		FCS	End
Byte #	1	2-8	9-15	16	17	18	19-106	107-108	109
Content	Start flag	Requesting GST callsign or ID	Satellite callsign	Control (0x3E)	PID (0xF0)	Packet type (0x06)	Compressed TLE info of satellite	FCS	End flag
Format	HEX	ASCII string	ASCII string	HEX	HEX	HEX	ASCII string	HEX	HEX

Fig. 17. Format of TLE packet sent by the Payload (AX.25 protocol-compliant packet format)

Byte #	Content	Example
19-23	Satellite Number	25544
25-26	Epoch Year	08
28-39	Epoch Day	264.51782528
41-44	Element Set Number	292
46-53	Inclination (degrees)	51.6416
55-62	Right ascension of the ascending node (degrees)	247.4627
64-70	Eccentricity (decimal point assumed)	0006703
72-79	Argument of perigee (degrees)	130.5360

Byte #	Content	Example
81-88	Mean Anomaly (degrees)	325.0288
90-100	Mean Motion (revolutions per day)	15.72125391
102-106	Revolution number at epoch (revolutions)	56353
24, 27, 40, 45, 54, 63, 71, 80, 89, 101	Space (0x20)	

Appendix 1: Derivation of terminal sdf

By considering a differential area da containing dn_k terminals, the following relations (14) to (23) can be derived. N_k expresses the number of active terminals within a region of $\Delta\alpha$ and $\Delta\varepsilon$, ρ_A is the terminal area density which is a parameter that can be expressed in terms of K and constant C . Equations (22) and (23) are the final working equations to be used for generating random terminal positions.

$$dn_k = \rho_A da = \rho_A R_E^2 \sin\beta d\beta d\alpha \quad (14)$$

$$\delta\beta(\varepsilon) \triangleq \frac{d\beta}{d\varepsilon} = \frac{R_E}{R_E+h} \cdot \frac{\sin\varepsilon}{\sqrt{1-\left(\frac{R_E}{R_E+h} \cos\varepsilon\right)^2}} - 1 \quad (15)$$

$$d\beta = \delta\beta(\varepsilon)d\varepsilon \quad (16)$$

$$N_k = \int_{\varepsilon=\varepsilon_{\min}}^{\varepsilon=\varepsilon_2} \int_{\alpha=\alpha_1}^{\alpha=\alpha_2} \rho_A R_E^2 \sin\left[\cos^{-1}\left(\frac{R_E}{R_E+h} \cos\varepsilon\right) - \varepsilon\right] \delta\beta(\varepsilon) d\alpha d\varepsilon \quad (17)$$

$$N_k = \int_{\varepsilon=\varepsilon_{\min}}^{\varepsilon=\varepsilon_2} \rho_A R_E^2 \Delta\alpha \sin\left[\cos^{-1}\left(\frac{R_E}{R_E+h} \cos\varepsilon\right) - \varepsilon\right] \delta\beta(\varepsilon) d\varepsilon \quad (18)$$

$$\rho_\varepsilon(\varepsilon) \triangleq \frac{dN_k}{d\varepsilon} \Big|_{\Delta\alpha=2\pi} = 2\pi\rho_A R_E^2 \sin\left[\cos^{-1}\left(\frac{R_E}{R_E+h} \cos\varepsilon\right) - \varepsilon\right] \delta\beta(\varepsilon) \quad (19)$$

$$\rho_A = \frac{K}{2\pi R_E^2 \int_{\varepsilon=\varepsilon_{\min}}^{\varepsilon=\pi/2} \sin\left[\cos^{-1}\left(\frac{R_E}{R_E+h} \cos\varepsilon\right) - \varepsilon\right] \delta\beta(\varepsilon) d\varepsilon} = \frac{K}{C} \quad (20)$$

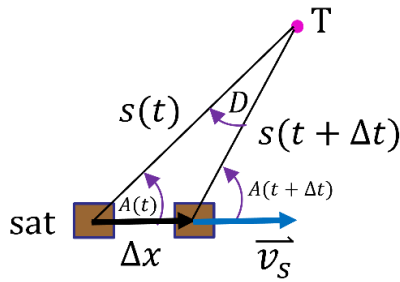
$$p_{\varepsilon\alpha}(\varepsilon, \alpha) \triangleq \frac{1}{K} \frac{d^2 N_k}{d\varepsilon d\alpha} = \frac{R_E^2}{C} \sin\left[\cos^{-1}\left(\frac{R_E}{R_E+h} \cos\varepsilon\right) - \varepsilon\right] \delta\beta(\varepsilon) \quad (21)$$

$$p_\varepsilon(\varepsilon) \triangleq \frac{1}{K} \frac{dN_k}{d\varepsilon} \Big|_{\Delta\alpha=2\pi} = \frac{2\pi R_E^2}{C} \sin\left[\cos^{-1}\left(\frac{R_E}{R_E+h} \cos\varepsilon\right) - \varepsilon\right] \delta\beta(\varepsilon) \quad (22)$$

$$p_\alpha(\alpha) \triangleq \frac{1}{K} \frac{dN_k}{d\alpha} = \int_{\varepsilon=\varepsilon_{\min}}^{\varepsilon=\pi/2} p_{\varepsilon\alpha}(\varepsilon, \alpha) d\varepsilon = \frac{1}{2\pi} \quad (23).$$

Appendix 2: Derivation of dA/dt

Consider a differential time interval Δt . By Law of Sines:



$$\frac{\Delta x}{\sin D} = \frac{s}{\sin(A + \Delta A)}$$

$$\frac{\Delta x}{\sin(\Delta A)} = \frac{s}{\sin(A + \Delta A)}$$

Dividing both sides by Δt , re-arranging, and taking the limit:

$$\frac{\Delta x}{\Delta t} = \frac{s \sin(\Delta A)}{\sin(A + \Delta A) \Delta t}$$

$$\lim_{\Delta t \rightarrow 0} \left(\frac{\Delta x}{\Delta t} \right) = \lim_{\Delta t \rightarrow 0} \left(\frac{s \sin(\Delta A)}{\sin(A + \Delta A) \Delta t} \right) = \frac{s}{\sin A} \lim_{\Delta t \rightarrow 0} \left(\frac{\approx \Delta A}{\Delta t} \right)$$

$$\frac{dx}{dt} = v_s = \frac{s}{\sin A} \frac{dA}{dt}$$

Appendix 3: Working Equations for Packet Detection and Rough Channel Estimation

$$r_{pre,\kappa} = r(\kappa: \kappa + N_{pre}N_c - 1) \quad (38)$$

$$r_{pre,\kappa,corr} = r_{pre,\kappa} \cdot \sqrt{T_s/2} \text{conj}(p_{pre}) \quad (39)$$

$$\mathcal{R}_{pre,\kappa}(\Omega_l) = \text{DFT}(r_{pre,\kappa,corr}) = \sum_{n=0}^{N_{pre}N_c-1} r_{pre,\kappa,corr}(n) \exp\left(-j \frac{2\pi l n}{N_{pre}N_c}\right)$$

$$l \in \left[\frac{-N_{pre}N_c}{2}, \frac{N_{pre}N_c}{2} - 1 \right] \quad (40)$$

$$V_{\kappa,pre} = \frac{1}{N_{pre}N_c} \max(|\mathcal{R}_{pre,\kappa}|) \quad (41)$$

$$V_{\kappa,pre} \gtrsim V_{th} \quad (42)$$

$$r_{pos,\kappa} = r(\kappa + N_{Tc} - N_{pos}N_c: \kappa + N_{Tc} - 1) \quad (43)$$

$$r_{pos,\kappa,corr} = r_{pos,\kappa} \cdot \sqrt{T_s/2} \text{conj}(p_{pos}) \quad (44)$$

$$\mathcal{R}_{pos,\kappa}(\Omega_l) = \text{DFT}(r_{pos,\kappa,corr}) = \sum_{n=0}^{N_{pos}N_c-1} r_{pos,\kappa,corr}(n) \exp\left(-j \frac{2\pi l n}{N_{pos}N_c}\right)$$

$$(45)$$

$$V_{\kappa,pos} = \frac{1}{N_{pos}N_c} \max(|\mathcal{R}_{pos,\kappa}|) \quad (46)$$

$$V_{\kappa,pos} \gtrsim V_{th} \quad (47)$$

$$A_{\kappa} = \frac{1}{2}(V_{\kappa,pre} + V_{\kappa,pos}) \quad (48)$$

$$V_{th} = A_{\kappa,L} + r_{th} \cdot [A_{\kappa,H} - A_{\kappa,L}] \quad (49)$$

$$\tau_k = \kappa \quad A_k^{(1)} = A_\kappa \quad f_k^{(1)} = \frac{R_{chip}}{N_{pre}N_c} l_{V_{\kappa,pre}} \quad f_{k,pos}^{(1)} = \frac{R_{chip}}{N_{pre}N_c} l_{V_{\kappa,pos}}$$

$$d_k^{(1)} = \frac{f_{k,pos}^{(1)} - f_k^{(1)}}{T_p - 0.5(T_{pre} + T_{pos})} \quad \phi_k^{(1)} = \angle \text{mean}(r_{pre,\kappa}(0:SF-1)) \quad (50a-f)$$

Note that before doing all chip-wise offset preamble-match detection, V_{th} is first determined by performing equations (38)-(41) on a small portion of overall signal samples. $A_{\kappa,L}$ is an estimate of “noise floor” so it is computed as the average of 100 highest elements of the lowest 99% of all preliminary $V_{\kappa,pre}$ values. $A_{\kappa,H}$ is a ceiling estimate and is computed as the average of 20 highest elements of preliminary $V_{\kappa,pre}$ values. The value of r_{th} is selected for a good balance between false alarm rate and misdetection rate: $r_{th} = 0.15$ for E-SSA iterations 1-4 and $r_{th} = 0$ for iteration 5.

Appendix 4: Working Equations for Fine Channel Estimation

$$r_{k,DC}(n_{c,DC}) = r(\tau_k + N_{pre}N_c + n_{c,DC}) \quad (51)$$

$$n_{c,DC} = 0, 1, 2, \dots, (N_{b,coded}SF - 1)$$

$$y_{k,DC}^{(1)} = r_{k,DC} \cdot c_k^{(1)} \cdot (1/A_u) \text{conj}(C_s) \quad (52)$$

$$c_k^{(1)}(n_{c,DC}) = \exp\left(-j \left[\phi_k^{(1)} + 2\pi f_k^{(1)}(N_{pre}N_c + n_{c,DC})/R_{chip} + \frac{2\pi d_k^{(1)}((N_{pre}N_c + n_{c,DC})/R_{chip})^2}{2} \right]\right) \quad (53)$$

$$y_{k,DC}^{(1)}(n_{c,DC}) = A_k \left[a_k \left(|n_{c,DC}|_{SF} \right) C_D \left(|n_{c,DC}|_{SF} \right) + j a_{CE} \beta_{CE} C_C \left(|n_{c,DC}|_{SF} \right) \right] \cdot e^{j\theta_{k,err}(n_{c,DC})} + MUI + \text{Noise} \quad (54)$$

$$a'_{CE}(n) = \text{average over every } SF \text{ chips of } \left[\text{Im} \left\{ y_{k,DC}^{(1)} \right\} \cdot C_C \right] = A_k a_{CE}(n) \beta_{CE} \cos(\theta_{k,err}(n)) + \text{ERR}_1 \quad (55)$$

$$a''_{CE}(n) = \text{average over every } SF \text{ chips of } \left[\text{Re} \left\{ y_{k,DC}^{(1)} \right\} \cdot (-C_C) \right] = A_k a_{CE}(n) \beta_{CE} \sin(\theta_{k,err}(n)) + \text{ERR}_2 \quad (56)$$

$$\left(\cos\theta_{k,err}(n) \right)_{est} = \frac{a'_{CE}(n)}{A_k^2 a_{CE}(n) \beta_{CE}} \quad (57)$$

$$\left(\sin\theta_{k,err}(n) \right)_{est} = \frac{a''_{CE}(n)}{A_k^2 a_{CE}(n) \beta_{CE}} \quad (58)$$

$$\left(\cos\theta_{k,err}(n) \right)'_{est} = \text{MAF} \left(\left(\cos\theta_{k,err}(n) \right)_{est} \right) \quad (59)$$

$$\left(\sin\theta_{k,err}(n) \right)'_{est} = \text{MAF} \left(\left(\sin\theta_{k,err}(n) \right)_{est} \right) \quad (60)$$

$$(\psi_k, \delta_k) = \text{argmax} \left\{ \text{mean} \left(\left[\left(\cos\theta_{k,err}(n) \right)'_{est} \cdot \cos\theta_{k,err,cand}(n) \right] + \left[\left(\sin\theta_{k,err}(n) \right)'_{est} \cdot \sin\theta_{k,err,cand}(n) \right] \right) \right\}$$

$$(61)$$

where $\theta_{k,err,cand}(n) = \text{acos}\left(\left(\cos\theta_{k,err}(0)\right)'_{est}\right) + 2\pi\psi_k \cdot \left((N_{pre} + n)/R_s\right) + \frac{2\pi\delta_k((N_{pre}+n)/R_s)^2}{2}$

$$\phi_k^{(2)} = \phi_k^{(1)} + \angle \text{mean}\left(r(\tau_k: \tau_k + N_{pre}N_c - 1) \cdot \text{conj}(p_{pre})\right) - 2\pi\left(\psi_k - \frac{\delta_k N_{pre}N_c}{R_{chip}}\right) \frac{N_{pre}N_c}{2R_{chip}}$$

(62a)

$$f_k^{(2)} = f_k^{(1)} + \psi_k - \delta_k N_{pre}N_c / R_{chip} \quad d_k^{(2)} = d_k^{(1)} + \delta_k \quad (62b-c)$$

Equation (61) calculates the correlation between the “noisy” channel error cosine/sine estimates obtained in (59) and (60) and those of the candidate. A strong correlation indicates packet presence with corresponding channel estimation error candidate parameters. Obtained highest correlation values (one for each k) are each compared to a threshold value, which is set to the minimum of the said correlation values plus 1/3 of the difference between the maximum and minimum.

Appendix 5: Other E-SSA Simulation Results

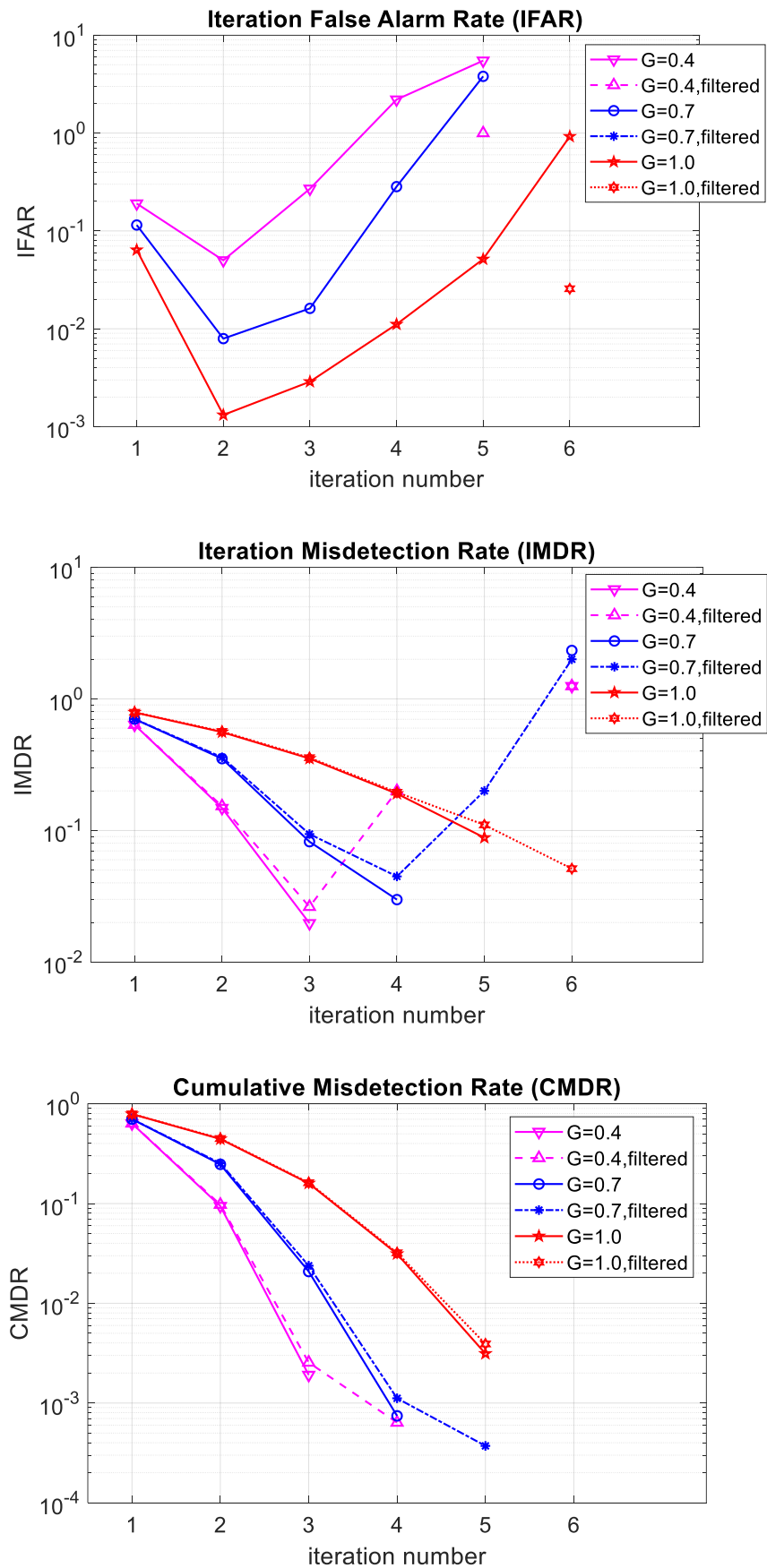


Figure 124. IFAR, IMDR and CMDR for different G values ($\sigma_{LN} = 3\text{dB}$, $E_b/N_0 = 14\text{dB}$)

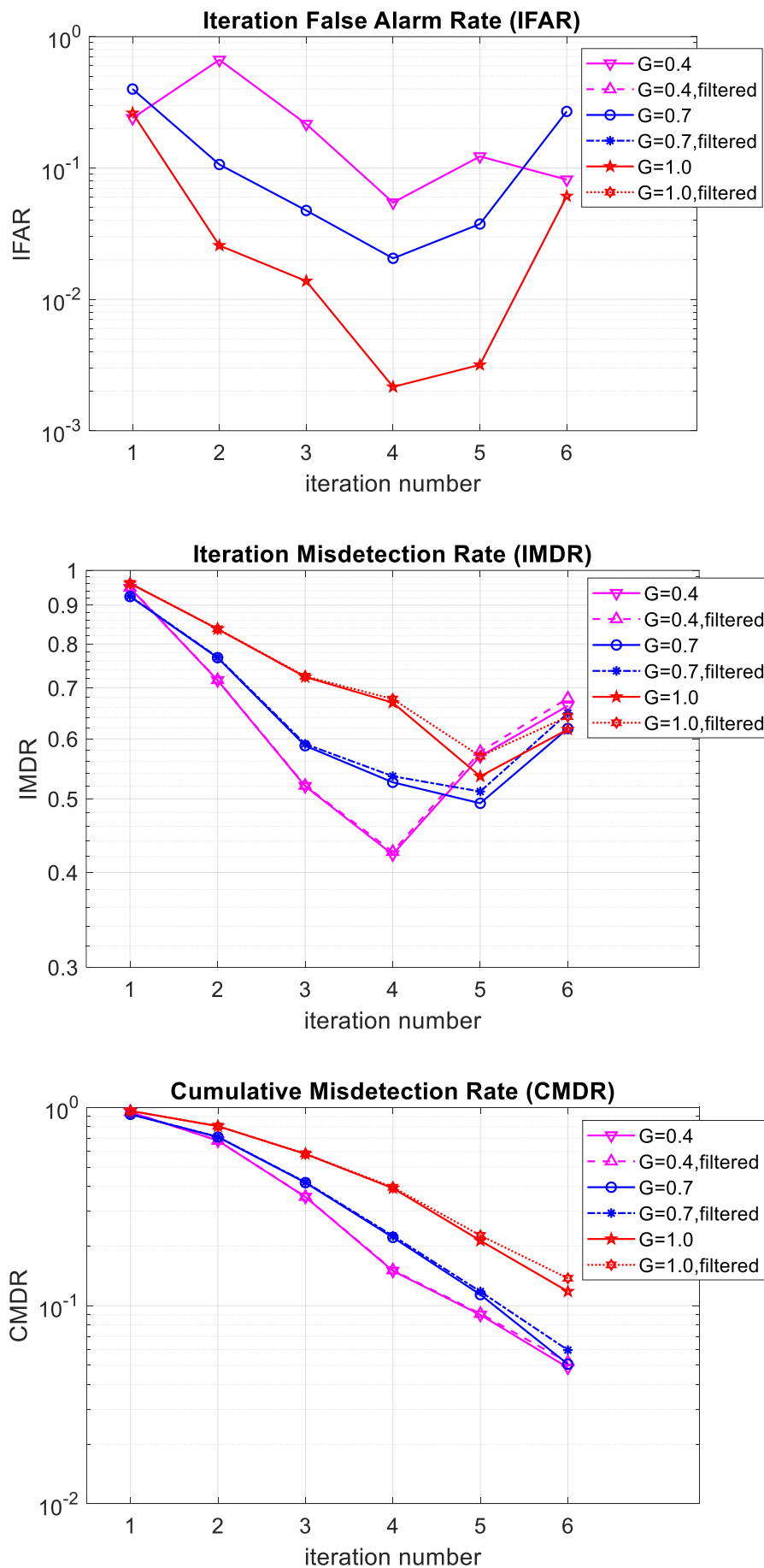


Figure 125. IFAR, IMDR and CMDR for different G values ($\sigma_{LN} = 9\text{dB}$, $E_b/N_0 = 14\text{dB}$)

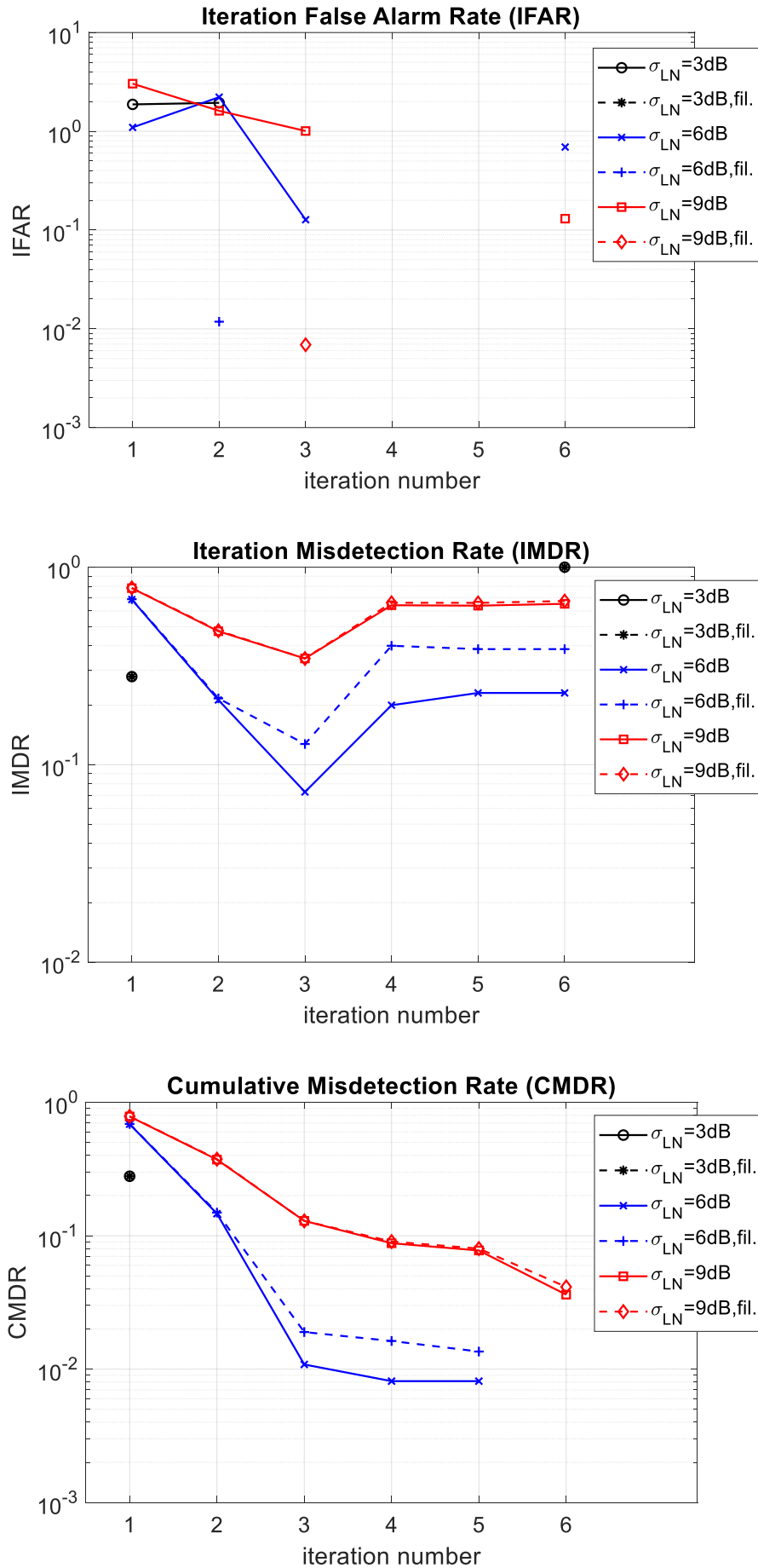


Figure 126. IFAR, IMDR and CMDR for different σ_{LN} values ($G = 0.1, E_b/N_0 = 14\text{dB}$)

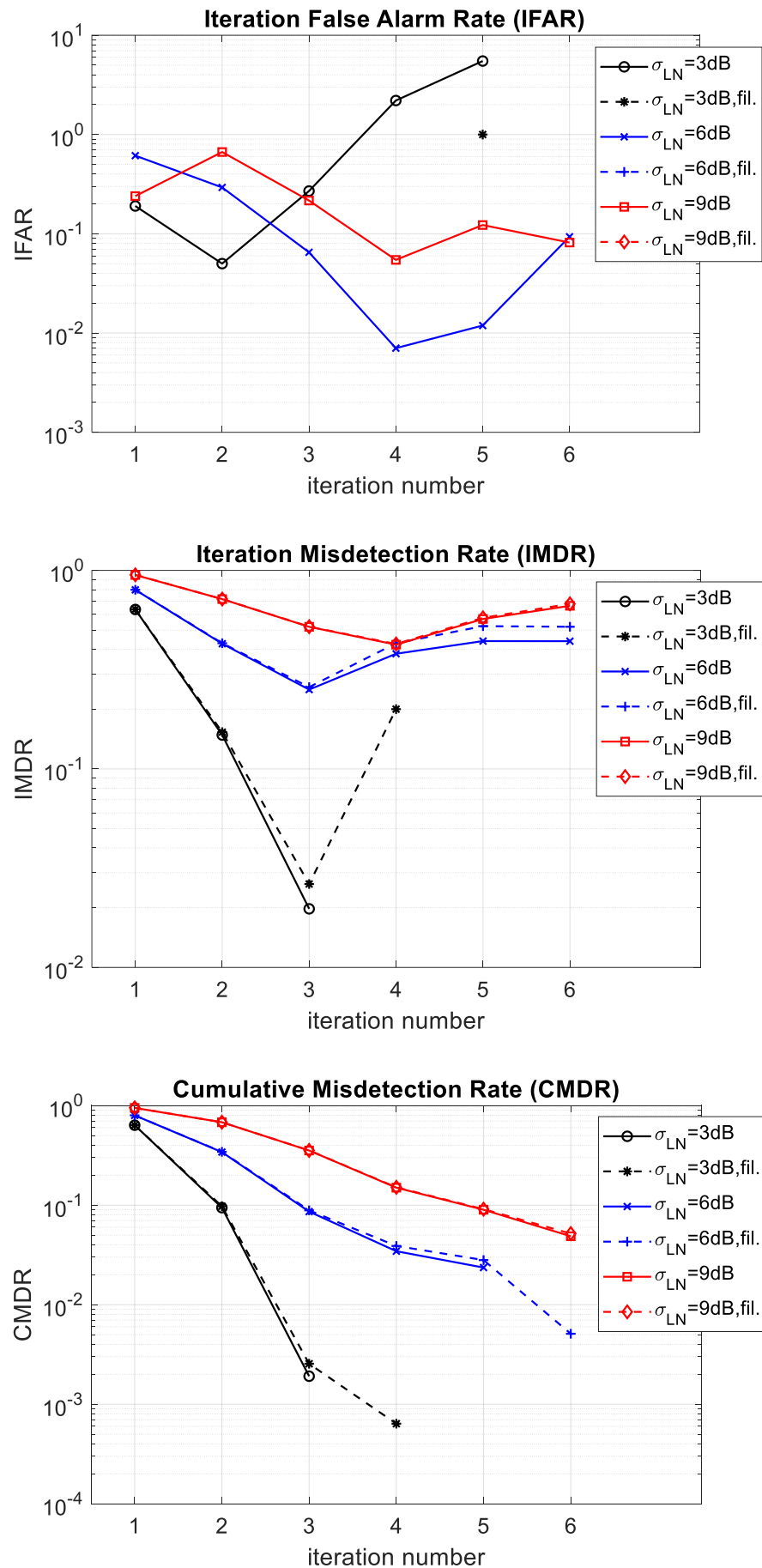


Figure 127. IFAR, IMDR and CMDR for different σ_{LN} values ($G = 0.4, E_b/N_0 = 14\text{dB}$)

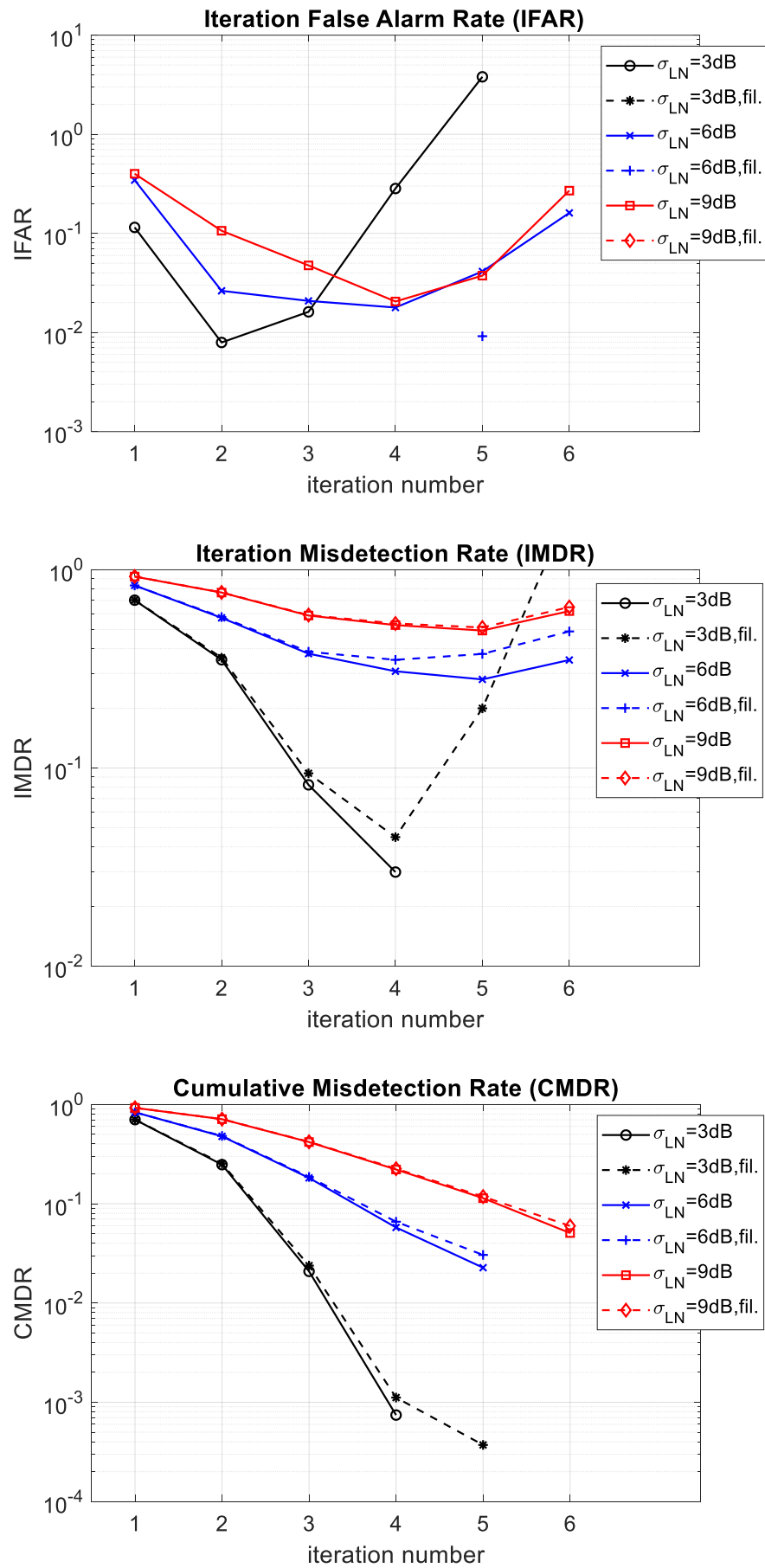


Figure 128. IFAR, IMDR and CMDR for different σ_{LN} values ($G = 0.7, E_b/N_0 = 14\text{dB}$)

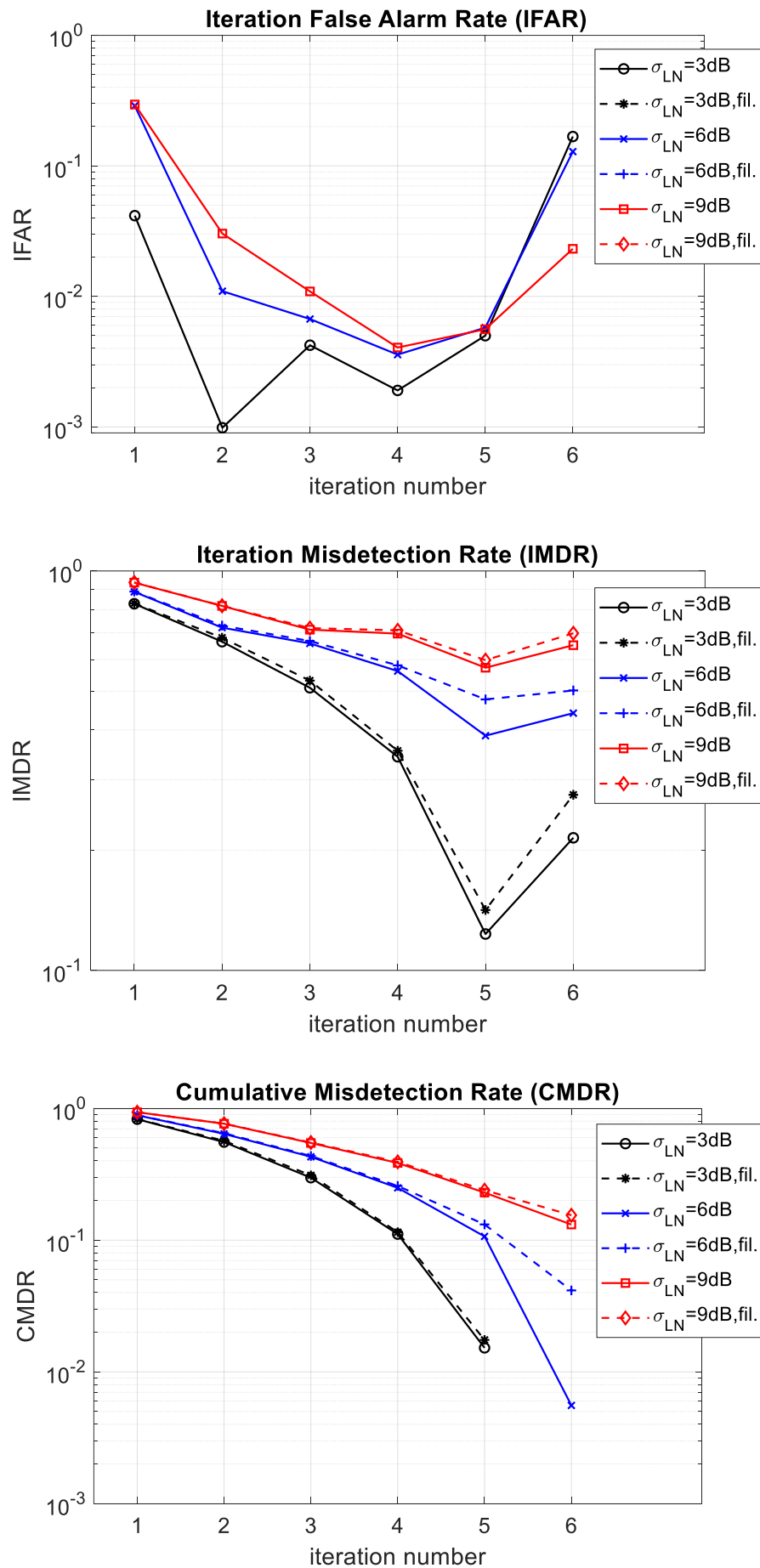


Figure 129. IFAR, IMDR and CMDR for different σ_{LN} values ($G = 1.3, E_b/N_0 = 14dB$)

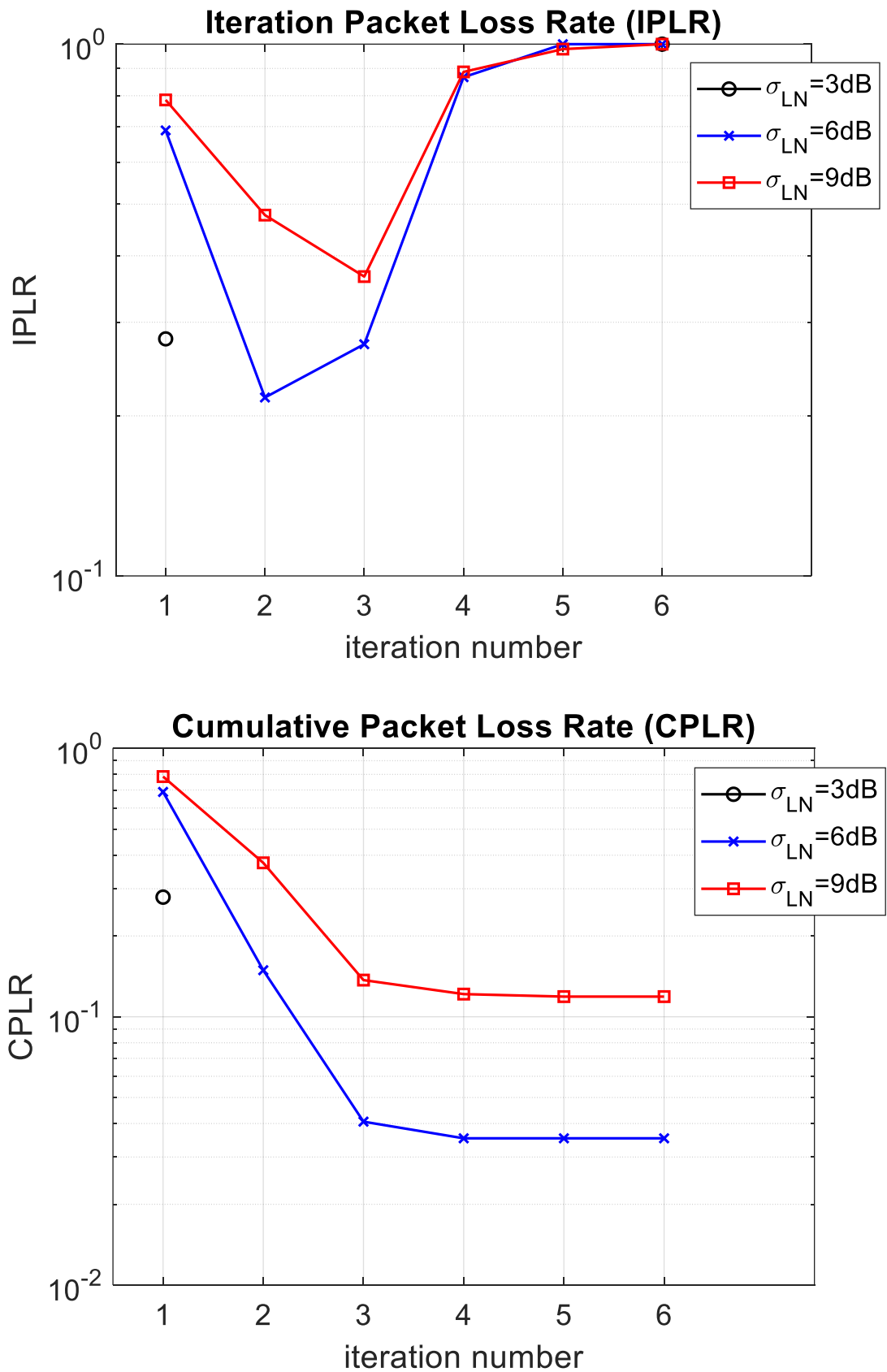


Figure 130. IPLR and CPLR for different σ_{LN} values ($G = 0.1, E_b/N_0 = 14\text{dB}$, actual algorithm)

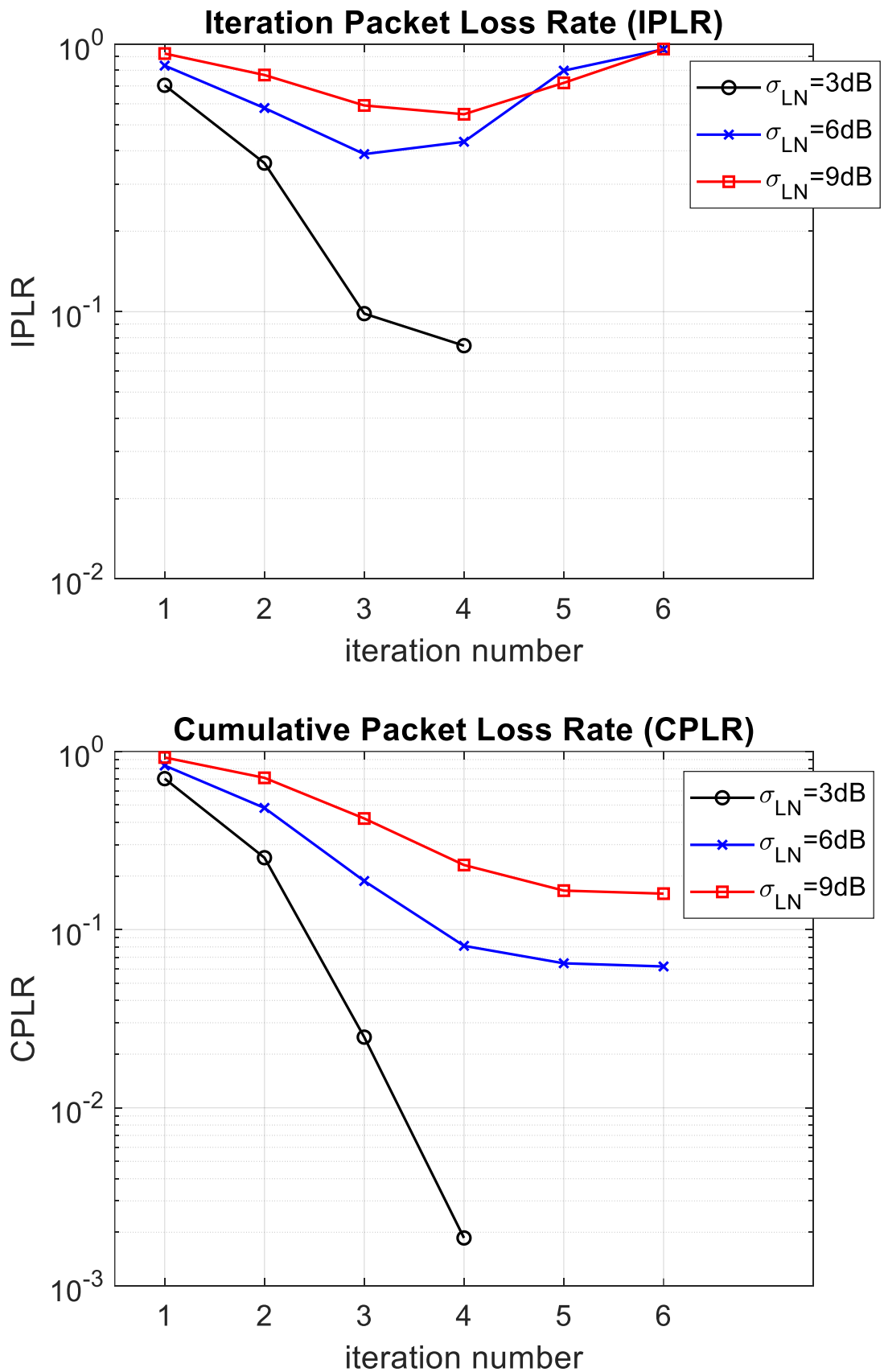


Figure 131. IPLR and CPLR for different σ_{LN} values ($G = 0.7, E_b/N_0 = 14\text{dB}$, actual algorithm)

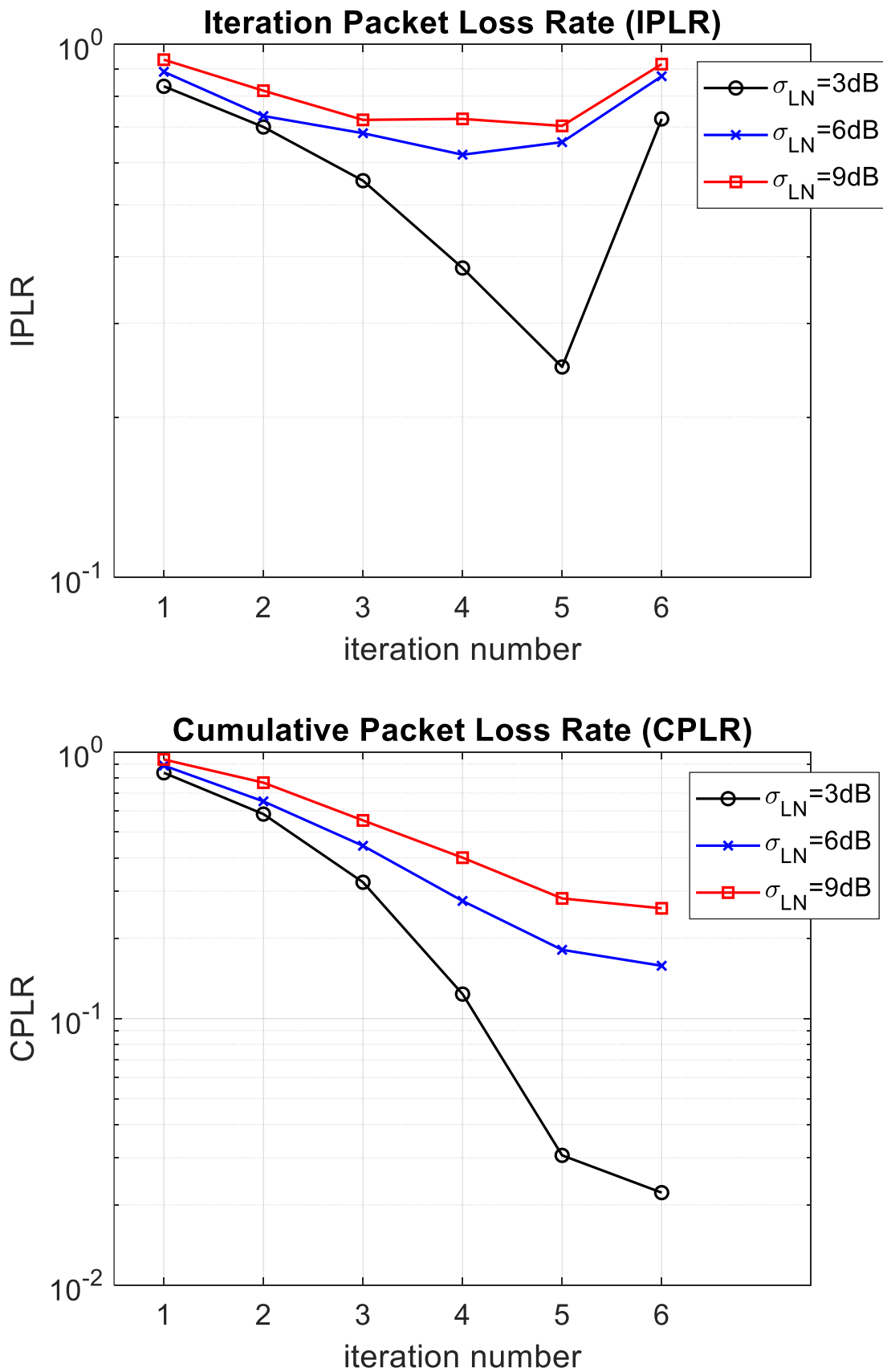


Figure 132. IPLR and CPLR for different σ_{LN} values ($G = 1.3, E_b/N_0 = 14\text{dB}$, actual algorithm)

Appendix 6: Constellation Design Details

Table 37. Constellation Configurations Simulated

Constellation Size and Configuration	Inclinations of Planes (°)	RAANs of Planes (°)	TA (°)
3 x 3 Hybrid	33	0	0, 120, 240
	67	120	0, 120, 240
	100	240	0, 120, 240
3 x 3 Walker Delta	98	0	Within a plane, uniformly distributed from 0° to 360° (120° interval); relative offset between two consecutive planes
	98	120	
	98	240	
4 x 4 Hybrid	25	0	0, 90, 180, 270
	50	90	0, 90, 180, 270
	75	180	0, 90, 180, 270
	100	270	0, 90, 180, 270
4 x 4 Walker Delta	98	0	Within a plane, uniformly distributed from 0° to 360° (90° interval); relative offset between two consecutive planes
	98	90	
	98	180	
	98	270	
5 x 5 Hybrid	20	0	0, 72, 144, 216, 288
	40	72	0, 72, 144, 216, 288
	60	144	0, 72, 144, 216, 288
	80	216	0, 72, 144, 216, 288
	100	288	0, 72, 144, 216, 288
5 x 5 Walker Delta	98	0	Within a plane, uniformly distributed from 0° to 360° (72° interval); relative offset between two consecutive planes
	98	72	
	98	144	
	98	216	
	98	288	
6 x 6 Hybrid	17	0	0, 60, 120, 180, 240, 300
	33	60	0, 60, 120, 180, 240, 300
	50	120	0, 60, 120, 180, 240, 300
	67	180	0, 60, 120, 180, 240, 300
	83	240	0, 60, 120, 180, 240, 300
	100	300	0, 60, 120, 180, 240, 300
6 x 6 Walker Delta	98	0	Within a plane, uniformly distributed from 0° to 360° (60° interval); relative offset between two consecutive planes
	98	60	
	98	120	
	98	180	
	98	240	
	98	300	

6 x 8 Hybrid	17	0	0, 45, 90, 135, 180, 225, 270, 315
	33	60	0, 45, 90, 135, 180, 225, 270, 315
	50	120	0, 45, 90, 135, 180, 225, 270, 315
	67	180	0, 45, 90, 135, 180, 225, 270, 315
	83	240	0, 45, 90, 135, 180, 225, 270, 315
	100	300	0, 45, 90, 135, 180, 225, 270, 315
7 x 7 Hybrid	14	0	0, 51, 103, 154, 206, 257, 309
	29	51	0, 51, 103, 154, 206, 257, 309
	43	103	0, 51, 103, 154, 206, 257, 309
	57	154	0, 51, 103, 154, 206, 257, 309
	71	206	0, 51, 103, 154, 206, 257, 309
	86	257	0, 51, 103, 154, 206, 257, 309
	100	309	0, 51, 103, 154, 206, 257, 309
7 x 7 Walker Delta	98	0	Within a plane, uniformly distributed from 0° to 360° (~51° interval); relative offset between two consecutive planes
	98	51	
	98	103	
	98	154	
	98	206	
	98	257	
	98	309	
8 x 8 Hybrid	13	0	0, 45, 90, 135, 180, 225, 270, 315
	25	45	0, 45, 90, 135, 180, 225, 270, 315
	38	90	0, 45, 90, 135, 180, 225, 270, 315
	50	135	0, 45, 90, 135, 180, 225, 270, 315
	63	180	0, 45, 90, 135, 180, 225, 270, 315
	75	225	0, 45, 90, 135, 180, 225, 270, 315
	88	270	0, 45, 90, 135, 180, 225, 270, 315
	100	315	0, 45, 90, 135, 180, 225, 270, 315
8 x 8 Walker Delta	98	0	Within a plane, uniformly distributed from 0° to 360° (45° interval); relative offset between two consecutive planes
	98	45	
	98	90	
	98	135	
	98	180	
	98	225	
	98	270	
	98	315	
8 x 10 Hybrid	13	0	0, 36, 72, 108, 144, 180, 216, 252, 288, 324
	25	45	0, 36, 72, 108, 144, 180, 216, 252, 288, 324
	38	90	0, 36, 72, 108, 144, 180, 216, 252, 288, 324
	50	135	0, 36, 72, 108, 144, 180, 216, 252, 288, 324
	63	180	0, 36, 72, 108, 144, 180, 216, 252, 288, 324

	75	225	0, 36, 72, 108, 144, 180, 216, 252, 288, 324
	88	270	0, 36, 72, 108, 144, 180, 216, 252, 288, 324
	100	315	0, 36, 72, 108, 144, 180, 216, 252, 288, 324
	13	0	0, 36, 72, 108, 144, 180, 216, 252, 288, 324
	25	45	0, 36, 72, 108, 144, 180, 216, 252, 288, 324
9 x 9 Hybrid	11	0	0, 40, 80, 120, 160, 200, 240, 280, 320
	22	40	0, 40, 80, 120, 160, 200, 240, 280, 320
	33	80	0, 40, 80, 120, 160, 200, 240, 280, 320
	44	120	0, 40, 80, 120, 160, 200, 240, 280, 320
	56	160	0, 40, 80, 120, 160, 200, 240, 280, 320
	67	200	0, 40, 80, 120, 160, 200, 240, 280, 320
	78	240	0, 40, 80, 120, 160, 200, 240, 280, 320
	89	280	0, 40, 80, 120, 160, 200, 240, 280, 320
	100	320	0, 40, 80, 120, 160, 200, 240, 280, 320
9 x 9 Walker Delta	98	0	Within a plane, uniformly distributed from 0° to 360° (40° interval); relative offset between two consecutive planes
	98	40	
	98	80	
	98	120	
	98	160	
	98	200	
	98	240	
	98	280	
	98	320	
9 x 10 Hybrid	11	0	0, 36, 72, 108, 144, 180, 216, 252, 288, 324
	22	40	0, 36, 72, 108, 144, 180, 216, 252, 288, 324
	33	80	0, 36, 72, 108, 144, 180, 216, 252, 288, 324
	44	120	0, 36, 72, 108, 144, 180, 216, 252, 288, 324
	56	160	0, 36, 72, 108, 144, 180, 216, 252, 288, 324
	67	200	0, 36, 72, 108, 144, 180, 216, 252, 288, 324
	78	240	0, 36, 72, 108, 144, 180, 216, 252, 288, 324
	89	280	0, 36, 72, 108, 144, 180, 216, 252, 288, 324
	100	320	0, 36, 72, 108, 144, 180, 216, 252, 288, 324
10 x 10 Hybrid	10	0	0, 36, 72, 108, 144, 180, 216, 252, 288, 324
	20	36	0, 36, 72, 108, 144, 180, 216, 252, 288, 324
	30	72	0, 36, 72, 108, 144, 180, 216, 252, 288, 324
	40	108	0, 36, 72, 108, 144, 180, 216, 252, 288, 324
	50	144	0, 36, 72, 108, 144, 180, 216, 252, 288, 324
	60	180	0, 36, 72, 108, 144, 180, 216, 252, 288, 324
	70	216	0, 36, 72, 108, 144, 180, 216, 252, 288, 324
	80	252	0, 36, 72, 108, 144, 180, 216, 252, 288, 324
	90	288	0, 36, 72, 108, 144, 180, 216, 252, 288, 324

Nanosatellite S&F Communication Systems for Remote Data Collection Applications

	100	324	0, 36, 72, 108, 144, 180, 216, 252, 288, 324
10 x 10 Walker Delta	10	0	Within a plane, uniformly distributed from 0° to 360° (36° interval); relative offset between two consecutive planes
	20	36	
	30	72	
	40	108	
	50	144	
	60	180	
	70	216	
	80	252	
	90	288	
	100	324	